Early Diagnosis of Cancer Using Light Scattering Spectroscopy

by

Vadim Backman

M.S., Physics, Massachusetts Institute of Technology
(1998)

SUBMITTED TO THE HARVARD UNIVERSITY – MIT DIVISION OF
HEALTH SCIENCES AND TECHNOLOGY IN PARTIAL FULFILLMENT OF
THE REQUIREMENTS FOR THE DEGREE OF DOCTOR OF PHILOSOPHY
IN MEDICAL ENGINEERING AND MEDICAL PHYSICS

ARCHIVES

at the
Massachusetts Institute of Technology
May 2001
[June 2001]

© 2001 Massachusetts Institute of Technology. All rights reserved.
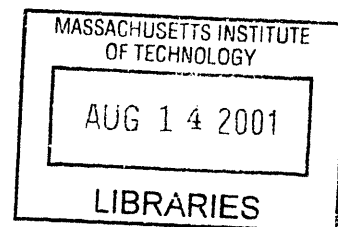
Signature of Author: _____
The Harvard-MIT Division of Health Sciences and Technology
May 2001

Certified by: _____
Michael S. Feld, Ph.D.
Professor, Department of Physics, MIT
Thesis Supervispor

_____
Lev T. Perelman, Ph.D.
Assistant Professor, Harvard Medical School
Thesis Supervisor

Accepted by: _____
Martha L. Gray, Ph.D.
Director, The Harvard-MIT Division of Health Sciences and Technology
Edward Hood Taplin Professor of Medical Engineering and
Electrical Engineering, MIT

Early Diagnosis of Cancer with Light Scattering Spectroscopy

by

Vadim Backman

Submitted to the Harvard-MIT Division of Health Sciences and Technology in partial fulfillment of the requirements for the Degree of Doctor of Philosophy in Medical Engineering and Medical Physics, May 2001

Abstract

This thesis presents a novel optical technique, light scattering spectroscopy (LSS), developed for quantitative characterization of tissue morphology as well as *in vivo* detection and diagnosis of the diseases associated with alteration of normal tissue structure such as precancerous and early cancerous transformations in various epithelia. LSS employs a wavelength dependent component of light scattered by epithelial cells to obtain information about subcellular structures, such as cell nuclei. Since nuclear atypia is one of the hallmarks of precancerous and cancerous changes in most human tissues, the technique has the potential to provide a broadly applicable means of detecting epithelial precancerous lesions and noninvasive cancers in various organs, which can be optically accessed either directly or by means of optical fibers.

We have developed several types of LSS instrumentation including 1) endoscopically compatible LSS-based fiber-optic system; 2) LSS-based imaging instrumentation, which allows mapping quantitative parameters characterizing nuclear properties over wide, several cm^2, areas of epithelial lining; and 3) scattering angle sensitive LSS instrumentation (a/LSS), which enables to study the internal structure of cells and their organelles, i.e. nuclei, on a submicron scale. Multipatient clinical studies conducted to test the diagnostic potential of LSS in five organs (esophagus, colon, bladder, cervix and oral cavity) have shown the generality and efficacy of the technique and indicated that LSS may become an important tool for early cancer detection as well as better biological understanding of the disease.

Thesis Supervisors: Michael S. Feld, Ph.D., Professor, MIT
                       Lev T. Perelman, Ph.D., Assistant Professor, HMS

Acknowledgements

First of all, I must sincerely thank my research advisors Prof. Michael S. Feld and Prof. Lev T. Perelman for their scientific guidance, support, and personal attention. It is not an overstatement to say that it was my great pleasure and privilege to work with you and have you as my mentors and friends. Michael, thank you for the opportunity to work in your lab and learn so much about research. Thank you for your drive, optimism, and scientific and personal guidance. Lev, I am grateful to my fortune for having the opportunity to work with you and learn not only about science, but also about life.

This thesis could not possibly be completed without contribution from many people. I thank all the members of the Spectroscopy Laboratory at MIT. I thank Dr. Irving Itzkan for his personal attention and for helping me during some of the most difficult periods of my graduate career. I thank Dr. Ramachandra Dasari for his constant scientific and personal support. I thank Dr. Kamran Badizadegan and Dr. Charles Boone for being my colleagues and for providing me with the crucial understanding of pathology. I would like to thank Dr. Rajan Gurjar for being my friend and partner. This work could not be completed without your hard work. I thank my friends and colleagues Dr. Venkatesh Gopal, Maxim Kalashnikov, Dr. Irene Georgakoudi, and Dr. Adam Wax who contributed immensely to the project. Special thanks goes to my friend Marcus Zaichick Mueller, who is a true optimist in the bottom of his heart, for shaping and sharing my vision on life. I would like to thank our clinical collaborators Dr. Stanley Shapshay, Dr. Michael Wallace, Dr. Fitzmaurice, Dr. Crowford, Dr. Van Dam. Special thank to Dr. Stanley Shapshay for letting me spend some time in his department at NEMC and learn a great deal about the head and neck surgery. I thank Dr. Martha Gray for constant support throughout my years at HST. It is thanks to you I will remember my years at HST as the best time of my life.

Saving the best for last. I thank my family for all the best that I am, because I owe it to you, and I ask you to forgive me for the rest, because it is against all you have done and I owe it to myself. There are no words that can describe how grateful I am to my mother, who passed away too early to see me being called a Doctor. You know that I thank you every single day of my life in my thoughts. If I try to put in words all my thanks to my father, it will take longer than the rest of my thesis. So let me just say that I love you and I owe all my success to you. I thank my sister for the joy she brings to my life. I thank Lev and Marina for their patience and support. I love you all. Finally, I thank my very special friend Eugenia for being by my side and for supporting me during the most difficult periods of my life. You made me keep running. You fill every single day of my life with happiness. This thesis is your accomplishment as much as it is mine. I could not have done this without you.

Table of Contents

List of Figures

5

List of Tables

Chapter 1

Introduction

Significant advances in medical diagnostic technologies have been achieved over the last decades in such areas as magnetic resonance imaging (MRI) and spectroscopy, computed tomography (CT), nuclear medicine and ultrasound. However, these advances largely focused on structural or anatomic changes at the organ or tissue level. There is clearly a need and opportunity to stimulate the development of novel diagnostic technologies that exploit our current knowledge of the cellular and sub-cellular bases of disease. These technologies will have great implications on prevention and detection of diseases as well as targeted therapy. Apparently, the diagnostic techniques applicable *in situ* (inside human body) that can provide structural and functional information about the tissue at the cellular and subcellular level, the kind of information that is currently obtainable using *in vitro* or techniques requiring tissue removal only, would be very useful.

Over the last decade several attempts have been made to develop methods to study human cells *in situ* non-invasively not only to provide accurate diagnosis but also to better understand the genesis of disease at the cellular level. Optical

methods have been shown to be very powerful tools for studying living tissues *in situ*. Elastic [Mourant et al., 1995; Yodh et al., 1995] and Raman [Rava et al., 1991; Manoharan et al., 1998; Buschman et al., 1999; Deinum et al., 1999] scattering, absorption [Anderson wt al., 1981; Patterson et al., 1987], and fluorescence [Alfano et al., 1989; Richards-Kortum et al., 1989; Schomacker et al., 1992; Zonios et al., 1998; Georgakoudi et al., 2001] of light can provide structural and functional information about the tissue. This information, in turn, can be used to diagnose and detect various diseases, including early cancer.

In this thesis we present a novel technology based on light scattering spectroscopy (LSS), which enables to identify and characterize premalignant abnormalities or other early changes in human tissues on cellular and subcellular level. Light scattering has long been used to study great variety of materials ranging from isolated atoms to complex condensed matter systems [Newton, 1969]. Biological tissue is yet another example of a complex system that can be studied with scattered light. One exciting application of LSS is non-invasive or minimally invasive detection of precancerous or early cancerous changes in human epithelium, a richly cellular layer lining the inner and outer surfaces of the body. Detection and diagnosis of such conditions is particularly important because most tumors are readily treatable if diagnosed at an early stage. Unfortunately, many forms of precancerous lesions are difficult to detect using conventional diagnostic techniques.

Cancers of epithelial origin, which represent more than 85% of all cancers [Landis et al., 1999], are generally preceded by a precursor condition known as dysplasia [Cotran et al., 1994]. Dysplasia is confined to the epithelial layer, and is characterized by cellular proliferation, abnormal appearance of the cell nuclei, and changes in tissue microarchitecture. In many cases the dysplastic tissue is flat and

indistinguishable from the surrounding non-dysplastic tissue. Since it cannot be distinguished, detection of such dysplastic tissue is based on random biopsy. The biopsied sample is then fixed, stained, and examined by a surgical pathologist. Microscopic examination of biopsy specimens of dysplastic tissue reveals characteristic morphologic changes in cell nuclei, which are hallmarks of dysplasia and early cancer. The nuclei become enlarged, crowded, hyperchromatic (abnormally darkly stained). The structure and organization of the cell nuclei is altered as well. Although the gross (macroscopic) appearance of dysplastic lesions in different organs and different types of epithelium can vary significantly, these cytologic changes are common to all types of precancerous and early cancerous conditions.

Despite these seemingly well-defined differences between normal and dysplastic tissues, there can be significant disagreement among even expert pathologists on the diagnosis. In some cases the inter-observer agreement can be as low as 50% [Riddell et al., 1983; Reid et al., 1988; Cotran, 1994]. The reason for this is that pathology is partly science and partly art. Pathologists do not have the advantage of using objective quantitative information. The diagnosis, the choice of treatment and, consequently, the patient's well-being depend on a pathologist's ability to recognize a morphological pattern known to be associated with the disease.

Approaches to the diagnosis of disease based on techniques enabling objective and reproducible measurements can supplement or even surpass standard methods of histological diagnosis. Here we discuss LSS-based methods to probe epithelial morphology in living tissues, which do not require tissue removal.

17

1.1 Optical Techniques in Medicine

Biomedical optics is a rapidly growing field that uses optical techniques for the purposes of biology and medicine. The applications of biomedical optics can be divided into two broad categories: therapeutic and diagnostic.

1.1.1 Therapeutic Applications of Biomedical Optics

Therapeutic applications employ the "effect of light on tissue" [Parrish et al, 1991]. These applications can be classified according to the type of changes induced in the tissue by light: mechanical, chemical, thermal, etc. Some of the major applications include laser ablation [Dixon et al., 1987, Itzkan et al, 1995] (mechanical changes), photodynamic therapy [Dougherty, 1989] (chemical changes), and laser hyperthermia [Anghilery et al, 1986] (thermal changes). Laser ablation usually uses short high power pulses of laser light. They result in removal of the irradiated tissue. For example, PRK, a modality of laser ablation, is used to reshape the cornea of the eye. An important modification of this technique uses laser induced shock waves to ablate the tissue with minimal effect on the surrounding tissues [Itzkan et al, 1995]. This results in clean minimally invasive surgical intervention. Photodynamic therapy uses laser light to generate toxic chemicals from endogenous or exogenous molecules that mark a diseased tissue. This results in cellular necrosis and tissue destruction. Laser hyperthermia uses light at targeted wavelengths to increase tissue, i.e.tumor, temperature and induce thermal shock that again leads to cellular necrosis and tissue destruction.

1.1.2 Diagnostic Applications of Biomedical Optics

Several modalities of non-invasive or minimally invasive biomedical optical diagnosis, i.e. diffuse reflectance spectroscopy (DRS) [Farrell et al., 1992; Zonios et al., 1999], laser induced fluorescence (LIF) spectroscopy [Zonios et al., 1996; Bigio et al., 1997], Raman spectroscopy [Manoharan et al., 1998], and light scattering spectroscopy (LSS) [Perelman et al., 1998; Backman et al., 2000], have been developed and have shown favorable results in the diagnosis of variety of diseases, particularly precancerous and early cancerous changes in various tissues. The applications of biomedical optics generally employ the "effect of tissue on light". One of the major advantages of optical diagnostic techniques is the fact that they can provide objective information about the tissue without need for tissue removal and in real time.

While most human organs can be examined by means of optical techniques, they are particularly suitable to diagnose pathological conditions in the organs easily accessed by optical fibers such as the organs of gastrointestinal, respiratory, urinary, and genital tracts. A tissue site or, in imaging applications, a wide area of tissue is irradiated by monochromatic or continuous wavelength light and light returned from or transmitted through the tissue is collected and analyzed. Thus, some tissue attributes can be revealed. These attributes include (1) macroscopic properties (architectural disorganization, changes in surface morphology, cell crowding, etc.), (2) cellular properties (enlargement and hyperchromasia of the cell nuclei, increased concentration of organelles, etc.), and (3) molecular (NAD/NADH shift, decreased activity of ferrochelatase, presence of abnormal proteins, etc.). Each of the spectroscopic techniques is sensitive to specific tissue

attributes. For example, fluorescence spectroscopy and Raman spectroscopy are sensitive to molecular attributes while diffuse reflectance spectroscopy and light scattering spectroscopy are well suited to provide information about morphological structure of the tissue at the cellular and macroscopic levels.

1.1.2.1 Spectral Diagnosis Using Elastically Scattered Light

Diagnosis of precancerous and early cancerous changes in various tissues using elastically scattered light has recently attracted significant research interest. Superficial targets, such as the uterine cervix and skin, can be accessed by open field optics. Epithelial tissues of some other hollow organs, such as esophagus or colon, can be accessed by means of optical fiber probes delivered through endoscopes and catheters. In any case, the tissue site under study is irradiated by monochromatic or broadband light, and the reflected light is collected and analyzed. Thus, some tissue attributes can be revealed. The ability to extract quantitative information in living cells, *in situ*, without perturbing them, could be used to study biophysical processes in living systems and to monitor morphological and physiological changes such as precancerous or cancerous conditions. Currently, such information can only be obtained by tissue removal or scraping. Techniques such as microscopy and flow cytometry can probe intracellular structure, but applying them *in situ* is not possible.

Light Scattering in Biomedical Optics

Studies have been conducted to relate morphological and light scattering properties of cell structures. Beauvoit et al. [Beauvoit et al., 1998] have measured

the reduced scattering and absorption coefficients of the liver. They showed that most of the scattering from the liver is attributed to the mitochondrial content of the hepatocytes. Schmitt and Kumar [Schmitt et al., 1996] measured the variation in the refractive index of fibroblasts and showed the evidence of a broad distribution of scatterers ranging in size from 0.2 to 10 μm. Beuhtan et al. [Beuthan et al., 1996] showed that the cell nucleus and membranes have refractive index significantly higher than that of the other subcellular structures. Sloot [Sloot et al., 1988] observed light scattering from lymphocytes and reported that the nuclei gave the main contribution to the forward scattering. Mourant and coworkers [Mourant et al., 1998] showed that the nucleus scatters more in the forward direction while smaller particles scatter at larger angles. Importantly, these results also showed that the scattering takes place due to the structures within the cells rather than from the cell surface. Most of these studies were done on cell suspensions. Hielscher and coworkers [Hielscher et al., 1997] used polarized back-scattered light to obtain images of biological cell suspensions. It was shown that in fibroblast, mitochondria were the strongest scatterers. Differences in mitochondria concentration were observed between healthy and diseased cells and tissues. However, neither of these works reported a technique capable of measuring sizes and refractive indexes of cells and their organelles *in situ*.

Diffuse Reflectance Spectroscopy

Diffuse reflectance spectroscopy (DRS) is a diagnostic modality of biomedical optics, which employs light returned from a tissue by means of elastic scattering. In DRS, white light is delivered to the tissue by means of an optical fiber probe. The scattered light is returned to a detector, usually by means of adjacent collection fibers, and its spectrum measured over a broad wavelength

range (e.g. 360-800 nm). Since light propagation in tissue is governed by elastic scattering and absorption, the reflected signal can provide information about these tissue properties. This, in turn, can give information about particular types of tissue absorbers (hemoglobin, for example) and scatterers (extracellular matrix, mitochondria, cell nuclei, etc.). Several reviews of this technique have appeared [Bigio et al., 1997; Farrell et al., 1992]. Researchers at G.R. Harrison Spectroscopy Laboratory have developed DRS techniques for characterizing and diagnosing adenomatous polypoid (precancerous) changes in human colon *in vivo* [Zonios et al., 1999], and for characterizing atherosclerotic lesions [Van de Pol et al., 1999]. Other groups have employed DRS to detect precancerous and cancerous transformations in organs such as the breast [Bigio et al., 2000], esophagus [Lovat et al., 2000], bladder [Mourant et al., 1995; Koenig et al., 1998], to characterize the orientation of collagen fibers and the integrity of connective tissues [Ferdman et al., 1993], and to measure tissue oxygenation *in vivo* [Liu et al, 1995].

1.1.2.2 Biomedical Diagnosis Using Fluorescence Spectroscopy

Fluorescence spectroscopy uses a monochromatic laser source to illuminate the tissue, and the fluorescence signal at the wavelengths longer than that of the illumination is collected. The signal is substantially weaker than that of the diffuse reflectance. While reflectance spectroscopy is best suited to detect changes in tissue morphology, fluorescence signals depend on the presence of various tissue fluorophores such as collagen, elastin, NADH, and porphyrins. Reviews of this technique can be found in [Bigio et al., 1997; Zonios et al., 1998]. Fluorescence spectroscopy enables to obtain information about chemical composition of the

tissue. It has been applied to detect atherosclerosis of aorta and coronary artery [Richards-Kortum et al., 1991; Van de Poll, et al., 1999], dysplasia in bladder [Arendt et al., 1999], adenomatous polyps in colon [Kapadia et al., 1990; Zonios et al., 1996; Mahadevan-Jansen et al., 1998], brain stroke [Schantz et al., 1998], and cancers in esophagus [Vo-Dinh et al., 1998], dysplasia in eaophagus [Georgakoudi et al., 2001], breast [Ganesan et al., 1998], cervix [Mitchell et al., 1999; Georgakoudi et al., 2001], oral cavity [Schantz et al., 1998], and bronchi [Kurie et al., 1998].

1.1.2.3 Biomedical Diagnosis Using Raman Spectroscopy

A Raman spectrum is generated by a frequency shift in the excitation light, which is due to the vibrations and rotations of the molecules within a sample. A fiber delivers laser light at an infrared wavelength. The back-scattered light is collected by a fiber bundle and is sent to the spectrometer. Since most biological molecules are Raman-active and have distinctive spectral features, Raman spectra can be used to obtain concentrations of various chemical tissue components such as proteins, glucose, lipids, nucleic acids, and many others. This technique has been used to diagnose breast malignancies [Manoharan et al., 1998], atherosclerosis in coronary artery [Brennan et al., 1997] and to estimate the glucose levels in blood [Berger et al., 1997].

1.1.2.4 Biomedical Optical Diagnostic Imaging

As discussed earlier, optical techniques such as fluorescence spectroscopy, Raman spectroscopy, and the spectroscopy of elastically scattering light provide

structural and biochemical information about the tissue, and have been shown to be powerful tools for studying living tissues *in situ*. A number of optical imaging modalities based on these techniques have been developed for near-surface diagnostic imaging.

Confocal Microscopy Imaging

Confocal microscopy eliminates multiple scattering in turbid samples, producing thin section images with high resolution and contrast. The images produced are due to light scattered backwards at interfaces of different refractive index. Multiple scattered light is rejected by means of a pinhole, which selects only light travelling in straight-line paths. The location and size of the pinhole, among other variables, determine the depth and lateral resolution of the system, Several research groups have demonstrated the use of confocal scanning microscopes for imaging human and animal tissues, both *in vivo* and *ex vivo* [Petroll et al., 1996]. Skin and oral mucosa are easily accessible with this technique. The technique has also been applied to image bladder [Koenig et al., 1999], embryo [Kulesa et al., 1999; Gonzalez et al., 1999], kidney [Kneen et al., 1999], skin [Rajadhyaksha et al., 1998], and retina [Vierra et al., 1999]. Reported image depth depended on the type of tissue studied, and ranged from 350 microns to 1 mm, with a lateral resolution of 0.5-1 microns and axial resolution of 3-5 microns.

Optical Coherence Tomography

Optical coherence tomography (OCT) utilizes the coherent properties of light to obtain cross sectional images of scattering media such as living tissue. This technique employs low coherence light (i.e. light with a short coherence length) in

a Michelson interferometer. The specimen is placed at the end of the sample arm. Backscattered light is combined with light returning from the mirror in the reference arm. Constructive interference occurs only when the distance to a scattering interface in the sample matches that to the reference mirror within the coherence length. Depth is probed by scanning the reference mirror position and detecting the envelope of the interference signal. Cross-sectional images can be built up from multiple axial scans at different transverse positions in the sample. As in confocal microscopy, image formation is again due to refractive index change. In turbid tissues, imaging depths of the order of 1 mm can be achieved, with resolution of the order of several tens of microns. OCT has been used to obtain *in vivo* images of clear tissues such as the human eye [Hee et al., 1995] and turbid tissues such as esophageal mucosa [Kobayashi et al., 1998]. It has also been used to image intra-arterial walls, arthritic cartilage and gynecologic neoplasms, and *in-vitro* frog embrios [Fujimoto et al., 1999; Boppart et al., 1998; Pitris et al., 1999].

Recently, a related set of techniques, based on interference light scattering spectroscopy has been developed in G.R. Harrison Spectroscopy Laboratory. These techniques combine dispersion spectroscopy with low-coherence interferometry [Yang et al., 1999; Yang et al., 2000; Yang et al., 2001].

Polarization-based Imaging

Several groups have used polarized light to image superficial tissues. Anderson et al. [Anderson et al., 1991] used polarized light to enhance contrast in skin images by separating the specular and multiple-scattered components of light emerging from the skin surface. Demos et al. [Demos et al., 1996; Demos et al., 1997] showed that polarized gating can enhance the images of surface and sub-

surface structures in biological tissues. Jacques et al. used polarized light to image superficial layers of human skin [Jacques et al., 2000]. Bartel and Heischler [Bartel et al., 2000] have imaged the spatial distribution of polarized light returned to the surface of a random media, such as a suspension of polystyrene micro-beads or cells, by means of scattering. They measured the degree of polarization retained after multiple scattering events, and compared the experimental results with those of models based on a Monte Carlo algorithm that computes two-dimensional elements of the diffuse backscattering Mueller matrix. They showed that model predictions and experimental data were in good agreement, and that some properties of the scattering particles comprising the medium can be inferred by measuring the spatial distribution of the polarized scattered light.

The above techniques all create physical images, based on refractive index changes at interfaces within the medium, and all are limited in resolution by optical wavelength considerations (so-called diffraction limit). In this thesis we introduce a novel modality of biomedical imaging based on LSS to study superficial tissues such as epithelia. It will be shown that LSS imaging allows exceeding the diffraction limit in a sense that it enables to measure the sizes of scattering objects, such as cell organelles, with sub-wavelength accuracy.

1.2 Organization of the Thesis

This thesis presents a novel optical technique, light scattering spectroscopy (LSS), developed for quantitative characterization of tissue morphology as well as *in vivo* detection and diagnosis of certain diseases associated with alteration of normal tissue structure such as precancerous and early cancerous transformations

in various epithelia. LSS employs a wavelength dependent component of light scattered by epithelial cells to obtain information about subcellular structures, such as cell nuclei. Since nuclear atypia is one of the hallmarks of precancerous and cancerous changes in most human tissues, the technique has the potential to provide a broadly applicable means of detecting epithelial precancerous lesions and noninvasive cancers in various organs, which can be optically accessed either directly or by means of optical fibers.

The thesis consists of eight chapters. Chapter 2 provides a brief introduction to histology of human epithelia and mucosal tissues as well as to histopathology of precancerous and early cancerous transformations.

Chapter 3 introduces the basics of light scattering and discusses the relationship between the structure of cells and tissues presented in Chapter 2 and their light scattering properties.

Chapter 4 introduces light scattering spectroscopy. The basic principles of LSS are discussed in this chapter. LSS aims to distinguish between a single scattering component and a multiple scattering component (diffusive background) of light returned from a tissue by means of elastic scattering. The spectrum of the single scattering component is then analyzed to provide quantitative information about cell and tissue structure. Chapter 4 discusses the methods of analysis of the single scattering component.

Chapter 5 discusses methods to remove the diffusive background. Experiments with tissue models and *ex vivo* and *in vivo* tissues testing principles and capabilities of LSS are discussed as well.

Chapter 6 builds on the foundations presented in Chapters 4 and 6. It reports the multipatient clinical studies showing that LSS enables to diagnose precancerous changes in four different organs (esophagus, colon, bladder, and oral cavity), thus, illustrating the generality and efficacy of the technique.

Chapter 7 presents a novel biomedical imaging modality based on LSS. LSS imaging allows probing the structure of the epithelial cell nuclei over wide areas of tissue. Studies with *ex vivo* tissues are presented.

Chapter 8 introduces another modality of LSS, scattering angle sensitive light scattering spectroscopy (a/LSS), that enables to probe the internal structure of cells and their organelles, i.e. cell nuclei, at a submicron scale.

Finally, Chapter 9 summarizes the main results of the work and discusses some of the potential future applications of LSS technology.

References

Alfano RR, Prahdan AA, Tang GC, Wahl SJ, "Optical spectroscopic diagnosis of cancer and normal breast tissues", *J. Opt. Soc. Amer. B* **6**(5) 1015-1023 (1989).

Anderson RR and Parish JA "The optics of human skin" *J. Invest. Dermatol.* **77**, 13-19 (1981).

Anderson RR, "Polarized light examination and photography of the skin", *Arch. Dermatol.*, **127**, 1000-1005, (1991).

Andersson-Engels S, Klinteberg C, Svanberg K, Svanberg S, "In vivo fluorescence imaging for tissue diagnostics", *Phys. Med. Biol.*, **42**, 815-24 (1997).

Anghilery LJ and Robert J, *Hyperthermia in Cancer Treatment*, (CRC Press, Boca Raton, 1986).

Arendt J T, "Detection of early cancerous changes and cancer in bladder tissue by autofluorescence and reflectance," V-1, thesis, School of Ohio State University (1999).

Backman V, Gurjar R, Badizadegan K, Zonios G, Itzkan I, Dasari RR, Crawford JM, Van Dam J, Perelman LT and Feld MS, "Light Scattering Spectroscopy for Early Cancer Diagnosis", *Laser Spectroscopy*, World Scientific Publishing Co., Rainer Blatt *et al.* ed., 286-295 (1999).

Backman V, Gurjar R, Badizadegan K, Itzkan I, Dasari R, Perelman LT, Feld MS, "Polarized light scattering spectroscopy for quantitative measurement of epithelial structures in situ", *IEEE J. Sel. Topics Quantum Electron*, **5**, 1019-1027 (1999).

Backman V, Wallace MB, Perelman LT, Arendt JT, Gurjar R, Muller MG, Zhang Q, G. Zonios G, Kline E, McGillican T, Shapshay S, Valdez T, Van Dam J, Badizadegan K, Crawford JM, Fitzmaurice M, Kabani S, Levin HS, Seiler M, Dasari RR, Itzkan I and Feld MS, "Light scattering spectroscopy: a new technique for clinical diagnosis of precancerous and cancerous changes in human epithelia", *Nature*, **406**, 35-36 (2000).

Backman V, L.T. Perelman, J.T. Arendt, R. Gurjar, M.G. Muller, Q. Zhang, G. Zonios, E. Kline, T. McGillican, T. Valdez, J. Van Dam, M. Wallace, K. Badizadegan, J.M. Crawford, M. Fitzmaurice, S. Kabani, H.S. Levin, M. Seiler, R.R.Dasari, I. Itzkan, and M. S. Feld, "Light Scattering Spectroscopy: A New Technique for Clinical Diagnosis of Precancerous And Cancerous Changes in Human Epithelia", *Lasers in Life Sciences*, in press (2001).

Bartel S and Hielscher AH. "Monte Carlo simulations of the diffuse backscattering Muller matrix for highly scattering media", *App Opt*, **39**, 1580-1588 (2000).

Beauvoit B, Chance B, "Time-resolved spectroscopy of mitochondria, cells and tissues under normal and pathological conditions", *Mol. Cell. Biochem.*, **184**, 445-55 (1998).

Berger AJ, Itzkan I, Feld MS, "Feasibility of measuring blood glucose concentration by near-infraredRaman spectroscopy", *Spectrochim Acta A Mol Biomol Spectrosc*, **53A**, 287-92 (1997)

Beuthan J, Minet O, Helfmann J, Herrig M and Muller G, "The spatial variation of the refractive index in biological cells", *Phys. Med. Biol.*, **41**, 369-382 (1996).

Bigio IJ and Mourant JR, "Ultraviolet and visible spectroscopies for tissue diagnostics: fluorescence spectroscopy and elastic-scattering spectroscopy", *Phys Med Biol*, **42**, 803-14 (1997).

Bigio IJ, Bown SG, Briggs G, Kelley C, Lakhani S, Pickard D, Ripley PM, Rose IG, Saunders C. "Diagnosis of breast cancer using elastic-scattering spectroscopy: preliminary clinical results." *J. Biomed. Optics.*, **5**, 221-228 (2000).

Boppart SA, Bouma BE, Pitris C, Southern JF, Brezinski ME, Fujimoto JG, "In vivo cellular optical coherence tomography imaging", *Nature Medicine*, **4**, 861-5 (1997).

Brennan JF 3rd, Romer TJ, Lees RS, Tercyak AM, Kramer JR Jr, Feld MS, "Determination of human coronary artery composition by Raman spectroscopy", *Circulation*, **96**, 99-105 (1997).

Brown GL, McEwan, Pratt M. "Macromolecular weight and size of deoxypentose nucleic acids", *Nature*, **176**, 161-162 (1955).

Buschman HPJ, Motz JT, Fitzmaurice M, van der Laarse A, Bruschke AV, Feld MS, "Human Coronary Atherosclerosis Studied by Morphological NIR Raman Confocal Microscopy", SPIE *Proceedings*, **3608**: 7-11 (1999).

Bruce J, Berne and Robert Pecora, *Dynamic light scattering - with applications to chemistry, biology and physics*, (Wiley New York 1976).

Chernyshev AV, Prots VI, Doroshkin AA and Maltser VP, "Measurement of scattering properties of individual particles with a scanning flow cytometer", *App. Opt.*, **34**, 6301-6309 (1995).

Cotran RS, Robbins SL, Kumar V, *Robbins Pathological Basis of Disease* (W.B. Saunders Company, Philadelphia, 1994).

Dainty JC ed., *Laser Speckle and related phenomena*, (Springer-Verlag, Berlin 1975).

Davies HG, Deeley EM, Denby EF, "Attempts at measurement of lipid, nucleic acid and protein content of cell nuclei by microscope-interferometry", *Exp. Cell Res.*, Suppl. 4, 136-149 (1957).

Demos SG and Alfano RR, "Temporal gating in highly scattering media by the degree of optical polarization ", *Opt. Lett.*, **21**, 161-163 (1996).

Demos S and Alfano RR, "Optical polarized imaging", *App. Opt.*, **36**, 150-155 (1997).

Deinum G, Rodriguez D, Romer TJ, Fitzmaurice M, Kramer JR, Feld MS. "Histological Classification of Raman Spectra of Human Coronary Atherosclerosis Using Principal Component Analysis", *Applied Spectroscopy*, **58**(8): 938-942 (1999).

Dixon J, *Surgical Applications of Lasers*, (Year Book Publisher, Chicago, 1987).

Dougherty TJ, *Oncology*, **3**, 67 (1989).

Farrell TJ, Patterson MS, Wilson B, "A diffusion theory model of spatially resolved, steady state diffuse reflectance for the noninvasive determination of tissue optical properties in vivo", *Med. Phys.*, **19**, 879-888 (1992).

Ferdman AG, Yannas IV, "Scattering of light from histologic sections – a new method for the analysis of connective tissue", *J Invest. Derm.*, **100**, 710-716 (1993).

Freysz E, Pouligny B, Argoul F and Arneodo A, "Optical wavelet transform of fractal aggregates", *Phys. Rev. Lett.* **64**, 745 (1990).

Fujimoto JG, Boppart SA, Tearney GJ, Bouma BE, Pitris C, Brezinski ME, "High resolution in vivo intra-arterial imaging with optical coherence tomography", *Heart.* **82**, 128-133 (1997).

Ganesan S, Sacks PG, Yang Y, Katz A, Al-Rawi M, Savage HE, Schantz SP, Alfano RR, "Native fluorescence spectroscopy of normal and malignant epithelial cells", *Cancer Biochem Biophys.*, **16**, 365-73 (1998).

Georgakoudi I, Jacobson BC, Backman V, Wallace M, Muller M, Zhuang Q, Badizadegan K, Sun D, Thomas G, Van Dam V, Feld MS, "The Combination of Fluorescence, Diffuse Reflectance, and Light Scattering Spectroscopy for the Improved Detection of Low- and High-grade Dysplasia in Patients with Barrett's Esophagus ", *Gastrointerology.* in press (2001).

Georgakoudi I, Sheets EE, Müller MG, Backman V, Crum CP, Badizadegan K, Dasari RR, Feld MS, "Tri-Modal Spectroscopy as a Tool for the Detection and Biochemical/Morphological Characterization of Cervical Pre-Cancers *In Vivo*", *Obstet. Gynecol.*, submitted (2001).

Giglio M, Carpineti M and Vailati A, "Space intensity correlations in the near field of the scattered light: a direct measurement of the density correlation function g(r)", *Phys. Rev. Lett.*, **85**, 1416 (2000).

Gonzalez S, Rajadhyaksha M, Gonzalez-Serva A, White WM, Anderson RR, "Confocal reflectance imaging of folliculitis in vivo: correlation with routine histology", *J Cutan. Pathol.*, 26, 201-5 1999).

Gurjar R, Backman V, Badizadegan K, Dasari R, Itzkan I, Perelman LT, Feld MS, "Functional Imaging of Human Epithelia with Polarized Light Scattering Spectroscopy", *Nature Medicine*, to be published (2001).

Hee MR, Izatt JA, Swanson EA, Huang D, Schuman JS, Lin CP, Puliafito CA, Fujimoto JG, "Optical coherence tomography of the human retina", *Arch Ophthalmol*, 113, 325-32 (1995).

Hielscher AH, Mourant JR, Bigio IJ, "Influence of particle size and concentration on the diffuse backscattering of polarized light from tissue phantoms and biological cell suspensions", *Appl. Opt.*, 36, 125-135 (1997).

Hielscher AH, Mourant JR, Bigio IJ, "Influence of particle size and concentration on the diffuse backscattering of polarized light from tissue phantoms and biological cell suspensions", *Appl. Opt.*, 36, 125-135 (1997).

Jacques, SL, Roman JR, Lee K, "Imaging Superficial Tissues with Polarized Light", *Las. Surg. Med.*, 26, 119-129 (2000).

Jain RK, "Determinants of tumor blood flow a review", 48, 2641-2658 (1988).

Ishimaru A, *Wave propagation and scattering in random media* (McGill, New York, 1978).

Itzkan I, Albagli D, Dark ML, Perelman LT, von Rosenberg C, Feld MS, *PNAS*, 92, 1960 (1995).

Kapadia CR, Cutruzzola FW, O'Brien KM, Stetz ML, Enriquez R, Deckelbaum LI, "Laser-induced fluorescence spectroscopy of human colonic mucosa. Detection of adenomatous transformation", *Gastroenterology*, 99, 150-7 (1990).

Kneen MM, Harkin DG, Walker LL, Alcorn D, Harris PJ, "Imaging of renal medullary interstitial cells in situ by confocal fluorescence microscopy", *Anat Embryol*, 200, 117-21 (1999).

Kobayashi K, Izatt JA, Kulkarni MD, Willis J, Sivak MV Jr, "High-resolution cross-sectional imaging of the gastrointestinal tract using optical coherence tomography: preliminary results", *Gastrointest Endosc*, 47, 515-23 (1998).

Koenig F, Larne R, Enquist H, McGovern FJ, Schomacker KT, Kollias N, Deutsch TF, "Spectroscopic measurement of diffuse reflectance for enhanced detection of bladder carcinoma", *Urology*, 51, 342-345 (1998).

Konig K, So PT, Mantulin WW, Tromberg BJ, Gratton E, "Two-photon excited lifetime imaging of autofluorescence in cells during UVA and NIR photostress", *J Microsc*, 183, 197-204 (1996).

Kulesa PM, Fraser SE, "Confocal imaging of living cells in intact embryos", *Methods Mol Biol*, 122, 205-222 (1999).

Kurie JM, Lee JS, Morice RC, Walsh GL, Khuri FR, Broxson A, Ro JY, Franklin WA, Yu R, Hong WK, "Autofluorescence bronchoscopy in the detection of squamous metaplasia and dysplasia in current and former smokers", J Natl Cancer Inst, 1, 991-5 (1998).

Lee L, Pappelis AJ, Pappelis GA, Kaplan HM, "Cellular and nuclear dry mass and area changes during human oral mucosa cell development", *Acta Cytol*, 17, 214-219 (1973).

Liu HL, Boas DA, Zhang YT, Yodh AG, Chance B, "Determination of optical properties and blood oxygenation in continuous NIR light", *Phys. Med. Bio.*, 40, 1983-1993 (1995).

Landis SH, Murray T, Bolden S, Wingo PA, "Cancer Statistics 1999", CA - A Cancer Journal for Clinicians, 49, 8-31 (1999).

Liu HL, Boas DA, Zhang YT, Yodh AG, Chance B, "Determination of optical properties and blood oxygenation in continuous NIR light", *Phys. Med. Bio.*, 40, 1983-1993 (1995).

Lovat LB, Pickard D, Novelli M, Ripley PM, Francis H, Bigio IJ, Bown SG, "A novel optical biopsy technique using elastic scattering spectroscopy for dysplasia and cancer in Barrett's esophagus", *Gastroint. Endoscopy*, 51, 4919 (2000).

Manoharan R, Shafer K, Perelman L, Wu J, Chen K, Deinum G, Fitzmaurice M, Myles J, Crowe J, Dasari RR, Feld MS, "Raman Spectroscopy and Fluorescence Photon Migration for Breast Cancer Diagnosis and Imaging", Photochemistry and Photobiology, 67, 15-22 (1998).

Mourant JR, Bigio IJ, Boyer J, Conn RL, Johnson T, Shimada T, "Spectroscopic diagnosis of bladder cancer with elastic light scattering spectroscopy", *Lasers Surg. Med.*, **17**, 350-357 (1995).

Mahadevan-Jansen A, Mitchell MF, Ramanujam N, Utzinger U, Richards-Kortum R, "Mevelopment of a fiber optic probe to measure NIR Raman spectra of cervical tissue in vivo", *Photochem Photobiol*, **68**, 427-31 (1998).

Mitchell MF, Cantor SB, Ramanujam N, Tortolero-Luna G, Richards-Kortum R, "Fluorescence spectroscopy for diagnosis of squamous intra-epithelial lesions of the cervix", *Obstet Gynecol*, **93**, 462-70 (1999).

Mourant J, Freyer A, Heilscher A, Eick D, Shen and Johnson T, "Mechanisms of light scattering from biological cells relevant to noninvasive optical-tissue diagnostics", *Appl. Opt.*, **37**, 3586-3593 (1998).

Newton RG, *Scattering Theory of Waves and Particles* (McGraw-Hill Book Company, New York, 1969).

Parrish JA and Wilson BC, *Photochem. Photobio.*, **53**, 731 (1991).

Patterson MS, Wilson BC, Feather JW, Burns DM, Pushka W, "The measurement of dihematoporhyrin ether concentration in tissue by reflectance spectrophotometry", *Photochem. Photobiol.* **46**(3) 337-343 (1987).

Perelman LT, Wu J, Itzkan I, Feld MS, "Photon migration in turbid media using path-integrals", *Phys. Rev. Lett.*, **72**, 1341-1344 (1994).

Perelman LT, Backman V, Wallace MB, Zonios G, Manoharan R, Nusrat A, Shields S, Seiler M, Lima C, Hamano T, Itzkan I, Van Dam J, Crawford JM and Feld MS, "Observation of periodic fine structure in reflectance from biological tissue: a new technique for measuring nuclear size distribution", *Phys. Rev. Lett.*, **80**, 627-630 (1998).

Petroll WM, Cavanagh HD, Jester JV, "Clinical confocal microscopy", *Curr. Opin. Ophthalmol.*, **9**, 59-65 (1998).

Pine DJ, Weitz DA, Chaikin PM and Herbolzheimer E, "Diffusing-wave spectroscopy", *Phys. Rev. Lett.*, **60**, 1134 (1988).

Pitris C, Goodman A, Boppart SA, Libus JJ, Fujimoto JG, Brezinski ME, "High-resolution imaging of gynecologic neoplasms using optical coherence tomography", *Obstet. Gynecol.*, **93**, 135-139 (1999).

Rajadhyaksha M, Anderson RR, and Webb RH, "Video-rate confocal scanning laser microscope for imaging human tissues in vivo", *Appl. Opt.*, **38** (1999).

Rava RP, Baraga JJ, Feld MS, "Near-infrared Fourier-transform Raman spectroscopy of human artery", *Spectrochemica Acta A* **47**(3-4), 509-512 (1991).

Reid BJ, Haggitt RC, Rubin CE, et al., "Observer Variation in the Diagnosis of Dysplasia in Barrett's Esophagus", *Hum. Pathol.*, **19**, 166-178 (1988).

Richards-Kortum RR, Rava R, Fitzmaurice M, Tong L, Ratliff NB, Kramer JR, Feld MS, "A one-layer model of laser-induced fluorescence for diagnosis of disease in human-tissue – applications to atherosclerosis" *IEEE Trans. Biomed. Eng.* **36**, 1222-1232 (1989).

Richards-Kortum R, Rava RP, Fitzmaurice M, Kramer JR, Feld MS, "476 nm excited laser-induced fluorescence spectroscopy of human coronary arteries: applications in cardiology", *Am Heart J.* **122**, 1141-50 (1991).

Riddell R, Goldman H, Ransohoff D, Appelman HD, Fenoglio CM, Haggitt RC, Ahren C, Correa P, Hamilton SR, Morson BC, Sommers SC, Yardley JH, "Dysplasia in Inflammatory Bowel-Disease, Standardized classification with provisional clinical applications", *Human Pathology*, **14**, 931-968 (1983).

Russ JC, *The Image Processing Handbook* (CRC Press, Boca Raton, Ann Arbor, London, Tokyo, 1992).

Schantz SP, Kolli V, Savage HE, Yu G, Shah JP, Harris DE, Katz A, Alfano RR, Huvos AG, "In vivo native cellular fluorescence and histological characteristics of head and neck cancer", *Clin Cancer Res*, **4**, 1177-82 (1998).

Schmitt JM and Kumar G, "Turbulent nature of refractive-index variations in biological tissues." *Opt. Lett.*, **21**, 1310-1312 (1996).

Schomacker KT, Frisoli JK, Compton CC, Flotte TJ, Richter JM, Nishioka NS, Deutsch TF, "Ultraviolet laser-induced fluorescence of colonic tissue – basic biology and diagnostic potential," *Lasers in Surgery and Medicine* **12**(1), 63-78 (1992).

Sloot PMA, "Elastic light scattering from nucleated blood cells", *Cytometry*, **9**, 636 (1988).

Sokolov K, Drezek R, Gossage K, Richards-Kortum R, "Reflectance spectroscopy with polarized light: is it sensitive to cellular and nuclear morphology", *Opt. Express*, **5**, 302-317 (2000).

Van de Poll, Mueller M, Myles J, Zhang Q, Kramer JR, Feld MS, "Combined fluorescence and reflectance spectroscopy of arterial wall improves the identification of atherosclerosis", *Circulation*, **100**, 2349, Suppl. S (1999).

Vieira P, Manivannan A, Lim CS, Sharp P, Forrester JV, "Tomographic reconstruction of the retina using a confocal scanning laser ophthalmoscope", *Physiol. Meas.*, **20**, 1-19 (1999).

Vo-Dinh T, Panjehpour M, Overholt BF, "Laser-induced fluorescence for esophageal cancer and dysplasia diagnosis", *Ann N Y Acad Sci*, **9**, 116-22 (1998).

Wallace MB, Perelman LT, Backman V, Crawford JM, Fitzmaurice M, Seiler M, Badizadegan K, Shields SJ, Itzkan I, Dasari RR, Van Dam J, Feld MS, "Endoscopic detection of dysplasia in patients with Barrett's esophagus using light-scattering spectroscopy", *Gastroenterology*, **119**, 677-682 (2000).

Yang C, Kyungwon A, Perelman LT, Dasari R, Feld MS, "Feasibility of Field-Based Light Scattering Spectroscopy", *J Biomed Optics*, **5**, 138 (2000).

Yang C, Wax A, Georgakoudi I, Hanlon E, Badizadegan K, Dasari RR, Feld MS, "Interpherometric Phase Dispersion Microscopy", *Optics Letters*, **25**, 1526 (2000).

Yang C, Wax A, Dasari RR, Feld MS, "Phase Dispersion Optical Tomography", *Optics Letters*, to be published (2001).

Yodh AG and Chance B, "Spectroscopy and imaging with diffusing light," *Physics Today*, 48(3), 34-40, (1995).

Zonios GI, Cothren RM, Arendt JT, Wu J, Van Dam J, Crawford JM, Manoharan R, Feld MS. "Morphological model of human colon tissue fluorescence." *IEEE Trans Biomed Eng*, 43, 113-22 (1996).

Zonios G, Cothren RM, Crawford JM, Fitzmaurice M, Manoharan R, Van Dam J, Feld MS. "Spectral Pathology", *Annals of the New York Academy of Sciences*, 838, 108-115 (1998).

Zonios G, Perelman LT, Backman V, Manoharan R, Fitzmaurice M, Feld MS, "Diffuse Reflectance Spectroscopy of Human Adenomatous Colon Polyps In Vivo", *Appl. Opt.*, 38, 6628-6637 (1999).

Chapter 2

Histology of Mucosal Tissues

The pattern of light scattering in biological tissues depends inherently on the structure of the tissue. Various tissue inhomogeneities such as cellular organelles, extracellular matrix, etc. may affect light propagation within the tissue. This translates into the unique spectroscopic, polarization, or angular features of the scattered light emerging from the tissue. Therefore, qualitative or quantitative information about tissue macroscopic and microscopic structure can be obtained with proper interpretation of these features. However, solving such *inversion problem* without any *a priori* knowledge of tissue structure is virtually impossible due to exceedingly complex organization of the biological tissues [Newton, 1969]. Most tissues are highly inhomogeneous and characterized by a high degree of complexity ranging from a few angstroms to centimeters. Thus, solving the inversion problem would require precise knowledge of the electromagnetic field at any point inside the tissue, which, of course, is never a possibility. Despite this

seemingly discouraging fact, if certain assumptions about the tissue structure can be made, some of its important properties can be measured with the scattered light.

In this section we discuss the basics of the morphology of the human tissues with special emphasis on the structure of the mucosal tissues lining the inner and outer surfaces of the human body. Our particular interest in the mucosal tissues is substantiated by the fact that, as mentioned in the introduction, it is the mucosal tissues that are most readily accessible with visible light. As well, detection of pathological changes such as precancerous conditions known as dysplasia and carcinoma *in situ* (CIS) in the mucosal epithelium represents one of the biggest challenges in modern medicine [Cotran et al., 1994].[1] The following discussion is by no means exhaustive. Rather, it aims to provide a brief introduction to histology of normal tissues and selected pathological conditions necessary to comprehend the principles and applications of light scattering spectroscopy. For a reader who searches for more detailed and complete information about the histology and pathology we would highly recommend texts [Cotran et al.. 1994; Fawcett et al., 1994; Hiatt et al.. 1994].

Any biological tissue consists of variable quantities of cells and extracellular matrix. Four types of tissues are being identified: epithelium, connective tissue, muscle, and nervous tissue. Some anatomists distinguish the fifth tissue type – the blood. Here, however, we follow a more standard classification and identify the blood as a specialized subtype of connective tissue. A number of tissues comprise functional units called organs. For example. the esophagus consists of epithelium covering its inner (lumenal) surface situated on top of the layers of connective tissue and muscle containing variable amounts of nerves and

---

[1] Malignant and pre-malignant transformations in the epithelium will be discussed in section 2.3 in greater detail.

blood vessels. Several organs compose organ systems such as skeletal, circulatory, respiratory, gastrointestinal, and genitourinary systems. For example, gastrointestinal system consists of organs of the oral cavity (tongue, lips, etc.), esophagus, stomach, small and large intestines, rectum, and glands of the digestive system located outside the walls of the alimentary canal (pancreas, liver, gallbladder, etc.). We start our discussion with the description of the organization of the cell considering an epithelial cell as a model. Then we discuss the major histological properties of the mucosa and tissues it is composed of.

2.1 Morphology of the Cell

So far more than 200 different cell types have been identified. Despite this diversity most cells possess many common features. We will consider a cell of a membranous epithelium lining surfaces of most human organs as a model. The cell is bounded by a membrane, the plasmalemma. It is phospholipid bilayer 8.5 to 10 nm in thickness with integral and peripheral proteins embedded in it. These proteins provide functional properties of the membranes and may extend out of the inner or outer surface of the plasmalemma by as much as 10 nm. Thus, the overall thickness of the plasmalemma might range from 8.5 to about 30 nm.

Two major cell compartments are the nucleus and the surrounding cytoplasm. The cytoplasm contains organelles, which are metabolically active subcellular organs, and inclusions, which are metabolically inactive. The following is a list of major cytoplasmic organelles and inclusions and their properties.

1. *Mitochondria* typically have prolate spheroidal shapes. Their size varies greatly even among the mitochondria of a single cell. The larger dimension

of a mitochondrion may range from 1 μm to 5 μm. The diameter typically varies between 0.2 μm to 0.8 μm. The mitochondria are quite flexible and may easily change their shape. Their major function is to generate ATP via oxidative phosphorilation, thus providing the energy required by the cell. Since metabolic activity of different cells vary, the numbers of mitochondria differ depending on the cell size and its energy needs. For example, non secreting cells of the epithelial lining of the internal surface of the colon have only few mitochondria. In contrast, the hepatocytes, liver cells, contain a few thousand mitochondria. A mitochondrion is composed of a 7 nm thick outer membrane and an inner membrane which is about 6 nm in thickness. The inner membrane is folded to form cristae. It is studded with numerous mushroom-like 15 nm particles which possess 10 nm head and 5 nm tail connecting them to the membranous wall. The 10-20 nm wide space between the outer and the inner membranes is called membrane space and appears relatively empty. The space between the cristae of the inner membrane is wider, ranging from 40 to 200 nm, and is filled with mitochondrial matrix. This matrix is not uniform, but rather is a meshwork of nearly spherical matrix granules composed of dₑ ℓely packed phospholipoprotines. These granules are 30 to 50 nm in diameter and have complex internal structure. They contain multiple 1-3 nm compartments separated by dense septa.

2. *Endoplasmic reticulum* (ER) is composed of tubules and flat sheets of membranes which are distributed over the intracellular space. The outer diameter of these tubules ranges from 30 to 100 nm. Their wall thickness is about 10 nm. There are two types of endoplasmic reticulum: rough endoplasmic reticulum (RER) that functions in the synthesis of cholesterol

42

and lipids, and smooth endoplasmic reticulum (SER) that functions in the synthesis of proteins. The RER differs from the SER in that it bears 20-25 nm spherical or sometimes spheroidal particles called ribosomes. Although small, the ribosomes are complex particles consisting of 1 nm units, which contain RNA and proteins.

3. *Golgi apparatus* is composed of a group of 4 to 10 flattened parallel membrane-bounded cisternae and functions in the modification and packaging of the macromolecules. The overall thickness of this organelle can ranges from 100 to 400 nm.

4. *Lysosomes* are 0.25-0.8 µm bodies of various shapes, ranging from highly irregular to almost perfect spherical. They differ in their internal structure as well: some can be homogeneous or may consist of collection of dense granules of 2ɔ to 100 nm in diameter embedded in a surrounding matrix of a lesser density. The numbers of lysosomes are highly variant for different cells as well: the cells of membranous epithelial lining of cervix, for example, contain just a few lysosomes, while hepatocytes may posses a few hundred ones. They filled with hydrolytic enzymes and other molecules and participate in intracellular digestion.

5. *Peroxisomas* are 0.2-1.0 µm spheroidal bodies of lower densities than lysosomes that are more abandoned in the metabolically active cells such as hepatocytes where they are counted in hundreds.

6. *Cytoskeleton* is composed of filamentous arrays of proteins. Its three major components are microtubules, which are about 25 nm in diameter with a

wall 9 nm thick and a 15 nm lumen, 10 nm in diameter intermediate filaments, and 7 nm in diameter microfilaments.

7. Various cytoplasmic *inclusions*, such as lipids, glycogen, secretory granules, and pigments, come in all different sizes ranging from 20 to 500 nm. They might have various shapes but usually appear to be nearly spherical. The roughness of their surface can range from 2 to 40 nm.

Although these cytoplasmic components appear to be greatly different in their structure and organization, a few generalizations can be made: 1) most of the cytoplasmic organelles and inclusions are smaller than 1-2 μm size; 2) they are not homogenous bodies but rather complex structures that possess exceedingly intricate internal structure.

At this point we turn our attention to the largest cell organelle, the nucleus, which deserves special attention. The nucleus is usually spherical or spheroidal, although in some cases, it may appear infolded or lobulated. The importance of the nucleus is apparent from its function. The nucleus houses the chromosomes, where most of the genetic material essential for the cell activity and replication is contained. It is the site of mRNA, tRNA, and rRNA transcription and of ribosome assembling from proteins and rRNA. The overall sizes of the nuclei vary depending on the cell type, its metabolic state and phase of the cycle – it is usually enlarged when active transcription of the genes occurs. Typical nuclei are from 5 to 10 μm in diameter. One of the striking differences between the nucleus and the other organelles is the fact that the majority of the nuclei of the cells of the same line and similar degree of maturation, for example the nuclei of the columnar epithelial cells of the intestine, are all have similar size and shape. In some cases, the standard deviation of the nuclear diameters is less than 5% of the average diameter. In

44

contrary, the sizes of most other organelles, mitochondria for instance, vary widely even within a single cell.[2]

The major components of the cell nucleus are nuclear envelope, chromatin, nucleolus, and nuclear matrix, all embedded in the nucleoplasm.

1. The nucleus is enclosed by the *nuclear envelope*, a system of two membranes separated by a 10-30 nm space, the prerinuclear cisterna. The outer membrane may have ribosomes attached to it. Some parts of the membrane contain fenestration called nuclear pores that are complex structures with circular shape about 100 nm in diameter covered by 15-20 nm spherical particles.

2. *Chromatin* is one of the major components of the nucleus. It contains the strands of deoxyribonucleic acid (DNA) that encode the genetic information of the cell. Although the DNA is organized in the chromosomes, these are not appreciable in the interphase, or non-dividing, nucleus and become apparent only with cell division. Two types of chromatin are distinguished. The portion of the DNA that is not being transcribed forms condensed or heterochromatin. The transcribed part of the DNA comprises an extended or euchromarin. This distinction was brought in use by the histologists who microscopically examined stained tissue sections. When stained with basophilic contrast dye, the nucleus appears bluish due to the high affinity of the heterochromatin to such dyes. On the other hand, the euchromatin is poorly stained and is not visible with the light microscopy. The fundamental etiology of this difference between

---

[2] Note that the statistical properties of the population of mitochondria and other small organelles are roughly preserved over a cell line.

these two types of chromatin has yet to be explained. Although it is known that the euchromatin is less dense than the heterochromatin, this fact itself is not sufficient to explain the difference in the staining pattern. The clumps of the heterochromatin are irregular and may vary from 0.5 to 2 µm in size. The heterochromatin is made up of closely tangled 30 nm fibrils. The fibrils are composed of beaded strands regularly spaced smaller subunits, the nucleosomes. These have a cylindrical shape and are connected by the filaments, which are 4 nm in diameter. In the euchromatin, the strands of the nucleosomes are uncoiled and do not form the fibrillar structure.

3. The *nucleolus* is responsible for transcription of ribosomal RNA (rRNA) and assembly of ribosomal subunits. The size of the nucleolus may range from 0.5 µm up to about 1 µm. It appears to be a more or less round network of anastomosing strands, called pars granulose. These strands are made up from 15 nm ribonucleoprotein particles surrounded by even smaller filaments. There are a few rounded structures within the nucleolus filled with fibrillar material of a lower density, called fibrillar centers, which have dimension of about 80 nm.

Apparently, the cell nucleus, like most other cell organelles, is not a uniform object. Rather, it possesses an intricate internal structure. The larger inhomogeneities are formed by smaller structures, which in turn are composed of even smaller building blocks. We have to notice, however, that studies have established that the density variations within the cell nucleus are smaller than one between the nucleus and the cytoplasm. The implications of this fact to the light scattering by the cells will be discussed in the following chapter.

46

2.2 Histology of Mucosa

The walls of most internal cavities of the body such as gastrointestinal tract, respiratory tract, cervix, etc. generally consist of four layers (not all layers are present in all organs' walls): mucosa, submucosa, tunica muscularis, and serosa or adventitia. Generally speaking, the walls of hollow human organs are formed by alternating layers of connective and muscular tissues and the epithelium coating the inner and outer surfaces of the wall (Fig. 2.1 and Fig. 2.2).

Mucosa, the innermost layer, may consist of four layers: epithelium, basement membrane, connective tissue of lamina propria, and muscularis mucosae. Its surface is always lined by some type of epithelium. Epithelia are separated from underlying tissues by a thin noncellular epithelial derived 100 nm thick layer called basement membrane. Thickness of the epithelium may vary from 10 to about 300 μm depending on its type. We will describe the various types of epithelium in greater detail later. The epithelium is usually supported by a layer of connective tissue whose thickness can range from 50 to a few hundred microns. Depending on the density of this connective tissue, it is classified as a part of mucosa or submucosa. For example, the loose connective tissue underlying the epithelial lining of the colon is considered to be a part of mucosa and is called lamina propria. Denser connective tissue supporting the epithelium of the uterine cervix is referred to as a part of submucosa. Some mucosae, distal esophagus is an example, include a layer of scattered or continuous smooth muscle cells just below the lamina propria. It is usually not thicker than 100 μm but in some cases may reach up to 400 μm.

The submucosa is a 400-1000 μm layer of moderately dense connective tissue that supports and provides vascular, nervous, and lymphatic supply to the mucosa. The tunica muscularis consists of a few layers of smooth muscle muscle cells, blood vessels of various sizes, and nerves. It is from 0.5 to 3 mm thick. The outermost layer of a tissue wall, a 0.5 to 3 mm thick serosa[3], consists of connective tissue covered by a single layer of epithelial cells called mesothelium.

Epithelia either form glands or membranes. It is the membranous epithelium that covers the mucosal surfaces and is of our major interest. Hereafter we will discuss the membranous epithelia only. Such epithelia are composed of very closely packed, contiguous cells, with very little or no intracellular material in the extracellular space. They are avascular and do not possess the nervous supply. Epithelia are classified according the number of cell layers, shape of the cells, and the free surface specializations.

Based on the number of cell layers, an epithelium can be classified as simple, stratified, pseudostratified, or transitional (Fig. 2.3).

1. The *simple* epithelium consists of a single cell layer. The examples are endothelium, the epithelium of the blood vessels (2 μm thick) and intestinal epithelium (15-20 μm thick). The thicknesses of such epithelia do not usually exceed 30 μm.

2. The *stratified* epithelium is formed by a number of cell layers. It can be as thick as 0.5 mm. In a common subtype of this epithelium, squamous stratified epithelium (see below), the cells flatten out while they move from the basal (bottom) to the apical (lumenal) surface during the process of

---

[3] The outermost layer in some organs is referred to as adventitia.

48

maturation. Stratified squamous epithelia are found in skin, oral cavity, esophagus, and exocervix.

3. The *pseudostratified* epithelium consists of a single layer of tall cells that appear to be stratified. It is about 30-50 μm thick. Examples are epithelia of male urethra and proximal respiratory tract (trachea and primary bronchi).

4. The *transitional* epithelium is found primarily in urinary bladder and consists of a multiple cell layers and characterized by large round cells on the surface and tall cells on the bottom. In bladder, it is usually composed of 7 cell layers and is about 150-200 μm thick.

Based on the shape of the cells, an epithelium is classified as squamous, cuboidal, or columnar.

1. The uppermost cells of a *squamous* epithelium are more or less flat. A squamous epithelium can be simple or stratified (see examples above). The squamous cells are just a few microns thick and have large surface area.

2. The shape of the cuboidal cells is suggested by their name. They are typically about 10-15 μm wide and thick. The nuclei are usually spherical. While truly stratified epithelium is rarely found, examples of simple cuboidal epithelia are abundant: epithelium of the ovary, ductal epithelium in the breast, etc.

3. A typical columnar cell has a cylindrical shape and is about 10 μm wide and 20 to 30 μm tall. The nuclei are located parabasely and are usually shaped as prolate spheroids with longer axis oriented along the axis of the cell.

Most of the columnar epithelia are simple. Examples are intestinal epithelium, epithelium of the uterus and endocerix.

The free surface of an epithelial cell may form several specialized structures such as microvilli, cilia, stereocilia, etc. Classification of epithelia based on such properties is frequently used. However, it is of less importance to the point of our discussion.

Since the connective tissue is one of the major components of the mucosa and/or submucosa, it is worth to discuss its structure. Among the eight types, there is one that is of our immediate interest, namely loose (areolar) connective tissue.[4] It is ubiquitously present in most mucosae and submucosae. The connective tissue has both cellular and intercellular components. The intercellular materials are fibers, amorphous ground substance, and tissue fluid.

Three types of fibers are recognized: collagen, reticular, and elastic fibers. Collagen fibers are composed of specific proteins. They appear as unbranched, randomly oriented strands 0.5-5 μm in diameter. They consist of clearly distinct parallel fibrils, which are 50-90 nm in diameter, separated by about 100 nm. Reticular fibers are thin, 10 nm in diameter, branching. Elastic fibers are almost as thin as reticular fibers. They branch and form loose three-dimensional network.

The cells of loose connective tissue are fibroblasts, macrophages, plasma cells, mast cells, and some others. Despite such variety, and in contrast to the epithelium, most connective tissues possess only limited quantities of the cells and are mainly composed of non-cellular materials.

---

[4] The other types are dense irregular, dense regular, adipose, reticular, cartilage, bone, and blood. Dense irregular connective tissue is found in some of the submucosae. We do not consider its structure in great detail due to its relative similarity to that of the areolar connective tissue.

2.3 Introduction to Histopathology of Early Cancer and Dysplasia

So far we have considered normal histology of the cells and tissues composing human mucorae. The major application of optical techniques such as LSS is thought to be studying, detection, and diagnosis of various pathological conditions. Detection of early cancer and precancerous conditions such as dysplasia or carcinoma *in situ* (CIS) has been a holy grail of biomedical optics for many years. It is the immense importance of the problem and attractiveness of potentially non-invasive diagnosis that stimulated researchers from various fields to attack this problem. It is important to notice that more than 85% of all cancers originate from the epithelia – colon, lung, and cervical cancers are examples [Landis et al., 1999]. Such cancers are referred to as carcinomas. If diagnosed at one of the pre-invasive stages, most would-be carcinomas are readily curable [Cotran et al., 1994]. However, detection of such lesions is not possible with conventional diagnostic techniques. During last few years light scattering spectroscopy (LSS) appeared to be a powerful tool to considerably advance the detection of early cancer [Backman et al., 2000]. Its success is based on the fact that the earliest and most ubiquitous changes occurring with precancer are alterations of histology of the affected epithelial cells and their nuclei in particular [Cotran et al., 1994; Boone et al., 2000]. The purpose of the following section is to outline the basic histopathology of early cancerous and precancerous changes in the epithelia.

While carcinomas may originate from perfectly healthy epithelium, it has been shown that the probability of a malignant transformation is much greater for the epithelium that has already been damaged [Cotran et al., 1994]. For example, many cancers grow on the basis of *metaplasia*. Term metaplasia describes

pathological condition in which a normal mucosa is replaced by mucosa of another type that is not normally present in the affected organ. One of the examples of metaplasia is replacement of normal stratified squamous epithelium of the esophagus by intestinal mucosa lined by the simple columnar epithelium, which is believed to be a consequence of the persistent gastroesophageal reflux commonly known as "heartburn". This condition is referred to as Barrett's esophagus. Patients with Barrett's esophagus are estimated to have 40 times increased chances to develop esophageal adenocarcinoma than the rest of the population [Ridell et al., 1983; Cotran et al., 1994]. Squamous cell carcinoma of the lung is another example. It originates from stratified squamous epithelium that has replaced respiratory (pseudostratified ciliated) epithelium normally found in the large bronchi.

Carcinogenesis is a complex process. It starts from exposure of a cell to a carcinogenic agent, such as ionizing radiation, a chemical, a virus, etc. This exposure results in DNA damage and mutation. It is said that the cell becomes "initiated". Many genes such as oncogenes and cancer suppressor genes whose mutations may lead to progression to malignancy have been identified. By definition, the cells become malignant when they are able to penetrate the basement membrane separating the epithelium from the underlying connective tissue. Almost never are cells able to penetrate the basement membrane immediately after their initiation. Thus, the malignancy is usually preceded by a precursor stage that is usually referred to as dysplasia[5]. The dysplastic cells exhibit disorderly but not malignant proliferation. Dysplasia is almost always precedes but not necessarily results in cancer. Thus, it would be proper to say that dysplastic cells have malignant potential. Depending on the severity of the disease, the

---

[5] In some cases dysplasia is referred to as "pre-malignant neoplasia".

dysplasia is classified as either low or high grade or as mild, moderate, or severe. Sometimes pathologists use term "indefinite for dysplasia" in cases when identifying dysplasia is difficult. Finally, if the overall thickness of the epithelial layer is affected, the dysplasia is called carcinoma *in situ* (CIS).[6]

Now we are ready to address the question of how the dysplastic epithelium is different from the normal epithelium. Despite the fact that dysplasia may vary greatly in its macroscopic appearance depending on the organ and the stage of the disease, there are a few major morphologic features that ubiquitously present in the affected cells and make them appear distinctly different from their normal counterparts. For instance, dysplastic cells and their nuclei exhibit considerable pleomorphism (variation in size and shape), the cell nuclei are hyperchromatic (appear darkly stained with nuclear dyes due to excessive quantities of chromatin) and abnormally enlarged (Fig. 2.4). Moreover, the mitotic figures are present in the non-basal portion of the epithelium, and abnormal mitosis may be observed. At higher level of organization, architectural changes such as overall disorganization of the epithelium, which is closely related to the loss of normal maturation of the cells, can be seen. It is important to reiterate, that although macroscopic appearance of dysplastic lesions may differ (for example, dysplasia in colon forms polyps called adenomas vs. flat dysplastic lesions found in Barrett's esophagus; both mucosae share the same type of epithelium – simple columnar), the morphologic features of dysplastic cells and architectural alterations occurring in the epithelial layer listed above are characteristic for essentially all types of dysplasia in all organs.

---

[6] In some organs such as cervix dysplasia and CIS might be called squamous interepithelial lesion (SIL), or squamous interepithelial neoplasia (SIN). Use of such different terminology, though may seem confusing, is widely accepted by the pathologists and clinicians.

As mentioned above, if a dysplastic lesion is detected, it can almost always be cured with surgery or other type of therapy. Therefore, it is not surprising that dysplasia surveillance is considered to be a crucial step toward cancer prevention. Despite significant attention, no universal means to detect dysilastic lesions has been found. Polypoid dysplastic lesions, such as colon adenomas, are apparently the easiest to detect. They can be detected and removed with endoscopy. Many dysplastic lesions, however, do not form grossly apparent formations and are indistinguishable from the surrounding non-dysplastic tissue. Moreover, the size of these "flat" dysplasias might not be larger than 1 mm in diameter. Even such small lesions can bear lethal metastatic potential. Detection of such lesions is possible only with random biopsy. For example, patients with Barrett's esophagus undergo annual surveillance with random biopsy at endoscopy. Other examples of flat dysplasia include bladder dysplasia, colon dysplasia associated with ulcerative colitis, cervix and many others.

The difficulties associated with random biopsy are apparent: the probability of detecting 1 mm lesion in a esophagus or any other organ with large surface area is minute. Moreover, the diagnosis and classification of dysplasia is purely qualitative and is based on subjective interpretation of the biopsied materials by a pathologist. Studies have shown that the intra- and inter-observer agreement among pathologists may be less than 50% in some cases [Reid et al., 1988; Cotran et al., 1994]. That is way the majority of the dysplastic lesions are left undetected until they lead to metastatic cancer.

Cancer starts with epithelial cells penetrating the basement membrane into the underlying connective tissue. Cancers are classified according to stage (spread of malignant cells) and grade (degree of cytologic abnormalities such as anaplasia). The higher the grade of the tumor, the more aggressive it is, and, generally

speaking, the poorer the patient's prognosis is. The anaplasia is marked by essentially the same morphologic features as dysplasia: cellular and nuclear pleomorphism, nuclear hyperchomasia and enlargement. The chromatin is usually coarsely clumped and distributed along the nuclear membrane. The malignant nuclei frequently possess large and dense nucleoli. This succinct overview suffices to describe the most important histologic features of dysplastic and malignant tissues. Further discussion of tumorigenesis is out of the scope of our discussion.
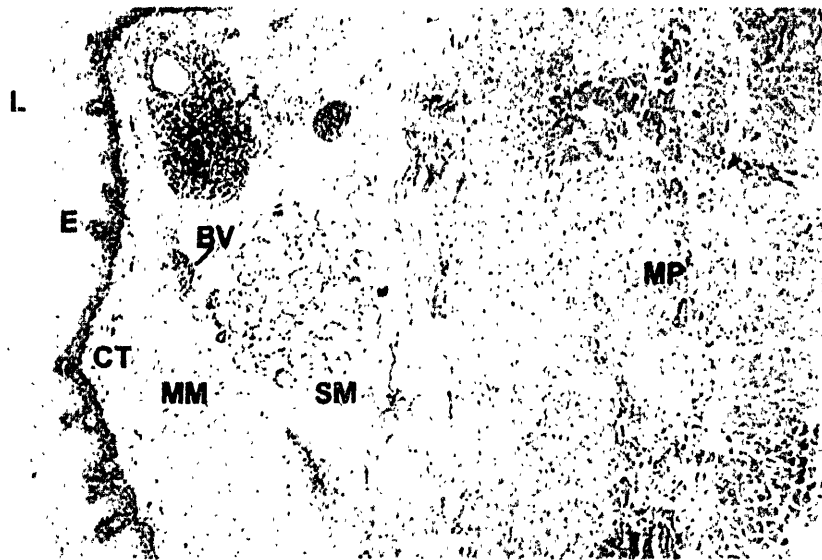
Figure 2.1 Low power microphotograph of a section of the esophageal wall illustrating the major structures of the gastrointestinal tube. L lumen, E epithelium, CT connective tissue, MM muscularis mucosa, BV submucosal blood vessel, SM submucosa, MP muscularis propria
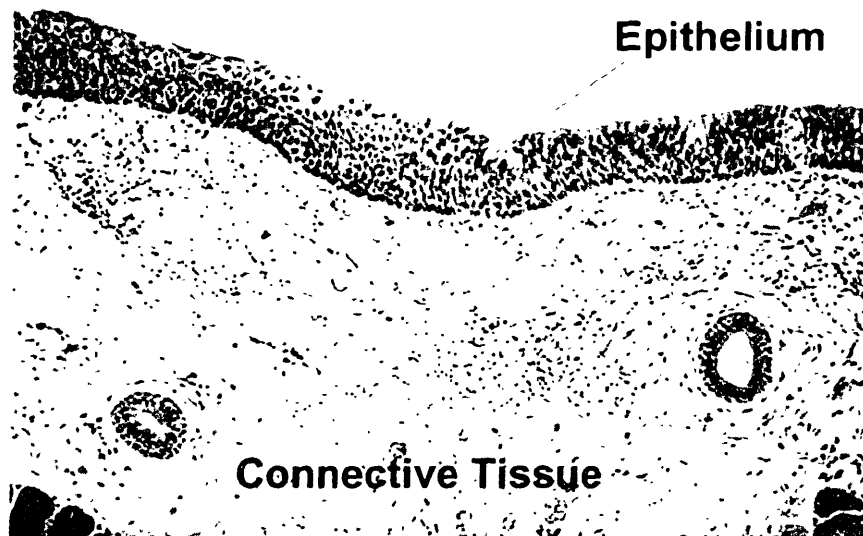
Figure 2.2 Microphotograph of an H&E stained section of the bronchial wall illustrating major components of the mucosa: epithelium and connective tissue.
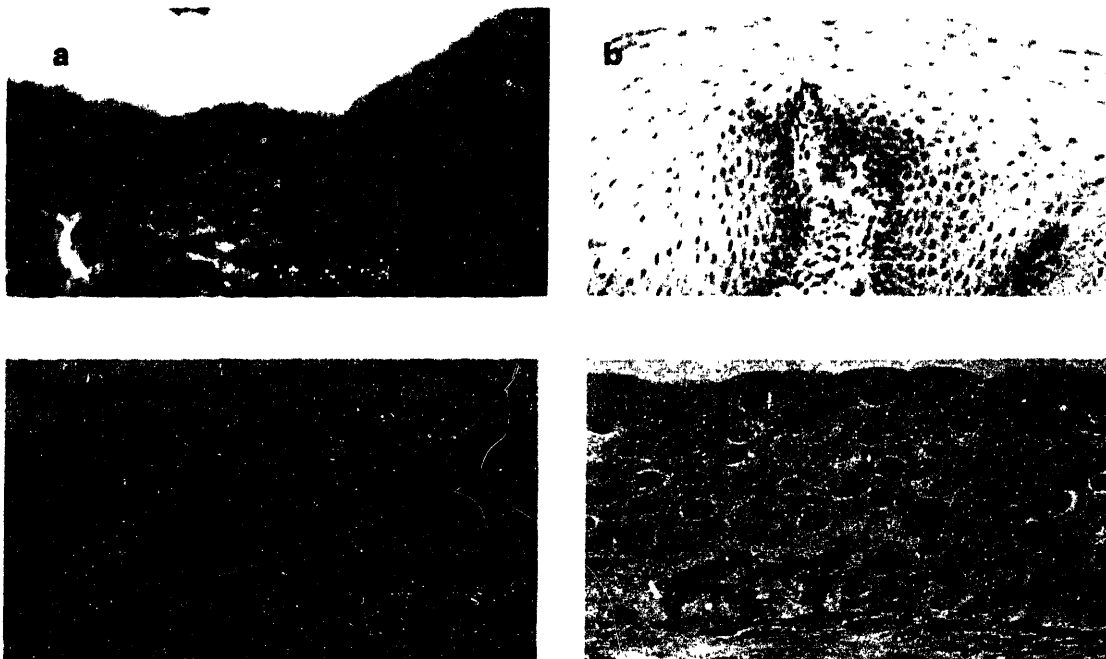
Figure 2.3 Examples of epithelia. (a) – simple coumnar epithelium, (b) – stratified squamous epithelium, (c) – pseudostratified epithelium, (d) – transitional epithelium.
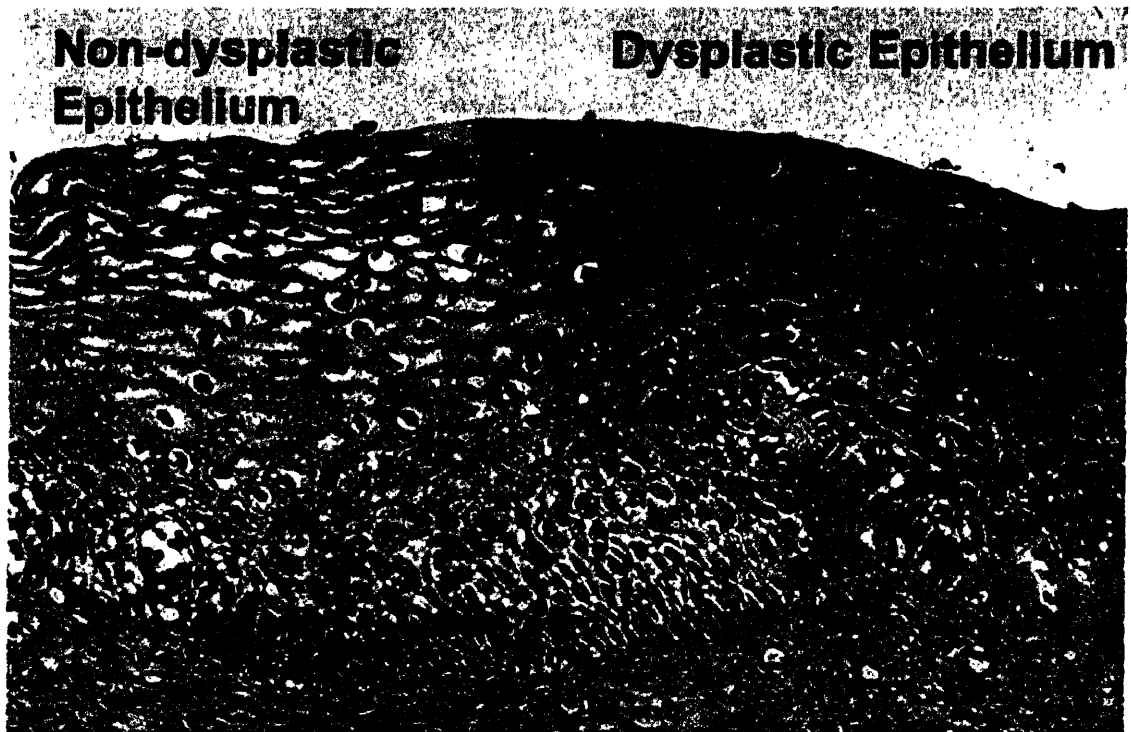
Figure 2.4 Dysplasia in the cervical stratified squamous epithelium. On the left, non-dysplastic epithelium is preserved. Dysplastic nuclei are pleomorphic (vary in size and shape), hyperchromatic (appear darkly stained with nuclear dyes due to excessive quantities of chromatin) and abnormally enlarged.

References

Backman V, Wallace MB, Perelman LT, Arendt JT, Gurjar R, Muller MG, Zhang Q, G. Zonios G, Kline E, McGillican T, Shapshay S, Valdez T, Van Dam J, Badizadegan K, Crawford JM, Fitzmaurice M, Kabani S, Levin HS, Seiler M, Dasari RR, Itzkan I and Feld MS, "Light scattering spectroscopy: a new technique for clinical diagnosis of precancerous and cancerous changes in human epithelia", *Nature*, **406**, 35-36 (2000).

Boone C.W. *et al.* Quantitative grading of rat esophageal carcinogenesis using computer-assisted image tile analysis. *Cancer Epidemiology, Biomarkers & Prevention*, **9**, 495-500 (2000).

Brown, G.L., McEwan, M., Pratt, M. Macromolecular weight and size of deoxypentose nucleic acids. *Nature*, **176**, 161-162 (1955).

Cotran RS, Robbins SL, Kumar V, *Robbins Pathological Basis of Disease* (W.B. Saunders Company, Philadelphia, 1994).

Davies, H.G., Deeley, E. M., Denby, E. F. Attempts at measurement of lipid, nucleic acid and protein content of cell nuclei by microscope-interferometry. *Exp. Cell Res.*, Suppl. 4, 136-149 (1957).

Davies, H.G. *General Cytochemical Methods* (Danielli, J.F., ed.) Vol I. (Academic Press, New York and London, 1958).

Fawcett DW, *A Textbook of Histology*, (Charman & Hall, New York, 1994).

Hiatt LD, *Color Atlas of Histology*, (Williams & Wilkins, Baltimor, 1994).

Landis SH, Murray T, Bolden S, Wingo PA, "Cancer Statistics 1999", CA – A Cancer Journal for Clinicians, **49**, 8-31 (1999).

Lee, L., Pappelis, A. J., Pappelis, G. A., Kaplan, H. M. Cellular and nuclear dry mass and area changes during human oral mucosa cell development. *Acta Cytol.* **17**, 214-219 (1973).

Newton RG, *Scattering Theory of Waves and Particles* (McGraw-Hill Book Company, New York, 1969).

Reid BJ, Haggitt RC, Rubin CE, "Observer Variation in the Diagnosis of Dysplasia in Barrett's Esophagus", *Hum. Pathol.*, **19**, 166-178 (1988).

Riddell R, Goldman H, Ransohoff D, Appelman HD, Fenoglio CM, Haggitt RC, Ahren C, Correa P, Hamilton SR, Morson BC, Sommers SC, Yardley JH, "Dysplasia in Inflammatory Bowel-Disease, Standardized classification with provisional clinical applications", *Human Pathology*, **14**, 931-968 (1983).

Chapter 3

Introduction to Light Scattering

In this section we overview several analytical and numerical techniques, which are often used to describe light scattering by biologically relevant objects such as cell organelles, inclusions, etc. listed in the previous section. Following the standard terminology of the theory of light scattering, we will refer to such objects that can scatter light as "scattering particles" [Newton, 1969]. By definition, a scattering particle is any bounded region of refractive index variation. (As discussed below, most subcellular organelles are not uniform and have complex shape and structure. Nevertheless, we will refer to them as scattering "particles".)

One can think of two types of problems related to light scattering by a single particle: direct and inverse scattering problems. The direct problem is formulated as follows: given a particle of known structure (alternatively, given complete information about the distribution of the refractive index inside the

particle) illuminated by a plane wave of particular polarization, find electromagnetic field inside and outside the particle. Usually, however, the simplified formulation of the problem suffices: find the electromagnetic field on large distances from the particle. The inverse problem is to find the distribution of the refractive index of the particle based on the measurable electromagnetic wave scattered by this particle. Although not solvable in a closed form in most cases, the first problem is much easier than the second one. In fact, it is virtually impossible to solve the inverse problem in case when the solution of the direct problem is not known. While inverse problem is not solvable in most relevant cases, one can get at least partial information about the scattering particle from the light scattering data. In order to achieve this, understanding the direct problem is crucial.

3.1 Rigorous Solution of Direct Scattering Problem

Consider a particle illuminated by a plane electromagnetic wave

$$\mathbf{E}_i = \mathbf{E}_0 e^{-i(\mathbf{kr} - \omega t)}. \tag{3.1}$$

where E_0 is the wave amplitude, $\mathbf{k}$ is the wavevector, and ω is the frequency. In the wave zone, distances r large compared to the wavelength λ and particle's characteristic dimension a, the radiation scattered by the particle is a spherical wave E_s. The amplitudes of both incident and scattered waves can be expressed as combination of two components, parallel, E_{i2} and E_{s2}, and perpendicular, E_{i1} and E_{s1}, to the plane of scattering, which is defined as the plane that includes the directions of propagation of the incident and scattered waves. The *scattering*

amplitude matrix S(θ,ϕ) relates components of the scattered wave and those of the incident one, $E_s=SE_i$ or, more explicitly [Newton, 1969],

$$\begin{pmatrix} E_{s2} \\ E_{s1} \end{pmatrix} = \frac{e^{-i(kr-\omega t)}}{ikr} \begin{pmatrix} S_2 & S_3 \\ S_4 & S_1 \end{pmatrix} \begin{pmatrix} E_{i2} \\ E_{i1} \end{pmatrix},$$ (3.2)

where $r=r(\theta,\phi)$ is a direction of propagation of the scattered light given by the polar angles θ and ϕ in the spherical system of reference associated with the particle and, generally speaking, complex functions $S_k=S_k(\theta,\phi)$, k=1,...,4. The scattering amplitude matrix is the fundamental property that gives complete description of the scattering process and solves the direct scattering problem. Moreover, all other properties describing the scattering event can be expressed through the matrix components. For example, the scattering cross section, σ_s, which is defined as the geometrical cross section of a particle which would produce amount of scattering equal to the total observed scattered power in all directions, is given by

$$\sigma_s = k^{-2} \int_0^{2\pi} \int_\pi^0 \left(|S_1 + S_4|^2 + |S_2 + S_3|^2 \right) d\cos\theta d\phi$$ (3.3)

The elements of the scattering matrix depend on the spatial distribution of the refractive index within the particle. For example, if the particle is homogenous and spherical, then there are only two parameters the matrix depends on: the diameter of the sphere and its refractive index. We note as well, that in case of a spherically symmetrical particle or, more generally, any particle that is cylindrically symmetrical in respect to the direction of propagation of the incident light, elements $S_3=S_4=0$ and the matrix is diagonal. Moreover, S_1 and S_2 are functions of scattering angle θ only and do not depend on ϕ. In this case, the expression for the

63

intensities of scattered light polarized along and orthogonally to the scattering plane are proportional to the respective components of the incident light:

$$I_{\parallel} = \frac{|S_2(\theta)|^2}{k^2 r^2} I_{\parallel},$$

(3.4)

$$I_{\perp} = \frac{|S_1(\theta)|^2}{k^2 r^2} I_{\perp}.$$

(3.5)

Generally speaking, to find the matrix elements, one needs to solve the Maxwell's wave equations with proper boundary conditions of electric and magnetic field continuity. The methods of solving the wave equations are not discussed here, since they can be found elsewhere [Jackson et al., 1975]. Such solution is the most rigorous and one which is usually the most difficult to obtain. In fact, there are just few cases in which the analytical solution to the wave equation has been found. Gustav Mie obtained the solution for the scattering of a plane wave by a uniform sphere in 1907. The functions S_1 and S_2 are expressed as infinite series of Bessel functions of two parameters, kd and kmd, with k the wavenumber, d the diameter of the sphere, and m the relative refractive index of the sphere [van de Hulst, 1957]. We notice that the parameters the Mie solution depends on are the maximal and the minimal phase shifts of the light wave passing through the system. If the sphere is optically denser than the surrounding medium, $m > 1$, the maximal phase shift, kmd, is achieved when a photon propagates through the center of the sphere. On the other hand, the photon that is not scattered by the particle is undergone the minimal phase shift, kd. Other examples of particles for which the scattering problem has been solved analytically are cylinders, coated spheres, uniform and coated spheroids, strips, and planes [Kerker, 1969]. In all these cases, the amplitudes are expressed as infinite series. The coefficients of

some of these series are obtained as yet another series. Some of the series are ill converging.

3.2 Numerical Solutions of the Scattering Problem

Apparent difficulties with rigorous solution of the wave equations had led to the development of other means of solving the scattering problem. Such alternative approaches, which are indeed used in practice much more extensively than the rigorous analytical solutions, have evolved in two directions: 1) methods of solving exact wave equations numerically and 2) approximate analytical solutions of the problem. We first overview how scattering problems can be addressed using rigorous numerical techniques following with an in-depth discussion of approximate analytical methods applicable to solve direct and inverse scattering problems.

The analytical approaches are dependent on strict simplifying assumptions about tissue scatterer's geometry and refractive index. It is not at all clear how limiting these assumptions are and how to proceed when they are not applicable in the first place. Recently, significant progress has been achieved in the development of numerical approaches to solve the scattering problem and address these issues. Here we will briefly discuss two numerical methods, which have been found to be very useful to study light scattering from biological objects: discrete particle model (DPM) [Schmitt et al., 1998] and three dimensional finite difference time domain (FDTD) method [Tafloe et al., 1995; Dunn et al., 1996].

The DPM is essentially an extension of the analytical methods presented in 3.1. It models a complex non-uniform scatterer as a combination of discrete uniform objects of simple, usually spherical, shape. To conduct these calculations one needs to assume particular distribution of scatterer's sizes and refractive indexes. Normal or log-normal distribution functions are used most frequently. Then the scattering fields are calculated numerically as a superposition of the scattering fields produced by each of the particles using either the Mie theory or its approximations. As one can see, although this model might give some insight into the impact of the internal structure of a particle on the scattering pattern, it is by no means rigorous.

The FDTD presents a more general approach that does not suffer from the limitation of the discrete particle model. It enables the computation of scattering amplitudes for inhomogeneous objects of arbitrary shape. The FDTD aims to find the numerical solution of the Maxwell's equations for electromagnetic wave propagating in a medium with given variations of the refractive index. The equations are discretized in time and space on a four dimensional grid. The value of the refractive index is given for each of the grid's pixels. Apparently, the higher the spatial and temporal frequencies of the grid, the more accurate the model is. However, there is a price to pay. The complexity of the algorithm increases as $l^{-6}\tau^{-2}$ with reducing the grid spatial spacing l and temporal interval τ. It was established that $l<\lambda/10$, where λ is the wavelength of the incident light, guarantees reasonable accuracy. Thus, the step is chosen as $l = \min\{\lambda/10, \delta_n\}$ with δ_n the special dimension of refractive index variations. Proper boundary conditions are to be applied as well. For example, the Liao boundary conditions have been used to simulate unbounded media [Liao et al., 1984]. The incident wave is considered to be a sinusoidal plane wave source. Thus, the system of the first order finite

difference equations is constructed. The values of six components of the electromagnetic wave (E_x, E_y, E_z, H_x, H_y, H_z) are to be found at each of the grid elements using conventional algorithms.

Although a powerful tool for solving scattering problems numerically, the FDTD suffers from a few drawbacks. First, it is computationally intensive. Second, although it does allow solution of the scattering problem, it does not necessarily help with the *understanding* the scattering characteristics. And, after all, the foremost important reason to solve the direct scattering problem is to elucidate general properties of the scattering that enable at least a partial solution of the inversion problem. On the other hand, the FDTD can be exceedingly useful in comparing various approximate analytical models with otherwise difficult to perform experiments and, therefore, in developing the most accurate analytical descriptions.

In the end, a word of caution must be said. It would be tempting to think that the use of numerical modeling allows avoiding the necessity for making any simplifying assumption regarding the origin of tissue scattering. While it is partially true and the numerical modeling can release some of the assumptions, it must always be kept in mind that the model is only as good as the validity of the input parameters. For example, to calculate scatted fields using the FDTD, one needs to assume certain spatial distribution of the refractive index in the tissue. However, we have virtually no information about the refractive index variations *inside* cell organelles. Moreover, even the average refractive indexes of cell organelles are known for just few cases.

3.3 Approximate Solutions of the Scattering Problem

As discussed in the previous section, numerical methods cannot provide a panacea to solve scattering problems due to three major difficulties: 1) numerical solutions are difficult to implement to solve the inverse problems; 2) they do not provide a clear insight into the physics of the scattering process, thus even a slightly modified problem requires a new numerical experiment; and 3) their implementation is time consuming and requires significant computational resources, which limits their application for real-time analysis. Moreover, one has to strictly define the geometrical and physical properties of the scattering object even to solve the direct problem, which is a high price to pay. In turns out that, as long as certain assumptions are allowed, the scattering problem is amenable to approximate solutions. At least some of these approximate scattering theories do not suffer from the limitations of the numerical approaches discussed above. In this section we discuss how the scattering problem can be simplified and solved under certain approximations.

3.3.1 Light Scattering by Particles with Sizes Smaller or Comparable to the Wavelength

A great variety of structures the cell organelles are built of are smaller than the wavelength of visible light. The examples are the tubules of endoplasmic reticulum, cisternae of Golgi apparatus, etc. Light scattering by such particles is known as the Rayleigh scattering and was introduced by Rayleigh in 1871

68

[Newton, 1969].[1] In this approximation, the electric field is considered to be homogenous over the volume of the particle. Therefore, the particle behaves as a dipole and radiates in all directions. In a most relevant case of isotropic polarizability α of the particle, the scattering amplitude matrix becomes

$$\begin{pmatrix} S_2 & S_3 \\ S_4 & S_1 \end{pmatrix} = ik^3\alpha \begin{pmatrix} \cos\theta & 0 \\ 0 & 1 \end{pmatrix}.$$ (3.6)

The scattered light has well known broad angular distribution. The scattering cross section is simply

$$\sigma_s = \frac{8}{3}\pi k^4\alpha^2.$$ (3.7)

We note that, because α is proportional to the particle's volume, the scattering cross scales with particle's linear dimension a as a^6 and varies inversely with λ^4.

When the particle is not small enough to allow the Rayleigh theory to be applied, the coupled dipole approximation (CDA) can be used [Draine et al., 1994]. It is particularly applicable to particles with size comparable to the wavelength. Thus, it may be useful to study light scattering by small organelles such as mitochondria, lysosomes, etc. From a certain point of view, CDA is an extension of the Rayleigh approximation. A scattering particle is considered to be an array of N point dipoles with the spacing between these dipoles being small compared to the wavelength. Thus, the particle needs not be assumed to be uniform. In contrary, this approximation might be a powerful tool to describe

---

[1] It has been argued that Raylegh was not the first who discovered small particle scattering. There are a number of claimants for this pride. However, it is out of the scope of this section to address the issue of the authorship. Therefore, we will refer to small particle scattering as the Rayleigh scattering and beg his opponents for their forgiveness.

scattering from composite particles, as most small organelles are. In this approximation, the elements of the scattering matrix are expressed through the dipole moments of each of the dipoles. To find the dipole moments, one needs to solve a system of $3N$ linear equations with coefficients dependent on the polarizabilities of the dipoles.

Another approach to describe the scattering by particles comparable to the wavelength involves the Rayleigh-Gans approximation [Van de Hulst, 1957]. It is applicable, if the following two conditions are satisfied.

(1) Relative refractive index of the particle is close to 1, $|\Delta m-1| \ll 1$, where

$$\Delta m = \frac{\max_{r \in V'}(n(\mathbf{r}))}{\min_{r \in V'}(n(\mathbf{r}))}$$ (3.8)

with $n(\mathbf{r})$ the refractive index at a point $\mathbf{r}$ and V' the volume encompassing the volume of the particle V and its immediate surroundings.

(2) The phase shift is small, $2ka|\Delta m-1| \ll 1$, with a the linear dimension of the particle. Such a "soft" particle can be considered as an array of non-interacting dipoles.

The refractive index of most cell organelles ranges from 1.38 to 1.42 [Beauvoit et al., 1994; Beuthan et al., 1996; Slot et al., 1988]. The refractive index of the cytoplasm of most cells varies from 1.34 to 1.36 (Tab. 3.1). Therefore, both conditions of the Rayleigh-Gans approximation are satisfied for most small organelles. This approximation is derived by applying the Rayleigh's formulas (3.6) to any volume element dV within the particle. It can be easily shown that

70

$$\begin{pmatrix} S_2 & S_3 \\ S_4 & S_1 \end{pmatrix} = \frac{ik^3 V}{2\pi} \Re(\theta,\phi) \begin{pmatrix} \cos\theta & 0 \\ 0 & 1 \end{pmatrix},$$ (3.9)

where

$$\Re(\theta,\phi) = \frac{1}{V} \int_{r'} (m(\mathbf{r})-1) e^{i\delta(r,\theta,\phi)} d\mathbf{r},$$ (3.10)

$m(\mathbf{r})$ is the relative refractive index at a point $\mathbf{r}$, and $\delta(\mathbf{r},\theta,\phi)$ is the phase of the wave scattered in direction (θ,ϕ) by the dipole positioned at the point $\mathbf{r}$.

If the particle is sufficiently homogenous,

$$\max_{r\in r'}(|m(\mathbf{r})-1|) - \min_{r\in r'}(|m(\mathbf{r})-1|) << \frac{1}{V}\int_{r'}|m(\mathbf{r})-1|dV,$$

then

$$\begin{pmatrix} S_2 & S_3 \\ S_4 & S_1 \end{pmatrix} = \frac{ik^3(m-1)V}{2\pi} R(\theta,\phi) \begin{pmatrix} \cos\theta & 0 \\ 0 & 1 \end{pmatrix},$$ (3.11)

where m is the relative refractive index averaged over the volume of the particle, and the function $R(\theta,\phi) = \frac{1}{V}\int e^{i\delta} dV$ is so called the form factor. One can predict that the total intensity of light scattered by a small organelle increases with the increase of its refractive index as $(m-1)^2$ and with its size as a^6. The angular distribution of the scattered light differs from that of the Rayleigh scattering. For $\theta=0$, the form factor equals unity. In other directions $|R|<1$, so the scattering in forward direction prevails.

71

3.3.2 Light Scattering by Particles Large Compared to the Wavelength

While most sub-cellular structures are smaller or comparable to the wavelength, there is one whose size is significantly larger that that of the other organelles, the nucleus. None of the approximations discussed above could be applied to the cell nucleus. Rather it falls into a different limiting case, namely it is much larger than the wavelength. Such large particles produce interesting but complicated scattering patterns. The approximate theory of light scattering by large particles was first proposed by Van de Hulst in 1957 [Van de Hulst, 1957]. The Van de Hulst approximation was originally formulated for spherical particles only. However, it can be extended to large particles of an arbitrary shape. Although Van de Hulst theory does not provide a universal means to find the scattering matrix for all scattering angles even in the case of a homogenous sphere, it enables obtaining scattering amplitudes in near forward direction, as well as the scattering cross section.

Consider a particle that satisfies the following two conditions. The first is the same as condition 1 of the Rayleigh-Gans approximation, $|\Delta m-1| \ll 1$. The other is directly opposite to condition 2. We require that the maximal phase shift is large, $2ka|m-1| \gg 1$. The phase shift of the ray emerging from the particle depends on where this ray enters the particle and how much it is deflected. The difference in the phase shift will create constructive or destructive interference on a screen positioned far from the particle. Applying the Huygens' principle, one can obtain [Van de Hulst, 1957]

72
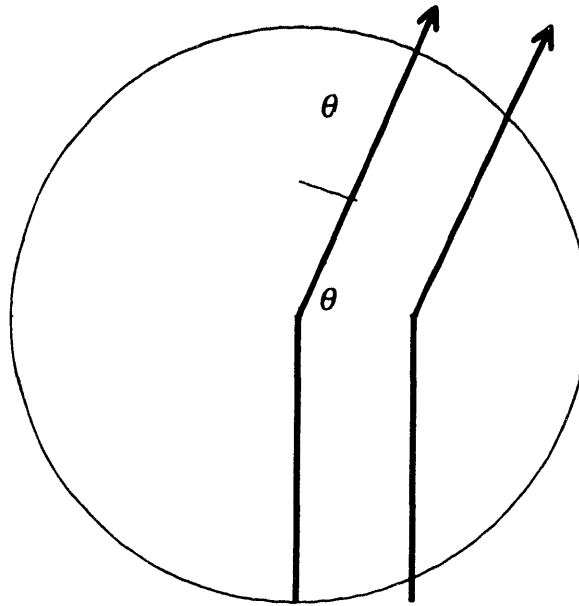
Figure 3.1 δ, the phase shift between the two light rays, is shown.

$$S(\theta) = \frac{k^2}{2\pi} \iint_A \left(1 - e^{-i\xi(r)}\right) e^{-i\delta(r,\theta)} d^2r,$$ (3.12)

where **r** is a vector in the plane orthogonal to the direction of propagation of the incident light, ξ is a phase shift gained by the light ray that enters the particle at the position given by **r** and passes through the particle along a straight trajectory relative to the phase shift gained by a ray propagating outside the particle, and δ is the phase difference between the rays scattered by different parts of the particle (Fig. 3.1). In addition we have omitted the subscript after S, since $S_1 \sim S_2$. The integration is performed over the geometrical cross section of the particle, A.

The phase shifts depend on the particle shape and refractive index. For example, for a spherical particle of radius a and relative refractive index m,

$$\xi = 2ka(m-1)\cos\gamma \qquad (3.13)$$

$$\delta = -ka\sin\theta\sin\gamma\cos\varphi, \qquad (3.14)$$

where γ is the angle between the radial direction and the direction of the initial ray, and φ is an azimuth angle of a vector oriented toward an element of the surface of the particle.

Expression (3.12) enables to obtain the scattering amplitude for a soft large particle of an arbitrary shape. In case of a sphere, substituting the expressions for the phase shifts (3.13) and (3.14) into (3.12), and performing the integration in the spherical coordinates, one can obtain [Van de Hulst, 1957]

$$S(\theta) = k^2 \int_0^a \left(1 - e^{-2ik(m-1)\sqrt{a^2-r^2}}\right) J_0(kr\theta)r\,dr. \qquad (3.15)$$

This integral cannot be evaluated analytically. It must be either expanded or approximated. The later approach gives the following expression for the intensity of small angle scattering [Backman, 1998]

$$I_s(\theta) = \frac{a^4 k^2 I_s}{r^2} \left\{ \left(\frac{J_1(x\theta)}{x\theta} - \sqrt{\frac{\pi}{2}} \frac{J_{1,2}(y(\theta))}{\sqrt{y(\theta)}} \right)^2 + \right.$$

$$\left. \left(\frac{2x(m-1)}{y^2(\theta)} \right)^2 \left(\cos y(\theta) - \frac{\sin y(\theta)}{y(\theta)} \right)^2 \right\}, \qquad (3.16)$$

where $x = ka$ is called the size parameter, and

$$y(\theta) = x\sqrt{\theta^2 + 4(m-1)^2}.$$

As one can see, the scattered intensity is highly forward directed. The width of the first scattering lobe is about λ/a. Generally speaking, the larger the particle, the stronger and narrower the first lobe.

The scattering cross section of a spherical particle can be obtained either from (3.16) [Backman, 1998] or (3.12) [Van de Hulst, 1957] using the optical theorem [Newton, 1969]

$$\sigma_t \approx \frac{4\pi}{k} \operatorname{Im} S(0),$$

with Im$S(0)$ the imaginary part of the complex amplitude of light scattered in the exact forward direction $S(0)$ and k the wavenumber. Substituting (3.12) into the optical theorem, we obtain the scattering cross section of a spherical particle

$$\sigma_t \approx 2\pi a^2 \left\{ 1 - \frac{\sin(2x(m-1))}{x(m-1)} + \left(\frac{\sin(x(m-1))}{x(m-1)} \right)^2 \right\}. \tag{3.17}$$

Defining the maximal phase shift as $\rho = 2ka(m-1)$, we rewrite this expression as follows

$$\sigma_t = 2\pi a^2 \left(1 - 2\frac{\sin \rho}{\rho} + 4\frac{\sin^2 \rho/2}{\rho^2} \right)$$

This is the famous expression first obtained by Van de Hulst. It shows that large spheres give rise to a very different type of scattering than small particles do. Both the intensity of the forward scattering and the scattering cross section are not monotonous functions of wavelength. Rather, they exhibit oscillations with wavelength, called the interference structure, (Fig. 3.2). The origin of these

75
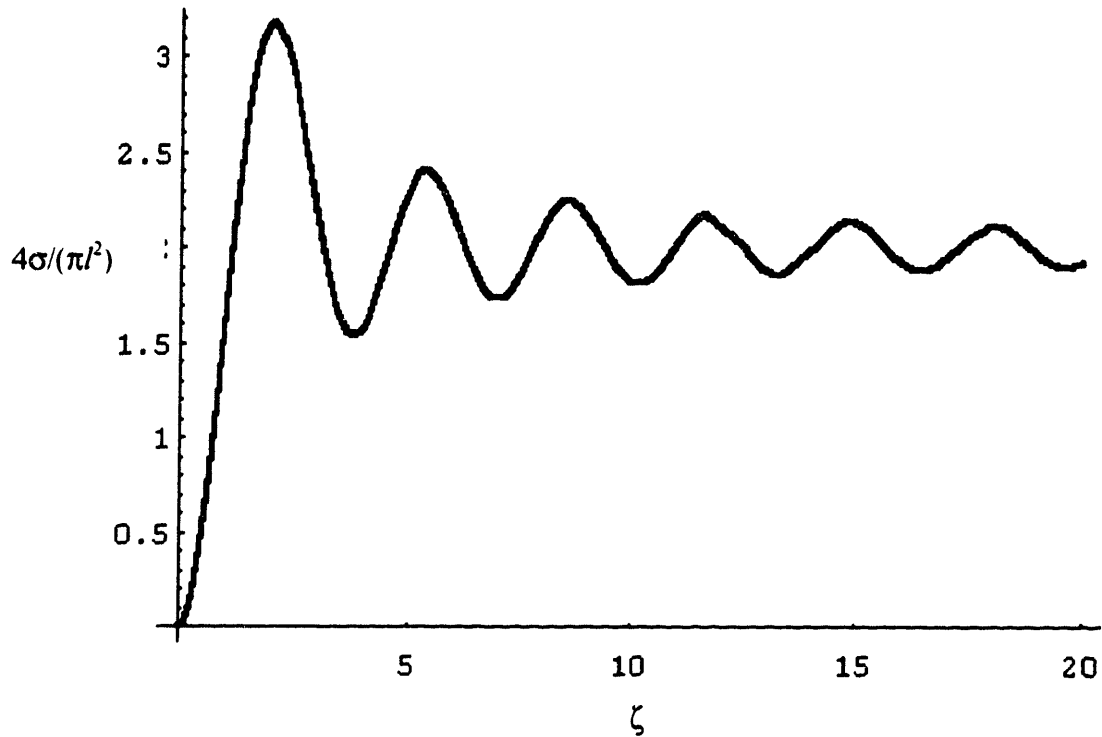
Figure 3.2 Total cross section σ as a function of $\zeta = x(m-1)$.

oscillations is indeed the interference between the light ray passing through the center of the sphere and one not interacting with it. The frequency of these oscillations is proportional to $x(m-1)$, so it increases with the sphere size and refractive index.

Before we leave the topic of light scattering by a sphere, let us discuss the scattering in near backward directions. Unfortunately, obtaining the intensity of light scattered at large angles is difficult, since one has to consider several effects influencing the scattering pattern. For example, multiple internal reflections, diffraction, and surface waves all contribute to the intensity in the backward direction [Van de Hulst, 1969]. Until recently, no closed form analytical solution to describe the scattering in near-backward directions has been derived.

We have obtained an approximate expression describing the near-backward scattering by a large particle using geometrical optics approximation[2] and correcting it for the diffraction of light ways multiply reflected inside the particle [Backman, 1998]

$$\left|S(\theta')\right|^2 \propto J_0^2(x\theta'+\eta),\qquad(3.18)$$

where angle θ' is counted from the exact backward direction, and η is an oscillating function of size parameter x and the phase shift xm. One can see that the intensity of scattered light peaks not only in the exact forward direction but in a near backward direction as well. However, the backscattering peak is significantly smaller than the forward scattering peak. Another difference is that it is shifted from the exact backward direction. This shift varies inversely with the size of the sphere and its refractive index.

Scattering by a sphere is by far the simplest problem in almost any approximate theory of light scattering. It has been studied most extensively as well. The question that remains is whether the results obtained for a homogenous sphere are anyhow applicable to the particles that exist in the biological tissue. Apparently, spherical particles are very good models for many natural objects including aerosols, water droplets in air, etc. However, as discussed in the previous chapter, biological scatters are rarely ideal spheres in shape and uniform in their structure. In fact, such an ideal spherical object would rather be a rare exception that testes the rule of complicatedly shaped inhomogeneous objects found in living tissues. We have already seen how much trouble one might need to get into in order to describe light scattering by a simple sphere: approximate formulas for the

---

[2] Geometrical optics approximation is applicable for large particles only.

scattering cross section are quite easy to derive [Van de Hulst, 1957], but expressions for the forward scattering are not that simple, no closed-form solution describing the near-forward and near-backward scattering has been found until recently [Backman, 1998], and, finally, no closed-form expression describing light scattered into intermediate angles that are in between the near-forward and near-backward angles, exists still. Is it really possible to get any insight into scattering properties of large non-uniform objects with shapes even slightly different from that of a sphere?

3.3.3 General Properties of Light Scattering by Large Non-Spherical Composite Particles

The goal of this section is to elucidate some of the general properties of light scattered by large particles that are not necessarily uniform spheres. We start with the discussion of the general properties of the scattering cross section. Let us take a look at general expression (3.12). Substituting $S(\theta)$ from (3.12) into the optical theorem

$$\sigma_s \approx \frac{4\pi}{k^2} \operatorname{Im} S(0),$$

(3.19)

one can obtain the scattering cross section of an arbitrarily shaped and not necessarily homogenous large particle:

$$\sigma_s = 2 \operatorname{Re} \iint_S \left(1 - e^{i\delta(\mathbf{r})}\right) d^2\mathbf{r}.$$

(3.20)

78
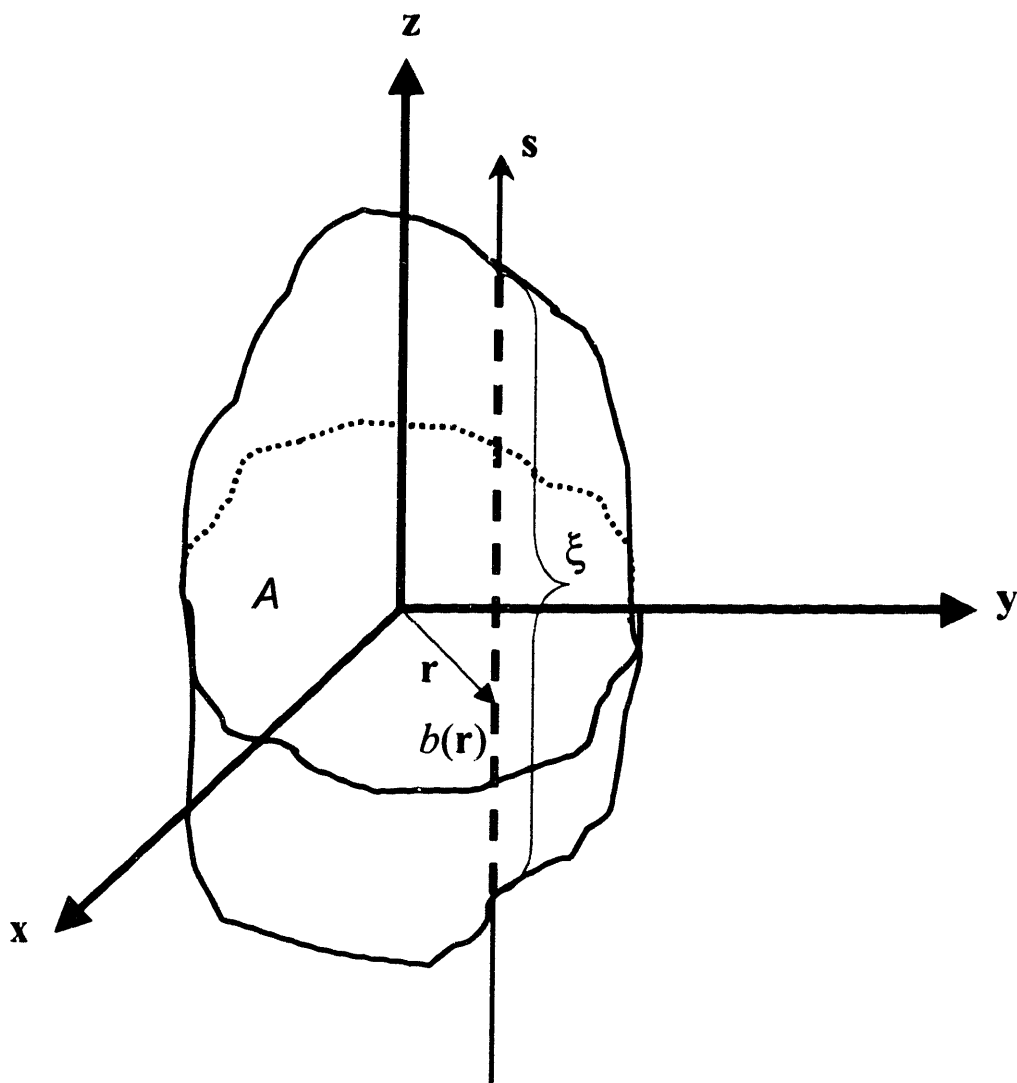
Figure 3.3 Schematic diagram illustrating phase shift ξ of the light ray traversing path b(r) inside a non-spherical and non-uniform particle.

where ξ is the phase shift of a light ray passing through the particles along the direction intersecting the geometrical cross section of the particle at point **r** (Fig. 3.3). The integration is performed over the cross sectional area of the particle, A. Despite the fact that this expression is valid for arbitrary shaped and non-uniform

particles, the integration can be performed analytically in just few cases. Examples include uniform or coated spheres, cylinders, and cubes. However, the value of the integral can be approximated for much wider class of scattering particles.

If the particle is non-uniform, the refractive index varies inside the particles, and therefore, the phase shift is a function of **r**. In polar coordinates

$$\sigma_s = 2\operatorname{Re}\iint_I \left(1 - e^{i\xi(\mathbf{r})}\right) d^2\mathbf{r} = 2\operatorname{Re}\int_0^a r\,dr \int_0^{2\pi} d\varphi\left(1 - e^{i\xi(r,\varphi)}\right). \qquad (3.21)$$

Let us choose the coordinate system in such a way that the axis **z** is oriented along the direction of propagation of the incident light. Moreover, the center of the coordinate system is chosen so that the corresponding phase shift is maximal:

$$\xi(0) = \max_{\mathbf{r} \in A}\left(\xi(\mathbf{r})\right).$$

For any given radial distance r, the phase shift can be written as

$$\xi(r,\varphi) = \xi_0(r) + \delta\xi(r,\varphi), \qquad (3.22)$$

where $\xi_0(r)$ is an average phase shift and $\delta\xi$ is a function of r and φ that describes the variations of the phase shift for a given angle φ and depends on the variations of the refractive index inside the particle. As long as the variations of the refractive index are sufficiently random and smaller than the average phase shift, an approximation of the integral over φ can be found

$$\int_0^{2\pi} d\varphi\left(1 - e^{i\xi(r,\varphi)}\right) = \int_0^{2\pi} d\varphi\left(1 - e^{i\xi_0(r)} e^{i\delta\xi(r,\varphi)}\right) =$$

$$2\pi - e^{\xi_0(r)} \int_0^{2\pi} d\varphi e^{i\delta\xi(r,\varphi)} \approx 2\pi\left(1 - e^{\xi_0(r)}\right) . \qquad (3.23)$$

By definition, the phase shift equals

$$\xi = \int_{b(r)} k(m(\mathbf{r},z)-1)dz , \qquad (3.24)$$

where $m(z)$ is the value of the refractive index inside the particle at a point with coordinates $(\mathbf{r},z)$ and the integration is performed over the total path, $b(\mathbf{r})$, a photon must travel inside the particle (Fig. 3.3). Let us introduce a function $\delta m(r)$ that defines the spatial variations of the refractive index as follows

$$m(r) = m_0 + \delta m(r) , \qquad (3.25)$$

where m_0 is an average refractive index. Accordingly, $b(\mathbf{r})$ can be expressed as follows

$$b(r) = b\cos\gamma(1 + \delta b(\gamma)) , \qquad (3.26)$$

where γ is the angle between the radial direction and the direction of the path of the photon (Fig. 3.3), $b = b(0)$, and function $\delta b(\gamma)$ describes non-spherical shape of the particle. For example, in case of a sphere $\delta b(\gamma) = 0$. With this notation,

$$\xi_0 \approx \rho\cos\gamma + \rho\cos\gamma\alpha \qquad (3.27)$$

with $\rho = 2kb(m_0 - 1)$ and $\alpha = \dfrac{\delta m}{m_0 - 1} + \dfrac{\delta m \delta b}{m_0 - 1} + \delta b$. Parameter ρ is the maximal phase shift a photon might have been exposed to, if the refractive index inside the particle was distributed uniformly. Function α quantifies the difference between the

particle and a uniform sphere. For instance, the first term in the expression for α shows how significant the variations of the refractive index inside the particle are compared to the average refractive index. The quantity $\rho\alpha$ quantifies the impact of the non-uniformity and non-sphericity of the particle on the phase shift.

To simplify the calculations we introduce a new variable, $t=a\cos\gamma$. To calculate the scattering cross section we need to substitute (3.27) into (3.23) and the latter into (3.21). If $\rho\alpha<<1$, we obtain

$$\sigma_s = 4\pi a^2 \operatorname{Re} \int_0^1 t\left(1 - e^{it\rho} e^{it\rho\alpha}\right) dt \approx$$

$$4\pi a^2 \operatorname{Re} \int_0^1 t\left(1 - e^{it\rho}\right) dt - 4\pi a^2 \rho\langle\alpha\rangle \operatorname{Im} \int_0^1 t^2 e^{it\rho} dt \quad (3.28)$$

with $\langle\alpha\rangle$ an average value of α.

The first integral can easily be evaluated and equals

$$\operatorname{Re} \int_0^1 t\left(1 - e^{it\rho}\right) dt = \frac{1}{2} - \frac{\sin\rho}{\rho} + 2\frac{\sin^2\rho}{\rho} . \quad (3.29)$$

The second integral can be evaluated as follows

$$\operatorname{Im} \int_0^1 t^2 e^{it\rho} dt = -\frac{\cos\rho}{\rho} + 2\frac{\sin\rho}{\rho^2} - 2\frac{\sin^2\rho/2}{\rho^3} . \quad (3.30)$$

Substituting (3.30) and (3.29) into (3.28), we obtain an expression for the scattering cross section

$$\sigma_s = 2\pi a^2 \left(1 - 2(1 + 2\langle\alpha\rangle)\frac{\sin\rho}{\rho} + 4(1 + \langle\alpha\rangle)\frac{\sin^2\rho/2}{\rho^2} + 2\langle\alpha\rangle\cos\rho \right). \quad (3.31)$$

This scattering cross section has several important properties:

1) it depends on only three parameters $\langle\alpha\rangle$, the cumulative characteristic of non-uniformity and non-sphericity of the particle[3], the maximal phase shift ρ and the geometrical cross section of the particle in the plane perpendicular to the direction of propagation of the incident light.

2) In the limit of a particle size approaching zero ($a\to0$ or $b\to0$) or small refractive index difference between the particle and the surrounding medium (m_0-1$\to$0), the scattering cross section, approaches zero as well ($\sigma_s\to0$) for any parameter $\langle\alpha\rangle$, which is required by common sense.

3) If the particle is almost uniform and has a near spherical shape ($\langle\alpha\rangle\to0$), (3.31) becomes

$$\sigma_s \underset{\langle\alpha\rangle\to0}{\longrightarrow} 2\pi a^2 \left(1 - 2\frac{\sin\rho}{\rho} + 4\frac{\sin^2\rho/2}{\rho^2} \right),$$

which is exactly the scattering cross section of a uniform sphere.

4) Expression (3.31) can easily be extended in case of absorbing particles as well. The refractive index of an absorbing particle m_0 is complex and one

---

[3] We have already discussed that parameter α depends on the variations of the refractive index inside the particle,δm, and difference between its shape and a sphere, δb. If variations of the refractive index can be considered close to random, the only major contribution to <α> is given by δb. In other words, it is not the internal structure but rather the overall shape that matters the most.

must use $\rho = 2kb(m_0' - 1) + i2kbm_0''$ in (3.28) with m_0' and m_0'' the real and imaginary parts of m_0 respectively.

5) Most importantly, we conclude that the spectral properties of light scattering by a non-uniform non-spherical particle are similar to those of a corresponding uniform sphere that gives rise to the same maximal phase shift as the composite particle. Such a particle would exhibit all the same wavelength dependent variations as the sphere but with a different amplitude. In other words, the scattering cross section depends primarily on the maximal phase shift that a light ray can gain while traveling along a straight trajectory inside the particle, rather than on the specifics of the particle's shape and internal structure. This fact has been confirmed in a number of experiments. For example, it was found that light scattering by red blood cells can accurately be described using the van de Hulst approximation, despite the fact that red blood cells are highly non-spherical [Hammer et al., 1998].

3.4 Origin of Light Scattering in Cells

In the previous sections we have overviewed the structure of epithelial cells and mucosal tissues and discussed some of the analytical and computational methods widely used to calculate the amplitudes of the light scattered by small particles. Now we shall see how histology and physics merge to provide understanding of light scattering by living cells and tissues. Our goal will be twofold. Firstly, we will examine what cell structures are responsible for various scattering patterns. Secondly, we will address the question of what kind of

Organelle	Refractive Index	References
Extracellular fluid	1.35-1.36	Beauvoit et al., 1994
Cytoplasm	1.36-1.37	Brunsting et al., 1974
Nucleus	1.38-1.47	Brunsting et al., 1974; Beuthan et al., 1996
Mitochondria	1.38-1.41	Beauvoit et al., 1994; Beuthan et al., 1996

Table 3.1 Values of refractive index for some components of the cell.

simplified models can be used to predict the scattering patterns produced by various subcellular structures.

As we have seen, the cells and tissues have complex structure with a very broad range of the sizes of the scattering particles: from a few nanometers, the size of a macromolecule, to 7-10 μm, a size of a nucleus, and to 20 μm, a size of a cell. The picture is complicated even further by the fact that only few cell structures are homogenous with refractive index distributed uniformly. Most cell organelles and inclusions are themselves complex objects with spatially varying refractive index. Thus, picturing a cell as being composed of a number of distinct uniform objects of proper geometrical shape is, generally speaking, not correct. On the other hand, several studies have confirmed that many organelles such as mitochondria, lysosomes, and nuclei do posses average refractive index substantially different from that of their surroundings (Table 3.1) and, therefore, viewing a cell as an object with randomly varying refractive index is not accurate either [Beuthan et al., 1996; Schmitt et al., 1998]. A more accurate model acknowledges subcellular compartments of various sizes with refractive index, though not constant over the

compartment's volume, but different from that of the surroundings. A similar model would describe an epithelium or a mucosal tissue, as well.

Studies of light scattering by cells have a long history. The first works in this area investigated the angular dependence of the scattered light. Most of the experiments were performed on a single wavelength and the angular distribution of the scattered light was measured either with an array of photodetectors, fiber optics, or CCD. Mullaney et al. initiated a series of experiments aiming to relate the internal structure of living cells with the scattering pattern by measuring forward and near forward scattering by cell suspensions [Brunsting et al., 1974]. This turned out to become one of the first attempts to explain the light scattering by cells using rigorous quantitative approaches.

The researchers used cells of several types such as Chinese hamster's oocytes (CHO), HeLa cells, and nucleated (white) blood cells. In each case, they compared the resulting angular distribution of the scattered light with one predicted by the Mie theory and found that a very good agreement between theory and experiment was found when the cell was approximated as denser sphere imbedded into a larger and softer sphere. The sizes of the spheres corresponded to the average sizes of the cell nuclei and cell themselves respectively. Including scatterers of smaller sizes into the model did not improve the fits. This result agrees well with the scattering theory. Indeed, as discussed in section 3.3, the particles large compared to the wavelength produce the scattered field that peaks in the forward and near backward directions in contrast to smaller particles, which scatter light more uniformly. In fact, the width of the forward peak, θ_f is proportional to the ratio of the wavelength λ to thee particle's size a:

$$\theta_f = \frac{\lambda}{a}. \qquad\qquad (3.32)$$

Therefore, it is not surprising that the structures with the biggest dimensions, namely cells and their nuclei, are the major scatterers in the forward direction.

Another interesting conclusion can be drawn from these experiments: despite non-homogeneity and not perfectly spherical shape of the cells and their nuclei, the experimental results were explained using the Mie theory, which deals with uniform spheres. This finding should not be surprising as well, because it can be anticipated in the light of the Van de Hulst theory. Indeed, the scattering pattern produced by a large[4] particle in near forward directions depends mostly on the maximal phase shift undergone by the incident light wave rather than variations of the refractive index inside the particle (see section 3.3.1 and equation 3.31). This result was later supported by Slot *et al.* [Slot et al., 1988] in the experiments with white blood cells (leukocytes) and Hammer *et al.* in the experiments with red blood cells (erythrocytes) [Hammer et al., 1998]. The former group of researches found that light scattering by the leukocytes in the near forward direction can be explained if each cell was approximated as being composed of two concentric spheres, one being the cell itself and the other being the nucleus.[5] The later group showed that near-forward scattering of light by red blood cells can accurately be described using the van de Hulst approximation, which was derived for large

---

[4] For simplicity, we refer to particles large compared to the wavelength as "large" particles.

[5] One important comment must be made. There is an apparent distinction between the experiments with cell suspensions and ones involving living epithelia: when the scattering by a cell suspension is measured, the cells, contrasted to their sub-cellular components, might give an important contribution to the scattering. In contrary, the epithelia consist of one or several layers of contiguous cells with minute (a few nanometers) or no extracellular space at all. Thus, the contribution to the scattering from a cell as a whole is expected to be much less and the sub-cellular structures are to be viewed as major scatterers.

particles of spherical shapes rather than concave-convex disks that the red blood cells really are.

Extensive studies of angular dependence of light scattering by cells was performed by Mourant *et al.* [Mourant et al., 1998]. The measurements were performed with a goniometer from $2°$ to $171°$. The unpolarized light was delivered by a He-Ne laser at 632.8 nm. The concentration of cells was 10^5 cells/ml. This concentration was chosen so that multiple scattering events would be rare. The researches used immortalized rat embryo fibroblast cells (M1) in their experiments. The cells were suspended in phosphate-buffered saline. Nuclei and mitochondria were isolated from cells by standard methods and resuspended in mannitol sucrose buffer. The researches found that the scattering by the nuclei most closely resembled the scattering by the cells. Particularly, the scattering at near-forward angles is attributable to the nuclei. At the same time, mitochondria were found to scatter stronger at larger angles, from $15°$ to $160°$.

Moreover, the researches found increased scattering by the nuclei and cells in the near-backward directions, for angles above $165°$. As discussed in the previous section, such increase is characteristic for scatterers large compared to the wavelength of the incident light. In contrast, particles with sizes smaller or comparable to the wavelength do not give rise to the backscattering peak. Their intensity profile is rather flat for these angles. For comparison, intensity of light scattered by the cell nuclei and cells themselves, which are more than an order of magnitude larger than the wavelength, does exhibit a prominent peak in near-backward direction, as expected.

These studies showed that the cell structures responsible for light scattering can be correlated with the angle of scattering. The following generalizations,

though by no means universal, can provide a convenient paradigm to think about light scattering by biological cells:

1. When a cell is suspended in a medium of a lower refractive index, i.e. buffer solution, the cell itself is responsible for small angle scattering. This result has been used in flow cytometry to estimate the sizes of cells [Watson, 1991]. However, this is not the case for contiguous layers of cells such as epithelia, where all cells are surrounded by other cells with similar optical properties rather than a medium of a different refractive index [Drezek et al., 1999]. In the later case, most of the scattering is attributable to particular structures *within* the cells.

2. At slightly larger angles the nucleus is primarily responsible for scattering. Moreover, if the cell is a part of a contiguous layer, the cell nucleus is the major scatterer in all forward and near-forward directions.

3. Smaller organelles, cell inclusions, sub-organellar and sub-nuclear inhomogeneities are likely to be responsible for scattering at larger angles. Unfortunately, it is difficult to be more specific due to the fact that there is too great variety of cell components with sizes smaller or comparable to the wavelength. To name a few, mitochondria, lysosomes, Golgi apparatus, essentially all cell organelles other than the nucleus, plus sub-nuclear inclusions such as nucleolus and clumps of chromatin, all have sizes comparable to or smaller than the wavelength of light. Scattering may originate from organelles themselves or their internal components. Moreover, one should not forget that light scattering may occur from the patterns formed by a number of neighboring objects. This does not mean that scattering at large angles cannot provide any clues about the origin of

89

the scattering. Potentially, the angular dependence of scattering might elucidate whether the scattering originates from the objects of regular or irregular shape, spherical or elongated, inhomogenous or uniform. Rigorous approaches to accomplish this have yet to be developed. In some cases the large angle scattering can be attributed to a specific predominant organelle. For example, the research conducted by B. Chance and coworkers provides strong evidence that mitochondria are primarily responsible for light scattering by hepatocytes, the cell known to posses very numerous mitochondria that can reach count of thousands [Beavoit et al., 1994]. However, the hepatocytes are exceptions in their rich mitochondrial content. Most other cells including most mucosal epithelia posses much less numerous mitochondria.

4. Finally, the increase of the light scattering intensity in the near backward directions is attributable to larger structures within the cell, such as the nucleus.

Not only does the light scattered by cell nuclei have characteristic angular distribution peaked in near backward directions, but it also exhibits spectral variations typical for large particles discussed in section 3.3. We have observed such spectral behavior in the light backscattered by the nuclei of human intestinal cells [Perelman et al., 1998]. These studies will be discussed in detail in Chapters 4 and 5.

References

Arnfield MR, J. Tulip, and M.S. McPhee, "C̣ ical propagation in tissue with anisotropic scattering", *IEEE Trans Biomed Eng* **35**, 372-381 (1988).

Backman V, "Reflectance Spectroscopy for Diagnosis of Precancerous Changes in Human Epithalium", M.S. Thesis, MIT (1998).

Backman V, Wallace MB, Perelman LT, Arendt JT, Gurjar R, Muller MG, Zhang Q, G. Zonios G, Kline E, McGillican T, Shapshay S, Valdez T, Van Dam J, Badizadegan K, Crawford JM, Fitzmaurice M, Kabani S, Levin HS, Seiler M, Dasari RR, Itzkan I and Feld MS, "Light scattering spectroscopy: a new technique for clinical diagnosis of precancerous and cancerous changes in human epithelia", *Nature*, **406**, 35-36 (2000).

Beauvoit B, T. Kitai, and B. Chance, "Contribution of the mitochondrial compartment to the optical properties of rat liver: a theoretical and practical approach", *Biophys. J.*, **67**, 2501-2510 (1994).

Beuthan J, O. Milner, J. Hefmann, M. Herrig, and G. Muller, *Phys. Med. Biol.*, **41**, 369 (1996).

Boone C.W. *et al.* Quantitative grading of rat esophageal carcinogenesis using computer-assisted image tile analysis. *Cancer Epidemiology, Biomarkers & Prevention*, **9**, 495-500 (2000).

Brown, G.L., McEwan, M., Pratt, M. Macromolecular weight and size of deoxypentose nucleic acids. *Nature*, **176**, 161-162 (1955).

Brunsting A and Mullaney F, "Differential light scattering from spherical mammalian cells", *Biophys. J.*, **14**, 439-453 (1974).

Cotran RS, Robbins SL, Kumar V, *Robbins Pathological Basis of Disease* (W.B. Saunders Company, Philadelphia, 1994).

Davies, H.G., Deeley, E. M., Denby, E. F. Attempts at measurement of lipid, nucleic acid and protein content of cell nuclei by microscope-interferometry. *Exp. Cell Res.*, Suppl. 4, 136-149 (1957).

Davies, H.G. *General Cytochemical Methods* (Danielli, J.F., ed.) Vol I. (Academic Press, New York and London, 1958).

Draine BT, P.J. Flatau, "Discrete dipole approximation for scattering calculations", *J Opt. Soc. America*, **A11**, 1491-1499 (1994).

Drezek R, A. Dunn, and R. Richards-Kortum, "Light scattering from cells: finite-difference time-domain simulations and goniometric measurements", *Appl. Opt.*, **38**, 3651-3661 (1999).

Dunn A and R. Richards-Kortum, "Three-dimensional computation of light scattering from cells", *IEEE J. Sel. Top. Quantum Electron.*, **2**, 898-905 (1996).

Fawcett DW, *A Textbook of Histology*, (Charman & Hall, New York, 1994).

Jackson JD, *Classical Electrodynamics*, (John Wiley & Sons, New York, 1975).

Hammer M, D. Schweitzer, B. Michel, E. Thamm, and A. Kolb, "Single scattering by red blood cells", *Appl. Opt.*, **37**, 7410-7418 (1998).

Hiatt LD, *Color Atlas of Histology*, (Williams & Wilkins, Baltimor, 1994).

Kerker M, *The Scattering of Light*, (Academic Press, New York, 1969).

Kienle A, L. Lilge, M.S. Patterson, et al., "Spatially resolved absolute diffuse reflectance measurements for noninvasive determination of the optical scattering and absorption coefficients of biological tissue", *Appl Opt* **35**, 2304-2314 (1996).

Landis SH, Murray T, Bolden S, Wingo PA, "Cancer Statistics 1999", CA – A Cancer Journal for Clinicians, **49**, 8-31 (1999).

Lee, L., Pappelis, A. J., Pappelis, G. A., Kaplan, H. M. Cellular and nuclear dry mass and area changes during human oral mucosa cell development. *Acta Cytol.* **17**, 214-219 (1973).

Liao Z, H. Wong, B. Yang, and Y. Yuan, "A transmitting boundary for transient wave analysis", *Sci Sin Ser. A*, **27**, 1063-1076 (1984).

Mourant JR, J. P. Freyer, A. H. Hielscher, A. A. Elick, D. Shen, and T. Johnson, "Mechanisms of light scattering from biological cells relevant to noninvasive optical-tissue diagnosis", *Appl. Opt.*, **37**, 3586-3593 (1998).

Newton RG, *Scattering Theory of Waves and Particles* (McGraw-Hill Book Company, New York, 1969).

Schmitt JM and G. Kumar, "Optical scattering properties of soft tissue: a discrete particle model", ", *Appl. Opt.* **37**, 2788-2797 (1998).

Schmitt JM, "Simple photon diffusion analysis of the effects of multiple scattering on pulse oximetry", *IEEE Trans Biomed Eng* **38**, 1194-1203 (1991).

Slot PMS, Hoekstra AG and Figdor CG, *Cytometry*, **9**, 636 (1988).

Tafloe A, Computational Electrodynamics: The Finite Difference Time Domain Method (Artech, Boston, 1995).

Takatani S and M. Graham, "Theoretical analysis of diffuse reflectance from a two-layer tissue model", *IEEE Trans Biomed Eng* **26**, 656-664 (1979).

Takatani S and J. Ling, "Optical oximetry sensors for whole blood and tissue", *IEEE Eng Med Biol*, **3**, 347-357 (1994).

Van de Hulst HC, *Light Scattering by Small Particles* (Dover Publications, New York, 1957).

Watson JV, *Introduction to Flow Cytometry* (Cambridge U. Press, Cambridge, 1991).

Chapter 4

Principles of Light Scattering Spectroscopy: Analysis of Single Scattering

In the previous chapters we discussed the fact that characterization of cellular structures in living systems is an important problem in biomedical science. The ability to extract quantitative information in living cells or tissues, *in situ*, without perturbing them, could be used to study biophysical processes in living systems and to monitor morphological and physiological changes such as precancerous or cancerous conditions. At present, such information can only be obtained by tissue removal or scraping. Currently, techniques such as microscopy and flow cytometry are used to probe intracellular structure, and applying them *in situ* is not possible [Watson, 1991]. In this chapter we discuss how a novel

technology called biomedical light scattering spectroscopy (LSS) can be applied to probe the structure of living cells and tissues.

4.1 Introduction to Light Scattering Spectroscopy

Elastic light scattering has long been used to study the size and shape of small particles such as colloids, water droplets, and cells. In this process, light of a given wavelength is incident on the target particle, and the particle's size is determined from the angular distribution and wavelength dependence of the scattered light [Newton, 1969]. Thus, elastic light scattering can be used to probe the morphology of living tissues. However, single scattering events cannot be directly measured in biological tissue [Yodh et al., 1995]. Only a small portion of the light incident on the tissue is returned after a single scattering. The rest enters the tissue and undergoes multiple scattering from a variety of constituents in the underlying tissue, where it becomes randomized in direction, producing a large background of diffusely scattered light (diffusive background). The single scattering component must be distinguished from this diffuse background. This requires special techniques, because the diffusive background itself exhibits prominent spectral features dominated by the characteristic absorption bands of hemoglobin and scattering of collagen fibers, which are in abundance in the connective tissue laying below epithelium. LSS aims to distinguish the single scattering component and analyze its spectral and angular properties in order to provide quantitative information about the morphology of the tissue. For example, as will be discussed above, LSS enables to measure the size and refractive index distribution of epithelial cell nuclei and, thus, to quantitatively characterize nuclear

Tissue elastic light scattering spectrum

Diffusive background removal
- Model-based
- Polarization discrimination

Single scattering spectrum

Model-based analysis
- Mie theory fit
- Fourier analysis

Size and refractive index distributions of subcellular structures
- cell nuclei
- sub-nuclear structures
- cell organelles

Diagnostic information
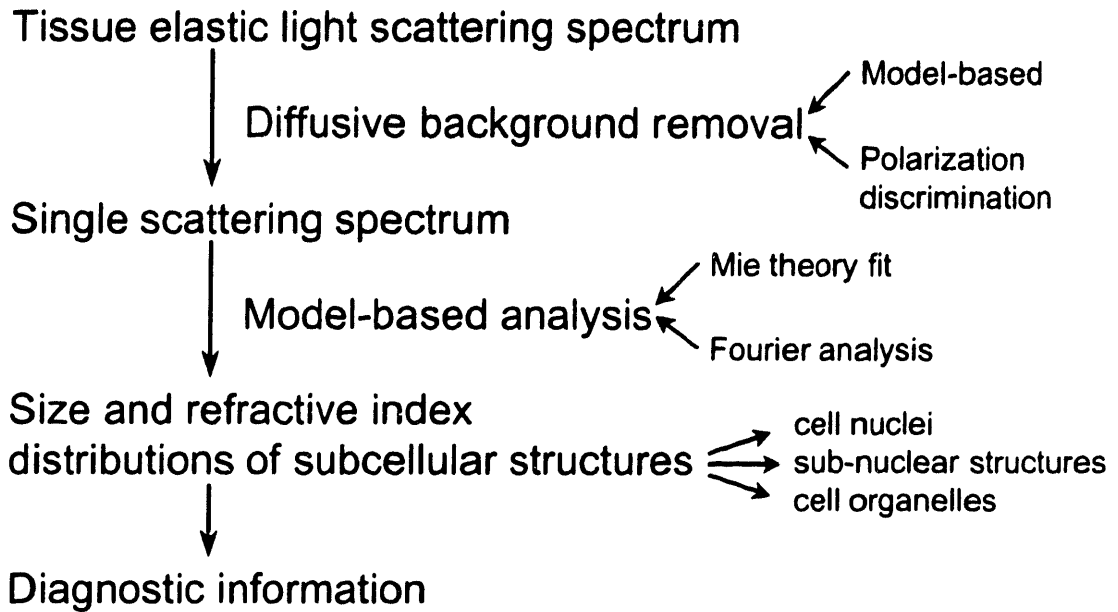
Exhibition 4.1 Principles of light scattering spectroscopy.

enlargement, crowding, hyperchromasia, and pleomorphism frequently associated with precancerous or cancerous transformations in virtually all types of epithelia [Cotran et al., 1994].

The basic principle underlying LSS is illustrated in Exhibition 4.1. First, the tissue under study is illuminated by visible light. LSS usually employs cw-light to illuminate the tissue (Chapters 5 and 6). However, consequent illumination at a number of selected wavelengths can be used as well (Chapter 7). Then the light returned from the tissue by means of elastic scattering is collected and its spectral and/or angular distribution is measured. This signal consists of two principal components: a single scattering component and diffusive background. The diffusive background is then removed. Generally speaking, there are several approaches to accomplish this. Coherent properties of light might be used [Yang et

al., 2000]. Another approach might use the fact that single scattered photons travel shorter distances than multiple scattered ones. Thus, by illuminating the tissue by short (nano- or femtosecond) pulses of laser light and measuring time delayed signal, one can select only the photons that returned after the shortest time intervals, traveled the shortest distance, and, therefore, single scattered [Chen et al., 2000]. A common disadvantage shared by both approaches rests on the fact that they require expansive equipment and do not allow simultaneous measurement of spectral distribution of the scattered light.

We have developed two methods of diffusive background removal: (1) by means of a mathematical model [Perelman et al., 1998], and (2) using polarized light [Backman et al., 1999]. In the former case, we have applied a mathematical model to account for the diffusive background. The model uses absorption and scattering coefficients of the tissue as free parameters to fit the spectral data. After the model fit is subtracted, the single scattering component becomes apparent. The latter case uses the fact that the polarization of light is lost after multiple scattering events. By using linearly polarized incident light, the contribution due to single scattering can be obtained as the difference between the components of light scattered from the tissue polarized parallel and perpendicular to the direction of polarization of the incident light.

As long as the spectrum of the single scattering component is identified, it can be analyzed to obtain information about the properties of the scatterers responsible for this component. As discussed in detail in Chapter 8, the origin of LSS signals depends on the geometry of collection. For example, when light scattered in the near-backward directions is collected, the largest intracellular structures, the cell nuclei, are primarily responsible for the LSS signal. On the other hand, other collection geometries may favor photons scattered by smaller

subcellular structures with sizes comparable to or smaller than the wavelength of light. In any case, the spectrum of light scattered by these particles contains a component that varies characteristically with wavelength. This variation depends on particle size and refractive index. When particles of several sizes are present, the resulting signal is a superposition of these variations. Thus, the size distribution and refractive index of the scatterers can be determined from the analysis of the spectrum of light backscattered by these particles. Once the size distribution and refractive index are known, quantitative measures characterizing alterations of morphology of the epithelial cells can be obtained and corresponding diagnostic algorithms can be developed. For example, if backscattering is observed, LSS enables to measured the size distribution of cell nuclei and their refractive index. Thus, some of the major features characterizing nuclear atypia associated with precancerous and cancerous transformations, namely nuclear enlargement, crowding, and hyperchromasia, can be quantified.

4.2 Diagnosis of Precancer with Single and Multiple Scattered Light

Before we discuss the principles of LSS and its application to diagnose and detect early cancerous and precancerous conditions in detail, we need to emphasize that the single scattering component is not the only component of the returned light that can provide diagnostically valuable information. The diffusive background of multiply scattered light should not be regarded as useless, rather it is fair to say that the spectra of both single scattering and diffusive signals contain valuable information about tissue properties. However, the types of information these components provide are different and, in many cases, complimentary. The

single scattering component is sensitive to the morphology of the upper tissue layer, which in case of a mucosal tissue includes or limited to the epithelium. Its spectroscopic features are related to the microarchitecture of the epithelial cells, the sizes, shapes, and refractive indexes of their organelles, inclusions, and suborganellar structures. Thus, analysis of this component might be useful in the diagnoses of diseases limited to the epithelium, such as pre-invasive stages of epithelial cancers, dysplasias and carcinomas *in situ* (CIS) (see Chapter 2).

The diffusive component provides information about tissue scatterers and absorbers as well. However, due to multiple scattering, information about tissue scatterers is randomized as light propagates into the tissue, typically over one transport scattering length (0.5-1.5 mm, depending on the wavelength). Moreover, the diffusive light samples considerably deeper tissue than the single scattered component does. With exception of few cases, such as thick skin on the sole of the foot, the tissue sampled by the diffusive light is never limited to the epithelium. Thus, the diffusive component is much less sensitive to individual structures inside the epithelial cells. Rather it carries important information about tissue architecture and composition and is particularly useful to diagnose diseases in the following cases:

1. The disease is not limited to the epithelium. Invasive cancer is an example.

2. The diseased epithelial cells themselves do not penetrate the basement membrane but the normal structure of the under-epithelial tissue is altered in the process of the disease. Some developed dysplastic lesions are able to induce angiogenesis resulting in the increased blood supply to the lesion. Since, the hemoglobin contained in the red blood cells is one of the major endogenous absorbers in most mucosal tissues, its concentration increase

affects the spectrum of the diffusive light [Zonios, 1998; Zonios et al, 1999; Georgakoudi et al, 2001].

3. The disease is limited to the epithelium but epithelial thickness is increased so much that a considerable portion of the diffusive light is confined to this layer. In some cases, the later stages of CIS of the stratified squamous epithelia of such organs as the uterine cervix or the oral cavity can make the epithelium appear thick enough to trap significant part of the diffusive photons. Because the scattering and particularly absorption properties of the epithelia and underlying connective tissues are different, such change in the epithelial thickness might affect the spectral features of the diffusive component.

Generally speaking, the single scattering component is more important in diagnosing the initial stages of the epithelial precancerous lesions, while the diffusive component carries valuable information about more advanced stages of the disease.

4.3 Analysis of Single Scattering Component

4.3.1 Analytical Treatment of Single Scattering Component

Consider a particle illuminated by a plane electromagnetic wave $E_i = E_0 e^{i(kr - \omega t)}$, where E_0 is the wave amplitude, k is the wavevector, and ω is the frequency. Consider scattered wave E_s propagating along direction $n(\theta, \phi)$, where θ and ϕ are polar angles in the spherical coordinate system such that axis z is

oriented along the direction of propagation of the incident light and the center of the system coincides with the particle[1]. As discussed in Chapter 3, the scattered spherical wave observed at a distance r has amplitude components E_{s2} and E_{s1}, parallel and orthogonal to the plane of scattering respectively, which can be expressed through the corresponding components of the incident wave E_{i2} and E_{i1} by means of scattering amplitude matrix notation [Newton, 1969]

$$\begin{pmatrix} E_{s2} \\ E_{s1} \end{pmatrix} = \frac{e^{-i(kr-\omega t)}}{ikr} \begin{pmatrix} S_2 & S_3 \\ S_4 & S_1 \end{pmatrix} \begin{pmatrix} E_{i2} \\ E_{i1} \end{pmatrix}, \qquad (4.1)$$

where the elements of the scattering matrix are, generally speaking, functions of polar angles θ and ϕ. In expression (4.1), the elements of the scattering matrix as well as amplitudes of the incident and scattered waves need not be considered to be real numbers. When the particle has axial symmetry or the observed scattering originates from an ensemble of non-symmetrical randomly oriented particles, $S_3=S_4=0$ and the only non zero components of the scattering matrix are S_1 and S_2, which are functions of scattering angle θ, but not azimuth ϕ [Newton, 1969]. The scattering angle varies from 0^0 (forward scattering) to 180^0 (backscattering). Because our major interest is the scattering in near-backward directions, we will distinguish between *scattering* angle that we measure from 0^0 and *backscattering* angle or angle of backscattering that is measured from the direction of exact backscattering, 180^0. For example, backscattering angle 5^0 corresponds to 175^0 scattering angle. θ will denote backscattering angle unless otherwise indicated.

---

[1] Because we observe the scattered wave in the wave zone at a distance r much larger than the characteristic size of the particle, we do not need to specify where exactly the origin of the reference system is in respect to the particle.

Without loss of generality, we can consider the incident wave to be linearly polarized. If axis x of the laboratory reference system is oriented along the polarization of the incident light,

$$\begin{pmatrix} E_{i2} \\ E_{i1} \end{pmatrix} = E_0 \begin{pmatrix} \cos\varphi \\ \sin\varphi \end{pmatrix}. \tag{4.2}$$

Amplitudes E_{s2} and E_{s1} are related to the projections of the scattered field $\mathbf{E}_s$ onto the axis x and z of the laboratory reference system, E_{sx} and E_{sy} respectively, as follows

$$\begin{pmatrix} E_{sx} \\ E_{sy} \end{pmatrix} = \begin{pmatrix} \cos\theta\cos\varphi & -\sin\varphi \\ \cos\theta\sin\varphi & \cos\varphi \end{pmatrix} \begin{pmatrix} E_{s2} \\ E_{s1} \end{pmatrix}. \tag{4.3}$$

Substituting (4.2) and (4.3) into (4.1), we obtain the following expression for the components of the scattered field in the laboratory reference system:

$$\begin{pmatrix} E_{sx} \\ E_{sy} \end{pmatrix} = \begin{pmatrix} \cos\theta\cos\varphi & -\sin\varphi \\ \cos\theta\sin\varphi & \cos\varphi \end{pmatrix} \begin{pmatrix} S_2 & 0 \\ 0 & S_1 \end{pmatrix} \begin{pmatrix} \cos\varphi \\ \sin\varphi \end{pmatrix} \frac{E_0 e^{-i(k+\omega t)}}{ikr} =$$

$$\begin{pmatrix} S_2\cos\theta\cos^2\varphi - S_1\sin^2\varphi \\ S_2\cos\theta c\cos\varphi\sin\varphi + S_1\cos\varphi\sin\varphi \end{pmatrix} \frac{E_0 e^{-i(kr+\omega t)}}{ikr}. \tag{4.4}$$

This expression defines the angular distribution of the scattered field. S_1 and S_2 are functions of the backscattering angle θ but not azimuth ϕ. Therefore, as long as these functions are known, the whole angular distribution can easily be calculated.

If the incident light is not coherent, information about the phases of the incident and scattered photons is not preserved. Therefore, in such an experiment it is not possible to measure complex amplitudes E_{sx} and E_{sy}. Instead, one can

measure intensities I_x and I_y of the scattered light polarized along axis **x** and **y** respectively. Intensities I_x and I_y can be measured by means of two polarizers oriented to transmit light polarized along axis **x** and **y** and collecting transmitted photons. Accordingly to (4.4), I_x and I_y are related to the intensity of the incident light I_0 as follows

$$I_x = \frac{I_0}{k^2 r^2}\left(|S_2|^2 \cos^2\theta \cos^4\varphi + |S_1|^2 \sin^4\varphi - 2\,\mathrm{Re}(S_1 S_2^*)\cos\theta\cos^2\varphi\sin^2\varphi\right)(4.5)$$

$$I_y = \frac{I_0}{k^2 r^2}\left(|S_2|^2\cos^2\theta + |S_1|^2 + 2\,\mathrm{Re}(S_1 S_2^*)\cos\theta\right)\cos^2\varphi\sin^2\varphi . \qquad (4.6)$$

The difference between these intensities is

$$I_x - I_y = \frac{I_0}{k^2 r^2}\left(|S_2|^2\cos^2\theta\cos^2\varphi\left(\cos^2\varphi - \sin^2\varphi\right)+ \right.$$

$$|S_1|^2\sin^2\varphi\left(\cos^2\varphi - \sin^2\varphi\right)-$$

$$\left. 4\,\mathrm{Re}(S_1 S_2^*)\cos\theta\cos^2\varphi\sin^2\varphi\right). \qquad (4.7)$$

The total intensity of the scattered light is

$$I_x + I_y = \frac{I_0}{k^2 r^2}\left(|S_2|^2\cos^2\theta\cos^2\varphi + |S_1|^2\sin^2\varphi\right). \qquad (4.8)$$

If the incident light is not polarized, the scattered intensity I_s can be found by integrating expression (4.8) over azimuth ϕ and equals

$$I_s = \frac{I_0 \pi}{k^2 r^2}\left(|S_2|^2\cos^2\theta + |S_1|^2\right). \qquad (4.9)$$

Finally, we notice, that if in the experiment the difference between I_x and I_y is integrated over all possible azimuths ϕ, the resulting signal equals

$$\Delta I_\varsigma = \frac{I_0 \pi}{2k^2 r^2} \left(\left| S_2 \cos\theta - S_1 \right|^2 \right) .$$ (4.10)

Expressions (4.5) – (4.10) describe the angular distribution of the scattered light and will be used later on, when we present the studies of angular distribution of light scattered by cells.

The angular distributions depend on the size and internal structure of the scattering particle. For example, particles much larger than the wavelength of light give rise to a prominent backscattering peak. The intensity profile is maximal for the exact backward or near-backward directions and vanishes with the increase of the backscattering angle. The larger the particle, the stronger the near-backward peaks are and the faster the decline is. Moreover, the intensity is higher for angles $\phi = j\pi/2$ with $j=0,1,2,3$ and is smaller for $\phi = \pi/4 + i\pi/2$ with $i=0,1,2,3$. On the other hand, particles with linear sizes comparable to or smaller than the wavelength give rise to a very different type of scattering. Their intensity profiles are smooth functions of the scattering and azimuthal angles. Examples of two angular distributions obtained using the Mie theory for uniform spheres are shown in Fig. 4.1. Figure 4.2 shows an example of I_s as a function of the scattering angle θ. Both figures illustrate strong backscattering peaks in the large particle scattering. As we will see in the following sections, it is these backscattering peaks characteristic for large particles, that allow us to distinguish between light scattered by cell nuclei, the largest cell structure, and light scattered by other cell organelles.

It can be shown that, according to the scattering theory [Newton, 1969], for a small backscattering angle θ,
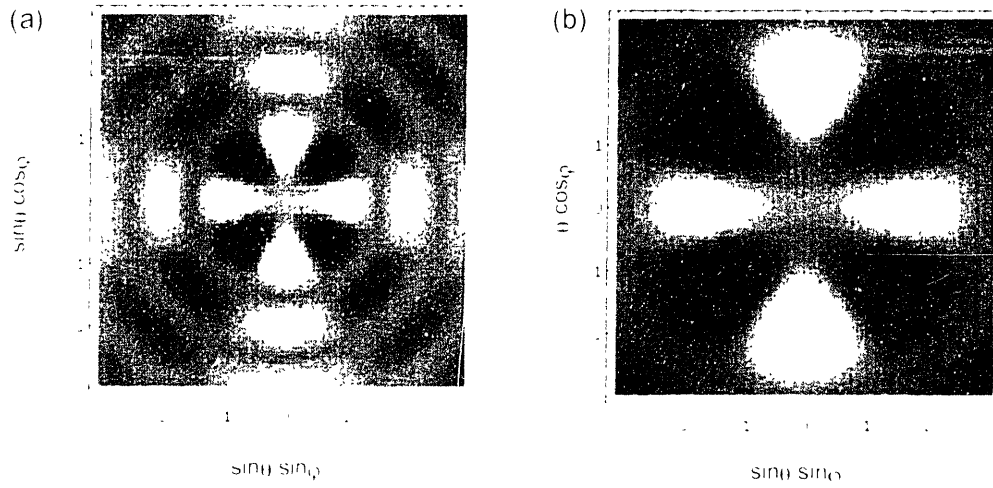
Figure 4.1. Patterns of angular distribution of light scattered at azimuthal angles θ and φ which are predicted by the Mie theory for spherical particles of (a) 20 μm and (b) 10 μm. Brightness indicates intensity of scattered light at particular angle.
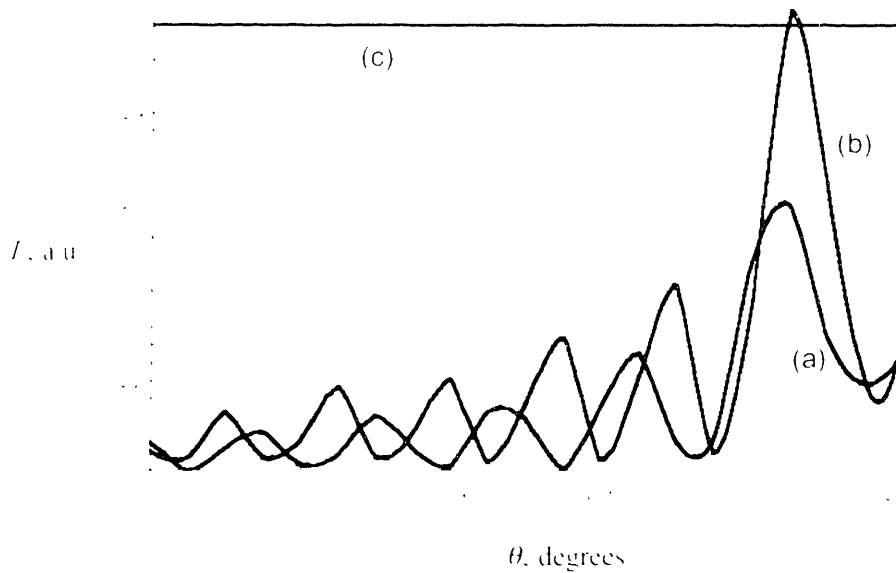
Figure 4.2. Angular distribution of light scattered by a large (10 μm in diameter) sphere for two wavelengths (a) λ 400nm, (b) λ 350nm. For comparison, (c) shows intensity of scattering by an "isotropic scatterer" that scatters all of the incident light isotropically.

105

$$S_2 \approx (-)S_1 \text{ and } S_2 \xrightarrow[\theta \to 0]{} (-)S_1 . \tag{4.11}$$

Therefore,

$$\Delta I_s = I_s \approx \frac{2\pi I_0}{k^2 r^2} |S|^2 , \tag{4.12}$$

where S-index is omitted. In other words, $I_x - I_y$ in case of polarized illumination is equal to the total intensity of the scattered light when unpolarized illumination is used. The physical reason for this is the fact that the scattering into small backscattering angles preserves polarization of the incident light and, thus, $I_x \gg I_y$. However, for scattering angles large enough so that (4.11) does not hold anymore, $I_x - I_y$ might become quite different from I_s. As we will see in the following section, this is one reason why the polarized LSS signal measured as the difference between I_x and I_y has quite different spectral behavior than the unpolarized LSS signal I_s.

In experiments, particularly when a cw-light source is used, the incident light is not perfectly collimated and its intensity is distributed within a solid angle Ω_0. Moreover, a detector usually collects light from a non-zero solid angle $\Delta\Omega$. Intensity components of the scattered light measured in such experiment can be calculated by integration of respective angular distributions given by (4.5) – (4.12) over the solid angles. For instance, if linearly polarized incident light is used, the polarization, $\hat{\varepsilon}_0$, of the incident light can be decomposed into a component $\hat{\varepsilon}_p^0$, in the scattering plane and a perpendicular component $\hat{\varepsilon}_s^0$. By means of analyzers, the detector collects two orthogonal components of the scattered light, I_p with

polarization $\hat{\varepsilon}'_a$ and $I_\perp$ with perpendicular polarization $\hat{\varepsilon}''_a$. The scattered intensity components can be obtained as follows

$$\begin{pmatrix} E_{i2} \\ E_{i1} \end{pmatrix} = E_0 \begin{pmatrix} \cos\varphi_0 \\ \sin\varphi_0 \end{pmatrix}$$ (4.13)

with $\varphi_0 = \cos^{-1}(\varepsilon_p^0 \cdot \hat{\varepsilon}_0)$,

$$\begin{pmatrix} E_{sx} \\ E_{sy} \end{pmatrix} = \begin{pmatrix} \cos\theta\cos\varphi & -\sin\varphi \\ \cos\theta\sin\varphi & \cos\varphi \end{pmatrix} \begin{pmatrix} E_{s2} \\ E_{s1} \end{pmatrix}$$ (4.14)

with $\varphi = \cos^{-1}(\hat{\varepsilon}'_a \cdot \hat{\varepsilon}_p)$ and $\varepsilon^{\wedge}_p$ a unit vector along the polarization of the scattered light in the plane of scattering. Therefore,

$$\begin{pmatrix} E_{sx} \\ E_{sy} \end{pmatrix} = \begin{pmatrix} \cos\theta\cos\varphi & -\sin\varphi \\ \cos\theta\sin\varphi & \cos\varphi \end{pmatrix} \begin{pmatrix} S_2 & 0 \\ 0 & S_1 \end{pmatrix} \begin{pmatrix} \cos\varphi_0 \\ \sin\varphi_0 \end{pmatrix} \frac{E_0 e^{-i(k+\omega t)}}{ikr}$$ (4.15)

and the scattered intensity components are given by

$$I_\parallel = \frac{1}{2\pi k r^2} \int_{\Delta\Omega} d\hat{s} \int_{\Delta\Omega_0} d\hat{s}_0 I_0(\hat{s}_0) \left| S_2(\vartheta)\cos^2\theta\cos\varphi\cos\varphi_0 - S_1(\vartheta)\sin\varphi\sin\varphi_0 \right|^2$$ (4.16)

$$I_\perp = \frac{1}{2\pi k r^2} \int_{\Delta\Omega} d\hat{s} \int_{\Delta\Omega_0} d\hat{s}_0 I_0(\hat{s}_0) \left| S_2(\vartheta)\cos^2\theta\cos\varphi\sin\varphi_0 + S_1(\vartheta)\sin\varphi\cos\varphi_0 \right|^2 ,$$ (4.17)

where $\hat{s}_0$ is a direction of propagation of the incident light, $\hat{s}$ is a direction of propagation of the scattered light, $\vartheta = \cos^{-1}(\hat{s} \cdot \hat{s}_0)$ is a scattering angle.

If the incident light is completely collimated ($\Delta\Omega_0 = 0$), light scattered directly backward ($\Delta\Omega = 0$) will be polarized parallel to the incident light

polarization. In this case we can orient one of the analyzers parallel to the incident polarization direction ($\hat{\varepsilon}_0 = \hat{\varepsilon}'_a$). If the solid angles of the incident and collected light are sufficiently small and approximately equal, both I and $I_\perp$ will be present. However, the analyzer can still be positioned such that ($\hat{\varepsilon}_0 \approx \hat{\varepsilon}'_a$). Thus, in this case, the collected light will still be highly polarized, and $I >> I_\perp$. For this case the expression for the residual intensity, $I - I_\perp$, can be simplified:

$$I - I_\perp \approx \frac{I_0}{4k^2r^2} \int_0^{\vartheta_u} |S_2(\theta) - S_1(\theta)|^2 \sin\theta d\theta \qquad (4.18)$$

with $\vartheta_u = \sqrt{\dfrac{\Delta\Omega}{\pi}}$.

If unpolarized illumination is used, the measured signal can be obtained integrating (4.9):

$$I_1 = \frac{I_0}{2k^2r^2} \int_0^{\vartheta_u} \left(|S_2(\theta)|^2 \cos^2\theta + |S_1(\theta)|^2\right) \sin\theta d\theta . \qquad (4.19)$$

We again notice that for a small collection angle $\Delta\Omega \rightarrow 0$, signals measured in case of polarized and unpolarized illumination are similar: $I - I_\perp \approx I_s$. However, this, generally speaking, does not hold for arbitrary large collection or illumination angles.

In the following section we will discuss in detail why, in case of polarized illumination, the difference between I and $I_\perp$ rather than any other combination is measured. For now, it suffices to say that by subtracting off the component of

the scattered light that is polarized orthogonally to the incident light polarization, the contribution from multiple scattering is removed and the resulting signal $I_\parallel$ - $I_\perp$ is indeed the single scattering component.

4.3.2 Analysis of Single Scattering Component

As long as the spectrum of a single scattering component, either $I_\parallel$ - $I_\perp$ or I_s, returned from a sample, which can be a physical tissue model or *ex vivo* or *in vivo* tissue, is measured in the experiment, it can be analyzed using expressions (4.18) or (4.19) depending on whether polarized or unpolarized illumination is used. In any case, the analysis is based on the fact that this signal exhibits spectral variations characteristic of the size, shape, structure, and refractive index of the scattering particles. However, in order to obtain this information one needs to know how scattering amplitudes S_1 and S_2 vary with these parameters. Even if the particle can be approximated as a uniform sphere, this dependence is not linear and rigorous inversion is not usually possible. To address this problem, we have developed two methods of analysis: 1) the Mie theory based analysis, which was used to obtain information about epithelial cell nuclear size distributions in the LSS studies with polarized light and in the LSS imaging studies [Backman et al., 1999; Gurjar et al., 2001]; and 2) Fourier transform-based analysis, which was used to measure size distributions of cell nuclei using unpolarized LSS and in the clinical studies with LSS [Perelman et al., 1998; Backman et al., 2000; Wallace et al., 2000].

4.3.2.1 The Mie Theory-Based Analysis

In the first method of analysis, the single scattering spectrum is fitted to the spectrum predicted by the Mie theory. The amplitudes S_1 and S_2 are calculated using the Mie theory (see Chapter 3). These amplitudes and, thus, the spectral variations of the signal depend on the particle diameter d via so-called size parameter $x = \dfrac{\pi d}{\lambda}$ and the relative refractive index of the particle $n = \dfrac{n_p}{n_m}$, where

n_p is the refractive index of the particle and n_m is the refractive index of the surrounding medium. Equation (4.18) can be fit to the data in case of polarized illumination and (4.19) if unpolarized light is used. The diameter and relative refractive index are used as the fitting parameters. The objective function is

$$\chi^2 = \sum_i \left| I^{(e)}(\lambda_i) - I^{(t)}(\lambda_i;d,n) \right|^2 . \qquad (4.20)$$

where $I^{(e)}(\lambda_i)$ is the scattering signal measured on wavelength λ_i and $I^{(t)}(\lambda_i)$ is the signal calculated using either (4.18) or (4.19). Because this objective function has multiple local minima, we used look-up table approach rather than robust minimization procedures such as the Levenberg-Marquardt minimization method. In the look-up table approach, the fitting parameters d and n are varied with a certain step. For each combination (d,n) a spectrum is calculated and saved in a database. Then the spectrum measured in the experiment is compared with each of the spectra from the database and corresponding value of χ^2 is calculated. As a result, a combination (d,n) that minimizes χ^2 is found.

To implement this technique, one first needs to choose proper steps to vary d, and n. If the step is too large, there is an increased probability to miss the

absolute minimum. However, too small a step will make the minimization procedure too time consuming. Moreover, in a realistic experiment there is always some level of noise present, which cannot be completely filtered out of the data. Therefore, if the step is so small that the change of the objective function within a single increment is smaller than the standard deviation of the noise, the minimum found might not be a true minimum, but an effect of a noise instead. As long as the level of noise expected in the data is know, the step for each fitting parameter is determined as the smallest step that, for a given range of the parameters, increments the objective function by a fraction of the standard deviation of the noise. This is illustrated by the following considerations.

Consider equation (4.20). To simplify the problem let us investigate the effect of noise on the position of the minimum of the objective function χ^2 in respect to only one parameter d. Let d_0 be the optimum. We can expand $I^{(t)}$ in the vicinity of d_0 as follows

$$I^{(t)}(\lambda_i;d) \approx I^{(t)}(\lambda_i;d_0) + \frac{\partial I^{(t)}(\lambda_i;d)}{\partial d}(d-d_0). \qquad (4.21)$$

Let

$$I^{(c)}(\lambda_i) = I^{(t)}(\lambda_i) + \delta f(\lambda_i), \qquad (4.22)$$

where δf is the noise. Substituting (4.21) and (4.22) into (4.20) we obtain

$$\chi^2(d) \approx \sum_i \left| \frac{\partial I^{(t)}(\lambda_i;d)}{\partial d}(d-d_0) - \delta f(\lambda_i) \right|^2. \qquad (4.23)$$

Therefore,

111

$$\chi(d) \approx (d - d_0)^2 \sum_i \left| \frac{\partial I^{(i)}(\lambda_i; d)}{\partial d} \right|^2 -$$

$$2(d - d_0) \sum_i \frac{\partial I^{(i)}(\lambda_i; d)}{\partial d} \delta f(\lambda_i) + \sum_i (\delta f(\lambda_i))^2 \qquad (4.24)$$

and the minimum is achieved when

$$d = d_0 + \delta d, \qquad (4.25)$$

where

$$\delta d = \frac{\displaystyle\sum_i \frac{\partial I^{(i)}(\lambda_i; d)}{\partial d} \delta f(\lambda_i)}{\displaystyle\sum_i \left| \frac{\partial I^{(i)}(\lambda_i; d)}{\partial d} \right|^2}. \qquad (4.26)$$

In a hypothetical situation, when there is no noise in the data, $\delta f = 0$ and the true minimum is achieved: $d = d_0$. However, in any experiment there is always at least some noise in the data and the argument of the minimum can be shifted by δd. Therefore, the increment, Δd, of parameter d needs not be chosen smaller then a fraction of δd. For instance, choosing Δd as small as $\delta d/2$ is sufficient. If the derivative $\dfrac{\partial I^{(i)}(\lambda_i; d)}{\partial d}$ does not vary significantly within domain $\{D, \Lambda\}$, where D constitutes a range of d where the minimum is sought and $\lambda_i \in \Lambda$ for all i, its value can be approximated as a constant ε_d for all $(d, \lambda) \in \{D, \Lambda\}$ and, therefore, δd can be approximated as follows

112

$$\delta d \approx \frac{\sum_i \delta f(\lambda_i)}{\varepsilon_d N} = \frac{\langle \delta f \rangle}{\varepsilon_d},$$ (4.27)

where N is the number of data points on each spectrum and $\langle \delta f \rangle$ is the value of the noise averaged over the spectrum. Therefore, δd might be small but not equal to zero. Expression (4.27) is convenient to estimate an optimal step for d, because it depends on only two parameters: $\langle \delta f \rangle$, which is estimated from a typical data set, and ε_d, which can obtained from the numerical simulations. The same procedure can be used to estimate an optimal step for the refractive index $\delta n \approx \dfrac{\langle \delta f \rangle}{\varepsilon_n}$ or any other fitting parameter p with ε_p to be taken as the sensitivity of $f^{(t)}$ to this parameter.

In many applications of LSS, a population of scatterers with many different sizes contributes to the observed LSS signal. In this case, it is not any more sufficient to use only two fitting parameters, d and n. A size distribution must be introduced. In many applications such size distribution can be modeled as a Gaussian with mean d_0 and standard deviation σ. In this case, the minimization depends on three fitting parameters, d_0, σ and n.

4.3.2.2 Fourier Transform-Based Analysis

The second approach is an elegant method that enables to obtain cell nuclear size information from the scattering spectra collected from a sufficiently large solid angle. It is discussed in detail in [Backman, 1998]. Here, we overview some of the major principles of this method.

In the visible range (λ=0.4-0.7 μm) the wavelength of light is much smaller than the sizes of cell nuclei $\lambda \ll d$. As discussed in Chapter 3, in this regime the scattering cross section exhibits characteristic oscillatory behavior with wavelength due to the interference of light waves traversing different parts of the particle. The Van de Hulst approximation [Van de Hulst, 1957] provides an analytical expression for the scattering cross section of such large particles:

$$\sigma_s(\lambda,l) = \frac{1}{2}\pi d^2 \left(1 - \frac{\sin(2\delta/\lambda)}{\delta/\lambda} + \left(\frac{\sin(\delta/\lambda)}{\delta/\lambda} \right)^2 \right), \qquad (4.28)$$

with $\delta = \pi d n_c(n-1)$, n_c the refractive index of the cytoplasm, and n the refractive index of the nucleus relative to that of the cytoplasm. Expression (4.28) shows that the frequency of these oscillations in inverse wavelength space is directly proportional to the particle size. As shown in [Perelman et al, 1998; Backman, 1998] this gives rise to an oscillatory component of the same frequency in the spectrum, $I_s(\lambda)$, of the photons that are elastically scattered by the epithelium in the near-backward directions and are collected within a solid angle that includes a complete backscattering peak. This usually requires collection of light scattered within a range of backscattering angles θ from 0^0 to at least 5^0. The amplitude of this oscillatory component increases with the population density of the cell nuclei.

If nuclei of several sizes are present in the epithelium, the resulting signal $I_s(\lambda)$ is the superposition of the single frequency oscillations. Therefore, if the spectrum of the photons reflected from the epithelium after a single scattering is measured in the range from λ_{min} and λ_{max}, the size distribution of the cell nuclei, $N(d)$, can be obtained as the Fourier transform of this spectrum [Perelman et al, 1998]:

$$N(d) \approx \frac{2}{q l \pi^2} \left| \int_0^K I_s(k) e^{ikd} (k + k_0) dk \right|, \tag{4.29}$$

where

$$k_0 = 2\pi n_c (n-1)/\lambda_{max}, \tag{4.30}$$

$$k = 2\pi n_c (n-1)/\lambda - k_0, \tag{4.31}$$

$$K = 2\pi n_c (n-1)(\lambda_{min}^{-1} - \lambda_{max}^{-1}), \tag{4.32}$$

and the value of normalization coefficient q depends on the geometry of light delivery and collection.

We first observed this oscillatory behavior in the light backscattered by the nuclei of human intestinal cells [Perelman et al., 1998]. The cells, approximately 15μm long, affixed to glass slides in buffer solution, formed a monolayer of contiguous cells similar to the epithelial lining of the colon mucosa. In the experiments, an optical fiber probe (NA=0.22) was used to deliver white light from a xenon arc flashlamp to the sample and collect the reflected signal. After the measurement was performed, the cells were fixed and stained with the H&E, a dye that renders otherwise transparent cell nuclei visible under microscope examinaⁱon and is widely used in biology and medicine to examine tissue morphology. Microphotographs of the monolayer were obtained, and the size distribution of the nuclei was measured. The size distribution centered at about 6μm and had a standard deviation of 0.5μm.

Figure 4.3 compares the oscillatory component $I_s(\lambda)$ measured in the experiments with one calculated using the Van de Hulst approximation and the size

distribution of the cell nuclei measured via microscopy. As can be seen, both spectra exhibit similar oscillatory behavior. Moreover, the nuclear size distribution
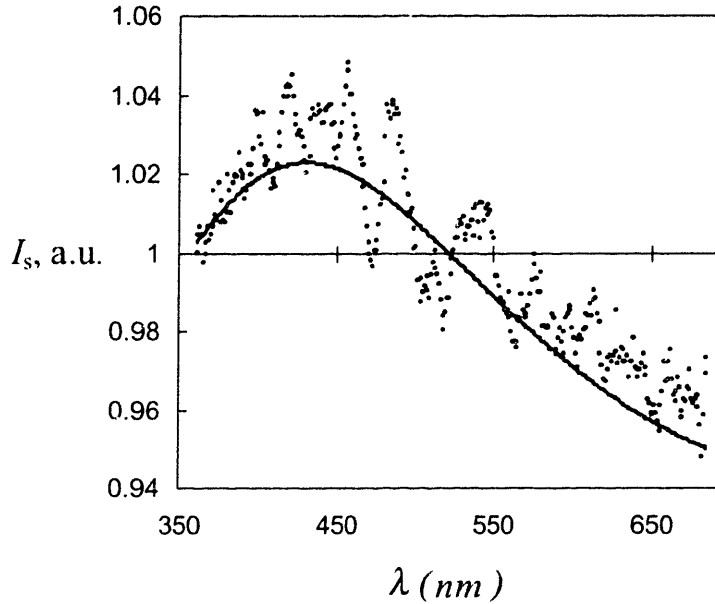
Figure 4.3. Oscillatory component of light scattered by a cell monolayer. The dotted line shows the spectrum measured in the experiment. The solid line shows the signal predicted by the Mie theory.

obtained from the light scattering data using expression (4.29) is in good agreement with the size distribution measured via microscopy (Fig. 4.4).

The Fourier transform based approach is computationally less intensive than the fitting procedure discussed in the previous section. Its major advantage over the fitting approach is its ability to obtain nuclear size distributions without need to make any assumptions about the type of the distribution. For example, the fitting approach can provide the mean and the standard deviation of nuclear sizes provided that the distribution is assumed to be Gaussian. Fourier transform

technique does not require to make this assumption and enables to obtain the size distribution in its true form.
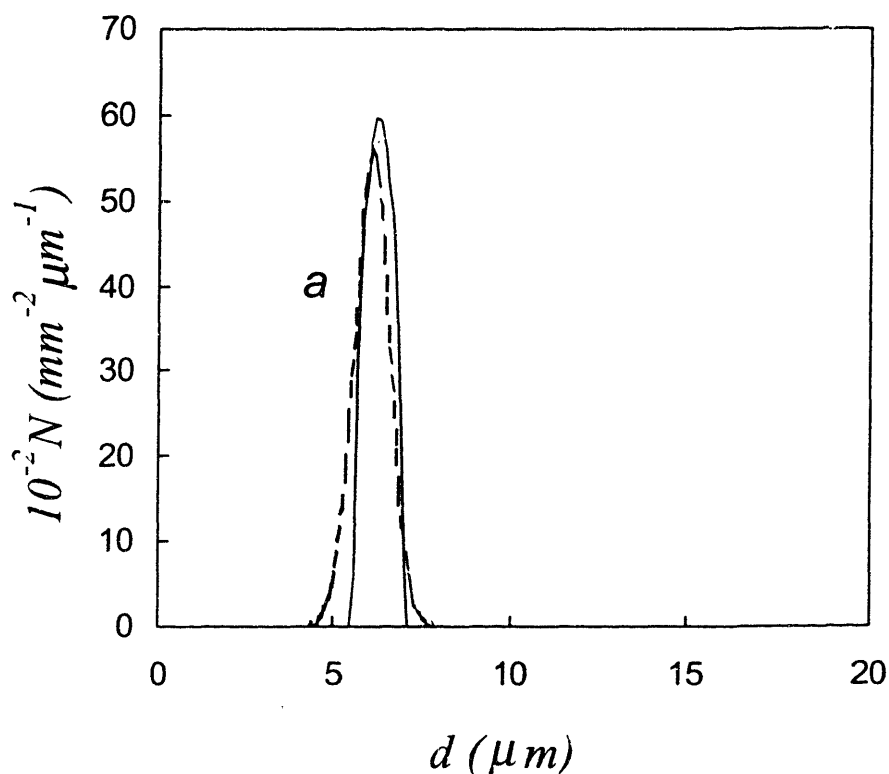
Figure 4.4. Size distributions of normal intestinal epithelial cell nuclei measured with LSS (solid line) and using conventional morphometry of the stained cell monolayer (dashed line).

The Fourier transform-based approach has its disadvantages as well. For example, it does not allow independent measurement of both the size distribution and the refractive indexes of the nuclei or any other scattering particle. This can be seen from equation (4.29), where d comes in a combination with $(n-1)$. Therefore, in order to obtain absolute values of the nuclear sizes one needs to make an assumption about the value of the refractive index of the scattering particle.

Another disadvantage of the Fourier transform-based approach is its inability to measure sizes of small particles, because the Van de Hulst approximation breaks down for small particles.

As discussed above, analysis of the single scattering component is only one part of the problem. In order for this component to be analyzed, it first has to be distinguished from the strong background of multiply scattered light (diffusive background), which dominates the signal of light elastically scattered by the tissue. In the following chapter we discuss the approaches to remove this background.

References

Backman V, "Reflectance Spectroscopy for Diagnosis of Precancerous Changes in Human Epithalium", M.S. Thesis, Massachusetts Institute of Technology (1998).

Backman V, Gurjar R, Badizadegan K, Itzkan I, Dasari R, Perelman LT, Feld MS, "Polarized light scattering spectroscopy for quantitative measurement of epithelial structures in situ", *IEEE J. Sel. Topics Quantum Electron*, **5**, 1019-1027 (1999).

Backman V, Wallace MB, Perelman LT, Arendt JT, Gurjar R, Muller MG, Zhang Q, G. Zonios G, Kline E, McGillican T, Shapshay S, Valdez T, Van Dam J, Badizadegan K, Crawford JM, Fitzmaurice M, Kabani S, Levin HS, Seiler M, Dasari RR, Itzkan I and Feld MS, "Light scattering spectroscopy: a new technique for clinical diagnosis of precancerous and cancerous changes in human epithelia", *Nature*, **406**, 35-36 (2000).

Beuthan J, Milner O, Hefmann J, Herrig M and Muller G, *Phys. Med. Biol.*, **41**, 369 (1996).

Boone C.W. *et al.* Quantitative grading of rat esophageal carcinogenesis using computer-assisted image tile analysis. *Cancer Epidemiology, Biomarkers & Prevention*, **9**, 495-500 (2000).

Brunsting A and Mullaney F, "Differential light scattering from spherical mammalian cells", *Biophys. J.*, **14**, 439-453 (1974).

Chen K, Perelman LT, Zhang Q, Dasari RR, Feld MS, "Optical Computed Tomography in a Turbid Medium Using Early Arriving Photons," *Journal of Biomedical Optics*, **5**, 144-154 (2000).

Cotran RS, Robbins SL, Kumar V, *Robbins Pathological Basis of Disease* (W.B. Saunders Company, Philadelphia, 1994).

Drezek R, Dunn A and Richards-Kortum R, "Light scattering from cells: finite-difference time-domain simulations and goniometric measurements", *Appl. Opt.*, **38**, 3651-3661 (1999).

119

Dunn A and Richards-Kortum R, "Three-dimensional computation of light scattering from cells", *IEEE J. Sel. Top. Quantum Electron.*, **2**, 898-905 (1996).

Fawcett DW, *A Textbook of Histology*, (Charman & Hall, New York, 1994).

Georgakoudi I, Jacobson BC, Backman V, Wallace M, Muller M, Zhuang Q, Badizadegan K, Sun D, Thomas G, Van Dam V, Feld MS, "The Combination of Fluorescence, Diffuse Reflectance, and Light Scattering Spectroscopy for the Improved Detection of Low- and High-grade Dysplasia in Patients with Barrett's Esophagus", *Gastrointerology*, in press (2001).

Georgakoudi I, Sheets EE, Müller MG, Backman V, Crum CP, Badizadegan K, Dasari RR, Feld MS, "Tri-Modal Spectroscopy as a Tool for the Detection and Biochemical/Morphological Characterization of Cervical Pre-Cancers *In Vivo*", *Obstet. Gynecol.*, submitted (2001).

Gurjar R, Backman V, Badizadegan K, Dasari R, Itzkan I, Perelman LT, Feld MS, "Functional Imaging of Human Epithelia with Polarized Light Scattering Spectroscopy", *Nature Medicine*, to be published (2001).

Hammer M, Schweitzer D, Michel B, Thamm E and Kolb A, "Single scattering by red blood cells", *Appl. Opt.*, **37**, 7410-7418 (1998).

Jackson JD, *Classical Electrodynamics*, (John Wiley & Sons, New York, 1975).

Kerker M, *The Scattering of Light*, (Academic Press, New York, 1969).

Lee, L., Pappelis, A. J., Pappelis, G. A., Kaplan, H. M. Cellular and nuclear dry mass and area changes during human oral mucosa cell development. *Acta Cytol.* **17**, 214-219 (1973).

Mourant JR, Freyer JP, Hielscher AN, Elick AA, Shen D and Johnson T, "Mechanisms of light scattering from biological cells relevant to noninvasive optical-tissue diagnosis", *Appl. Opt.*, **37**, 3586-3593 (1998).

Newton RG, *Scattering Theory of Waves and Particles* (McGraw-Hill Book Company, New York, 1969).

Perelman LT, Wu J, Itzkan I, Feld MS, "Photon migration in turbid media using path-integrals", *Phys. Rev. Lett.*, **72**, 1341-1344 (1994).

Perelman LT, Backman V, Wallace MB, Zonios G, Manoharan R, Nusrat A, Shields S, Seiler M, Lima C, Hamano T, Itzkan I, Van Dam J, Crawford JM and Feld MS, "Observation of periodic fine structure in reflectance from biological tissue: a new technique for measuring nuclear size distribution", *Phys. Rev. Lett.*, **80**, 627-630 (1998).

Schmitt JM and Kumar G, "Optical scattering properties of soft tissue: a discrete particle model", ", *Appl. Opt.* **37**, 2788-2797 (1998).

Slot PMS, Hoekstra AG and Figdor CG, *Cytometry*, **9**, 636 (1988).

Tafloe A, Computational Electrodynamics: The Finite Difference Time Domain Method (Artech, Boston, 1995).

Van de Hulst HC, *Light Scattering by Small Particles* (Dover Publications, New York, 1957).

Watson JV, *Introduction to Flow Cytometry* (Cambridge U. Press, Cambridge, 1991).

Yang C, Kyungwon A, Perelman LT, Dasari R, Feld MS, "Feasibility of Field-Based Light Scattering Spectroscopy", *J Biomed Optics*, **5**, 138 (2000).

Yang C, Wax A, Georgakoudi I, Hanlon E, Badizadegan K, Dasari RR, Feld MS, "Interpherometric Phase Dispersion Microscopy", *Optics Letters*, **25**, 1526 (2000).

Yodh AG and Chance B, "Spectroscopy and imaging with diffusing light," *Physics Today*, **48**(3), 34-40, (1995).

Zonios G, Ph.D. Thesis, Massachusetts Institute of Technology (1998).

Zonios G, Perelman LT, Backman V, Manoharan R, Fitzmaurice M, Feld MS, "Diffuse Reflectance Spectroscopy of Human Adenomatous Colon Polyps In Vivo", *Appl. Opt.*, 38, 6628-6637 (1999).

Chapter 5

Principles of Light Scattering Spectroscopy: Removal of Diffusive Background

We have developed two methods to remove the diffusive background. The first method is based on the observation that this background is typically responsible for more than 95% of the total signal of light elastically scattered by a typical living tissue. Therefore, it gives rise the coarse features of the reflectance spectra. We employed two physical models to describe this background [Perelman et al, 1998; Zonios et al, 1998 and 1999]. Both take into account that oxygenated and de-oxygenated hemoglobin species present in the blood are two major absorbers in most mucosal tissues. The model uses hemoglobin concentration and oxygenation and average size of scatters in the tissue as free parameters to fit the

model to the spectral data. After the model fit is subtracted, the single scattering component becomes apparent and is further analyzed to obtain nuclear size distribution.

The second method [Backman et al, 1999] is based on the observation that initially polarized light looses its polarization when traversing a turbid medium such as a biological tissue [Demos et al., 1996]. Consider a mucosal tissue illuminated by linearly polarized light. A small portion of the incident light will be backscattered by the epithelial cell nuclei. The rest of the signal diffuses into the underlying tissue and is depolarized by multiple scattering. In contrast, the polarization of the light scattered backward after a single scattering event is preserved. Thus, by subtracting off the unpolarized component of the reflected light, the contribution due to the backscattering from epithelial cell nuclei can be readily distinguished. The residual spectrum can then be analyzed to extract the size distribution of the nuclei, their population density, and their relative refractive index.

5.1 Model Based Approaches to Diffusive Background Removal

In this section we overview the model based approaches of diffusive background removal, which were discussed in detail in [Backman, 1998]. Consider a beam of light incident on a mucosal tissue. A portion of this light is backscattered by the epithelial cells, while the remainder is transmitted to deeper tissue layers, where it undergoes multiple scattering and becomes randomized. All of the diffusive light which is not absorbed in the tissue eventually returns to the surface,

passing once more through the epithelium, where it is again subject to scattering by the cells. Thus, the emerging light will consist of a large component of multiply scattered light and a smaller component of singly scattered light. For a thin slab of epithelial tissue an approximate solution of the transport equation for the signal $R(\lambda)$ collected within acceptance solid angle Ω_c is given by the following expression [Perelman et al., 1998; Backman, 1998]:

$$\frac{R(\lambda)}{\overline{R}(\lambda)} = e^{-\tau(\lambda)} + \frac{1 - e^{-\tau(\lambda)}}{\left\langle I_d(\lambda,\mathbf{s})\right\rangle_{\Omega_c}} \left\langle \left\langle I_i(\lambda,-\mathbf{s}')p(\lambda,\mathbf{s},-\mathbf{s}')\right\rangle_{\Omega_i} + \right.$$

$$\left. \left\langle I_d(\lambda,\mathbf{s}')p(\lambda,\mathbf{s},\mathbf{s}')\right\rangle_{2\pi}\right\rangle_{\Omega_c}, \tag{5.1}$$

where τ is the optical thickness (see below), I_i $(\lambda,\mathbf{s})$ is the intensity of the incident light delivered in solid angle Ω_i, $I_d(\lambda,\mathbf{s})$ is the intensity of the light emerging from the underlying tissue, and

$$\left\langle f(\mathbf{s},\mathbf{s}')\right\rangle_{\Omega} = \int_{\Omega} f(\mathbf{s},\mathbf{s}')d\mathbf{s}' \tag{5.2}$$

for any function f and solid angle Ω, with $\mathbf{s}$ a unit vector pointing outward from the tissue surface in an arbitrary direction. The quantity

$$\overline{R}(\lambda) = \left\langle I_d(\lambda,\mathbf{s})\right\rangle_{\Omega_c} \Big/ \left\langle I_i(\lambda,\mathbf{s})\right\rangle_{\Omega_i} \tag{5.3}$$

is the reflectance of the diffusive background.

In case when the scatterers are distributed uniformly throughout the thickness of the epithelium and the discrete particle approximation is applicable, the optical depth is simply

$$\tau(\lambda) = \sum_{j} \sigma_s(\lambda, j) N_j \qquad (5.4)$$

with $\sigma_s(\lambda, j)$ the scattering cross section of a particle of type j (type of a particle may be defined as its shape, size, refractive index, etc.) and N_j the distribution function of the particles depending on their type (number of scatterers of type j per unit area). In the same approximation, the effective scattering phase function is

$$p(\lambda, s, s') = \frac{1}{\tau} \sum_{j} |S(\theta, \lambda, j)|^2 N_j , \qquad (5.5)$$

with θ the backscattering angle, $\theta = \arccos(ss')$, and $S(\theta, \lambda, j)$ the scattering amplitude of a particle of type j. In a case of spherical scatterers, this function is determined by the Mie theory. The first term in equation (5.1) describes the attenuation of the diffusive component, and the terms in brackets describe backscattering of the incident light and forward scattering of diffusive component by the scatterers within the epithelium, respectively.

Equation (5.1) enables to find the single scattering component provided that the diffusive background is known. If unpolarized uncoherent light is used, this background cannot be measured directly. Therefore, it must be modeled. Transport theory provides the most rigorous approach to model light propagation in a random medium such as a biological tissue [Ishumaru, 1988]. According to this theory a so-called transport equation must be solved. The transport equation is an integro-partial differential equation. In a simpler case, when the optical, scattering and absorptive, properties of tissue are distributed uniformly throughout the tissue, the transport equation can be reduced to a Fredholm equation of a second kind [Morse et al., 1953]. This equation allows analytical solutions for few limiting cases and, in a general case, allows numerical solutions only. Therefore, to

model the diffusive background, an approximate solution to the transport equation must be developed. We have developed two methods to model this background. The first method uses the diffusion approximation to the transport equation [Zonios et al., 1999; Farrell et al., 1992; Ishumaru, 1983]. The second method is based on so-called exponential approximation to the transport theory [Perelman et al., 1998; Backman, 1998].

5.1.1 Modeling of Diffusive Background Using Diffusion Approximation

The diffuse background of white light from a mucosal tissue results from the interplay of absorption and scattering. In the visible spectral range, hemoglobin is the dominant absorber, although other absorbers such as bilirubin, β-carotene etc. are also present in certain tissues. Diffuse reflectance is determined by μ_a and μ_s', the absorption and reduced scattering coefficients, which depend linearly on the concentrations of the various tissue absorbers and scatterers. By employing an appropriate model for diffuse reflectance, it is possible to extract these coefficients, and thereby to model the background.

We have developed a method to model clinical tissue reflectance in terms of the underlying tissue scatterers and absorbers using colon adenomas as an example [Zonios et al, 1999]. This method provides both direct physical insight and quantitative information about the tissue constituents that give rise to the reflectance spectra. The method is based on an analytical model, based on the diffusion approximation, to describe the tissue reflectance spectrum collected by a finite sized probe with an effective probe radius r_t . Biological tissue is treated as a

homogeneous medium with wavelength–dependent absorption coefficient μ_a and reduced scattering coefficient μ'_s. Incident photons are absorbed and scattered in the tissue, with the survivors eventually escaping from the tissue surface. A fraction of the escaping diffusely reflected light is collected by a probe or detector of a finite size.

Starting with the expression derived by Farrell, Patterson and Wilson [Farrell et al., 1992], one obtains a simple analytical expression for the diffuse reflectance collected by the probe:

$$R = \frac{1}{2}a'\left[e^{-x} + e^{-\eta x} - \frac{e^{-r_1 x}}{r_1} - \frac{e^{-\eta r_2 x}}{r_2}\right],$$

(5.6)

with

$$a' = s/(a+s), \quad x = \sqrt{3(1-a')}, \quad r_1 = \sqrt{1+(a+s)^2}, \quad r_2 = \sqrt{1+[(a+s)/\eta]^2},$$

and $\eta \cong 5.3$, $a = \mu_a r_c$, $s = \mu'_s r_c$. For a given probe geometry there is an optimal value of r_c, the effective probe radius, which can be determined by calibrating Eq. (5.6) using the reflectance measurement of a tissue phantom with known optical properties.

For the tissue reflectance spectra collected in the visible spectral range in several mucosal tissues, such as colon, bladder, and esophagus, hemoglobin (Hb) has been found to be the only significant light absorber. Hb is encountered in both oxygenated and deoxygenated forms. Thus the total absorption coefficient, $\mu_a(\lambda)$ is given by
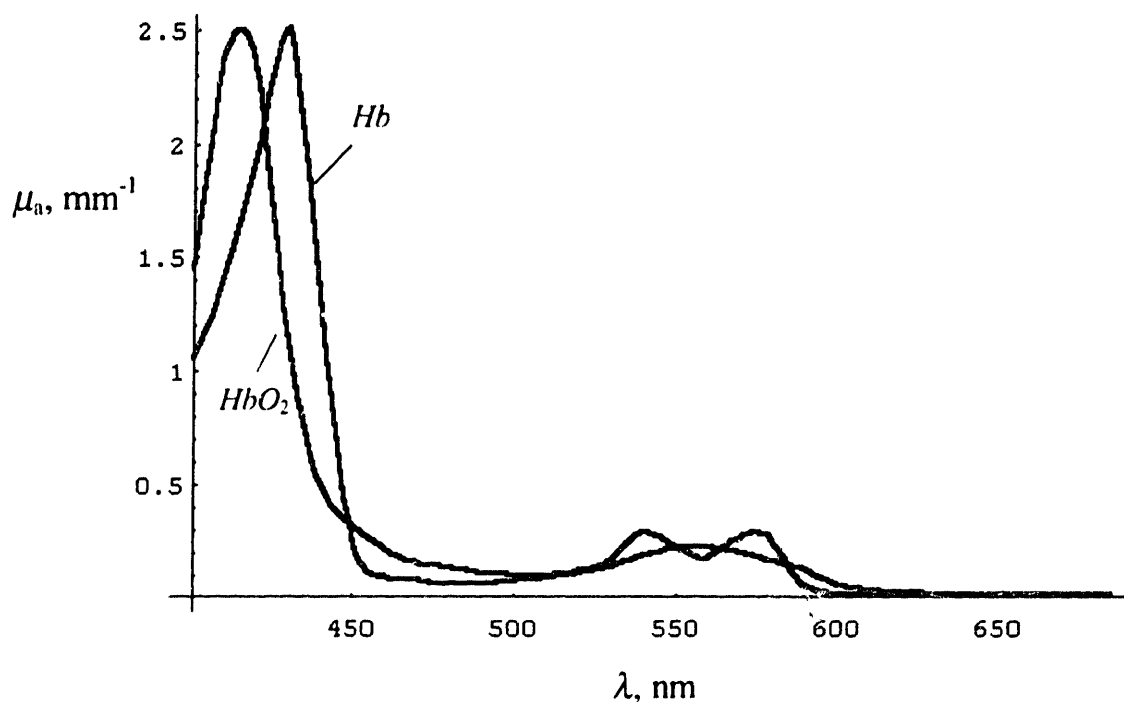
Figure 5.1 Absorption coefficient $\mu_a(\lambda)$ of oxygenated (HbO_2) and deoxygenated (Hb) forms of hemoglobin.

$$\mu_a(\lambda) = \ln 10 \; c_{Hb} \left[\alpha \, \varepsilon_{HbO_2}(\lambda) + (1 - \alpha) \, \varepsilon_{Hb}(\lambda) \right], \tag{5.8}$$

with α the Hb oxygen saturation parameter and c_{Hb} the total hemoglobin concentration. The wavelength dependent extinction coefficients (i.e., the ε's) of both forms of hemoglobin are well documented [Ishumaru, 1988] (Fig. 5.1).

The reduced scattering coefficient $\mu_s'(\lambda)$ is the sum of contributions from the various tissue scatterers. Detailed information about these individual scatterers is not presently known. Therefore, we write

$$\mu_s'(\lambda) = \rho_s \sigma_s'(\lambda), \tag{5.9}$$

with ρ_s the *effective* scattering density and $\sigma'_s(\lambda)$ the *effective* reduced scattering cross section. With this, tissue scattering properties are modeled in an average way, as if tissue contained a single well–defined type of scatterer. In general, $\sigma'_s(\lambda)$ depends on the refractive index, shape and size of the scatterer, as well as on the refractive index of the surrounding medium.

According to the model, for each reflectance spectrum two absorption parameters (c_{Hb}, α) and three scattering parameters (ρ_s, $\sigma'(\lambda)$ and relative refractive index, n) can be obtained by fitting the model to the data using the Levenberg-Marquardt minimization method. We tested this model on physical tissue models composed of various mixtures of hemoglobin and polystyrene microspheres, and found that the parameters of these constituents could be extracted with 5-10% accuracy.

As discussed above, to separate a single scattering component from the diffusive background, the intensity of the diffusive component, $I_d(\lambda, s)$, is obtained by fitting the model to the data, and the single scattering component $\langle I_s(\lambda, -s')p((\lambda, s, -s'))\rangle_\Omega$ is then obtained using equation (5.1). We used this model to remove the diffusive background in our studies of dysplasia in Barrett's esophagus [Georgakoudi et al, 2001] and cervical dysplasia [Georgakoudi et al, 2001].

Not only does this model enable diffusive background removal, but it also provides valuable information for tissue characterization and diagnosis. For example, the hemoglobin concentration c_{Hb} characterizes blood supply to the tissue, hemoglobin oxygenation, α, indicates if the tissue is hypoxic, and the scattering parameters provide information about tissue composition. Moreover, we have shown that this information can be translated into an accurate diagnosis of

early cancerous or precancerous changes in human mucosa [Zonios et al, 1998 and 1999; Georgakoudi et al, 2001].

5.1.2 Modeling of Diffusive Background Using Exponential Model

Diffusion approximation-based model of multiple scattering in tissues is a powerful tool to obtain information about tissue scattering and absorption properties and to remove the diffusive background. However, it suffers two major drawbacks.

1) It is computationally intensive. To implement this method, one needs to find the absolute minimum of a nonlinear function of five variables, which has multiple minima. The Mie theory is used at each iteration to find the values of the objective function. This is computationally intense as well, because it requires to estimate a sum of a poorly converging infinite series with coefficients defined through Bessel functions, which themselves can only be evaluated numerically as sums of infinite series.

2) In the diffusion model, the tissue is assumed to be a semi-infinite layer with spatially uniform scattering and absorption properties throughout. While our studies have shown that in most cases this approximation is adequate, it is not *a priori* obvious that the model is valid for any given mucosal tissue. Therefore, to obtain accurate results it might be necessary to modify this model to take into account specific organization of the tissue. However, the model allows little flexibility. For example, it cannot model a

two-layer system, where each layer has distinct scattering and absorption properties.

To address these problems we have developed another approximation. This so-called "exponential model" is less rigorous than the diffusion model but is adequate for diffusive background removal and is significantly less computationally intensive and can be easily modified to take into account specific geometry of the tissue, i.e. multi-layered structure.

5.1.2.1 Exponential Model

In this approximation, light incident on the tissue is assumed to be exponentially attenuated. At any given depth z, an amount of light proportional to the reduced scattering coefficient μ_s' is scattered back towards the surface and further exponentially attenuated. Since light attenuation depends on both scattering and absorption, the attenuation coefficient is assumed to be the sum of absorption coefficient μ_a and effective scattering coefficient $\mu_s^{(e)} = \beta\mu_s'$. The parameter β was determined by comparison with more accurate models of light transport and Monte Carlo simulations, and was found to be $\beta \cong 0.07$ [Perelman et al., 1998; Backman, 1998].

We then obtain the following approximate expression for the diffusive light returned from the tissue by means of multiple elastic scattering [Perelman et al., 1998; Backman, 1998]:

$$I_d(\lambda,\mathbf{s}) = F(\mathbf{s})\langle I_i(\lambda,\mathbf{s})\rangle_{\Omega_i} \frac{1-\exp[-(\mu_s^{(e)} + c\mu_a)L]}{1+c(\mu_a/\mu_s^{(e)})} \qquad (5.10)$$

and the corresponding diffusive background

$$\bar{R}(\lambda) = \frac{1 - \exp[-(\mu_s^{(e)} + c\mu_a)L]}{1 + c(\mu_a / \mu_s^{(e)})} R_0,$$ (5.11)

where function

$$F(s) = \frac{\Delta + \cos\theta}{\pi(2\Delta + 1)}$$ (5.12)

describes the angular dependence of light emerging from the diffusive layer, s is a unit vector pointing outward from the tissue surface in an arbitrary direction, θ is the angle between vector s and normal to the surface of the tissue pointing outward, $\Delta = 0.7104$, parameter L is proportional to the effective thickness of the diffusive layer, parameter c is proportional to the concentration of hemoglobin (which is the predominant absorber) to the concentration of the scatterers in the diffusive layer, and R_0 is the normalization parameter that depends on the probe size, angular aperture, distance from the probe to the tissue surface, etc. Because both oxygenated and de-oxygenated hemoglobin species are present, the total hemoglobin absorption is modeled as

$$\mu_a = (1 - \alpha)\mu_a^{(Hb)} + \alpha\mu_a^{(HbO_2)}$$ (5.13)

with oxygen saturation parameter α ($0 \leq \alpha \leq 1$). The scattering coefficient μ_s' is modeled as a monotonously declining polynomial function of λ. Despite the fact that this model might seem too simplistic, it was found to describe the diffusive background of light returned form various tissues, such as mucosae of esophagus, colon, bladder, and oral cavity, quite accurately. The following section provides an

example of diffusive background subtraction in the experiments with *in vivo* esophageal tissues using the exponential model.

5.1.2.2 Studies with *In Vivo* Esophageal Tissue

In the experiments with *in vivo* tissues, an optical fiber probe was used to deliver white light from a xenon arc flashlamp [EC&G] with a 10 µsec pulse duration and an average pulse energy of 5J to the sample and to collect the reflectance signal (Fig. 5.2) [Perelman et al., 1998]. The probe tip, 1 mm in diameter, consisted of a central delivery fiber surrounded by a ring of six collection fibers, all of which were covered with a 1 mm thick quartz optical shield [Brennan et al., 1993]. The optical fibers were fused silica, 200 µm core diameter, NA=0.22. The tip of the probe was beveled at 17° angle in order to eliminate specular reflection from the shield/air or shield/water interface. At the proximal end of the probe the collection fibers were arranged in a line and imaged onto the input slit of a spectrograph [Instruments SA CP-200], which dispersed the collected light. An electronically gated diode array detector [EG-G PAR OMA III] recorded the reflectance spectra over the wavelength range 360-685 nm.

Because the intensity of light emitted by the xenon lamp, detector response and the properties of the optical components used in the device vary with wavelength, a collected spectrum must be calibrated. Therefore, before data collection, the spectrum of a reference signal of light elastically scattered by a "white standard", a highly diffusive and reflective solution of Ba_2SO4, $R_r(\lambda)$, was measured. Then the optical fiber probe was inserted into the biopsy channel of an endoscope, brought into gentle contact with the tissue surface and the signal of
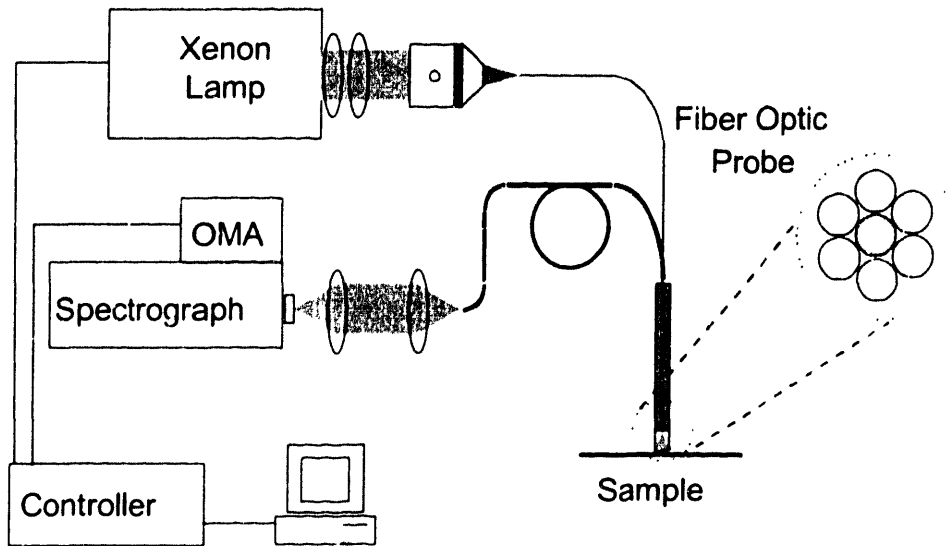
Figure 5.2. Experimental setup used in the experiments with *in vivo* tissues.

light returned from the tissue by means of scattering, $R_t(\lambda)$, was collected. The signal of light elastically scattered by the tissue (reflectance signal) was found as follows

$$R(\lambda) = \frac{R_t(\lambda)}{R_r(\lambda)} .$$

(5.14)

Figure 5.3(a) shows the reflectance spec*r* a from two Barrett's esophagus tissue sites, both independently diagnosed by three pathologists as (1) normal and (2) precancerous, i.e. dysplastic. As can be seen, the differences in these unprocessed spectra are small. To analyze them, equation (5.11) was first fit to the broad features of the data by varying the parameters c, α, L, and R_0. The resulting fits are quite accurate. After removing the diffusive background by calculating $R(\lambda)/\overline{R}(\lambda)$, the single scattering component exhibiting characteristic

134
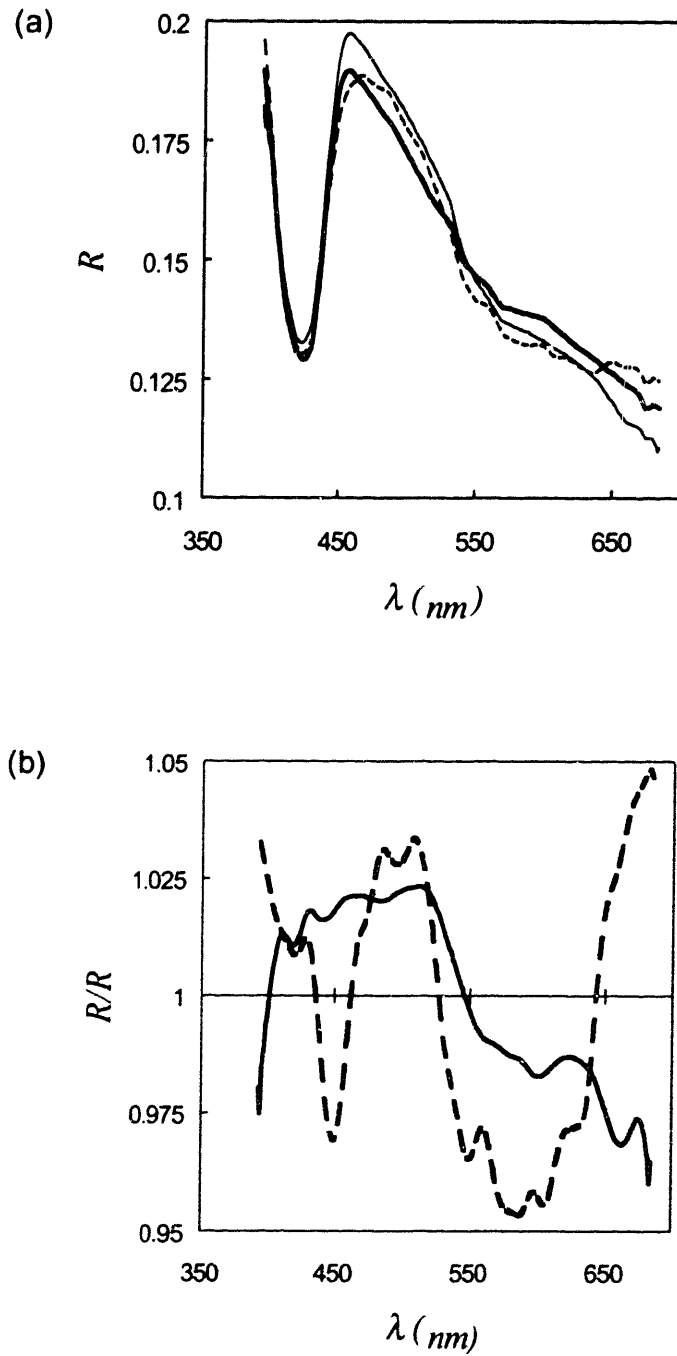
Figure 5.3   Reflectance from Barrett's' esophagus.   (a) Reflectance from non-dysplastic site (solid line), dysplastic site (dashed line), and model fit (thick solid line); (b) corresponding single scattering components.

o
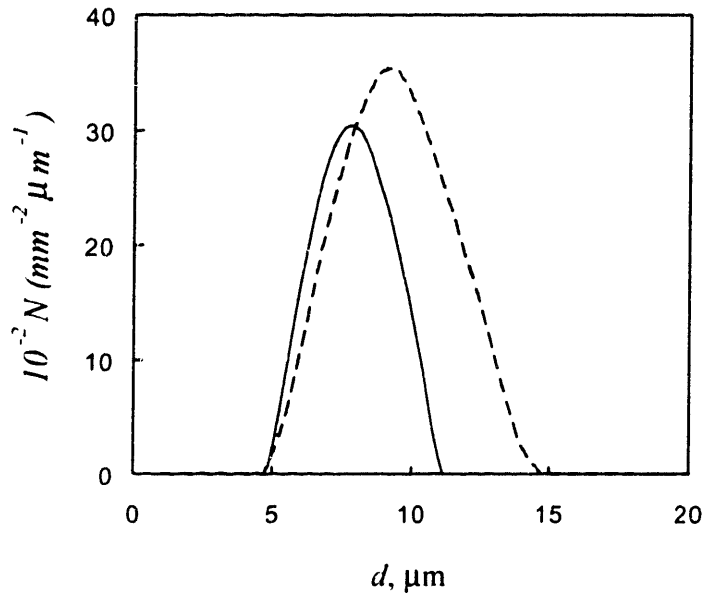
Figure 5.4 Nuclear size distribution obtained from the reflectance spectra from Barrett's' esophagus tissue sites: non-dysplastic site (solid line) and dysplastic site (dashed line).

oscillations in wavelength is seen clearly (Fig. 5.3(b)). In particular, the oscillatory component from the dysplastic tissue site exhibits higher frequency components than that from the normal site. Fourier transform-based analysis of the single scattering component discussed in the previous chapter was then employed to extract the respective nuclear size distributions, yielding Fig. 5.4. As can be seen, the difference between normal and dysplastic tissue sites is pronounced. The distribution of nuclei from the dysplastic site is much broader than that from the normal site, the peak diameter is shifted from ~7 μm to about ~10 μm, and the shape exhibits distinct structure. In addition, both the relative number of large nuclei (>10 μm) and the total number of nuclei are significantly increased. In the following chapter we will see that reflectance signals from such different tissues as

136

Barrett's esophagus, colon, bladder, and oral cavity can be analyzed using the exponential or diffusion models and quantitative measurement of nuclear enlargement and crowding can be obtained to characterize, detect and diagnose dysplastic lesions *in vivo*.

5.2 Removal of Diffusive Background Using Polarization Discrimination

In the previous section we discussed the diffusive background removal by means of modeling. These methods are easy to implement in the experiment but are computationally intensive. Moreover, their application is limited to organs and tissues in which light propagation can be analytically modeled. Although we have established that the list of such organs is quite extensive and includes esophagus, colon, cervix, bladder, and oral cavity (see next chapter), a general means of diffusive background removal that can be used in any tissue would have a clear advantage over the modeling approach. In this section we discuss an experimental means of isolating the scattering from epithelial cell nuclei using polarized light.

It is well known that initially polarized light looses its polarization when traversing a turbid medium such as biological tissue [Anderson, 1991; Demos et al., 1996; Yoo et al., 1989]. In contrast, the polarization of the light scattered backward after a single scattering event is preserved. This property of polarized light has been used to image surface and near surface biological tissues [Demos et al., 1998]. Thus, by subtracting off the unpolarized component of the scattered light, the contribution due to backscattering from epithelial cell nuclei can be readily distinguished. The residual spectrum can be further analyzed to extract the

size distribution of the nuclei, their population density, and their relative refractive index.

5.2.1 Polarization Discrimination of Multiple Scattered Light

Consider a scattering medium such as mucosal tissue in which a thin layer of epithelium covers a highly turbid underlying tissue. When such medium is eliminated by a linearly polarized light, each of these layers gives rise to a different type of scattering. A small portion of the linearly polarized incident light will be backscattered by the particles in the upper layer. The rest of the signal diffuses into the underlying tissue and is depolarized by means of multiple scattering. This diffusive light, if not absorbed in the underlying tissue, returns to the surface. Thus the emerging light has two components, one from light backscattered by particles of the first layer, I_b, and the other being diffusely reflected from the second layer, I_d. I_b has a high degree of linear polarization that is parallel to the polarization of the incident light: $I_{\parallel}^b >> I_{\perp}^b$. As a result of multiple scattering in the second layer, diffusely reflected light is mainly unpolarized, and $I_{\parallel}^d \approx I_{\perp}^d$. Therefore, the residual intensity of the emerging light $I_{\parallel} - I_{\perp} \approx I_{\parallel}^b - I_{\perp}^b$, is dominated by the contribution from the upper layer, and is mainly free from both absorption and scattering from the tissue below. It can be further analyzed using equation (4.18).

To test polarization discrimination approach and to study the spectrum of polarized backscattered light, we employ an instrument that delivers collimated polarized light on tissue and separates two orthogonal polarizations of backscattered light. In our system (Fig. 5.5), light from a broadband source (250

138
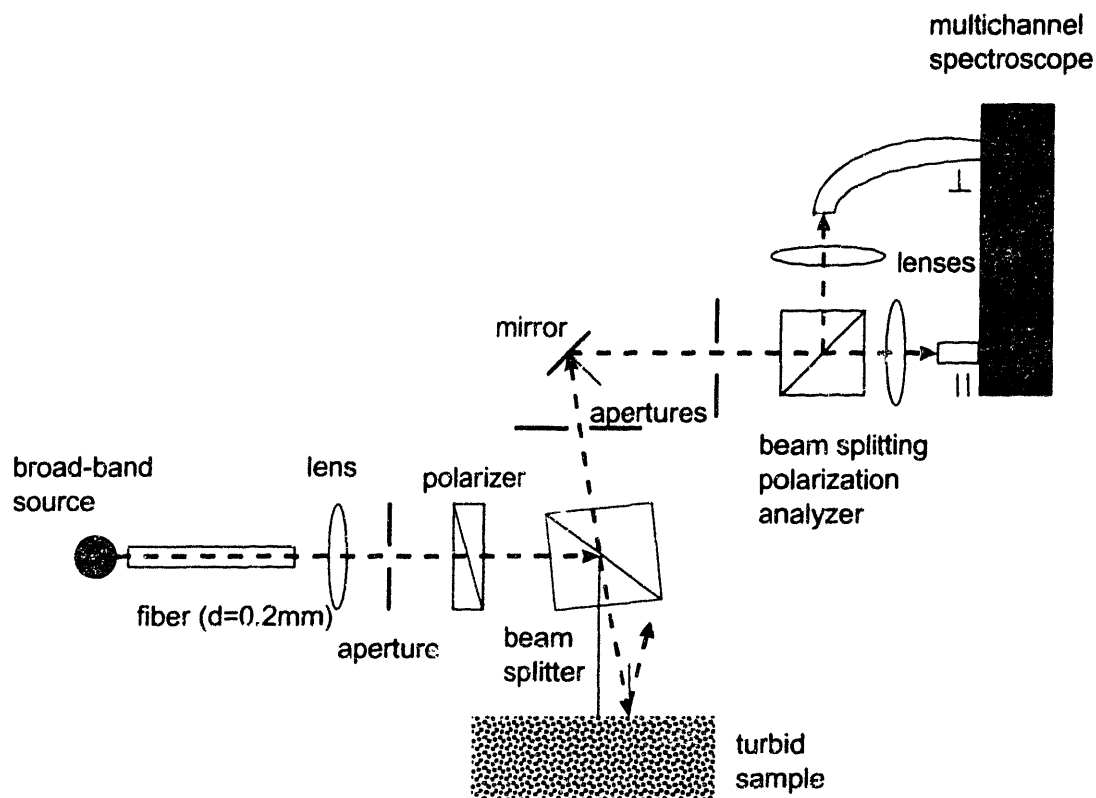
Figure 5.5. Schematic diagram of LSS system for polarization discrimination of the diffusive background.

W cw tungsten lamp) is collimated and then refocused with a small solid angle onto the sample, using lenses and an aperture. A broadband polarizer linearly polarizes the incident beam. In order to avoid specular reflectance, the incident beam is oriented at an angle of ~15° to the normal to the surface of the sample. The sample is illuminated by a circular spot of light of 2 mm in diameter. The reflected light is collected in a narrow cone (~0.015 radian), and two polarizations are separated by means of a broadband polarizing beam splitter cube, which also serves as our analyzer. The output from this analyzer is delivered through 200μm

core diameter optical fibers into two channels of a multichannel spectroscope (quadruple spectroscope, Model SQ2000, Ocean Optics, Inc.). This enables the spectra of both components to be measured simultaneously in the range from 400 to 900 nm.

The beams are not perfectly collinear, and when they pass through the polarizer and analyzer cubes this gives rise to a small amount of distortion. Furthermore, the beamsplitter has different reflectivities for s and p polarizations. A diffusely reflective white surface was used as a standard to correct for wavelength non-uniformity, and to calibrate the signals in the two channels. $I_{\parallel}(\lambda)$ and $I_{\perp}(\lambda)$ were each normalized to the corresponding background spectra, $I^{B}(\lambda)$ and $I_{\perp}^{B}(\lambda)$ taken with the white diffusing surface. This removed spectral non-uniformities in the light source. Thus, the experiments actually measured the

normalized residual intensity $\Delta I = \dfrac{I}{I^{B}} - \dfrac{I_{\perp}}{I_{\perp}^{B}}$.

5.2.2 Experiments with Physical Tissue Models

Our first experiments employed a single-layer physical model to simulate epithelium. The model consisted of polystyrene beads of diameters ranging from 0.5 μm to 10 μm to simulate cellular organelles (Polyscience, Inc), embedded in de-ionized water, glycol or glycerol. The thickness of these layers was varied so that the optical depth $\tau = \mu_{s}z$ with μ_{s} the scattering coefficient[1] and z the distance

---

[1] Notice the distinction between μ_{s} the scattering coefficient, and μ'_{s}, the *reduced* scattering coefficient used in the previous section. These coefficients are related, $\mu'_{s} = \mu_{s}(1-g)$, where g is so-called anisotropy coefficient and is ~0.9 for typical biological tissues. Typical values of the

into the tissue ranged from 0.1 to 5. (A photon propagating through a medium with $\tau=1$ will undergo one scattering event on average.) Large diameter polystyrene beads (d = 4-10 μm, refractive index $n_{particle}$ = 1.59) were used to simulate cell nuclei. Since the relative refractive index of the beads in water, $n=n_{particle}/n_{medium} \sim 1.2$, is substantially higher than that of the cell nuclei relative to the cytoplasm, which is in the range n=1.03 - 1.1 [Beauvoit et al., 1994; Beuthan et al., 1996], some experiments used glycol ($n_{medium}=1.45$) and glycerol ($n_{medium}=1.48$) to decrease the relative refractive index of the beads, and therefore better approximate biological conditions.

We found that for $\tau<<1$, I is almost 100 times larger than I_L. This demonstrates that single scattering from large spheroidal particles preserves polarization. As can be seen from Fig. 5.6, the residual signal ΔI increases with τ. However, it saturates for values of $\tau>1$. Because of the decollimation of the incident beam, the number of photons contributing to the residual signal decreases exponentially with optical depth τ. More than 85% of all polarized photons contributing to the residual signal are collected from optical depths less than 1, and 98% are collected from an optical depth of then 2. This indicates that ΔI provides spectroscopic information about the uppermost scatterers only.

Our next experiments employed two-layer models. The upper layer consisted of polystyrene beads embedded in water, glycol or glycerol, as in the single layer experiments, with $\tau\sim1$. The bottom layer was a gel containing mixtures of powdered Ba_2SO_4 to provide scattering and human blood, the hemoglobin of which provided absorption. This physical model simulated human

---

reduced scattering coefficient $\sim$1-2 mm^{-1}, while $\mu_s \sim$ 10-20 mm^{-1}, which corresponds to typical scattering length $\sim$ 0.05 mm.
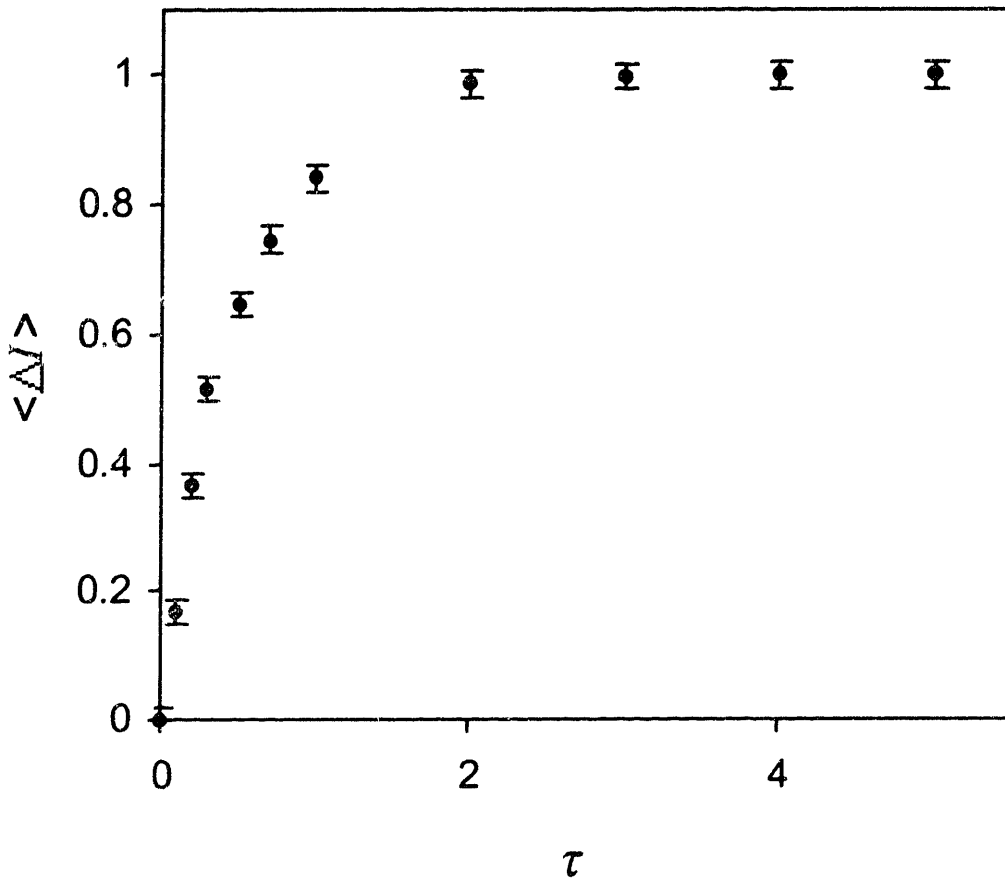
Figure 5.6. Residual signal $<\Delta I>$ from a single layer model averaged over 450-750 nm wavelength range measured for various values of optical depth τ. $<\Delta I>$ is normalized to one when $\tau \to \infty$.

epithelial tissues. By adjusting the concentrations of the Ba_2SO_4 and blood, the absorption and scattering properties could be made similar to those of biological tissue, since hemoglobin is known to be the major absorber in tissue in the optical spectral range [Yodh et al., 1995]. The reduced scattering coefficient of the second layer μ_s' varied in the range from 2.0 mm^{-1} to 3.0 mm^{-1}. The concentration of

(a)   (b)

λ, nm   λ, nm
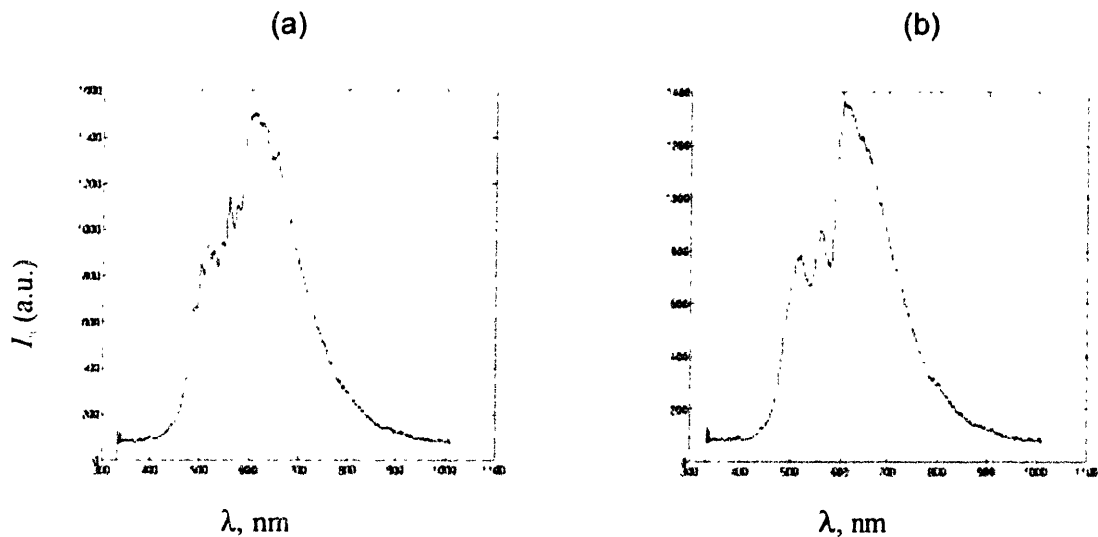
Figure 5.7. Reflectance spectra of two-layer tissue model. The top layer consists of polystyrene beads in water, d=4.65 μm, n=1.19. (a) Parallel polarization, (b) perpendicular polarization. Note the characteristic hemoglobin dips.

hemoglobin solution was approximately 200 mg/dl so that the corresponding absorption coefficient varied from 0.002 mm^{-1} to 0.4 mm^{-1} in the wavelength region 450-780 nm.

Figure 5.7 shows the spectra of $I_{\parallel}$ and $I_{\perp}$ components of the light reflected from a two-layer model. In this experiment the top layer contained polystyrene beads with d=4.56 μm, embedded in glycol. The standard deviation of their diameter, Δd, was 0.03 μm. The optical depth of the upper layer was τ~0.85. The bottom layer was optically thick, and its scattering and absorption properties were comparable to those of biological tissue [Zonois et al., 1996]. As can be seen, strong hemoglobin absorption features are present in both $I_{\parallel}$ and $I_{\perp}$. However, $I_{\parallel}$

exhibits additional characteristic features due to backscattering by the beads in the upper layer. The residual spectrum, ΔI, is shown as the dashed line in Fig. 5.8(a). No hemoglobin absorption features are present, and the diffusive background from the lower layer is completely removed. The ripple structure [Van de Hulst, 1957; Bohren et al., 1983] characteristic for the scattering by large spheres is now clearly apparent. The predictions of the Mie theory for scatterers with d=4.56 μm, Δd=0.03 μm and n=1.19 are in good agreement with experiment (solid line).

The residual spectra obtained in experiments with other bead diameters (5.7 μm, 8.9 μm and 9.5 μm), embedded in any of the media used (water, glycol and glycerol) had no measurable diffusive background component, and also agreed with the Mie theory predictions. Figure 5.8(b) shows theory and experiment for 5.7 μm diameter beads in glycerol (n=1.09). Again, there is good agreement between experiment and theory. One can clearly see that the high frequency ripple structure decreases as the relative refractive index gets smaller. However, the low frequency oscillations are still clearly seen. Small disagreements between theory and experiment may have resulted from imperfect calibration of the instrument for the wavelength dependence of the optical elements used.

The experiments with two-layer models with polystyrene beads embedded in glycol or glycerol as the upper layer allowed to estimate the accuracy of the inverting size and refractive index information from the scattering data. To analyze the single scattering component the predictions of the Mie theory provided by equation (4.18) were fit to the observed residual spectra according to the procedure discussed in section 4.3.2.1. This fitting procedure used three parameters, average size of the particle, standard deviation in size (a Gaussian size distribution was assumed), and relative refractive index. A true bead size was
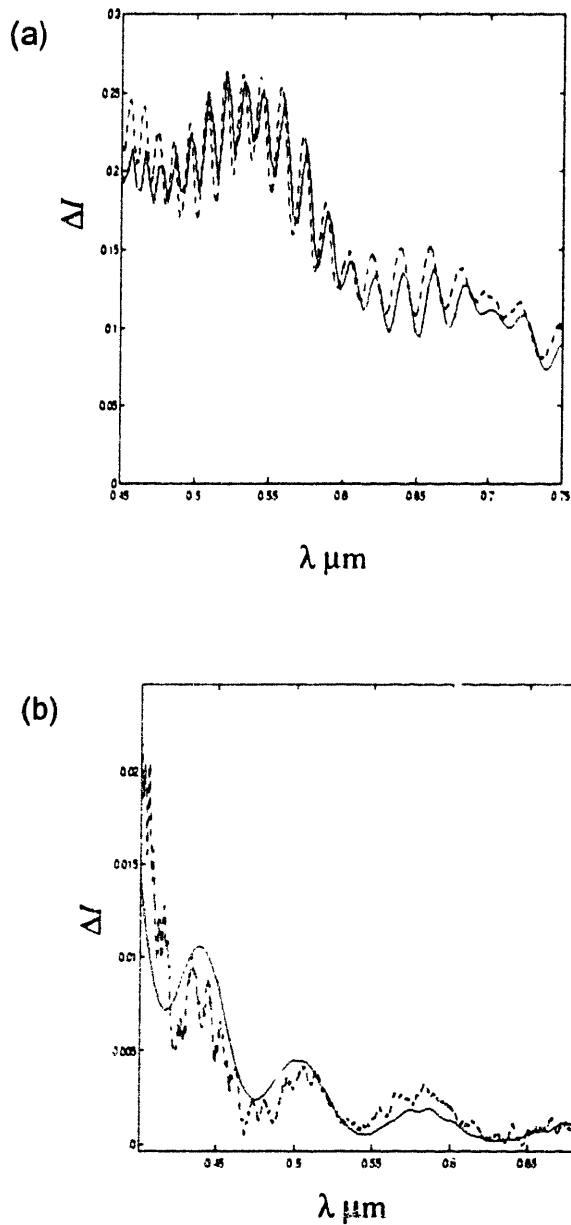
Figure 5.8. Spectra of polarized (residual) component of backscattered light from two-layered tissue model. Top layer: (a) d=4.65 μm beads in water (n=1.19); (b) d=5.7 μm beads in glycerol (n=1.09). The data (dashed lines) are in good agreement with the Mie calculations (solid lines). Absorption features of hemoglobin are completely removed.
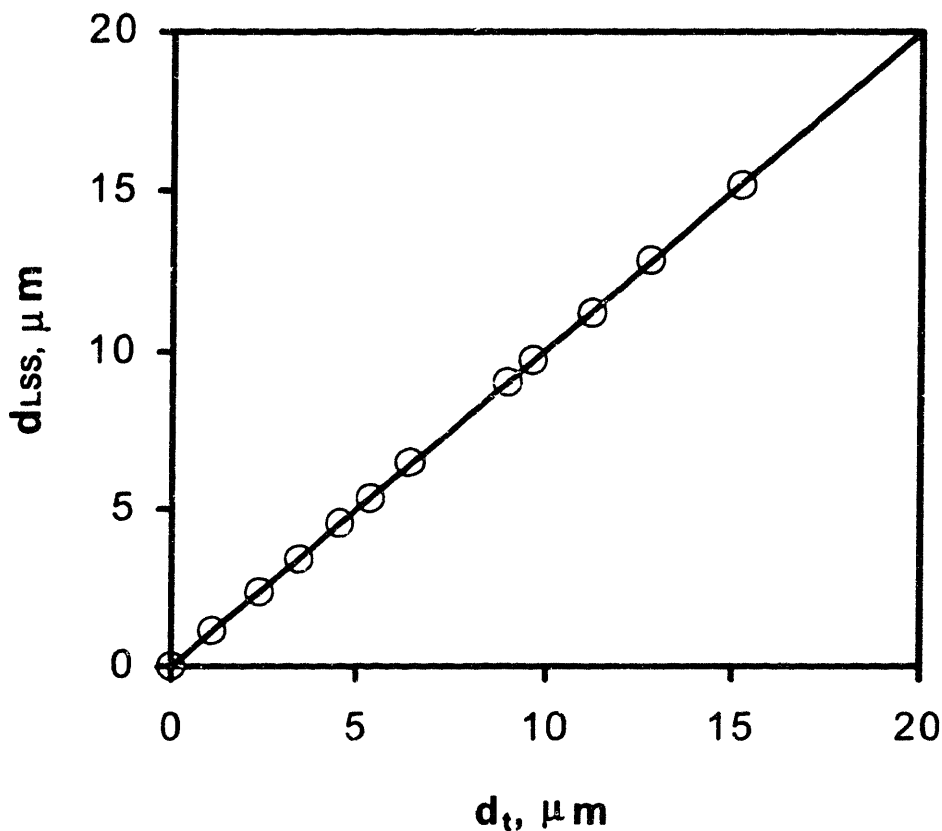
Figure 5.9 Binary plot showing an agreement between the true diameters of polystyrene beads (d_t) obtained with non-optical techniques and the diameters obtained with LSS (d_{LSS}). Each population of beads is represented by an open circle. The more accurate the measurement, the closer the corresponding circle to the diagonal line.

provided by the Polyscience Inc. and was confirmed by the experiments of forward light scattering by the beads in water. Polyscience Inc. used non-optical methods to measure the bead size. One of such methods employs the fact that the speed of bead diffusion in a viscous medium depends on their diameter.[2] Figure 5.9 shows

---

[2] We must notice that methods of particle sizing based on light scattering are much faster and cheaper to implement than existing non-optical techniques. Moreover they are capable of

the agreement between the true bead size and one obtained using LSS. These experiments established that LSS allows sizing spherical particles with diameters from 1 μm to 15 μm with an accuracy approaching 0.005 μm.

5.2.3 Experiments with Cell Monolayers

We performed experiments with cell monolayers (Fig. 5.10). As before. a thick layer of gel containing Ba_2SO_4 and blood was placed underneath to simulate underlying tissue. Three types of cells were prepared: isolated normal intestinal epithelial cells [Blumberg et al., 1991], intestinal epithelial tumor cell of T84 line [Dharmsathaphorn et al., 1990], and Chinese hamster ovary (CHO) fibroblasts [Freshney et al., 1992].

The setup was similar to one used in the experiments with beads. The cell nuclei however, had relative refractive indexes smaller then those of beads, as well as larger size distributions, which almost completely eliminates the ripple structure [Bohren et al., 1983]. The predictions of the Mie theory were fit to the observed residual spectra according to the procedure discussed in section 4.3.2.1. The fitting procedure used three parameters: average size of the nucleus d, standard deviation in size σ (a Gaussian size distribution was assumed), and relative refractive index n. First, the data-base of the LSS spectra for various combinations of d, σ, and n calculated using the Mie theory was built. Diameter d was varied from 0.1 μm to 20 μm with increment 0.005 μm. The wide range of sizes incorporated in the database ensured that the non-nuclear contribution to the LSS signals was not ignored. Standard deviation σ was varied from 0.1 μm to 5 μm with step 0.005μm. Relative

providing size information with accuracy, which is similar or may even exceed that of the state-
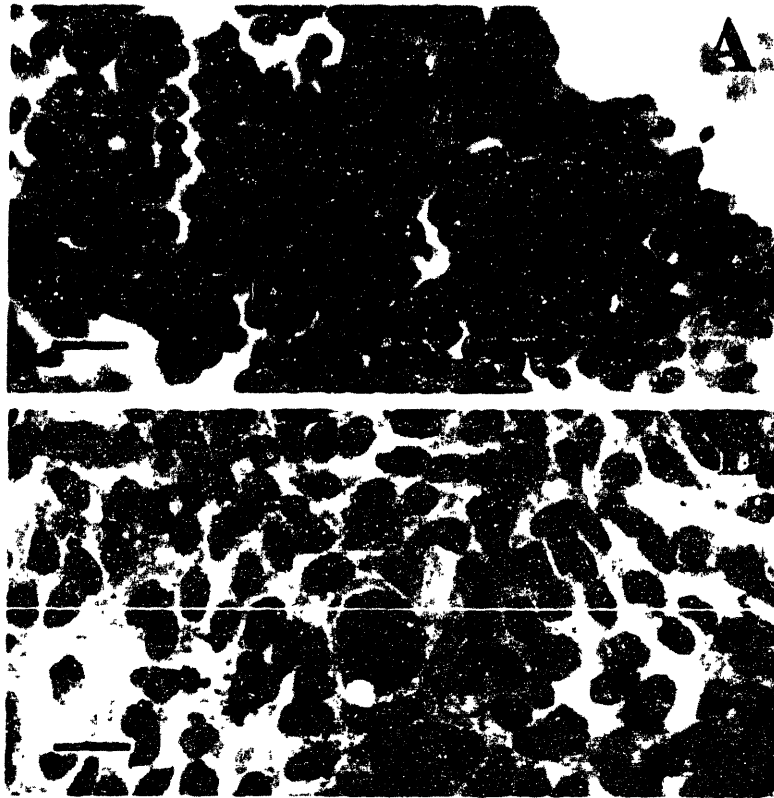
Figure 5.10 Microphotograph of the stained isolated normal intestinal epithelial cells (panel A) and intestinal malignant cell line T84 (Panel B). Note the uniform nuclear size distribution of the normal epithelial cell (A) in contrast to the T84 malignant cell line which at the same magnification shows a larger nuclei and more variation in nuclear size (B). Solid bars equals 20μm in each panel.

refractive index n was varied from 1.02 to 1.1 with step 0.001. Then each of the spectra from this data-base was compared with the LSS spectrum measured in the experiment and the values of χ^2 were calculated. The parameters d, σ, and n of the

of-the-art non-optical techniques.

Mie spectrum that fitted the data the best (corresponded to the smallest χ^2) were chosen as the optimal parameters.

For normal intestinal epithelial cells, the best fit was obtained using $d=5.0$ μm, $\Delta d=0.5$ μm, and $n=1.035$ (Fig. 5.11(a)). For CHO fibroblasts, we obtained $d=7.0$ μm, $\Delta d=1.0$ μm and $n=1.051$ (data not shown). For T84 intestinal malignant cells the corresponding values were $d=9.8$ μm, $\Delta d=1.5$ μm, and $n=1.04$ (Fig 5.11(b)).

In order to check these results, the distribution of the average size of the cell nuclei was measured by morphometry on identical cell preparations that were processed in parallel for light microscopy (Fig. 5.10). The nuclear sizes and their standard deviations were found to be in very good agreement with the parameters extracted from the Mie theory. A histogram showing the size distributions obtained for the normal intestinal epithelial cells and T84 cells is shown in Fig. 5.12. The accuracy of the average size is estimated to be 0.1μm, and the accuracy in n as 0.001. Note the larger value of n obtained for T84 intestinal malignant cells, which is in agreement with the hyperchromasia of cancer cell nuclei observed in conventional histopathology of stained tissue sections.

5.2.3 Experiments with *Ex Vivo* Tissues

We have performed studies with *ex vivo* normal and tumorous human colon tissue samples obtained immediately after surgical resection. Figure 5.13 shows the residual spectra. As can be seen, the spectral features are similar to the corresponding spectra obtained in the experiments with the normal colon cell and T84 colon tumor cell monolayers (Fig. 5.11). Figure 5.13 shows the size
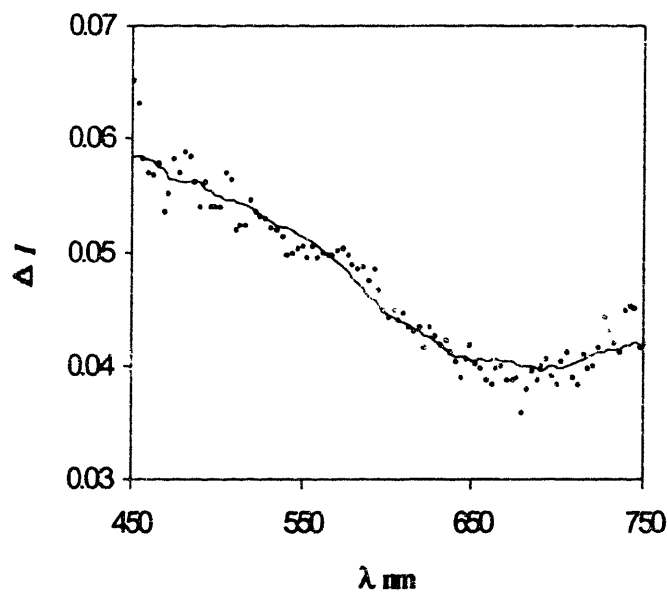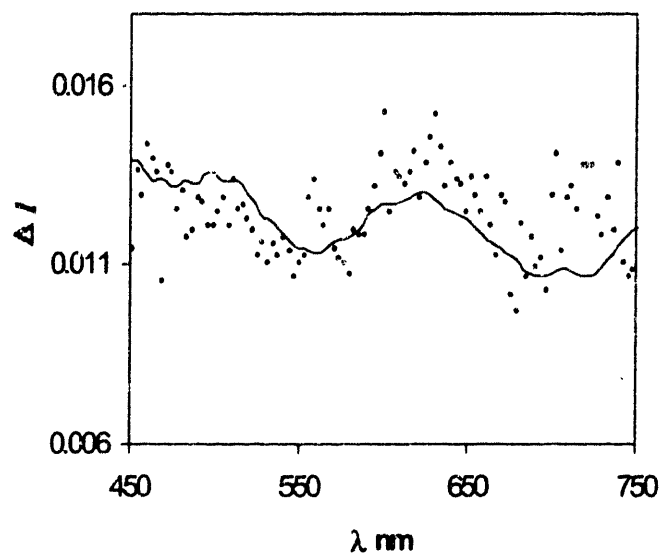
Figure 5.11 Spectra of polarized components of light backscattered by (a) normal intestinal cells and (b) T84 intestinal malignant cells. A monolayer of cells was placed on top a gel containing hemoglobin and barium sulfate. Dashed line, experimental data; solid line, the Mie theory fit. See text for details.

dist
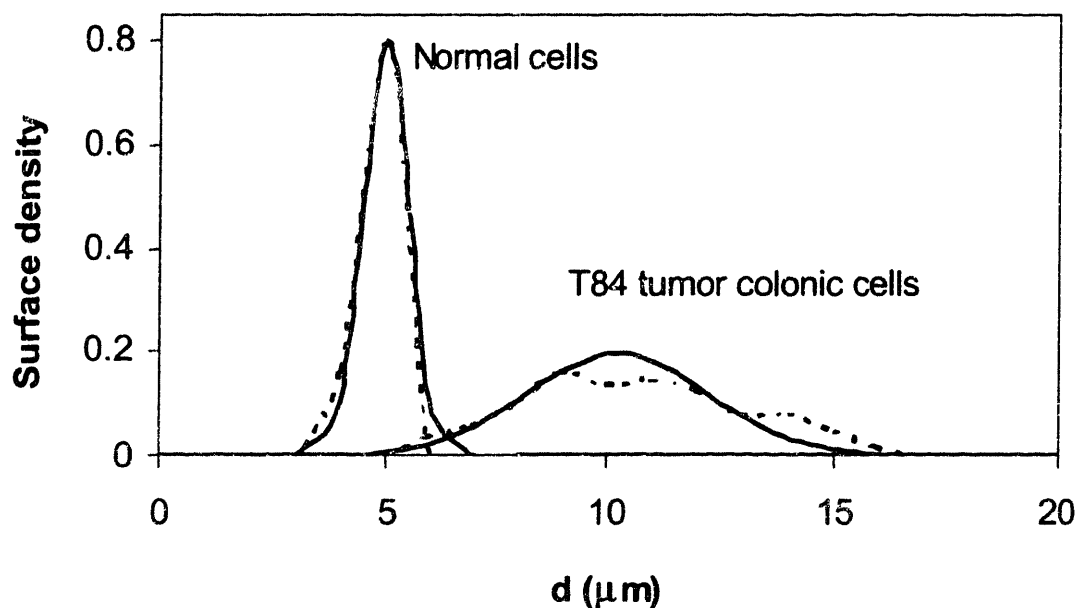
Figure 5.12 Nuclear size distributions for T84 intestinal malignant cells and normal intestinal cells. In each case, the solid line is the distribution extracted from the data, and the dashed line is the distribution measured using light microscopy of stained cells.

ributions and average refractive indexes obtained for the normal and the cancerous tissues by fitting the Mie theory to the data. For the normal tissue, the best fit was obtained using d=4.8 μm, Δd=0.4 μm, and n=1.035. For the tumorous tissue the corresponding values were d= 9.75 μm, Δd=1.5 μm, and n=1.045. The analysis clearly differentiates the normal and tumourous tissues. The relative increase in the
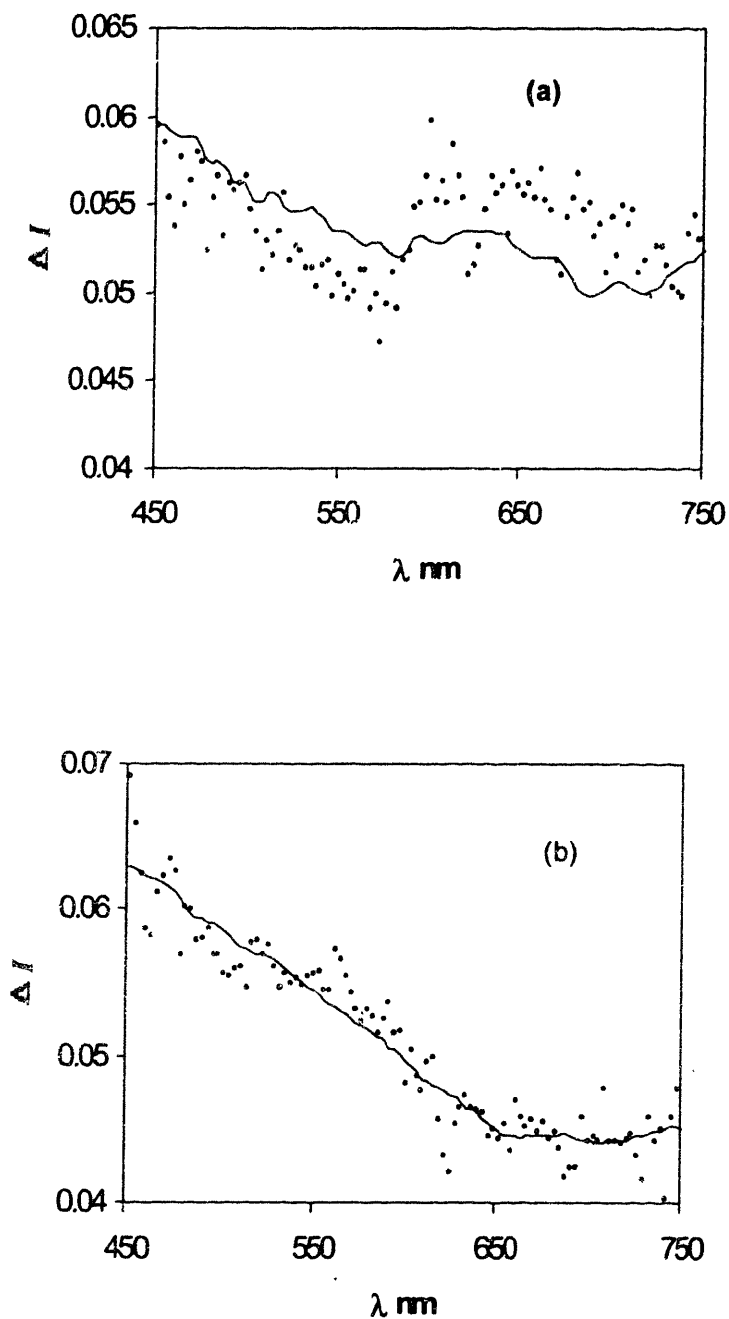
Figure 5.13 Spectra of the polarized components of light backscattered by (a) normal human colon tissue and (b) tumorous colon tissue. Dashed line, experimental data; solid line, the Mie theory fit.
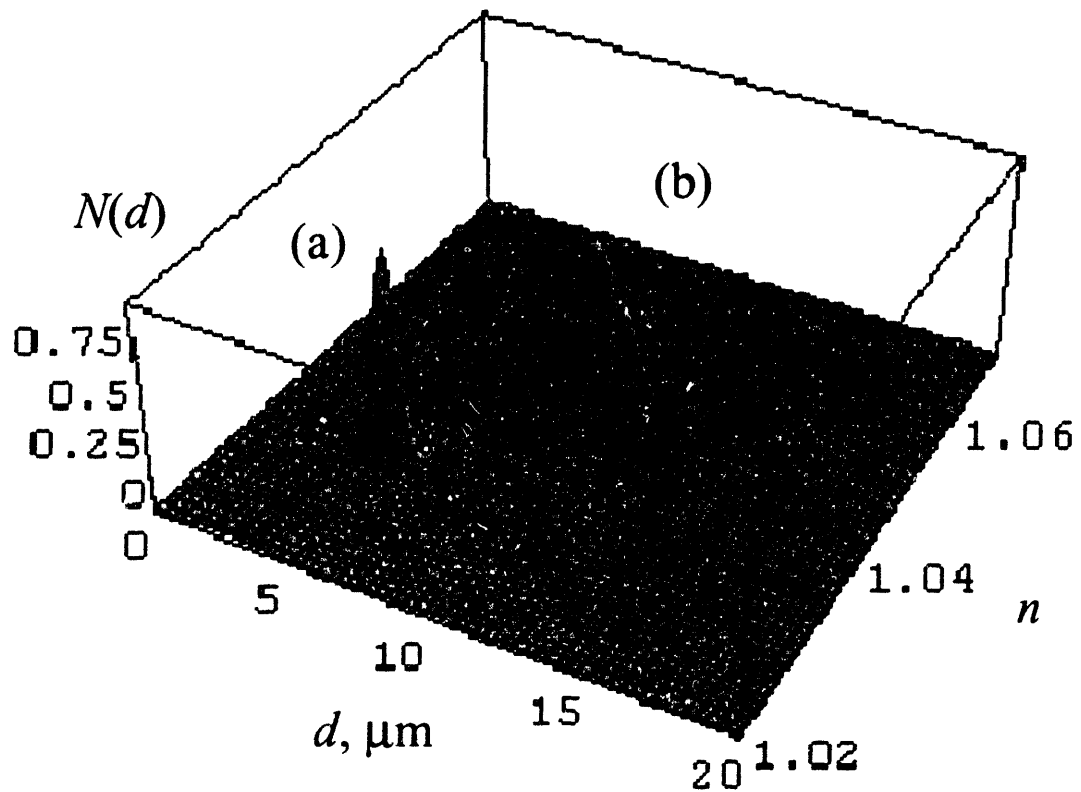
Figure 5.14 Size distributions of epithelial cell nuclei obtained with LSS for (a) normal and (b) cancerous colon tissue samples. Size distribution of the nuclei form the cancerous site illustrates nuclear enlargement, pleomorphism, and hyperchromasia (increased refractive index).

nuclear refractive index from normal to cancerous tissue, illustrated in Fig. 5.14, is also consistent with those of the cell monolayers.

Furthermore, polarized LSS device was used to collect data from other *ex vivo* and *in vivo* tissues. For example, Fig. 5.15(a) shows the nuclear size distributions measured *ex vivo* with LSS at two sites of the uterine cervix. The first measurement was taken in the endocervical region of the cervix. Endocervix is

153
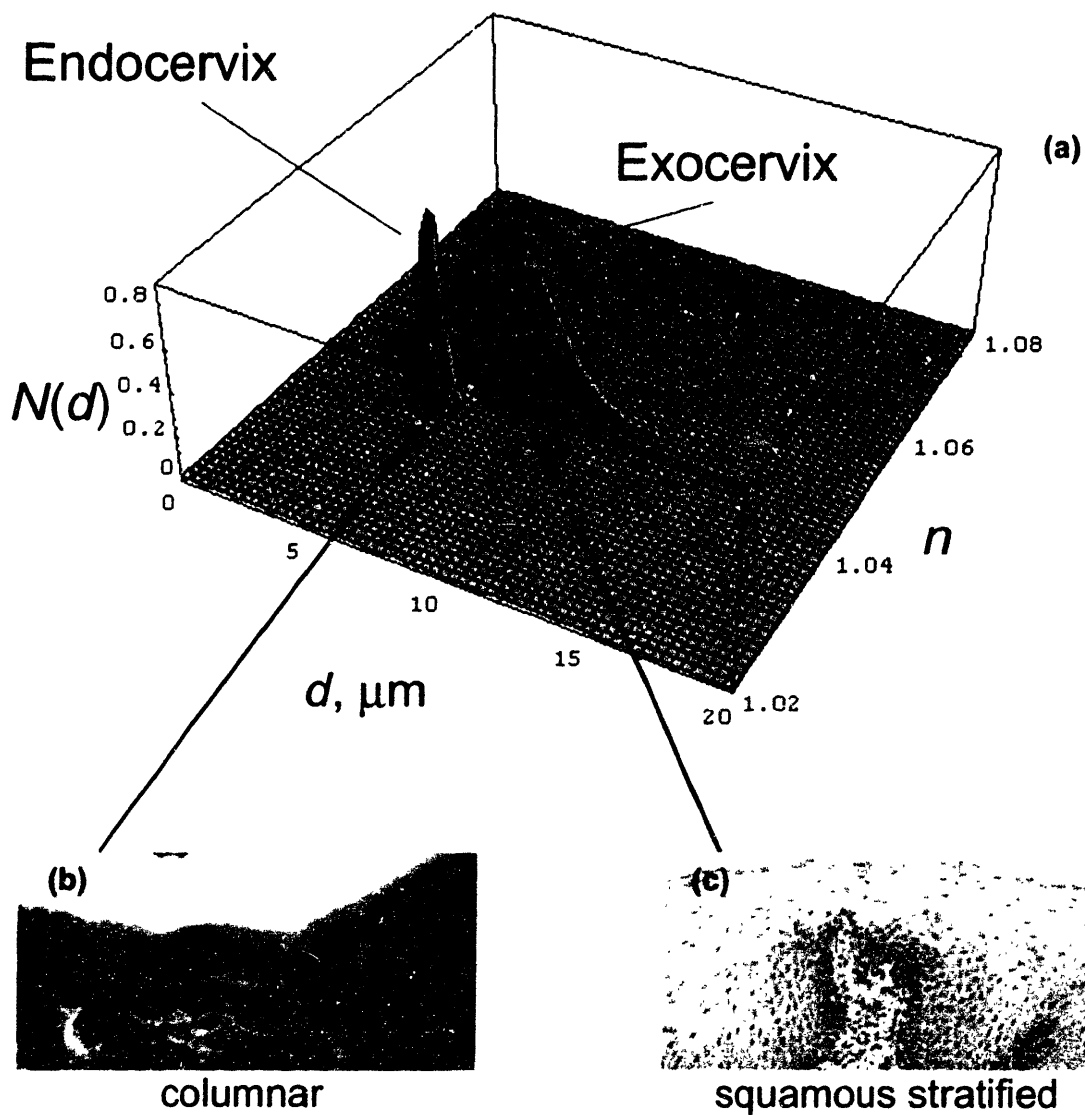
Figure 5.15 (a) Size distributions of the epithelial cell nuclei measured with LSS from the endo- and exocervix. (b) A typical histological section of the simple columnar epithelium lining the surface of the endocevix. (c) A typical histological section of the squamous stratified epithelium lining the surface of the exocevix.

154
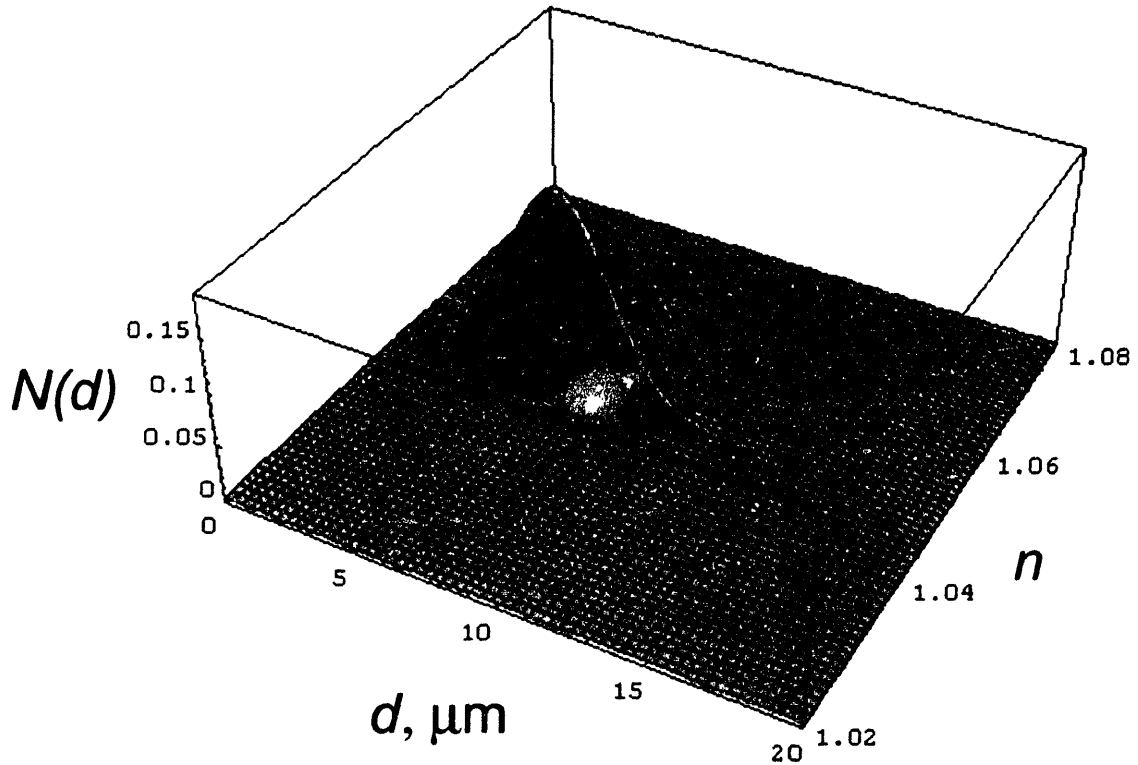
Figure 5.16 Size distributions of epithelial cell nuclei of the oral cavity obtained *in vivo* with LSS.

lined by the simple columnar epithelium formed by a single layer of uniform cells similar to those of normal epithelium of the colon (Fig. 5.15(b)). As seen in Fig. 5.15(a), the nuclei of the endocervical epithelium are quite uniform and are narrowly distributed in size, similar to the intestinal epithelial cell nuclei.

The second measurement was taken from the exocervical portion of the cervix. As seen in Fig. 5.15(a), these exocervical nuclei exhibit quite different size distribution, which is characterized by a considerably larger standard deviation.

155

This is consistent with the notion that exocervix is lined by the squamous stratified epithelium, which is thicker than the simple columnar epithelium (Fig. 5.15(c)). Moreover, the nuclei of the squamous stratified epithelium are not uniform in size due to maturation of the cells progressing from the basal layer to the top. Figure 5.16 shows that a similar squamous stratified epithelium of a different organ, the oral cavity, exhibits a similar nuclear size distribution. The later was measured with LSS *in vivo*. We notice as well that in either case, the nuclei are not enlarged.

5.2.4 LSS with Polarized Light

These experiments show that LSS with polarized light is capable of extracting morphological information from living cells in the presence of a large background from underlying tissue. The size distributions for monolayers were compared to light microscopy and found to be in good agreement with all three cell lines studied. The accuracy of the values extracted for both size and standard deviation was approximately 0.1 μm, which makes the method useful in differentiating cell nuclei of different cell types, including cancerous and non-cancerous cells of the same organ. The ability to detect nuclear enlargement and changes in refractive index, which can be related to the amount of DNA and protein in the nucleus, has potentially valuable clinical applications.

Because the relative refractive index of cell organelles is small and the epithelial layer is thin, the signal from the cellular layer is weak compared to the background from the underlying tissue. Thus, extracting signatures of the cellular structures requires finding a small signal in a large background. However, the residual spectrum, obtained by subtracting the parallel and perpendicular components of the reflectance from polarized incident light, effectively removes

both the diffuse background and spectral distortions due to absorption. This should be contrasted with our earlier approach in which reflectance from unpolarized incident light was studied, and a model based on diffusion theory was then used to remove the effects due to hemoglobin absorption and scattering from the underlying tissue. The resulting signal could then be analyzed to extract information about the structures in the epithelial tissue layer.

The polarization discrimination-based approach is not constrained by the limitations of a model, other than the assumption that the light backscattered by the cells in the epithelial layer retains the polarization of the incident light. Multiple scattering events randomize the polarization, enabling removal of the background simply by subtracting the two orthogonal polarization components. Generally, the signals seen in the monolayers have a pronounced polarization content, of the order of 1-10%, depending on the relative refractive index and the size of the particles.

As seen in Fig. 5.11 and Fig. 5.13, the Mie theory can be used to accurately describe the residual spectra of the epithelial cell layer. Furthermore, Fig. 5.12 establishes that the resulting morphological information is in good agreement with the directly measured distributions. This shows that the Mie theory provides an adequate method for extracting information about cell nuclei. The Mie theory was used to analyze the backscattered signal by varying the average nuclear size, d, the standard deviation in size, Δd, and the relative refractive index, n. We found that good agreement could be achieved only for a single set of parameters. Interestingly, in the rigorous Mie theory, the dependence on d and n does not enter only as the product $(n-1)d$. Thus, the residual experimental spectra contain sufficient information to extract d and n independently.

As pointed out in [Mourant et al., 1998; Perelman et al., 1998], elastic scattering by cells is due to a variety of cellular organelles, including mitochondria, a variety of endosomes and other cytoplasmic vesicles, nucleoli, and nuclei. The smaller organelles are responsible for intermediate angle scattering, whereas the nucleus contributes primarily to the scattering in near-backward directions. Our experiments confirm that the variation in backscattering as a function of wavelength is mainly associated with scattering by nuclei, as well. As will be discussed in Chapter 8, by changing the angle of collection, it is possible to study the structure of other cellular organelles as well.

References

Anderson RR, "Polarized light examination and photography of the skin", *Arch. Dermatol.*, **127**, 1000-1005 (1991).

Backman V, "Reflectance Spectroscopy for Diagnosis of Precancerous Changes in Human Epithalium", M.S. Thesis, Massachusetts Institute of Technology (1998).

Backman V, Gurjar R, Badizadegan K, Itzkan I, Dasari R, Perelman LT, Feld MS, "Polarized light scattering spectroscopy for quantitative measurement of epithelial structures in situ", *IEEE J. Sel. Topics Quantum Electron*, **5**, 1019-1027 (1999).

Backman V, Wallace MB, Perelman LT, Arendt JT, Gurjar R, Muller MG, Zhang Q, G. Zonios G, Kline E, McGillican T, Shapshay S, Valdez T, Van Dam J, Badizadegan K, Crawford JM, Fitzmaurice M, Kabani S, Levin HS, Seiler M, Dasari RR, Itzkan I and Feld MS, "Light scattering spectroscopy: a new technique for clinical diagnosis of precancerous and cancerous changes in human epithelia", *Nature*, **406**, 35-36 (2000).

Beauvoit B, Kitai T and Chance B, "Contribution of the mitochondrial compartment to the optical properties of rat liver: a theoretical and practical approach," *Biophys. J.*, **67**, 2501-2510 (1994).

Beuthan J, Milner O, Hefmann J, Herrig M and Muller G, *Phys. Med. Biol.*, **41**, 369 (1996).

Blumberg RS, C. Terhost, P. Bleicher, F. V. McDermott, C H Allan, S B Landau, J S Trier, S P Balk, "Expression of a nonpolymorphic MHC class I- like molecule, CDID, by human intestinal epithelial cells", *J. Immunol.*, **147**, 2518-2524 (1991).

Bohren CF and Huffman DR, *Absorption and Scattering of Light by Small Particles* (John Wiley & Sons, New York, 1983).

Boone C.W. *et al.* Quantitative grading of rat esophageal carcinogenesis using computer-assisted image tile analysis. *Cancer Epidemiology, Biomarkers & Prevention*, **9**, 495-500 (2000).

Brennan JF, Zonios GI, Wang TD, Rava RP, Hayes GB, Dasari RR and Feld MS, *Appl. Spectr.*, **47**, 2081 (1993).

Brunsting A and Mullaney F, "Differential light scattering from spherical mammalian cells", *Biophys. J.*, **14**, 439-453 (1974).

Chen K, Perelman LT, Zhang Q, Dasari RR, Feld MS, "Optical Computed Tomography in a Turbid Medium Using Early Arriving Photons," *Journal of Biomedical Optics*, **5**, 144-154 (2000).

Cotran RS, Robbins SL, Kumar V, *Robbins Pathological Basis of Disease* (W.B. Saunders Company, Philadelphia, 1994).

Dharmsathaphorn K and Madara JL., "Eastablished intestinal cell lines as model systems for electrolyte transport studies", *Methods Enzymol.* **192**, 354-389 (1990).

Drezek R, Dunn A and Richards-Kortum R, "Light scattering from cells: finite-difference time-domain simulations and goniometric measurements", *Appl. Opt.*, **38**, 3651-3661 (1999).

Demos SG and Alfano RR, "Temporal gating in highly scattering media by the degree of optical polarization ", *Opt. Lett.*, **21**, 161-163 (1996).

Demos SJ and Alfano RR, "Optical polarized imaging", *App. Opt.*, **36**, 150-155 (1997).

Dunn A and Richards-Kortum R, "Three-dimensional computation of light scattering from cells", *IEEE J. Sel. Top. Quantum Electron.*, **2**, 898-905 (1996).

Farrell TJ, Patterson MS, Wilson B, "A diffusion theory model of spatially resolved, steady state diffuse reflectance for the noninvasive determination of tissue optical properties in vivo", *Med. Phys.*, **19**, 879-888 (1992).

Fawcett DW, *A Textbook of Histology*, (Charman & Hall, New York, 1994).

Freshney RI, *Animal Cell Culture: A practical approach.* 2nd ed. IRL Press. Oxford (1992).

Georgakoudi I, Jacobson BC, Backman V, Wallace M, Muller M, Zhuang Q, Badizadegan K, Sun D, Thomas G, Van Dam V, Feld MS, "The Combination of Fluorescence, Diffuse Reflectance, and Light Scattering Spectroscopy for the Improved Detection of Low- and High-grade Dysplasia in Patients with Barrett's Esophagus", *Gastrointerology*, in press (2001).

Georgakoudi I, Sheets EE, Müller MG, Backman V, Crum CP, Badizadegan K, Dasari RR, Feld MS, "Tri-Modal Spectroscopy as a Tool for the Detection and Biochemical/Morphological Characterization of Cervical Pre-Cancers *In Vivo*", *Obstet. Gynecol.*, submitted (2001).

Gurjar R, Backman V, Badizadegan K, Dasari R, Itzkan I, Perelman LT, Feld MS, "Functional Imaging of Human Epithelia with Polarized Light Scattering Spectroscopy", *Nature Medicine*, to be published (2001).

Ishimaru A, Wave Propagation and Scattering in Random Media (Academic Press, Orlando, 1978).

Jackson JD, *Classical Electrodynamics*, (John Wiley & Sons, New York, 1975).

Kerker M, *The Scattering of Light*, (Academic Press, New York, 1969).

Morse PM and Feshbach H, *Methods of Theoretical Physics* (McGraw-Hill, New York, 1953).

Mourant JR, Freyer JP, Hielscher AN, Elick AA, Shen D and Johnson T, "Mechanisms of light scattering from biological cells relevant to noninvasive optical-tissue diagnosis", *Appl. Opt.*, 37, 3586-3593 (1998).

Newton RG, *Scattering Theory of Waves and Particles* (McGraw-Hill Book Company, New York, 1969).

Perelman LT, Wu J, Itzkan I, Feld MS, "Photon migration in turbid media using path-integrals", *Phys. Rev. Lett.*, 72, 1341-1344 (1994).

Perelman LT, Backman V, Wallace MB, Zonios G, Manoharan R, Nusrat A, Shields S, Seiler M, Lima C, Hamano T, Itzkan I, Van Dam J, Crawford JM and Feld MS, "Observation of periodic fine structure in reflectance

from biological tissue: a new technique for measuring nuclear size distribution", *Phys. Rev. Lett.*, **80**, 627-630 (1998).

Slot PMS, Hoekstra AG and Figdor CG, *Cytometry*, **9**, 636 (1988).

Van de Hulst HC, *Light Scattering by Small Particles* (Dover Publications, New York, 1957).

Watson JV, *Introduction to Flow Cytometry* (Cambridge U. Press, Cambridge, 1991).

Yang C, Kyungwon A, Perelman LT, Dasari R, Feld MS, "Feasibility of Field-Based Light Scattering Spectroscopy", *J Biomed Optics*, **5**, 138 (2000).

Yang C, Wax A, Georgakoudi I, Hanlon E, Badizadegan K, Dasari RR, Feld MS, "Interpherometric Phase Dispersion Microscopy", *Optics Letters*, **25**, 1526 (2000).

Yodh AG and Chance B, "Spectroscopy and imaging with diffusing light," *Physics Today*, **48**(3), 34-40, (1995).

Yoo KM, Alfano RR, "Time resolved depolarization of multiple backscattered light from random media", *Phys. Lett. A*, **142**, 531-536 (1989).

Zonios GI, R. M. Cothren, J. T. Arendt, J. Wu, J. Van Dam, J. M. Crawford, R. Manoharan, and M. S. Feld, "Morphological model of human colon tissue fluorescence, " *IEEE Trans. Biomed. Eng.*, **43**, 1-10 (1996).

Zonios G, Ph.D. Thesis, Massachusetts Institute of Technology (1998).

Zonios G, Perelman LT, Backman V, Manoharan R, Fitzmaurice M, Feld MS, "Diffuse Reflectance Spectroscopy of Human Adenomatous Colon Polyps *In Vivo*", *Appl. Opt.*, **38**, 6628-6637 (1999).

Chapter 6

Clinical Diagnosis of Precancerous Changes Using LSS

In the previous chapters we established that LSS provides morphological information about the structure of superficial tissues, i.e. morphology of epithelial cells. In particular, LSS enables measuring the size distribution of epithelial cell nuclei. In this chapter we discuss potential of LSS as a broadly applicable technique for clinical detection and diagnosis of precancerous and early cancerous changes in human epithelia *in vivo* and present clinical studies conducted in Barrett's esophagus, bladder, oral cavity, and colon [Backman et al., 2000].

Application of LSS for characterization, detection, and diagnosis of precancerous and early cancerous changes in human epithelia is particularly important because over 85% of all cancers originate in the epithelium and are

163

readily treatable if diagnosed at an early stage [Cotran et al., 1994; Landis et al., 1999]. However, many types of precancerous epithelial lesions and early (noninvasive) cancers are difficult to detect and diagnose clinically using current methods.

As discussed in detail in Chapter 2, the epithelium is a highly cellular tissue covering the inner mucosal and outer skin surfaces of the body [Fawcett, 1994]. Its structure depends on organ and tissue type. For example, the columnar epithelium lining the inner mucosal surface of the colon consists of a single contiguous layer of cells approximately 20 μm thick, whereas the stratified squamous epithelium of the oral cavity consists of multiple cell layers, and can be a few hundred μm thick. Epithelial layers are usually supported by paucicellular vascularized loose connective tissue. Beneath it there are layers of muscular and connective tissues.

Cancers of epithelial origin, or carcinomas, are generally preceded by a precursor lesion known as dysplasia [Cotran et al., 1994; Boone et al., 2000]. These precancerous lesions and the earliest (noninvasive or *in situ*) forms of carcinoma are confined to the epithelial layers. The hallmarks of these lesions are nuclear atypia, cellular proliferation and alterations in architecture of the cell layer. The atypical nuclei become enlarged, crowded and hyperchromatic (abnormally darkly stained with a contrast dye), features which can currently only be assessed by histologic examination of biopsy specimens. It is important to note that although the gross and microscopic appearance of dysplasia and carcinoma *in situ* (CIS) in different organs and different types of epithelium can vary significantly, these nuclear changes remain constant.

Two difficulties arise in the clinical diagnosis of dysplasia. First, dysplasia is difficult to detect. In many cases it is invisible to the eye of the physician even through the endoscope. Therefore, random biopsy is often used to sample tissue at risk for dysplasia. The odds of encountering dysplasia in a random biopsy are substantially less than 1 percent for some organs. Second, once a biopsy is taken there can be significant interobserver disagreement in the histological diagnosis and grading of dysplasia, even among expert pathologists [Reid et al., 1988]. Similar difficulties exist in the clinical diagnosis of CIS.

Let us remind the reader that typical non-dysplastic cell nuclei range in size from 5 to 10 µm. Dysplastic nuclei can be as large as 20 µm. The spectrum of light backscattered by these particles, which are large compared to the wavelength of visible light (λ=0.4-0.7 µm), contains a component that varies characteristically with wavelength (see Chapter 4 for details). This variation depends on particle size and refractive index. When nuclei of several sizes are present, the resulting signal is a superposition of these variations. Thus, the nuclear size distribution and refractive index can be determined from the analysis of the spectrum of light backscattered by the nuclei [Backman et al, 1998; Perelman et al, 1998; Backman et al, 1999]. Once the nuclear size distribution and refractive index are known, quantitative measures of nuclear enlargement, crowding, and hyperchromasia can be obtained.

In the following section we present the results of multipatient clinical studies illustrating the potential of LSS to detect and diagnose precancerous and early cancerous changes in epithelia of several human organs [Backman et al., 2000]. This will be followed by a more detailed discussion of the clinical studies in Barrett's esophagus [Wallace et al., 2000].

6.1 Clinical Diagnosis of Dysplasia in Human Epithelia using LSS

We have performed *in vivo* human studies to test the potential of LSS to diagnose dysplasia and CIS in four different organs with three different types of epithelium: columnar epithelia of the colon and Barrett's esophagus, transitional epithelium of the urinary bladder, and stratified squamous epithelium of the oral cavity [Backman et al., 2000]. All clinical studies were performed during routine endoscopic screening or surveillance procedures. The study of dysplasia in Barrett's esophagus was performed during esophagogastroduodenoscopy in 16 adult patients with a known history of Barrett's esophagus. Since this form of dysplasia is not visible with endoscopy, random biopsies were taken from four quadrants every 2 cm along the length of the esophagus. The study of colonic dysplasia was performed during colonoscopy in 8 adult patients being screened for dysplastic (adenomatous) colon polyps. The study transitional cell CIS of the urinary bladder was performed during cystoscopy in 7 adult patients being screened for a history of either transitional cell carcinoma or hematuria. The study of dysplasia and CIS in the oral cavity was performed during routine oral examination in 5 adult patients suspected with squamous cell carcinoma. In each case informed consent from the patients was obtained prior to the procedure.

The data were collected with the device of Fig. 5.2 as in the experiments with cell monolayers and *in vivo* tissue discussed in section 5.1. In all of the studies, an optical fiber probe was used to deliver a weak pulse of white light from a xenon arc lamp to the tissue. The probe tip was brought into gentle contact with the tissue. The same probe was used to collect light returned from the tissue by means of elastic scattering (reflectance signal). In the studies of dysplasia and CIS

166
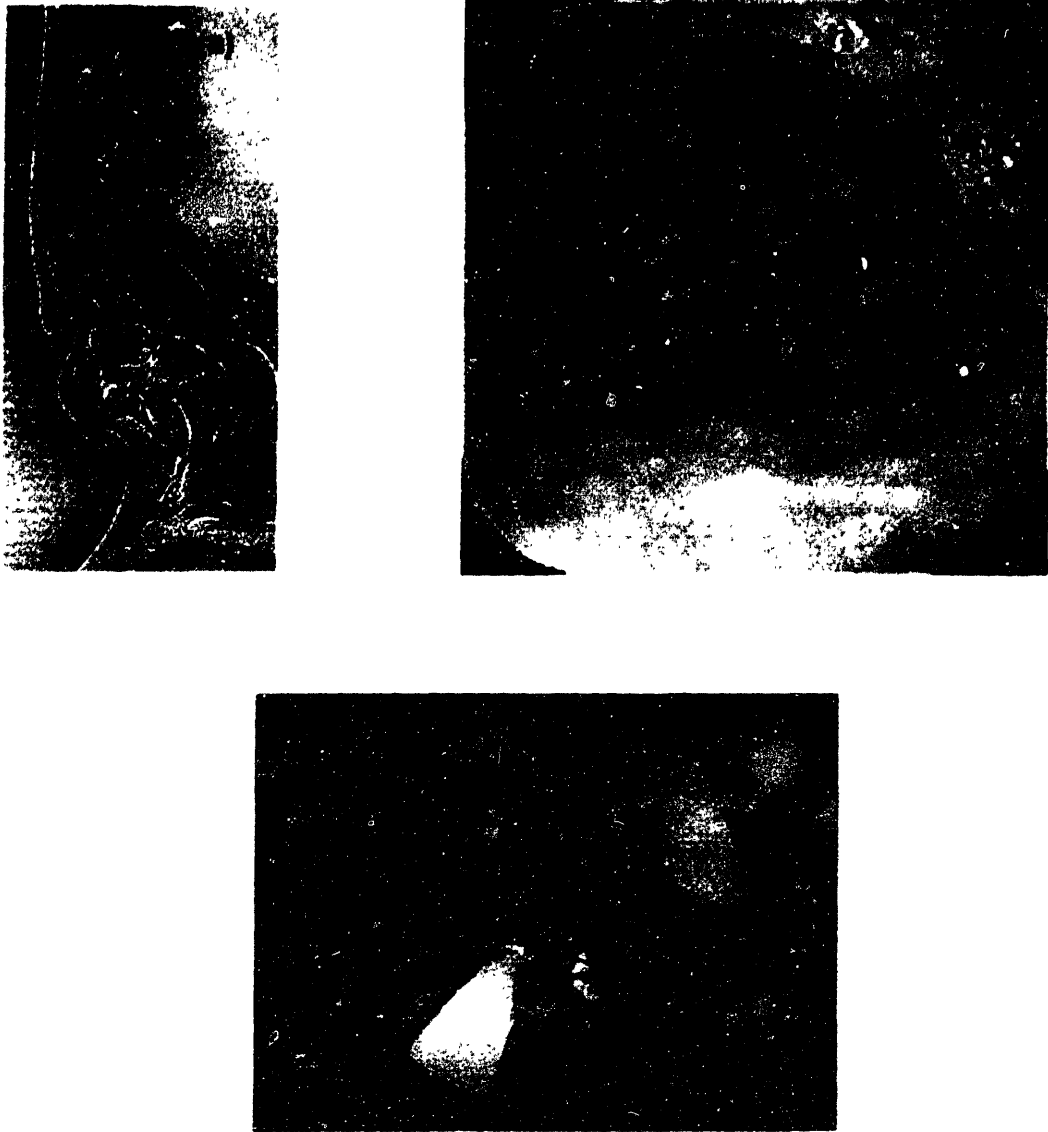
Figure 6.1. (a) Schematic diagram illustrating measurement of reflectance signal from esophageal tissue using fiber optic probe An endoscope and a probe approaching the esophageal wall is shown (b) Photograph obtained during the endoscopy Esophageal wall and a Barrett's esophagus segment are seen (c) Photograph obtained during the collection of the spectroscopic data from the esophageal tissue during a routine esophagoscopy Fiber optic probe and biopsy forceps are shown.

in the Barrett's esophagus, colon, and the urinary bladder, the probe was inserted into the biopsy channel of the endoscope. In the studies of dysplasia in the oral cavity, the probe was manipulated directly. The probe tip, 1 mm in diameter, consisted of a central delivery fiber surrounded by six collection fibers (fused silica, 200 micron core, NA=0.22), bonded at the tip to a cylindrical quartz optical shield 1 mm in length [Brennan et al., 1993]. This probe sampled tissue over a circular spot approximately $1mm^2$ in area. The pulse duration was 50 milliseconds and the wavelength range was 350-685 nanometers. The site was then carefully biopsied, and the sample submitted for histologic examination (Fig. 6.1).

In each study, both non-dysplastic and dysplastic tissues were sampled. The biopsied tissue was prepared and examined histologically by experienced pathologists in the conventional manner. The spectrum of the reflected light was analyzed. A typical reflectance spectrum consisted of a large diffusive background on which is superimposed a small (2-3%) single scattering component due to scattering by cell nuclei in the mucosal layer. The diffusive background was removed using exponential model approach presented in section 5.1.2. The single scattering component was analyzed using equation (4.29) of section 4.2.2.2. Thus, the nuclear size distributions were obtained for each tissue site. These size distributions were then used to calculate two statistics characterizing nuclear enlargement and cell crowding, namely percentage of enlarged (larger than a certain characteristic size, see below) nuclei and nuclear population density (number of nuclei per unit surface area). Examples of the epithelial nuclear size distributions obtained *in vivo* from benign transitional epithelium and transitional cell CIS of the urinary bladder are shown in Figure 6.2. As can be seen, the distribution of CIS cell nuclei extends to larger size.
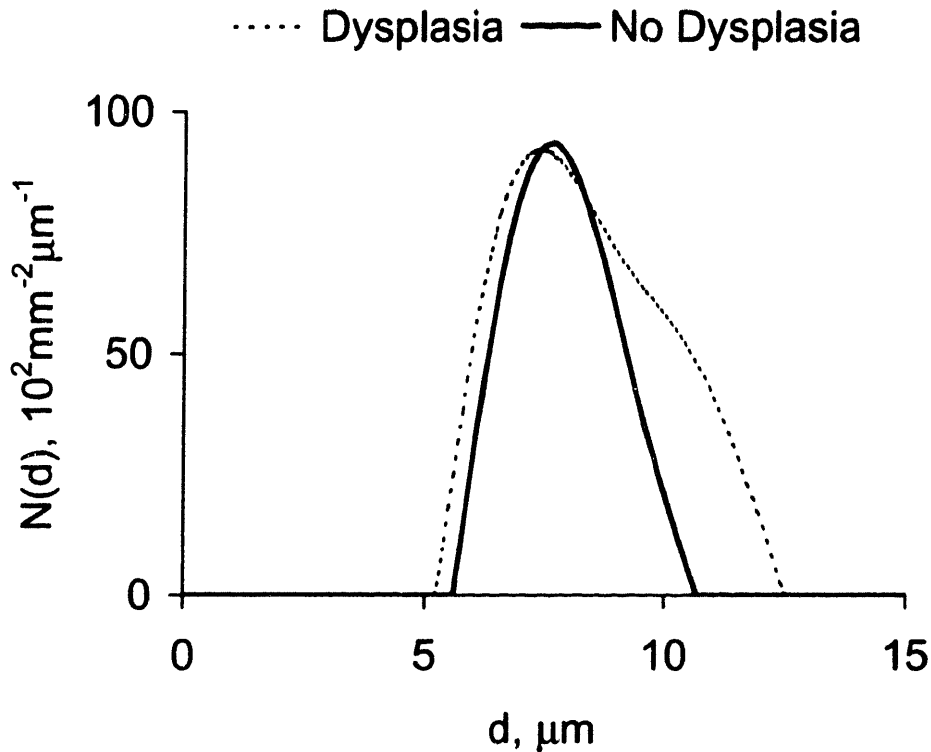
Figure 6.2. Examples of the epithelial nuclear size distributions $N(d)$ obtained *in vivo* with LSS from the urinary bladder. Transitional cell CIS epithelium exhibits greater nuclear population density (total number of nuclei per unit area) and percentage of large ($>10\mu m$) nuclei relative to the non-dysplastic transitional epithelium (~20% vs. 3%).

Before prospective (double-blinded) evaluation was initiated, classification criteria were established based on un-blinded analysis of an initial "modeling set" consisting of eight samples from the Barrett's esophagus study and consultation with the study pathologists. First, the optimal definition of "enlarged nucleus" was established using receiver-operation characteristic (ROC) method [Mantel et al., 1959; Barnoon et al., 1972; Landis et al., 1977] by varying the threshold diameter from 8 to 14 microns in 2 micron steps. The resulting values of sensitivity and

specificity for each diameter were then used to construct an ROC curve. The threshold diameter of 10 μm associated with the point closest to the left upper corner of the ROC plot (corresponding to a sensitivity and specificity of 100%) was taken to be the optimum value and used in subsequent analysis. Thus, in this study, a nucleus was considered to be "enlarged" if its diameter exceeded 10 μm.

For each tissue spectrum, the corresponding size distribution was used to obtain the percentage of nuclei larger than 10 μm in diameter and the total number of nuclei per unit area (population density). As noted above, these parameters quantitatively characterize the degree of nuclear enlargement and crowding, respectively. Figure 6.3 displays these LSS parameters in binary plots to exhibit their histologic correlation. In all four organs there is an appreciable distinction between these nuclear parameters dysplasia or CIS and non-dysplastic or benign epithelium. Both dysplasia and CIS have a higher percentage of enlarged nuclei and, on average, a higher population density, which can be used as the basis for a spectroscopic tissue diagnosis. The few outliers may have resulted from a number of factors, including the failure of LSS to provide proper size distributions, histologic misdiagnosis, or a failure of the probe and biopsy to precisely sample the same area.

These data demonstrate that LSS can be used to assess nuclear features of epithelial cells *in vivo* which can now only be assessed *in vitro*. They further demonstrate that this technique can be applied to the diagnosis of dysplasia and CIS in four organs with three different types of epithelium. This shows that LSS has the potential to provide a broadly applicable means of detecting epithelial precancerous lesions and noninvasive cancers in all organs which can be optically accessed either directly or by means of optical fibers inserted in endoscopes, catheters, needles and cannulas. Other important examples of the organs that can
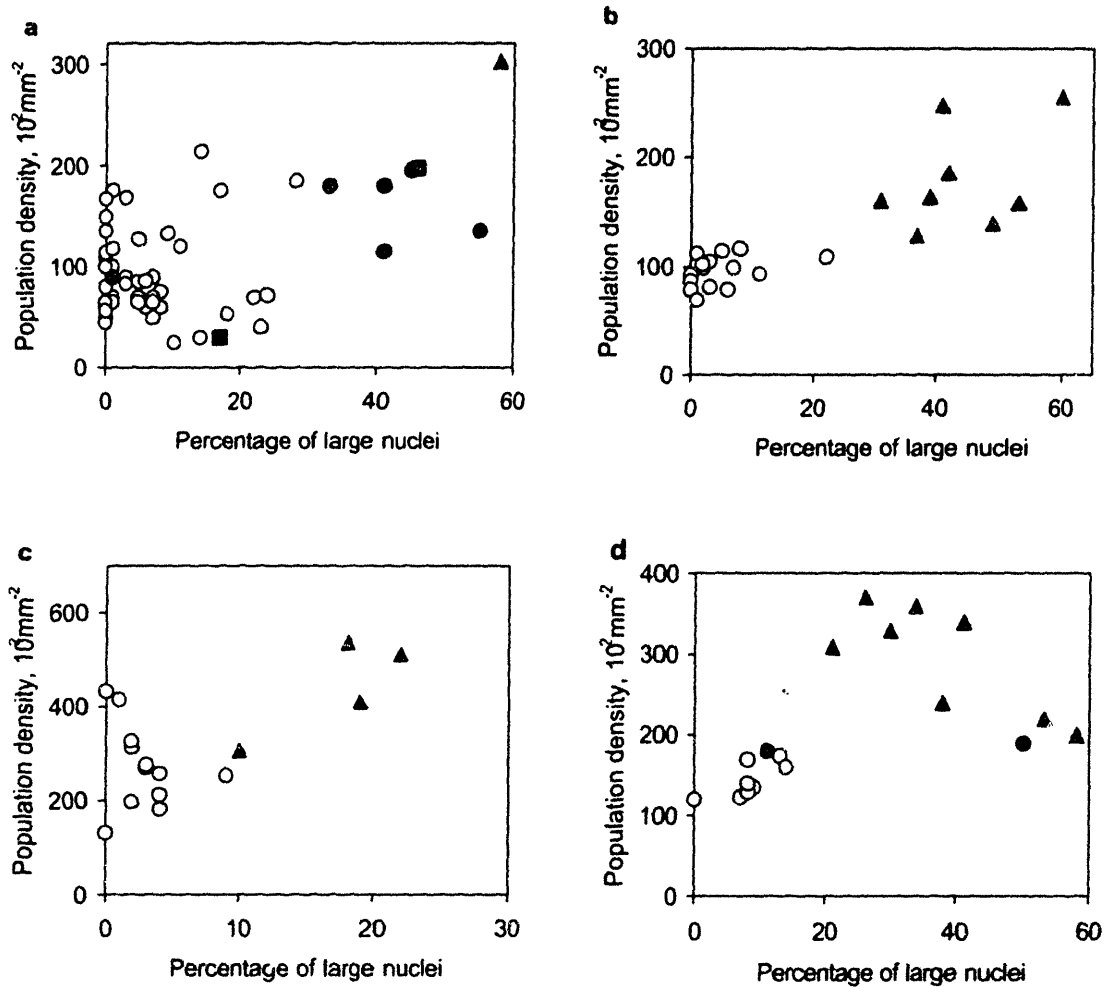
Figure 6.3. Comparison of the parameters of the nuclear size distributions obtained *in vivo* using LSS with the histologic diagnosis in: (a) Barrett's esophagus (non-dysplastic Barrett's mucosa (circles), indefinite for dysplasia (filled squares), low grade dysplasia (filled circles), or high grade dysplasia (filled triangles)); (b) colon (normal colonic mucosa (circles) or adenomatous polyp (filled triangles)): (c) urinary bladder (benign bladder mucosa (circles) or transitional cell carcinoma *in situ* (filled triangles)); and (d) oral cavity (normal (circles), low grade dysplasia (filled circles), or squamous cell carcinoma *in situ* (filled triangles)).

potentially be analyzed using LSS include the lung, stomach, breast and uterine cervix. The cancers originating from the epithelia of such organs are responsible for approximately 50% of all cancer deaths in the United States [Landis et al., 1999]. Early detection of dysplasia and CIS by means of LSS may significantly decrease the mortality associated with these cancers. Moreover, the LSS technique has a number of advantages over other conventional diagnostic techniques. It does not require tissue biopsy. Quantitative parameters are provided in an objective fashion. The apparatus is inexpensive. The analysis can be performed in a fraction of a second and the results can be provided in real time, as the measurement is being made. The technique need not be considered as a replacement for biopsy and subsequent histologic evaluation. Rather, by using this technique to guide random biopsy of invisible lesions and directed biopsy of suspicious lesions, sampling error can be reduced. Thus, the specificity and sensitivity of screening and surveillance procedures might be significantly increased.

In summary, the LSS technique can be used to detect and diagnose previously undetectable precancerous lesions and early (noninvasive) cancers *in vivo*, and, therefore, reduce cost and increase the efficacy of conventional diagnostic methods.

6.2 Clinical Diagnosis of Dysplasia in Barrett's Esophagus

In this section we discuss the clinical study of dysplasia in Barrett's esophagus using LSS, one of the four clinical studies reported in the previous

section, in grater detail. The incidence of adenocarcinoma of the esophagus is increasing in the United States [Blot et al, 1991]. Almost 100% of cases occur in patients with Barrett's esophagus (BE) [Antonioli et al., 1993], a condition in which metaplastic columnar epithelium replaces the normal squamous epithelium of the esophagus. Although periodic endoscopic surveillance of patients with BE has been shown to detect carcinoma in its earlier stages [Streitz et al., 1993; Peters et al., 1994; Lerut et al., 1994], surveillance has significant limitations. Dysplastic and early carcinomatous lesions arising in BE are not visible macroscopically, thus surveillance requires extensive random biopsies of the esophagus and histologic examination of the excised tissue for dysplasia. Random biopsy is prone to sampling error and significantly increases the cost and risk of surveillance. The dependence on histology delays the time between endoscopy and diagnosis, and there is significant inter-observer disagreement between pathologists in diagnosing dysplasia [Reid et al., 1988; Petras et al., 1991].

LSS study was approved by the institutional review boards of the Brigham and Women's Hospital, West Roxbury VA Medical Center, and the Massachusetts Institute of Technology. After informed consent, the study was performed in 16 adult patients with a known history of Barrett's esophagus undergoing surveillance esophagogastroduodenoscopy for a diagnosis of Barrett's esophagus or suspected carcinoma of the esophagus. Since dysplasia in Barrett's esophagus is not visible with endoscopy, random biopsies were taken from four quadrants every 2 cm along the length of the esophagus. In patients with suspected adenocarcinoma, biopsies for this study were taken from the Barrett's mucosa adjacent to the tumor.

The data were taken as discussed in section 6.1. The fiber optic probe was inserted into the accessory channel of the endoscope and used to illuminate its

surface with white light and to collect the reflectance signal. The site was then carefully biopsied, and the sample submitted for histologic examination.

The biopsy samples were evaluated by four gastrointestinal study pathologists from four different institutions. The histologic diagnosis of dysplasia in Barrett's epithelium was made using published criteria adapted to Barrett's epithelium [Riddell et al., 1983; Haggitt et al., 1994], using a scoring system of 1-non dysplastic Barrett's (NDB); 2-indefinite for dysplasia (IND); 3-low grade dysplasia (LGD); 4-high grade dysplasia (HGD); and 5-invasive carcinoma. One pathologist examined all biopsies, and then a subset of all abnormal biopsies (indefinite or dysplasia) plus a random selection of normal biopsies were examined by all four pathologists. The pathologists were blinded to the spectroscopic diagnosis and the diagnoses of the other pathologists. The spectroscopic diagnosis was compared to two pathological diagnoses, the "average diagnosis" and the "consensus diagnosis". The average diagnosis followed the method of Riddell et al [Riddell et al., 1983]. The mean score of all four pathologists was computed, and then converted to discrete diagnoses by assigning [Riddell et al., 1983]: 1-1.74=NDB, 1.75-2.49=IND, 2.5-3.24=LGD, >3.25=HGD. The consensus diagnosis was the diagnosis for which at least three pathologists reported the same result. When this method was used, samples for which less than three pathologists agreed were excluded.

To analyze the reflectance spectra, the diffusive background was removed using the exponential model approach, the single scattering component was analyzed using equation (4.29), and the nuclear size distributions were obtained for each tissue site. These size distributions were then used to calculate two statistics characterizing nuclear enlargement and cell crowding, namely percentage of enlarged (larger than 10 μm) nuclei and nuclear population (surface) density.

For prospective evaluation, a single classification criterion was established based on un-blinded analysis of an initial "modeling set" of eight samples and consultation with the study pathologists. A site was classified as dysplasia if more than 30% of the nuclei were enlarged, with "enlarged" defined as exceeding a 10 μm threshold diameter, and classified as non-dysplasia otherwise. Using this criterion, all subsequent samples were prospectively analyzed, employing both the consensus and average pathology diagnoses as comparison standards, with dysplasia defined as LGD or HGD, and non-dysplasia defined as NDB or IND.

Having established this, multivariate logistic regression [Kleinbaum et al., 1998] was employed to evaluate the use of two LSS-derived parameters, percentage of enlarged nuclei and nuclear population density, to classify dysplasia. In this part of the analysis the four histologic grades were combined into dichotomous (negative/positive) groups. Three such groups were formed, based on the following histological thresholds: [NDB/(IND or LGD or HGD); (NDB or IND)/(LGD or HGD); and (NBD or IND or LGD)/HGD]. For each dichotomous group, the two parameters were used to construct a binary decision graph, with nuclear population density plotted on the ordinate and percentage of large nuclei plotted on the abscissa. Every site in the study set can be assigned to a point on this graph. For each group, the decision threshold was determined from the logistic regression coefficients, using the probability threshold defined above.

The inter-observer variability between each pathologist and the average diagnosis of the other three pathologists, and between LSS and the mean pathology score (of all four pathologists), were then calculated using the Kappa statistic. Both the average and consensus diagnoses were used as comparison standards. For the consensus diagnosis, only samples for which a consensus was

175

reached were considered. The pathologic diagnoses, as determined by the average and consensus methods, are listed in Table 6.1.

Table 6.1. Summary of histologic diagnoses of study set.

Histologic diagnosis	Average method # of samples (%)	Consensus method * # of samples (%)
Non-dysplastic Barrett's	52 (68)	52 (85)
Indefinite for dysplasia	12 (16)	2 (3)
Low grade dysplasia	8 (11)	6 (10)
High grade dysplasia	4 (5)	1 (2)

* For 15 of the samples there was no consensus among three pathologists.

Figure 6.4 plots the population density and percentage of enlarged nuclei, as measured by LSS for each of the 76 samples in the study set, using the 10 microns as the threshold diameter for "enlarged". The average histological diagnosis for each sample is also indicated. As can be seen, non-dysplastic samples tend to cluster at low values of nuclear enlargement and population density whereas the samples diagnosed as high grade dysplasia exhibit the largest values of both. The mean values of enlarged nuclei measured for non dysplastic, indefinite, low grade and high grade dysplasia were 6%, 28%, 41% and 53%, respectively (p < 0.001 for trend).

The 8 samples of the modeling set were removed from the overall study set, and the remaining 68 samples (validation set) were then prospectively classified using the criterion that at least 30% of the nuclei be larger than 10

176
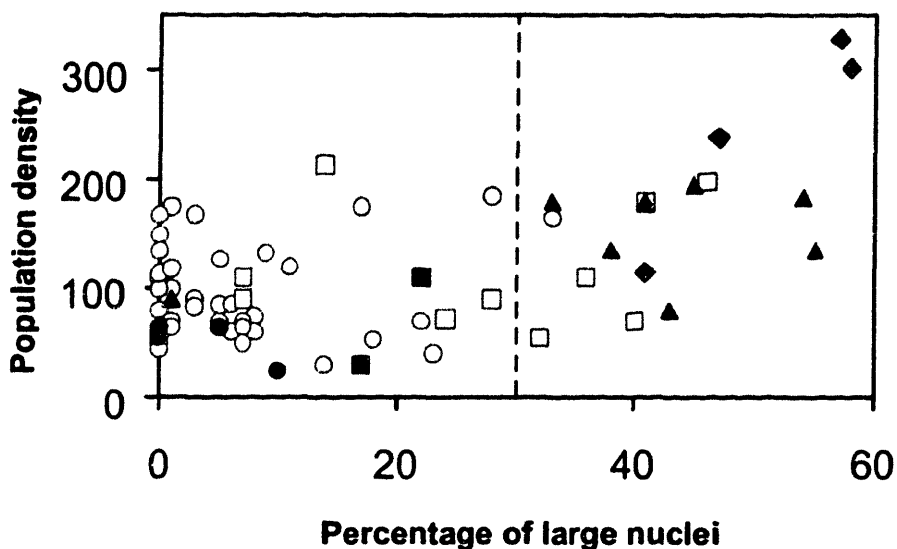
Figure 6.4. Percentage of enlarged (≥10 microns) nuclei and nuclear population density (number of nuclei per 100 square microns), as determined by LSS, for each of the 76 biopsy sites of the study set. The average histological diagnoses are indicated: NDB-circles; IND-squares; LGD-triangles; HGD-diamonds. The filled symbols denote samples diagnosed as dysplasia. The shaded symbols denote the 8 samples of the modeling set. The dashed line indicates the dysplasia/non dysplasia threshold used in the prospective evaluation.

microns (dashed line in Fig. 6.4). The sensitivity and specificity of the resulting LSS diagnoses were 90% and 90%, respectively, with the average histological diagnoses used as the standard, and 83% and 96%, respectively, with the consensus diagnoses used (Table 6.2).

After the prospective double-blinded analysis was completed, a retrospective analysis was initiated. All 76 samples were analyzed based on the average diagnoses. Multivariate logistic regression was used to determine the optimal thresholds for diagnosing dysplasia based on nuclear population density and percent of enlarged nuclei. The sensitivity and specificity of LSS to classify

177

	Sensitivity	Specificity
Compared to average histologic diagnoses	90%	90%
Compared to consensus histologic diagnoses	83%	96%

Table 6.2. Sensitivity and specificity of the 68 sites prospectively evaluated by LSS in distinguishing samples diagnosed as non dysplastic and indefinite from those classified as low grade and high grade dysplasia.

Histologic Comparison	Sensitivity	Specificity
NDB vs. IND, LGD, HGD	88%	89%
NDB, IND vs. LGD, HGD	92%	97%
NDB, IND, LGD vs. HGD	100%	86%

Table 6.3. Sensitivity and specificity of multivariate LSS model at three different histologic thresholds.

the three dichotomous groups are given in Table 6.3. The binary decision graphs and decision lines for each group are shown in Fig. 6.5. Multivariate analysis improved the sensitivity and specificity for identifying dysplastic sites based on the average diagnoses [(NDB or IND)/(LGD or HGD)] from 90% and 90% to 92% and 97%, respectively.
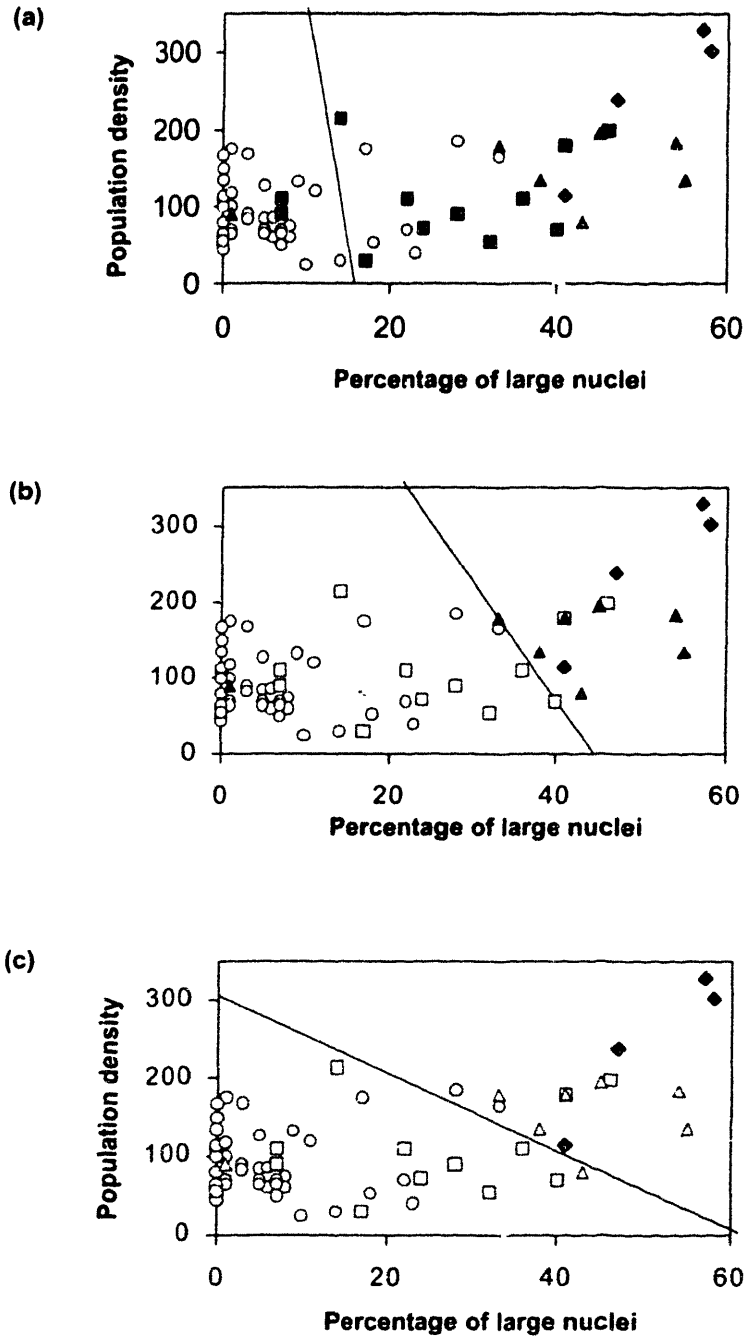
Figure 6.5. Binary decision graphs for the dichotomous groups representing the three histological thresholds. (a) NDB vs. (IND, LGD, HGD); (b) (NDB, IND) vs. (LGD, HGD); (c) (NDB, IND, LGD) vs. HGD. The decision thresholds, determined by logistic regression, are also shown. Key: NDB-circles; IND-squares; LGD-triangles; HGD-diamonds. For each graph the filled symbols denote the group with the higher grades of dysplasia.

179

	Kappa	% Agreement
Pathologist 1 vs. colleagues	0.31	66%
Pathologist 2 vs. colleagues	0.22	62%
Pathologist 3 vs. colleagues	0.34	65%
Pathologist 4 vs. colleagues	0.37	65%
Spectroscopy vs. Pathology, average diagnoses	0.57	80%
Spectroscopy vs Pathology consensus diagnoses	0.63	90%

Table 6.4. Inter-observer agreement between individual pathologists and the averag diagnosis of the three other pathologists, and between the multivariate LSS model an the average diagnosis of all four pathologists.

LSS reliably categorized tissue sites into the four histologic categories (NDB, IND, LGD, HGD). The inter-observer agreement between LSS and the average and consensus pathologic diagnoses, and between the individual pathologists and the average diagnosis of their three colleagues, is given in Table 6.4. The Kappa score showed poor agreement between individual pathologists and the average of their colleagues, and much better agreement between LSS and the average and consensus diagnosis of the four pathologists.

In conclusion, we must point out that LSS provides only a few pieces of diagnostic information. Other optical techniques such as intrinsic fluorescence spectroscopy (IFS) and diffuse reflectance spectroscopy (DRS) can provide valuable diagnostic information as well, which is complementary to that of LSS.

For example, IFS is well suited to study chemical changes in the tissue, i.e. NADH/NAD shift. DRS is a powerful tool to probe blood supply and oxygen saturation of the mucosal and submucosal tissues. Therefore, it is combination of these techniques (called tri-model spectroscopy: TMS) that can potentially provide the most complete and most diagnostically significant information. For example, recent studies of dysplasia in Barrett's esophagus and the uterine cervix have shown that TMS is more sensitive and specific than LSS alone [Georgakoudi et al., 2001].

References

Antonioli D. The esophagus. In: Henson D, Alobores-Saavdera J, eds. *The pathology of incipient neoplasia*. (Philadelphia: WB Saunders, 1993).

Backman V, "Reflectance Spectroscopy for Diagnosis of Precancerous Changes in Human Epithalium", M.S. Thesis, Massachusetts Institute of Technology (1998).

Backman V, Gurjar R, Badizadegan K, Zonios G, Itzkan I, Dasari RR, Crawford JM, Van Dam J, Perelman LT and Feld MS, "Light Scattering Spectroscopy for Early Cancer Diagnosis", *Laser Spectroscopy*, World Scientific Publishing Co., Rainer Blatt *et al.* ed., 286-295 (1999).

Backman V, Gurjar R, Badizadegan K, Itzkan I, Dasari R, Perelman LT, Feld MS, "Polarized light scattering spectroscopy for quantitative measurement of epithelial structures in situ", *IEEE J. Sel. Topics Quantum Electron*, 5, 1019-1027 (1999).

Backman V, Wallace MB, Perelman LT, Arendt JT, Gurjar R, Muller MG, Zhang Q, G. Zonios G, Kline E, McGillican T, Shapshay S, Valdez T, Van Dam J, Badizadegan K, Crawford JM, Fitzmaurice M, Kabani S, Levin HS, Seiler M, Dasari RR, Itzkan I and Feld MS, "Light scattering spectroscopy: a new technique for clinical diagnosis of precancerous and cancerous changes in human epithelia", *Nature*, 406, 35-36 (2000).

Backman V, L.T. Perelman, J.T. Arendt, R. Gurjar, M.G. Muller, Q. Zhang, G. Zonios, E. Kline, T. McGillican, T. Valdez, J. Van Dam, M. Wallace, K. Badizadegan, J.M. Crawford, M. Fitzmaurice, S. Kabani, H.S. Levin, M. Seiler, R.R.Dasari, I. Itzkan, and M. S. Feld, "Light Scattering Spectroscopy: A New Technique for Clinical Diagnosis of Precancerous And Cancerous Changes in Human Epithelia", *Lasers in Life Sciences*, in press (2001).

Barnoon S, Wolfe H. *Measuring the effectiveness of medical decsions: An operations research approach*. (Springfield, Ill: Charles C. Thomas, 1972).

Blot W, Devesa SS, Kneller R, Fraumeni J. "Rising incidence of adenocarcinoma of the esophagus and gastric cardia", *JAMA*, **265**,1287-89 (1991).

Boone C.W. *et al.* Quantitative grading of rat esophageal carcinogenesis using computer-assisted image tile analysis. *Cancer Epidemiology. Biomarkers & Prevention*, **9**, 495-500 (2000).

Brennan JF, Zonios GI, Wang TD, Rava RP, Hayes GB, Dasari RR and Feld MS. *Appl. Spectr.*, **47**, 2081 (1993).

Cotran RS, Robbins SL, Kumar V, *Robbins Pathological Basis of Disease* (W.B. Saunders Company, Philadelphia, 1994).

Fawcett DW, *A Textbook of Histology*, (Charman & Hall, New York, 1994).

Georgakoudi I, Jacobson BC, Backman V, Wallace M, Muller M, Zhuang Q, Badizadegan K, Sun D, Thomas G, Van Dam V, Feld MS, "The Combination of Fluorescence, Diffuse Reflectance, and Light Scattering Spectroscopy for the Improved Detection of Low- and High-grade Dysplasia in Patients with Barrett's Esophagus ", *Gastrointerology*, in press (2001).

Georgakoudi I, Sheets EE, Müller MG, Backman V, Crum CP, Badizadegan K, Dasari RR, Feld MS, "Tri-Modal Spectroscopy as a Tool for the Detection and Biochemical/Morphological Characterization of Cervical Pre-Cancers *In Vivo*", *Obstet. Gynecol.*, submitted (2001).

Gurjar R, Backman V, Badizadegan K, Dasari R, Itzkan I, Perelman LT, Feld MS, "Functional Imaging of Human Epithelia with Polarized Light Scattering Spectroscopy", *Nature Medicine*, to be published (2001).

Haggitt RC. "Barrett's esophagus, dysplasia, and adenocarcinoma". *Hum Pathol*. 25:982-93 (1994).

Hiatt LD, *Color Atlas of Histology*, (Williams & Wilkins, Baltimor, 1994).

Ishimaru A, *Wave propagation and scattering in random media* (McGill, New York, 1978).

Kleinbaum DG, Kupper LL, Muller KE, Nizam A. *Applied Regression Analysis and Other Multivariable Methods*, (3rd edition, Pacific Grove, CA: Duxbury Press, 1998).

Landis J, Koch G. "The measurement of observer agreement for categorical data". *Biometrics*, 33:159-74 (1977).

Landis SH, Murray T, Bolden S, Wingo PA, "Cancer Statistics 1999", CA – A Cancer Journal for Clinicians, 49, 8-31 (1999).

Lerut T, Coosemans W, Van Raemdonck D, et al. "Surgical treatment of Barrett's carcinoma. Correlations between morphologic findings and prognosis", *J Thorac Cardiovasc Surg*, 107:1059-65 (1994).

Mantel N, Haenzel W. "Statistical aspects of the analysis of data from retrospective studies of disease". *J Natl Cancer Inst*, 22:719-48 (1959).

Newton RG, *Scattering Theory of Waves and Particles* (McGraw-Hill Book Company, New York, 1969).

Perelman LT, Backman V, Wallace MB, Zonios G, Manoharan R, Nusrat A, Shields S, Seiler M, Lima C, Hamano T, Itzkan I, Van Dam J, Crawford JM and Feld MS, "Observation of periodic fine structure in reflectance from biological tissue: a new technique for measuring nuclear size distribution", *Phys. Rev. Lett.*, 80, 627-630 (1998).

Peters JH, Clark GW, Ireland AP, Chandrasoma P, Smyrk TC, DeMeester TR. "Outcome of adenocarcinoma arising in Barrett's esophagus in endoscopically surveyed and nonsurveyed patients", *J Thorac Cardiovasc Surg*, 108:813-21 (1994).

Petras RE, Sivak MV, Rice TW. "Barrett's esophagus. A review of the pathologists role in diagnosis and management", *Pathol Annual*, 26:1-32 (1991).

184

Reid BJ, Haggitt RC, Rubin CE, "Observer Variation in the Diagnosis of Dysplasia in Barrett's Esophagus", *Hum. Pathol.*, **19**, 166-178 (1988).

Riddell R, Goldman H, Ransohoff D, Appelman HD, Fenoglio CM, Haggitt RC, Ahren C, Correa P, Hamilton SR, Morson BC, Sommers SC, Yardley JH, "Dysplasia in Inflammatory Bowel-Disease. Standardized classification with provisional clinical applications", *Human Pathology*, 14, 931-968 (1983).

Streitz JM, Jr., Andrews CW, Jr., Ellis FH, Jr. "Endoscopic surveillance of Barrett's esophagus. Does it help?" *J Thorac Cardiovasc Surg*, **105**:383-7 (1993).

Wallace MB, Perelman LT, Backman V, Crawford JM, Fitzmaurice M, Seiler M, Badizadegan K, Shields SJ, Itzkan I, Dasari RR, Van Dam J, Feld MS, "Endoscopic detection of dysplasia in patients with Barrett's esophagus using light-scattering spectroscopy", *Gastroenterology*, 119, 677-682 (2000).

Chapter 7

Biomedical Imaging with Light Scattering Spectroscopy

In the previous chapters we have established that LSS can provide quantitative, objective measurement of cell nuclear morphology without the need for tissue removal. Up to now, this technique has been restricted to sampling of the millimeter-size regions of *in vivo* or *ex vivo* tissues using either a contact probe (LSS with unpolarized light, see section 5.1 and chapter 6) [Perelman et al., 1998; Backman et al., 2000] or an open-air white light delivery system (LSS with polarized light, see section 5.2) [Backman et al., 1999]. In this chapter we discuss an LSS-based imaging technique, which employs both polarization and spectroscopic differences in the intensity of light elastically scattered by tissue components [Gurjar et al., 2001]. In contrast to conventional images of cells or tissues, LSS-based imaging provides quantitative images of the histological

properties, such as cell nuclear enlargement, pleomorphism, and increased chromatin content of the nuclei, which are some of the most important diagnostic criteria used by pathologists to diagnose dysplasia and cancer [Cotran et al., 1994; Boone et al., 2000]. Methods for providing such quantitative, functional[1] information without tissue removal are not currently available. The technique can be used for non-invasive or minimally invasive detection of precancerous changes in a variety of organs, such as the uterine cervix, colon, and oral cavity.

LSS imaging is based on the same principles as LSS with polarized light discussed in section 5.2 [Backman et al., 1999]. The angular and wavelength distributions of the light scattered by a cell organelle such as the nucleus depends on its size and refractive index [Newton, 1969]. Thus, if light backscattered by the cell is observed, sizes and refractive indexes of intracellular structures can be obtained from the spectral variations of the signal. However, single scattering events cannot be measured directly in biological tissue. The total signal scattered back from a tissue specimen can be divided into two parts: the single scattering signal component, and the background due to multiply scattered light (diffusive background).

To analyze the single scattered component, one needs first to separate it from the diffusive background. LSS imaging uses polarization discrimination to achieve this. Removal of the diffusive background using polarized light is discussed in detail in section 5.2. The method is based on the fact that initially polarized light loses its polarization when traversing a turbid medium such as a biological tissue [Sankaran et al., 1999]. A small portion of the linearly polarized

---

[1] Because LSS images do not provide direct measure of a functional state of the tissue, term "functional" can only be used in its extended context. For example, LSS imaging provides

light illuminating the tissue is backscattered by the epithelial cells. The rest of the signal diffuses into the underlying tissue and is depolarized by means of multiple scattering. In contrast, the polarization of the light scattered backward after a single scattering event is preserved [Newton, 1969]. Thus, by subtracting off the unpolarized component of the reflected light, the contribution due to the backscattering from epithelial cell nuclei can be readily distinguished. The resulting spectrum can then be analyzed to extract the size distribution of the nuclei, their population density, and their refractive index relative to that of the cytoplasm [Backman et al., 1999]. The nuclear refractive index is higher due to the presence of chromatin, and so the chromatin content can be obtained from the refractive index [Davies et al., 1957]. As discussed below, the resolution provided by LSS far exceeds the pixel size of an imaging CCD and the wavelength of light used to measure the sizes of cell nuclei, in contrast to conventional optical techniques.

7.1 LSS Imaging Device

We have developed a prototype of a clinical LSS imaging instrument [Gurjar et al., 2001]. This lab-based device allows mapping morphological properties of epithelia of *ex vivo* tissue. Figure 7.1 shows the set-up for LSS-based imaging. A 75 W xenon arc lamp (Oriel, Inc.) illuminates the sample that can be a living tissue, a cell monolayer or a physical tissue model. The light from the lamp is collimated (see below), polarized using polarizer P1 and transmitted through one of the 11 narrow-band (4 nm) filters (Edmund Scientific, Inc.) to

---

information about chromatin content of the cell nuclei. This parameter is "functional" in a sense that chromatin content relates to the functional state of the cell.
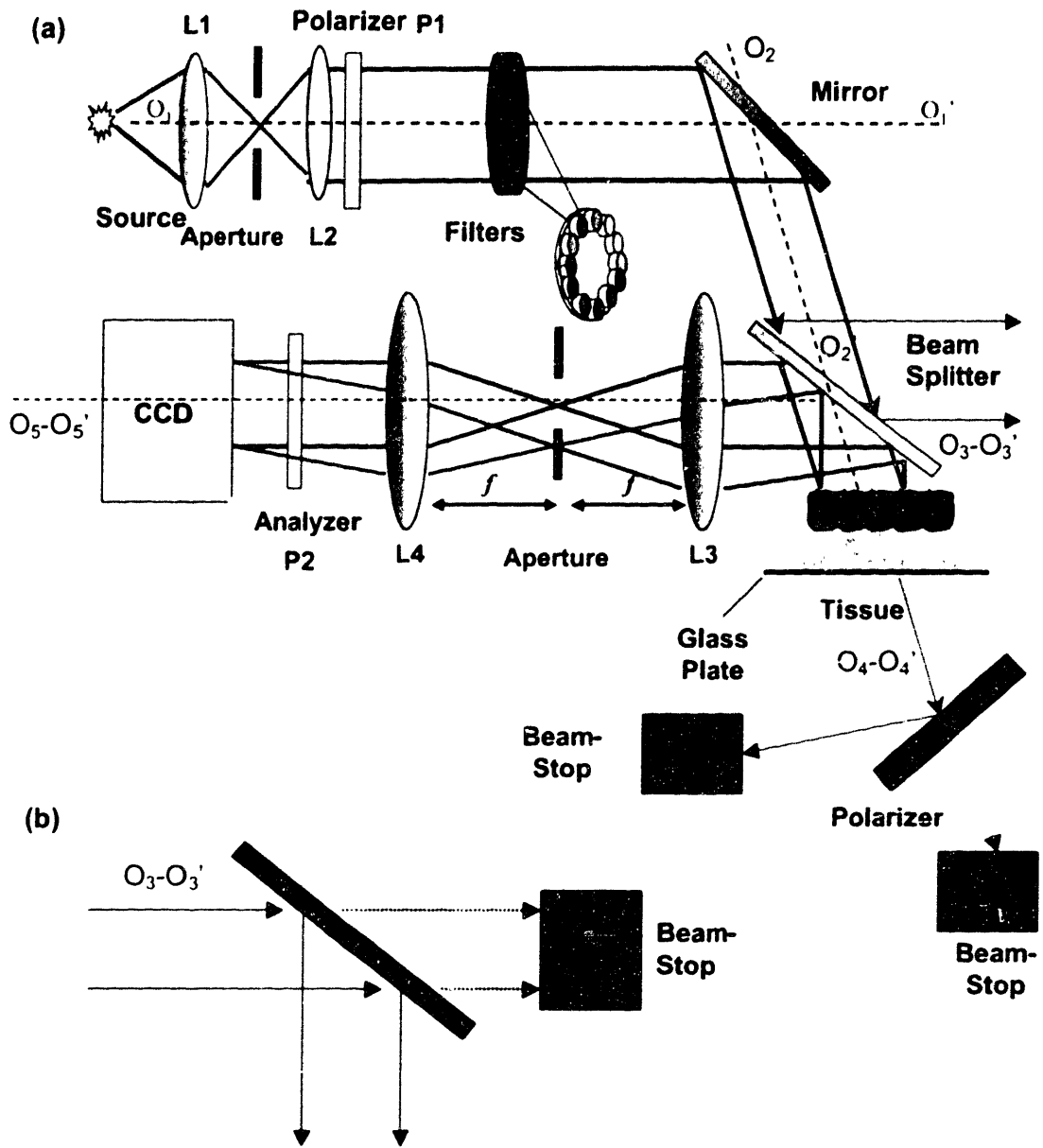
Figure 7.1 Schematic diagram of the LSS imaging set-up. (b) View from the top of the part of the device used to eliminate spurious beam O_1-O_1'

select the desired wavelength, λ_i i=1,...,11, in the range from 450 to 700 nm (457, 470, 488, 532, 550, 568, 589, 620, 650, 671 and 694 nm).

The delivery arm of the device is designed to achieve two goals: 1) to deliver a beam collimated as possible and 2) to illuminate a wide area of tissue. According to a fundamental law of optics, the product of the solid angle of divergence of a light beam, Ω, and the area illuminated by this beam, S, is constant throughout any optical system, provided that no photon leaves the system [Born et al., 1965]:

$$\Omega S = const. \tag{7.1}$$

It can easily be shown that this rule is related to the energy conservation law. Equation (7.1) indicates that no system of lenses or other non-active optical components enables to achieve both the desired degree of collimation and desired area of illumination. Therefore, some photons must be taken away from the system in order to achieve the desired characteristics of the beam. This can usually be achieved by means of using apertures that are used as filters. To collimate the incident beam we employed a pair of equifocal achromatic lenses (L1 and L2) (Edmund Scientific, Inc.) and an aperture. This 4f-system is an important part of the LSS imaging system [Born et al., 1965].

Figure 7.2 illustrates the propagation of a non-collimated light beam through a 4f-system. Consider planes PL1, PL2, and PL3. The distance between plane PL1 and lens L1 equals the focal length, f, of lens L1. The distance between plane PL2 and each of lenses L1 and L2 is f. Finally, the distance between PL3 and the outer lens L2 is f again. Because the incident light is not perfectly collimated, light passing through plane PL1 is distributed in angle. According to the laws of

190
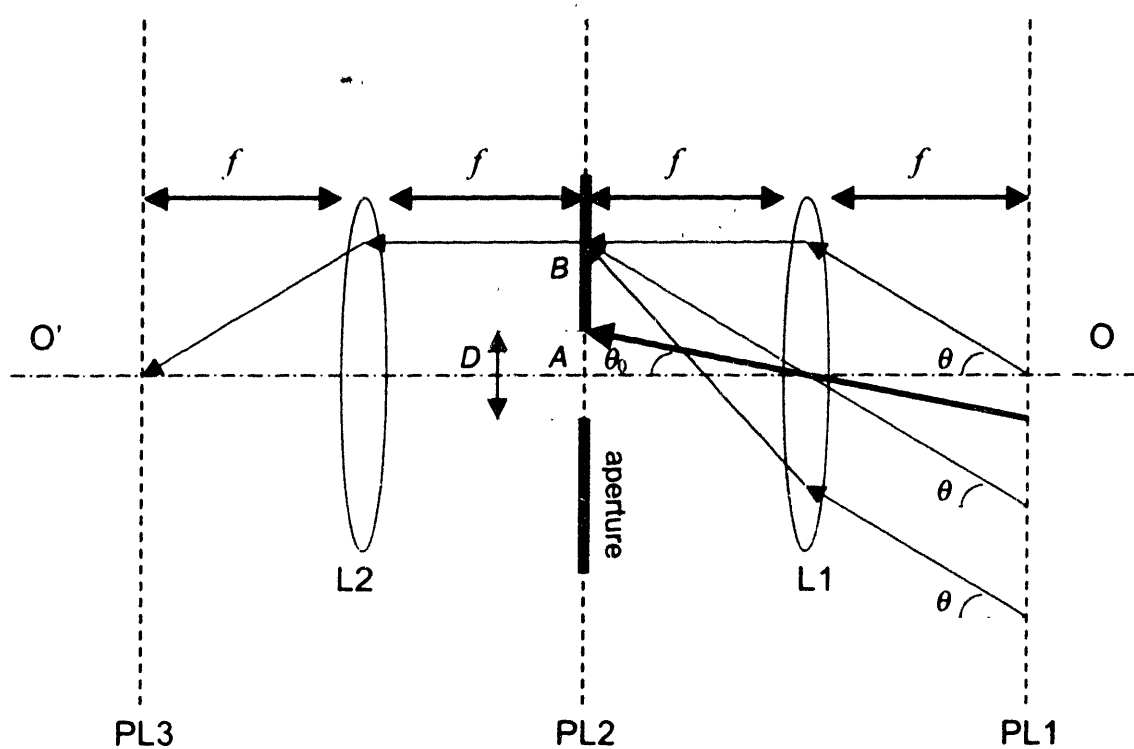
Figure 7.2 Schematic diagram illustrating the principles of 4f-system. See text for details.

optics, lens L1 projects this angular distribution onto plane PL2. Photons that travel parallel to the major axis of the lens system (O-O') cross plane PL2 at point A that is on the intersection of O-O' and PL2. On the other hand, light rays that propagate along a direction forming an angle θ with axis O-O' are focused to point B, with distance $|AB| = f \tan(\theta)$. Thus, the larger angle θ of the light ray, the larger the distance between A and the focal point for this ray on plane PL2.

Lens L2 performs a transform that is inverse to one provided by lens L1. It projects a real image of plane PL1 onto plane PL3. If all photons reaching plane

PL2 are allowed to pass through lens L2, the spatial and angular image on PL3 is exactly the same as one on PL1. However, if an aperture is used in plane PL2, only rays with selected angles θ are allowed to reach lens L2. For example, if the aperture is positioned in the center of the system, it filters out all photons that travel along directions with $\theta > \theta_0$, where $\theta_0 = \arctan\left(\dfrac{D}{2f}\right)$ and D is the diameter of the aperture. Therefore, light passing trough this system is collimated within angle θ_0. In our system, the focal length of lens L1 was 210 mm and the diameter of the aperture was 0.51 mm. This ensured that the beam delivered to the sample has divergence no more than 0.07°.

This collimated beam passes through a mirror and a 50/50-beamsplitter and illuminates an area of ~5 cm^2. The beamsplitter divides the incident light into two beams of similar intensity. The first beam (O_2-O_2' in fig. 7.1) passes straight through the beamsplitter and illuminates the tissue. The other beam (O_3-O_3') is a spurious reflection from the beamsplitter and must be eliminated. To accomplish this, we used a polarizer diverting this beam away from the system, which was oriented to minimize the transmission through the polarizer (see fig. 7.1(b)). Some portion of beam O_3-O_3' is still transmitted through and is absorbed by a beam-stop (Newport, Inc.). We found that this scheme is the most effective means to reduce the impact of beam O_3-O_3' to the signal detected by the device.

Now let us discuss what happens with beam O_2-O_2'. A portion of this beam is backscattered by the sample, is reflected by the beamsplitter and goes to the collection arm of the device (O_5-O_5'). However, if the sample does not reflect all of the incident light back, a portion of light transmitted through the sample (O_4-O_4') might eventually be reflected from the surface of the optical table and influence the signal measured by the device. Therefore, this beam must be

eliminated. This is accomplished by means of a combination of a polarizer and a beam-stop similar to those used to eliminate beam O_3-O_3'. This ensures that the signal collected by the device is the result of backscattering of beam O_2-O_2' by the sample (beam O_5-O_5' in Fig. 7.1).

A 4f-system is used to collect and filter backscattered light O_5-O_5'. It consists of a pair of equifocal achromatic lenses (L3 and L4) separated by twice their focal length. An aperture positioned at the center of this lens system ensures that the CCD detector (Princeton Instruments, Inc.), placed one focal length away from the outer lens, collects only light scattered in a solid angle corresponding to a half angle of 0.2°. The collection angle can easily be changed during the experiments by opening or closing the aperture. Moreover, by moving the aperture away from the major axis of the lens system or changing its shape, one can select a desired collection geometry.

The CCD collects 1:1 images of the illuminated surface. The CCD detector consists of a 512 x 512 pixel array, with each pixel having dimensions 25 μm x 25 μm. Before reaching the detector, light passes through an analyzing polarizer P2, which can be rotated to select the polarization state of the backscattered light. When P2 is oriented parallel to polarizer P1, only backscattered light polarized along the direction of the incident polarization is collected by the CCD. When P2 is rotated by 90°, the CCD collects light that is backscattered by the sample and is polarized orthogonally to the direction of the polarization of the incident light.

The data acquisition is illustrated in Fig. 7.3. For each of the eleven illumination wavelengths, the CCD collects two images. The first image, $I(\lambda, x, y)$, with (x, y) pixel coordinates and wavelength λ, is taken with the analyzer P2 oriented to collect backscattered light that is polarized along the polarization
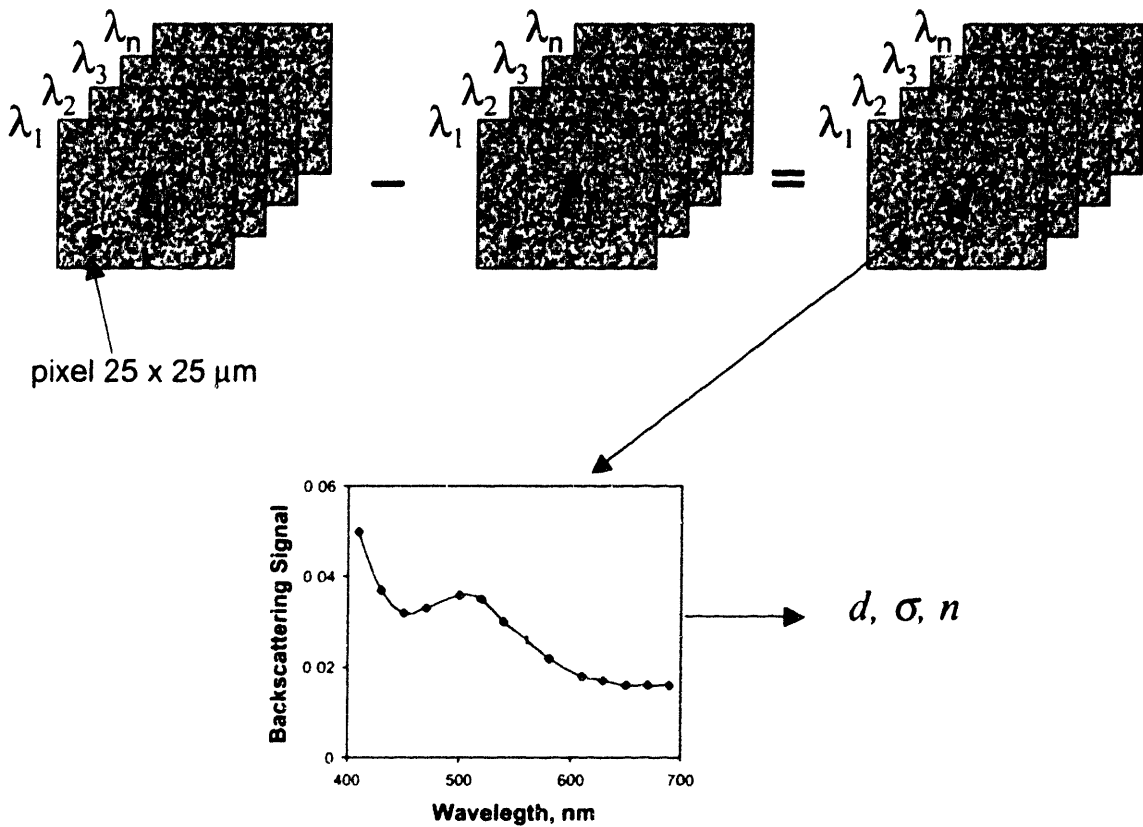
Figure 7.3 Schematic diagram illustrating the principles of LSS imaging. See text for details.

direction of the incident light. The second image, $I_\perp(\lambda,x,y)$, is taken with the analyzer oriented to collect the orthogonally polarized component. To correct for varying responses of different pixels and non-uniformities in wavelength response, the images are normalized using a highly diffusive and reflective white standard (Ocean Optics, Inc), which scatters incident light izotropically and uniformly across the visible wavelength range. We then subtract $I_\perp(\lambda,x,y)$ from $I_\parallel(\lambda,x,y)$ to

remove the contribution from the unpolarized diffusive background (see section 5.2 and 7.3 below).

This procedure results in image $\Delta I(\lambda_i,x,y) = I_\parallel(\lambda_i,x,y) - I_\perp(\lambda_i,x,y)$ constituted almost entirely from single scattered photons, which, for most epithelial tissues, corresponds to a sampling depth of 30-50 μm [Backman et al., 1999]. To compensate for the cross talk between neighboring pixels, we constructed new images for each wavelength, in which the intensity of any pixel is a weighted average of the values $\Delta I(\lambda_i,x,y)$ of the adjacent pixels from the original image [Russ, 1992]. The principles of LSS imaging are further illustrated in the experiments with physical models and *ex vivo* tissues discuss below.

7.2 Calibration of LSS Imaging Device

We performed three series of experiments with LSS imaging device: 1) experiments with physical tissue models; 2) experiments with cell monolayers; and 3) experiments with *ex vivo* tissues. Studies with physical models were conducted to calibrate the experimental setup and estimate the accuracy of the measurements. The first set of experiments employed an optically thin layer of polystyrene beads (optical depth $\tau=0.3$) of mean diameter $d=4.5$ μm and standard deviation of diameters $\sigma=0.03$ μm in a glycol solution. Eleven images with parallel orientation, $I_\parallel(\lambda,x,y)$, and eleven images with orthogonal orientation $I_\perp(\lambda,x,y)$, were obtained for each of the wavelengths: 457, 470, 488, 532, 550, 568, 589, 620, 650, 671 and 694 nm. Single scattering images $\Delta I(\lambda,x,y)=I_\parallel(\lambda,x,y)-I_\perp(\lambda,x,y)$ were computed at each wavelengths. In these experiments, $I_\parallel(\lambda,x,y)>>I_\perp(\lambda,x,y)$ for the points of illumination. To compensate for the movement of the beads during the
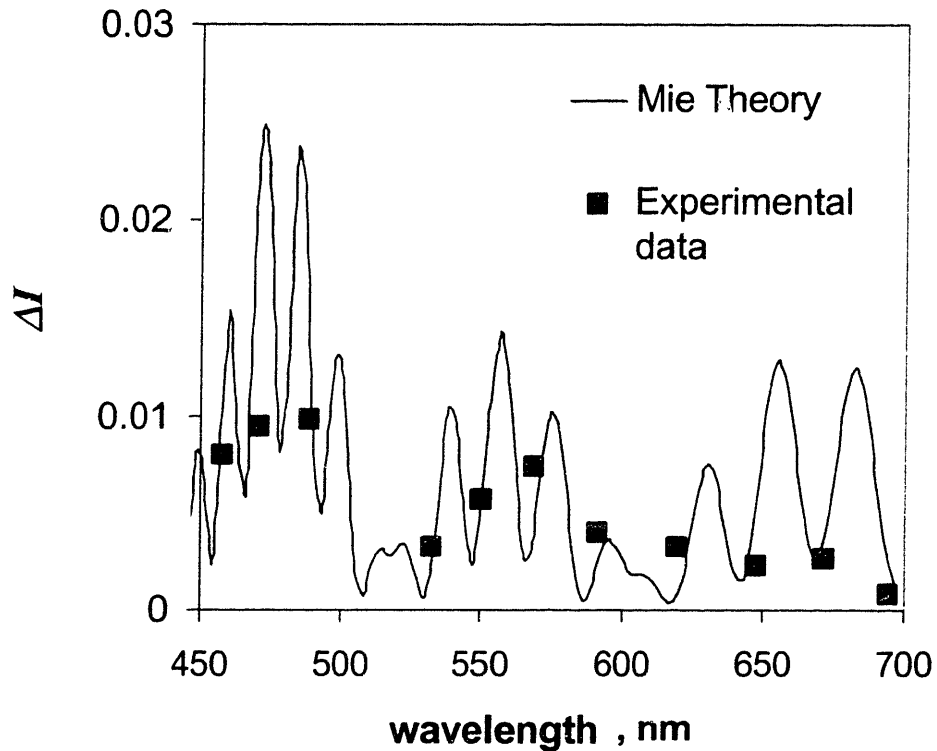
Figure 7.4 Comparison of the backscattering signal from 4.54 micron polystyrene beads in polyethylene glycol predicted by the Mie theory and signal measured experimentally using LSS device.

measurements due to Brownian motion, new polarized images, $\Delta I^{(b)}(\lambda,x,y)$ were constructed from the original images $\Delta I(\lambda,x,y)$ by binning 5x5 pixels. Each image zone was then 125 μm x 125 μm, and contained about 150 beads on average.

Figure. 7.4 compares the spectrum $\Delta I^{(b)}(\lambda,x,y)$ measured for one of the binned region with the backscattered intensity spectrum calculated using the Mie theory (equation 4.18) with d=4.5 μm and σ=0.03 μm. As can be seen, the experimental values are in good agreement with the theory predictions.

As discussed in the Chapters 4-6, one can obtain the sizes and refractive indexes of the scattering particles near the surface by analyzing the spectral variations of the polarized backscattered light. LSS imaging allows to create spatial images of these quantities over large surface areas. Figure 7.5(a) shows a cross section of three wells containing suspensions of polystyrene microspheres in polyethylene glycol with average diameters of 4.5, 6, and 10 μm respectively. Polyethylene glycol is used to decrease the refractive index of the beads relative to the surrounding medium in order to better simulate the actual refractive index mismatch of cell nuclei in surrounding cytoplasm. The relative refractive index of beads in water is about 1.2, while that of beads in glycol is 1.066, a value closer to the relative refractive indexes of biologically relevant objects which usually vary between 1.02 and 1.10 [Slot et al., 1988; Beauvoit et al., 1994; Beuthan et al., 1996]. The diameter of each well is approximately 2 mm and the depth is about 5mm. The optical thickness τ of the bead suspensions was prepared to be ~0.3. The measurements were performed similar to those discussed above.

The images $\Delta I^{(b)}(\lambda,x,y)$ were analyzed to obtain the bead diameters over the entire field of illumination. The Mie theory was fitted to the spectral curves measured in the experiment based on the algorithm described in section 4.3.2.1 and 5.2.3. The fitting parameters were the average bead diameter, d, the standard deviation of the diameters σ and the relative refractive index $n = \dfrac{n_b}{n_m}$ with n_b the refractive index of the beads and n_m the refractive index of the medium (polyethylene glycol). First, the data-base of the backscattering spectra for various combinations of d, σ, and n calculated using the Mie theory was built. Diameter d was varied from 0.1 μm to 20 μm with increment 0.005 μm. Standard deviation σ was varied from 0.1 μm to 5 μm with 0.005 μm step. Relative refractive index n

197
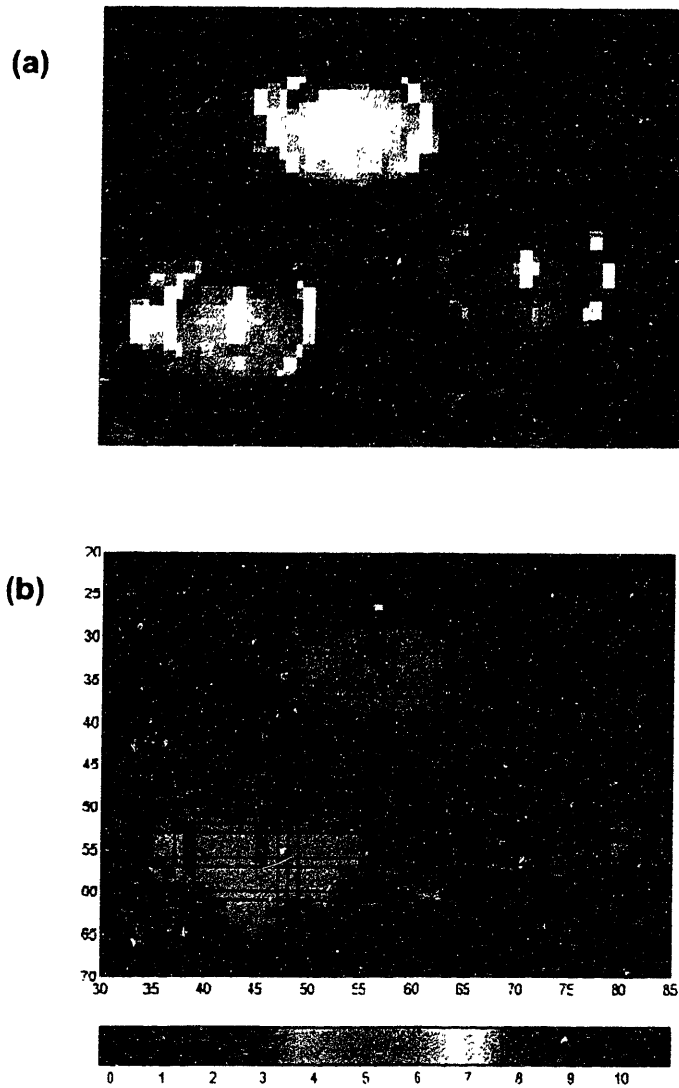
Figure 7.5   LSS imaging of three wells with polystyrene microspheres of different sizes. (a) Photograph of the wells containing microspheres. Bead diameters, from left to right, are 5, 10 and 6 μm repectively. (b) LSS image of of the three wells. Diameter is indicated by the color-bar.

wa

198

s varied from 1.02 to 1.1 with 0.001 step. Then each of the spectra from this database was compared with the spectrum measured with LSS from any given pixel and the values of χ^2 were calculated (see section 4.2.2.1). The parameters d, σ, and n of the Mie spectrum that fitted the data the best (corresponded to the smallest χ^2) were chosen as the optimal parameters. Thus d, σ, and n were obtained for each 125 μm x 125 μm region.

Figure 7.5(b) shows the resulting color-coded map of average diameters. The non-uniformity of the wells' walls gave rise to specular reflections observed as markedly increased intensity of the signal for some of the pixels. Since the specularly reflected signal could not be used to obtain the parameters of the scatterers, the signal from these regions was not analyzed, and such regions are color-coded in black. The resulting image clearly shows the presence of beads of different diameters in corresponding wells. Moreover, we found that the algorithm allows determination of the bead diameters with accuracy approaching 0.01 μm.

7.3 Experiments with Cell Monolayers

The second series of experiments employed cells to model living tissue. The models consisted of two layers. The upper layer of the model simulated epithelium, and consisted of a monolayer of T84 colon tumor cells grown on a glass cover slip. The bottom layer was an optically thick solution of Ba_2SO_4 and hemoglobin simulating diffusive connective tissue beneath the epithelium. Before data collection, a portion of the cell layer was scraped off from the cover slip (Fig. 7.6). The polarized images were then obtained. The imaged field was chosen so that the parts of the cover slip with and without cells were imaged. Figure 7.7
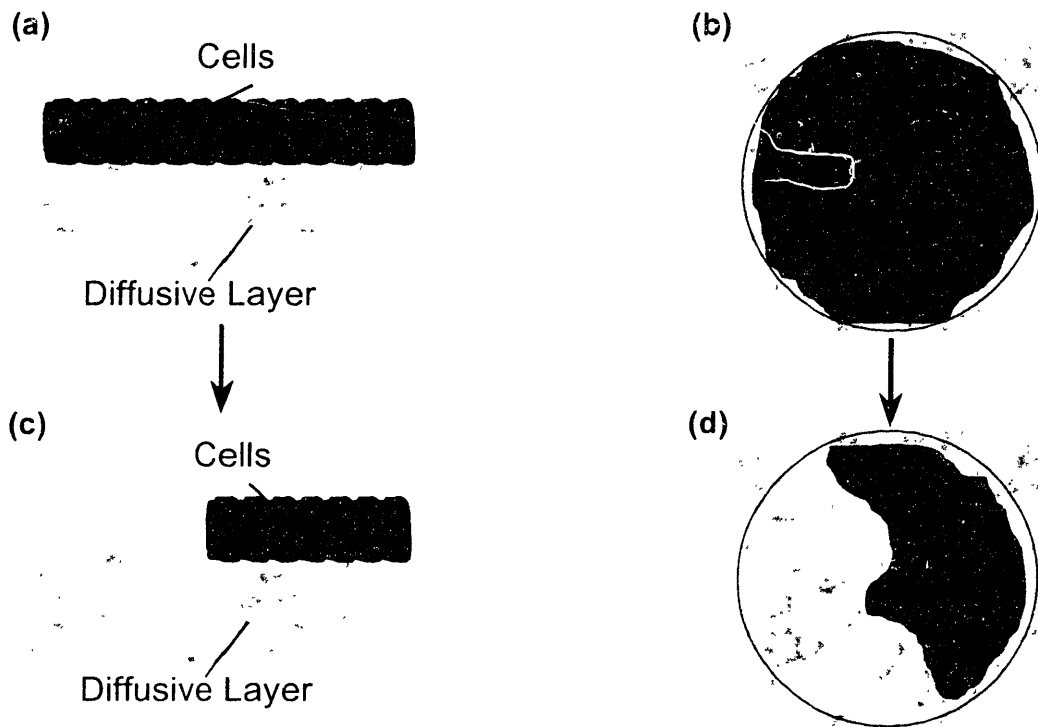
Figure 7.6 Two-layer tissue model with T84 cell monolayer on top of a suspension of Ba_2SO_4 particles and human blood used in LSS imaging studies shown in Fig. 7.7. (a) Original model with intact monolayer of cells as the top layer. (b) View from the top on model (a). (c) Model after a group of cells was removed. (d) View from the top on model (c).

shows three images: (a) $I_{\parallel}(\lambda,x,y)$, (b) $I_{\perp}(\lambda,x,y)$, and (c) $\Delta I(\lambda,x,y)$, with $\lambda=589$ nm. Each image shows an area of 1.28 cm x 1.28 cm. Since cells are quite transparent, it was expected that most of the detected light (from 96% to 99% depending on wavelength) would originate from the second layer. However, this multiply scattered light is depolarized. In contrast, most of the light backscattered by the cells is polarized. Thus, although the cells are not discernable in either $I_{\parallel}(\lambda,x,y)$ or

(a)

$I_{\parallel}$

Cells

No cells

1.3 cm

(b)

$I_{\perp}$

Cells

No cells

(c)

ΔI

Cells

No cells
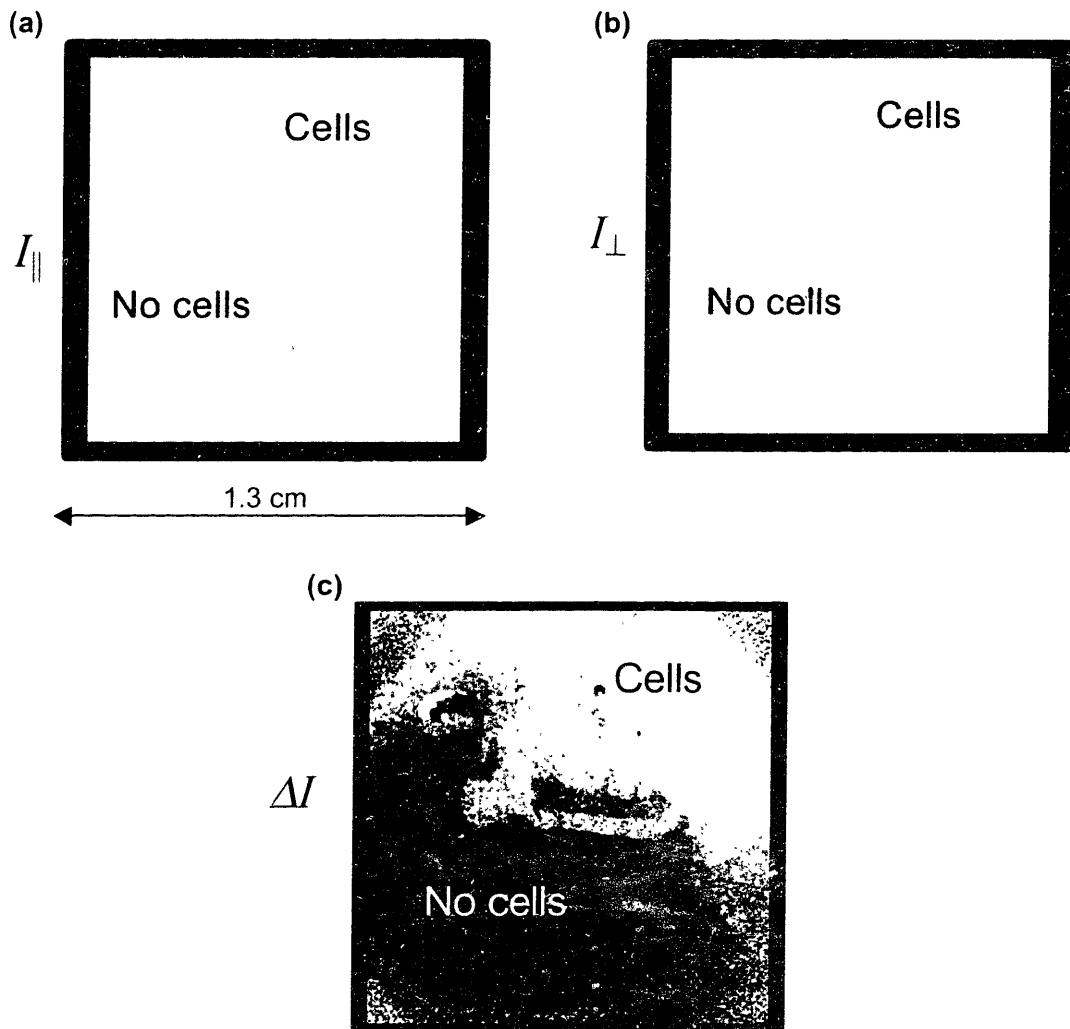
Figure 7.7 LSS imaging of a two-layer tissue model with a monolayer of T84 cells on top of a diffusive layer. Polarized backscattering signal is shown for $\lambda=589$ nm. (a) image I; (b) image $I_{\perp}$; (c) image ΔI. Although the cells are not discernable on images (a) and (b), their backscattering is readily apparent when the the duffisive background us removed using polarization discrimination on image (c).

201

$\Delta I(\lambda;x,y)$ (Fig. 7.7 (c)) as bright areas due to the signal of polarized light backscattered by these cells.

An image collected for a single wavelength, such as one shown in Fig. 7.7(c), is not sufficient to obtain information about the sizes of the cell nuclei or other morphological properties of the cells. To obtain this information, a succession of such images at different wavelengths must be taken, and the spectral curves $\Delta I(\lambda;x,y)$ must be then analyzed for each pixel (x,y). Each pixel has 25 µm x 25 µm area and contains only few nuclei, typically 1 or 2. Some nuclei appear on two adjacent pixels, (x_1,y_1) and (x_2,y_2). Light backscattered by these nuclei contributes to both $\Delta I(\lambda;x_1,y_1)$ and $\Delta I(\lambda;x_2,y_2)$. To compensate for the cross-talk between neighboring pixels, we constructed new images for each wavelength λ, $\Delta I^b(\lambda,\bar{x},\bar{y})$ in which the intensity of any pixel is a weighted average of the values $\Delta I(\lambda;x,y)$ of the adjacent pixels from the original image,

$$\Delta I^{(b)}(\lambda;\bar{x},\bar{y}) = \sum_{i,j=-1,0,1} \Delta I(\lambda;x,y)a_{ij} , \qquad (7.2)$$

with

$$a = \begin{pmatrix} 0.075 & 0.125 & 0.075 \\ 0.125 & 0.2 & 0.125 \\ 0.075 & 0.125 & 0.075 \end{pmatrix}$$

where the indexes i,j =0 refer to the given pixel and i,j = ± 1 to the adjacent pixels. This procedure is known to diminish the effect of the cross-talk [Russ et al., 1992].

T84 cells typically have a wide distribution of sizes and also have large mean diameters, $d >10$ µm. Figure 7.8 (a) shows a microphotograph of a portion
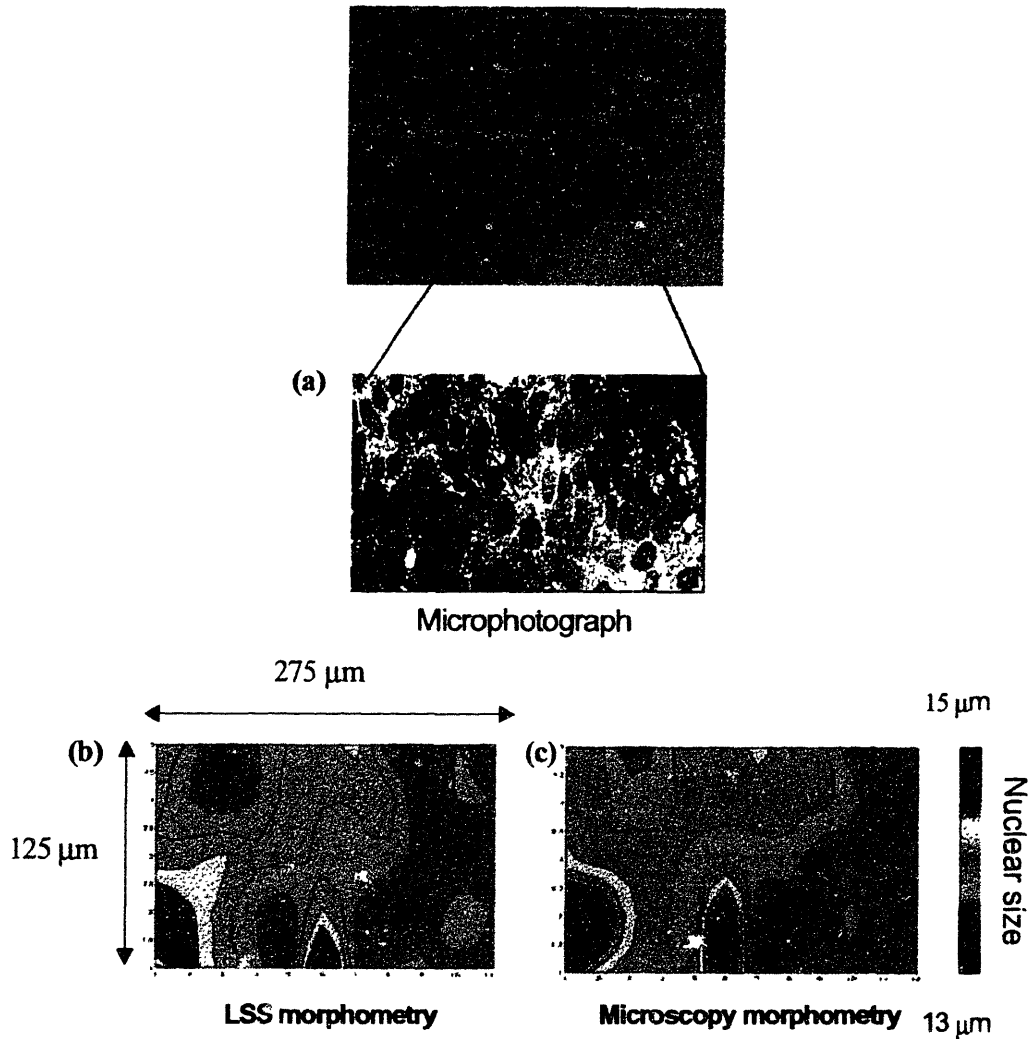
Figure 7.8 LSS imaging of two-layer tissue model with T84 colon tumor cell monolayer on top of a diffusibe background. (a) Micophotographs of the cell monolayer stained with a nuclear stain. (b) Color-coded contour map of nuclear sizes obtained using LSS. (c) Color-coded contour map of nuclear sizes obtained using morphometry on a stained microphotograph (a).

203

of the cell monolayer stained with a nuclear stain that makes otherwise almost transparent cell nuclei appear blue. A part of this microphotograph is further magnified to show a representative 275 μm x 125 μm region (Fig. 7.8 (a)). Color-coded contour plots of the cell nuclear sizes from this region obtained from the analysis of the LSS imaging data and using standard morphometry on the stained monolayer are shown in figs. 7.8 (b) and (c) respectively. The agreement between the spatial distributions of nuclear size in these two images is evident. As c · he seen, the nuclei are smaller (average size $d \approx 13$ μm) in the right field and tend to be larger in the remaining regions (some of these nuclei are as large as 15 μm).

7.4 Measurement of Concentration and Mass of Nuclear Chromatin Using LSS

As can be seen, LSS imaging can elucidate subtle morphological variations such as a difference in nuclear sizes of a fraction of a micron. Furthermore, the analysis allows determination of the refractive index of the nuclei relative to the surrounding cytoplasm. The refractive index of nuclei and many other cell organelles is a linear function of the ratio of the solid mass of an organelle, which is formed by DNA, RNA, and proteins, to its volume [Davies et al., 1957]. A higher concentration of nuclear chromatin (the solid component of the nucleus) results in a deeper staining of these nuclei with nuclear stains, such as H&E. This effect is referred to as hyperchromasia and has been known to correlate with dysplasia and malignancy [Cotran et al., 1994; Boone et al., 2000].

To determine the concentration of nuclear chromatin using LSS one needs to estimate so-called mass ratio η using the following equation [Davies et al., 1957]

$$n_n = n_0 + \alpha\eta ,$$ (7.3)

where n_n is the refractive index of the nucleus measured using LSS, n_0 is the refractive index of water, α is a proportionality coefficient, which was found to be equal 0.18 for most cellular structures including the cell nucleus, major organelles and the cytoplasm, and

$$\eta = \frac{\rho_n}{\rho_0}$$ (7.4)

with ρ_n the mass density of the chromatin measured in mass/volume-units and ρ_0 the mass density of water.

According to equation (7.3), the refractive index of a nucleus equals to that of water when the concentration of chromatin is zero and approaches approximately 1.514 when the nucleus is almost completely filled with proteins, DNA, and RNA. Thus, chromatin density ρ_n can be found as

$$\rho_n = \frac{\rho_0}{\alpha}(n_n - n_0).$$ (7.5)

Let us now estimate the accuracy of such measurements. Generally speaking, if parameters $x_1, x_2, \ldots, x_k$ are measured in an experiment with a standard errors δx_i, $i=1, \ldots, k$, the standard error of estimating the value of $f(x_1, x_2, \ldots, x_k)$ that depends on these parameters is

$$\delta f = \sqrt{\sum_i \left(\frac{\partial f}{\partial x_i}\right)^2 (\delta x_i)^2} . \tag{7.6}$$

Therefore a relative standard error of measuring chromatin density ρ_n is

$$\frac{\delta \rho_n}{\rho_n} = \frac{1}{\rho_n} \sqrt{\left(\frac{\partial \rho_n}{\partial (n_n - n_0)}\right)^2 (\delta(n - n_0))^2} = \frac{\delta(n_n - n_0)}{n_n - n_0}. \tag{7.7}$$

However, LSS does not measure $n_n - n_0$ directly. Rather it allows to determine the relative refractive index $n = \frac{n_n}{n_c}$, where the value of the refractive index of the cytoplasm n_c must be postulated. Fortunately, the refractive indexes of the cytoplasm do not vary as much as those of the organelles. Because

$$n_n - n_0 = n_c n - n_0 = (n_0 + \alpha \eta_c)n - n_0 \tag{7.8}$$

with η_c the mass ratio for the cytoplasm, $\delta(n_n - n_0)$ can be found according to (7.6) as follows

$$\delta(n_n - n_0) = \sqrt{\left(\frac{\partial(n_n - n_0)}{\partial \eta_c}\right)^2 (\delta \eta_c)^2 + \left(\frac{\partial(n_n - n_0)}{\partial n}\right)^2 (\delta n)^2} =$$

$$\alpha \eta_c n \sqrt{\left(\frac{\delta \eta_c}{\eta_c}\right)^2 + \left(\frac{\delta n}{n}\right)^2}. \tag{7.9}$$

Substituting (7.9) into (7.7) we obtain

$$\frac{\delta \rho_n}{\rho_n} = \frac{\alpha \eta_c n}{n_n - n_0} \sqrt{\left(\frac{\delta \eta_c}{\eta_c}\right)^2 + \left(\frac{\delta n}{n}\right)^2}.$$

This standard error should be determined for each measurement, because it depends on n. However, we can get at least some idea for how accurate LSS measurements of ρ_n typically are. The relative standard error $\frac{\delta \eta_c}{\eta_c} \approx 0.2$ [Davies et al., 1957; Davies et al., 1958; Lee et al., 1973; Beauvoit et al., 1994; Beuthan et al., 1996] and $\frac{\delta n}{n} \approx 0.2$. Substituting these typical values into (7.9) and (7.7) we obtain $\frac{\delta \rho_n}{\rho_n} \approx 0.05$. According to LSS studies with cell monolayers, *ex vivo* and *in vivo* tissues, most epithelial cell nuclei have $\rho_n \sim 0.3 - 0.6$ pg/μm^3 and, therefore, $\delta \rho_n \sim 0.015 - 0.03$ pg/μm^3.

Not only does LSS allow measurement of the *concentration* of nuclear chromatin, but it enables to estimate the total *mass* of the chromatin as well. Chromatin mass was shown to correlate with the amount of chromosomal DNA present in the nucleus [Brown et al., 1955; Davies et al., 1958]. Increased amount of DNA is thought to be an indicator of increased DNA transcription and protein synthesis associated with higher proliferative activity of precancerous and cancerous cells [Watson et al., 1991; Cotran et al., 1994]. Currently, the amount of DNA can be measured using ploidy analysis on cells removed from the body. There is no technique that would allow such analysis to be performed *in vivo* or even *in vitro* on living cells. Moreover, ploidy analysis does not provide objective quantitative information so that the amount of DNA from one tissue sample could not be compared with that of another.

For a nucleus of volume V, the chromatin mass can be found as $M_n = V\rho_n$.

Although LSS allows measurement of nuclear diameter d, the volume cannot simply be expressed in terms of d unless certain assumptions about the shape of the nucleus are made. Typical nuclei have shape that resembles sphereoids and are randomly oriented in tissue. Therefore, it is reasonable to estimate nuclear volume as that of a sphere with diameter d,

$$V \approx \frac{4}{3}\pi\left(\frac{d}{2}\right)^3.$$ (7.10)

Thus, the mass of nuclear chromatin

$$M_n \approx \frac{4}{3}\rho_n\pi\left(\frac{d}{2}\right)^3 \approx \frac{4}{3}\left(\frac{d}{2}\right)^3\frac{\pi\rho_0}{\alpha}(n_n - n_0).$$ (7.11)

Determination of chromatin mass using (7.11) is by no means rigorous. However, it can provide some information about how much chromatin a *population* of cell nuclei contains on average. In fact, as shown in [Paramonov, 1994], equation (7.10) is quite accurate, $\frac{\delta V}{V} \leq 0.1$, in estimating the average volume of a population of randomly oriented spheroids with shape parameter[2] not exceeding 2. Epithelial nuclei typically fall into this category: their shape parameter rarely exceeds 2 and they are randomly oriented. Even when there exists certain preferred orientation of the nuclei in respect to the basement membrane[3], in many cases the nuclei are randomly oriented in respect to an externally defined direction,

---

[2] Shape parameter is defined as the ratio of the longer dimension of the spheroid to its smaller dimension.

[3] In many epithelia such orientation does exist.

such as the direction of the propagation of the incident light, due to the folding of the epithelial basal surface.

7.5 LSS Imaging of *Ex Vivo* Tissues

The third set of experiments was performed on *ex vivo* colon tissues. The *ex vivo* colon tissue samples were obtained immediately after resection from patients undergoing colectomy for familial adenomatous polyposis. Colonic adenomas are precancerous dysplastic lesions. Typical adenomas are polypoid structures that can vary in size from less than a millimeter to several centimeters, and are covered by an epithelial layer exhibiting all of the characteristics of dysplastic lesions, including cell nuclear enlargement, pleomorphism and hyperchromasia. The adenomas are surrounded by normal tissue covered by a single layer of epithelial cells. Figure 7.9(a) shows a 2 mm x 2 mm region of resected colon tissue with the adenoma, about 1 mm in diameter, in the center.

We imaged an adenoma surrounded by nondysplastic colon mucosa using the LSS apparatus. Data were taken as in the experiments with cell monolayers. A series of polarized images at different wavelengths were taken, and the spectra were analyzed for each pixel of the imaged field as in the experiments with cell monolayers. The parameters obtained were the mean nuclear size, standard deviation of nuclear sizes, and refractive index of the nuclei in each pixel. The imaged field was 1.3 cm x 1.3 cm. This field was divided in smaller 125 μm x 125 μm regions and the percentage of nuclei larger than 10 μm was obtained for each of these areas. As we discussed in Chapter 6, our previous studies have shown that this statistic, which characterizes the degree of nuclear enlargement, is highly
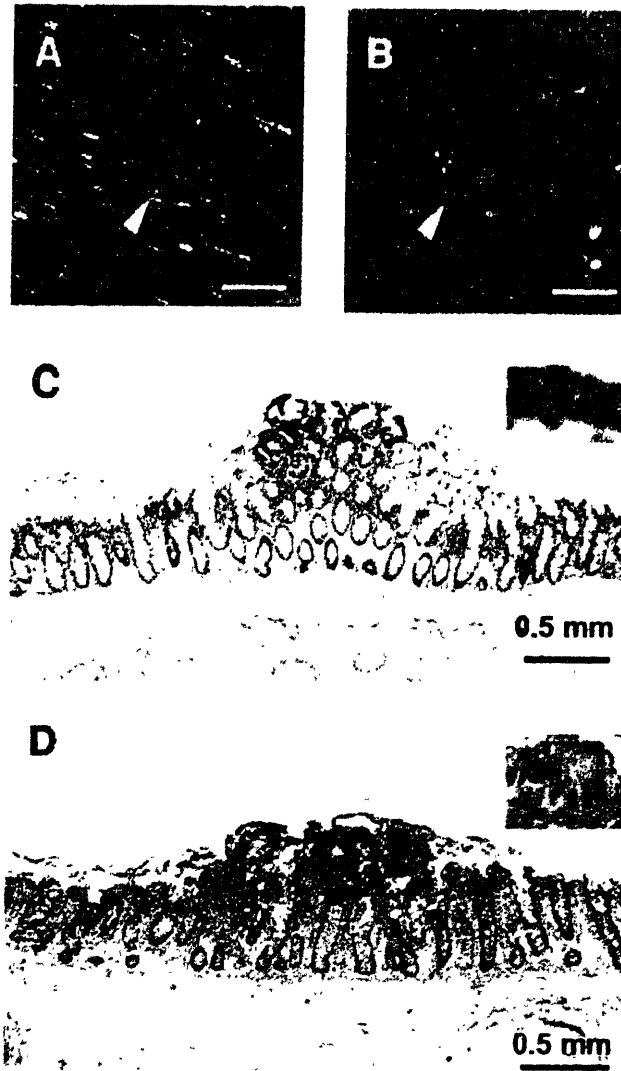
Figure 7.9 Gross and microscopic photographs of colonic polyps used for LSS imaging shown in Fig. 7.10. (a) and (b) show two polyps highlighted by arrows. (c) and (d) show microscopic sections of these polyps. Although the polyps are grossly similar, only one of them is dysplastic. Histological features identify polyp (a) as an adenoma and polyp (b) as an inflammatory polyp with no dysplasia. The insets show each polyp's surface epithelium at high magnification, illustrating dysplastic nuclear features in (c) but not in (d). Representative photomicrographs from each polyp and the surrounding normal tissue were used to measure the average diameter of the nuclei and their variations in size.

signifi

210

Enlarged
Nuclei, %

■ 40-50
□ 30-40
■ 20-30
■ 10-20

Chromatin
pg/nucleus

■ 115-140
□ 90-115
■ 65-90
■ 40-65

Adenoma

Non-dysplastic
mucosa

Enlarged
Nuclei. %

■ 40-50
□ 30-40
■ 20-30
■ 10-20

Chromatin,
pg/nucleus

■ 115-140
□ 90-115
■ 65-90
■ 40-65

Polyp

Normal
mucosa
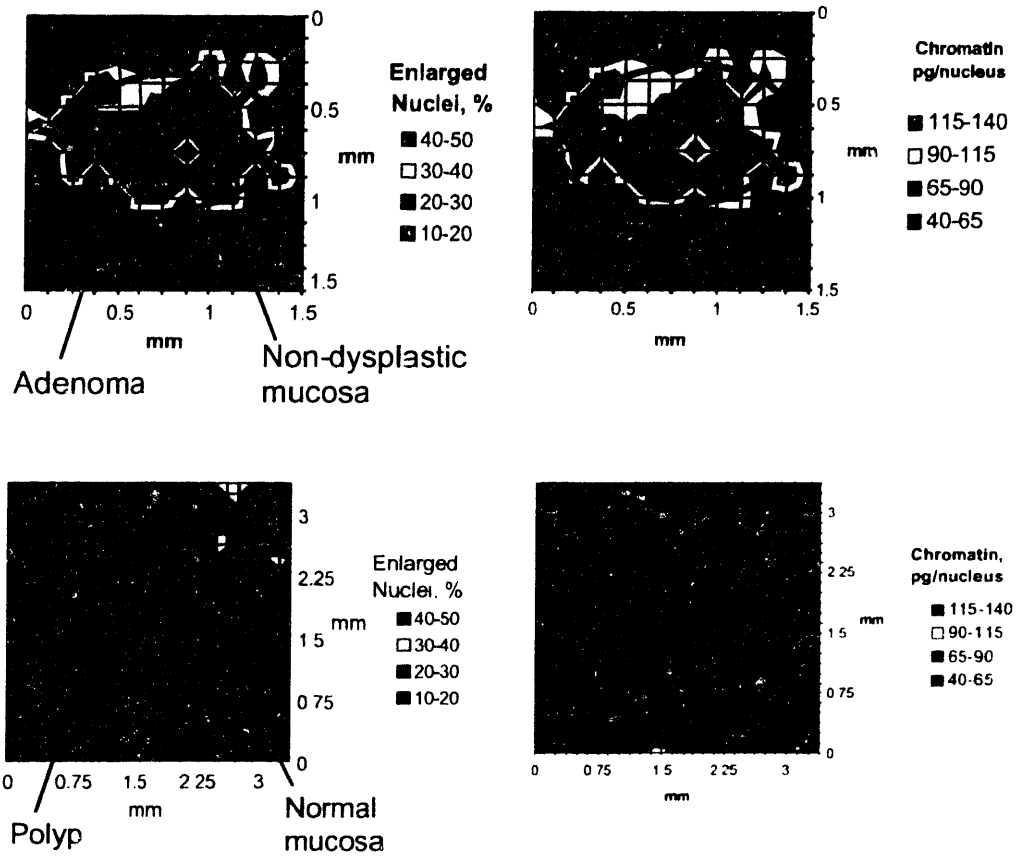
Figure 7.10 LSS images of colon tissue samples (a) and (b) LSS images showing the spatial distribution of the percentage of enlarged nuclei and amount of nuclear chromatin for the polyp of Fig. 7.9(a), respectively; (c) and (d) LSS images showing the spatial distribution of the percentage of enlarged nuclei and amount of nuclear chromatin for the polyp of Fig. 7.9(b), respectively. The polyps are marked by ellipses.

significant for diagnosis ^f dysplastic lesions in the colon and several other organs [Backman et al., 2000]. The resulting color-coded plot is shown in Fig. 7.10(a). As expected, the nuclei are enlarged in the central. adenomatous region, but not in the surrounding tissue.

		Morphometry	LSS
Normal mucosa	Mean nuclear diameter and standard error of measurement, μm	5.60 ± 0.20	5.70 ± 0.13
	Standard deviation of nuclear diameters, μm	1.01	0.82
Adenoma	Mean nuclear diameter and standard error of measurement, μm	7.44 ± 0.23	7.67 ± 0.40
	Standard deviation of nuclear diameters, μm	1.59	2.19

Table 7.1 Comparison of the values of the mean nuclear diameters and standard deviations of nuclear sizes in the colon adenoma of Fig. 7.9(a) and surrounding non-dysplastic epithelium measured with LSS and using standard morphometry of the stained tissues.

To verify these results, after the LSS measurements we studied stained tissue sections of both the polyp and surrounding normal region. Figure 7.9(c) shows a histological section of the same polyp. The size of each stained nucleus was measured, and the average size of the dysplastic nuclei was estimated. A similar procedure was carried out for a normal region surrounding the polyp. Table 7.1 lists the resulting average sizes and standard deviations for both the polyp and normal regions, obtained from the LSS measurements, along with the corresponding values obtained by standard morphometry. As can be seen, very good correlation is obtained. The average size of the nuclei in the normal region is smaller than those in the polyp, with a smaller standard deviation. Figure 7.10(b) is an LSS image of the spatial distribution of the mass of nuclear chromatin

displayed in units of picograms per nucleus. These values were derived using (7.10) from the knowledge of the diameter and the refractive index of the nuclei, obtained from our LSS image. One can see that in the region of the adenoma, the chromatin content is larger than in the surrounding normal tissue. As discussed in section 7.3, this condition is indicative for dysplasia. The resulting values are in good agreement with the results obtained using biochemical techniques and reported elsewhere [Brown et al., 1955; Davies et al., 1957; Davies et al., 1958; Lee et al., 1973;].

As further proof of our imaging ability, fig. 7.9(b) shows a colonic polyp from another patient who underwent partial colectomy for adenocarcinoma arising in the setting of a polyposis syndrome. The LSS image of the polyp and the surrounding region was obtained. Although the clinical presentation was suggestive of an adenoma, Figs. 7.10(c) and (d) show that the spatial distribution of nuclear sizes is uniform, with very few enlarged or hyperchromatic nuclei. Histological examination of the polyp (Fig. 7.9(d)) by an expert pathologist verified our findings and showed a benign polyp with no dysplasia. Furthermore, histological examination of all polyps from this patient was diagnostic for juvenile polyposis syndrome with no dysplasia. This illustrates that our imaging technique can differentiate dysplastic polyp from non-dysplastic polyps, even when the macroscopic appearance of the lesions is so similar that an experienced clinician could not differentiate the two.

These results show that LSS is capable of providing morphological information about epithelial cells *in situ*. In contrast to conventional images of cells or tissues, the LSS imaging provides quantitative images of the histological properties, such as cell nuclear enlargement, pleomorphism and increased chromatin content. Methods for providing such quantitative, functional information

without tissue removal are not currently available. It is important to emphasize that in contrast to conventional optical images, the images produced by LSS do not depict tissue structure as a microphotograph would. Rather, they provide quantitative maps of distributions of parameters such as nuclear enlargement, degree of pleomorphism, and increased chromatin content, features that relate to the functional state of the tissue. Furthermore, the pixel size and wavelength of light do not limit the resolution of the technique. For example, in our tissue images, the nuclear size is determined with an accuracy exceeding 0.1 μm, whereas the pixel size is 25 μm and the light wavelength ~ 0.5 μm. Such accuracy is obtainable because the information is derived from spectral variations of the backscattered light. These results indicate the promise of LSS-based imaging for clinical use, and as a biomedical research tool to study the dynamics of nuclear changes accompanying the progression of cancer and other diseases. Particularly important applications include detection of early cancer and precancerous conditions in cervix and oral cavity.

References

Anderson, R.R. Polarized light examination and photography of the skin. *Arch. Dermatol.* **127**, 1000-1005 (1991).

Backman V, "Reflectance Spectroscopy for Diagnosis of Precancerous Changes in Human Epithalium", M.S. Thesis, Massachusetts Institute of Technology (1998).

Backman V, Gurjar R, Badizadegan K, Itzkan I, Dasari R, Perelman LT, Feld MS, "Polarized light scattering spectroscopy for quantitative measurement of epithelial structures in situ", *IEEE J. Sel. Topics Quantum Electron*, **5**, 1019-1027 (1999).

Backman V, Wallace MB, Perelman LT, Arendt JT, Gurjar R, Muller MG, Zhang Q, G. Zonios G, Kline E, McGillican T, Shapshay S, Valdez T, Van Dam J, Badizadegan K, Crawford JM, Fitzmaurice M, Kabani S, Levin HS, Seiler M, Dasari RR, Itzkan I and Feld MS, "Light scattering spectroscopy: a new technique for clinical diagnosis of precancerous and cancerous changes in human epithelia", *Nature*, **406**, 35-36 (2000).

Beauvoit B, T. Kitai, and B. Chance, "Contribution of the mitochondrial compartment to the optical properties of rat liver: a theoretical and practical approach", *Biophys. J.*, **67**, 2501-2510 (1994).

Beuthan J, O. Milner, J. Hefmann, M. Herrig, and G. Muller, *Phys. Med. Biol.*, **41**, 369 (1996).

Boone C.W. *et al.* Quantitative grading of rat esophageal carcinogenesis using computer-assisted image tile analysis. *Cancer Epidemiology, Biomarkers & Prevention*, **9**, 495-500 (2000).

Born M and Wolf E, Principles of Optics (Oxford: Pergamon, 3rd edition, 1965).

Brown, G.L., McEwan, M., Pratt, M. Macromolecular weight and size of deoxypentose nucleic acids. *Nature*, **176**, 161-162 (1955).

Cotran RS, Robbins SL, Kumar V, *Robbins Pathological Basis of Disease* (W.B. Saunders Company, Philadelphia, 1994).

Davies, H.G., Deeley, E. M., Denby, E. F. Attempts at measurement of lipid, nucleic acid and protein content of cell nuclei by microscope-interferometry. *Exp. Cell Res.*, Suppl. 4, 136-149 (1957).

Davies, H.G. *General Cytochemical Methods* (Danielli, J.F., ed.) Vol I. (Academic Press, New York and London, 1958).

Demos SG and Alfano RR, "Temporal gating in highly scattering media by the degree of optical polarization ", *Opt. Lett.,* 21, 161-163 (1996).

Demos SJ and Alfano RR, "Optical polarized imaging", *App. Opt.*, 36, 150-155 (1997).

Fawcett DW, *A Textbook of Histology*, (Charman & Hall, New York, 1994).

Georgakoudi I, Jacobson BC, Backman V, Wallace M, Muller M, Zhuang Q, Badizadegan K, Sun D, Thomas G, Van Dam V, Feld MS, "The Combination of Fluorescence, Diffuse Reflectance, and Light Scattering Spectroscopy for the Improved Detection of Low- and High-grade Dysplasia in Patients with Barrett's Esophagus", *Gastrointerology*, in press (2001).

Gurjar R, Backman V, Badizadegan K, Dasari R, Itzkan I, Perelman LT, Feld MS, "Functional Imaging of Human Epithelia with Polarized Light Scattering Spectroscopy", *Nature Medicine*, to be published (2001).

Jackson JD, *Classical Electrodynamics*, (John Wiley & Sons, New York, 1975).

Jacques, S.L., Roman, J.R., Lee, K. Imaging Superficial Tissues with Polarized Light. *Lasers in Surgery and Medicine*, 26, 119-129 (2000).

Hiatt LD, *Color Atlas of Histology*, (Williams & Wilkins, Baltimor, 1994).

Ishimaru A, Wave Propagation and Scattering in Random Media (Academic Press, Orlando, 1978).

Kerker M, *The Scattering of Light*, (Academic Press, New York, 1969).

Landis SH, Murray T, Bolden S, Wingo PA, "Cancer Statistics 1999", CA – A Cancer Journal for Clinicians, **49**, 8-31 (1999).

Lee, L., Pappelis, A. J., Pappelis, G. A., Kaplan, H. M. Cellular and nuclear dry mass and area changes during human oral mucosa cell development. *Acta Cytol.* **17**, 214-219 (1973).

Newton RG, *Scattering Theory of Waves and Particles* (McGraw-Hill Book Company, New York, 1969).

Paramonov LE, "On optical equivalence of randomly oriented ellipsoidal and polydisperse spherical particles", *Opt. Spekt.*, **77**, 660-663 (1994).

Perelman LT, Backman V, Wallace MB, Zonios G, Manoharan R., Nusrat A, Shields S, Seiler M, Lima C, Hamano T, Itzkan I, Van Dam J, Crawford JM and Feld MS, "Observation of periodic fine structure in reflectance from biological tissue: a new technique for measuring nuclear size distribution", *Phys. Rev. Lett.*, **80**, 627-630 (1998).

Russ, J.C. *The Image Processing Handbook* (CRC Press, Boca Raton, Ann Arbor, London, Tokyo, 1992).

Sankaran, V., Schonenberger, S., Walsh, Jr., J.T., Maitland, D.J. Polarization discrimination of coherently propagating light in turbid media. *Appl Opt.* **38**, 4252-4261 (1999).

Slot PMS, Hoekstra AG and Figdor CG, *Cytometry*, **9**, 636 (1988).

Sokolov, K., Drezek, R., Gossage, K, Richards-Kortum, R. Reflectance spectroscopy with polarized light: is it sensitive to cellular and nuclear morphology. *Opt. Express*, **5**, 302-317 (2000).

Van de Hulst HC, *Light Scattering by Small Particles* (Dover Publications, New York, 1957).

Wallace, M. *et al.* Endoscopic Detection of Dysplasia in Patients with Barrett's Esophagus Using Light Scattering Spectroscopy. *Gastroenterology*, **119**, 677-682 (2000).

Watson JV, *Introduction to Flow Cytometry* (Cambridge U. Press, Cambridge, 1991).

Zonios G, Ph.D. Thesis, Massachusetts Institute of Technology (1998).

Zonios G, Perelman LT, Backman V, Manoharan R, Fitzmaurice M, Feld MS, "Diffuse Reflectance Spectroscopy of Human Adenomatous Colon Polyps *In Vivo*", *Appl. Opt.,* **38**, 6628-6637 (1999).

Chapter 8

Measurement of Tissue Structure on Submicron Scale with LSS

The diagnoses of a variety of diseases have traditionally relied on microscopic examination of differentially stained biopsy material [Cotran et al., 1994]. By far the most common tissue dyes used for diagnostic purposes are hematoxylin, which stains the histones and nucleic acids within nuclei blue, and eosin, which stains proteins red. In a given tissue, the intensity of staining by hematoxylin and eosin increases with the concentration of stainable solids. On the other hand, the refractive index of a tissue structure is a linear function of the concentration of the solid component of this structure (see section 7.4 for more details) [Davies et al., 1957; Davies et al., 1958]. When the cell is illuminated by visible light, refractive index variations lead to light scattering. The spectral and angular distribution of this scattered light is dependent on the size and refractive

index distribution of the scattering structures. Thus, LSS, which enables the measurement and analysis of light that is backscattered by the tissue after a single scattering event, can be used to probe the cell structure and provide diagnostic information of use to the pathologist.

In the previous chapter we established that LSS enables to measure size and refractive index distributions of the nuclei of epithelial cells *in vitro*, in cultured cell monolayers and *in vivo* or *ex vivo* in living human tissues [Perelman et al., 1998; Backman et al., 1999; Backman et al., 2000; Gurjar et al., 2001]. Since presence of enlarged and hyperchromatic (intensely stained) nuclei of high refractive index are among the most important diagnostic criteria used by pathologists to diagnose early cancerous or precancerous transformations, LSS has the potential to provide a broadly applicable tool to detect epithelial precancerous and early cancerous lesions in a majority of optically accessible organs.

Cell nuclei are good targets to be probed with LSS, because they are the largest cellular organelles, with sizes ranging from 5 to 15 μm, and they have one of the highest indices of refraction amongst the components of epithelial cells [Fawcett et al., 1994; Beuthan et al., 1996]. Since the intensity of light backscattered by such large particles has a characteristic variation with wavelength, LSS was used to measure the sizes and refractive indices of the nuclei. However, changes in the nuclear size and density are not the only diagnostic criteria used by pathologists. Coarse clumping of hematoxylyn-stained nuclear chromatin (chromatin being a general term for all of the solid material within a nucleus), with a sharp falloff of the optical density gradient at the borders of the clumps (so called sharp margination), and a general coarsening of the chromatin texture, have also been shown to correlate with the degree of dysplasia and have been used to assess the prognosis of the disease [Cotran et al., 1994; Boone et al.,

2000]. It is important to point out that these alterations of cellular architecture are associated with the changes of the spatial distribution of the refractive index inside a cell on a scale that is of the order of or less than the wavelength of visible light. Therefore, conventional LSS does not have the ability to probe these changes.

In this chapter we discuss how capabilities of LSS may be extended to enable quantitative assessment of the distributions of submicron scale refractive index variations in living cells and tissues. This can be achieved using angular distribution of scattered light to differentiate between light scattered by large and small scatterers. As discussed in chapter 3, light scattered by large particles dominates LSS signals measured near the exact backward direction. However, the intensity of large particle scattering vanishes with increase of the scattering angle and scattering by smaller structures becomes more pronounced. Therefore, by varying the angle of collection, LSS can be rendered to be more sensitive to cell and tissue structures of smaller size. This is the basic principle of scattering angle sensitive light scattering spectroscopy (a/LSS).

8.1 Scattering Angle Sensitive Light Scattering Spectroscopy

We have developed a/LSS apparatus based on the LSS imaging device (see section 7.1, Fig. 7.1, and [Gurjar et al., 2001]). A schematic diagram of the a/LSS set-up is shown in Fig. 8.1. A 75 W xenon arc lamp (Oriel, Inc.) is used to illuminate the sample. The light from the lamp is collimated, polarized and delivered onto the sample via a mirror and a beamsplitter as in the LSS imaging device. The beam is incident on the sample at an angle of about 15 degrees to
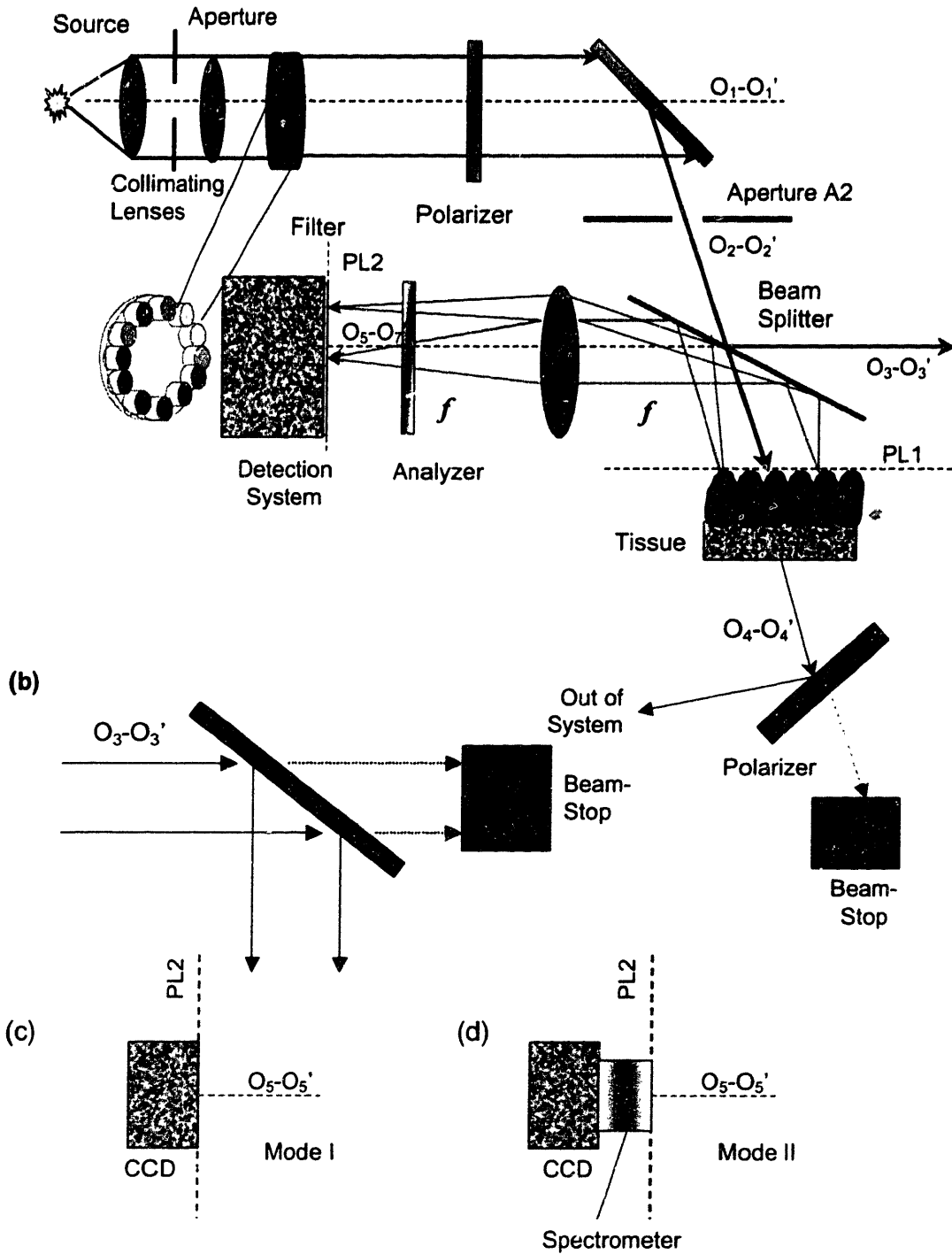
Figure 8.1 Schematic diagram of the a/LSS apparatus. (b) Set-up to eliminate spurious beam O_3-O_3'. (c) Detection system used in Mode I. (d) Detection system used in Mode II.
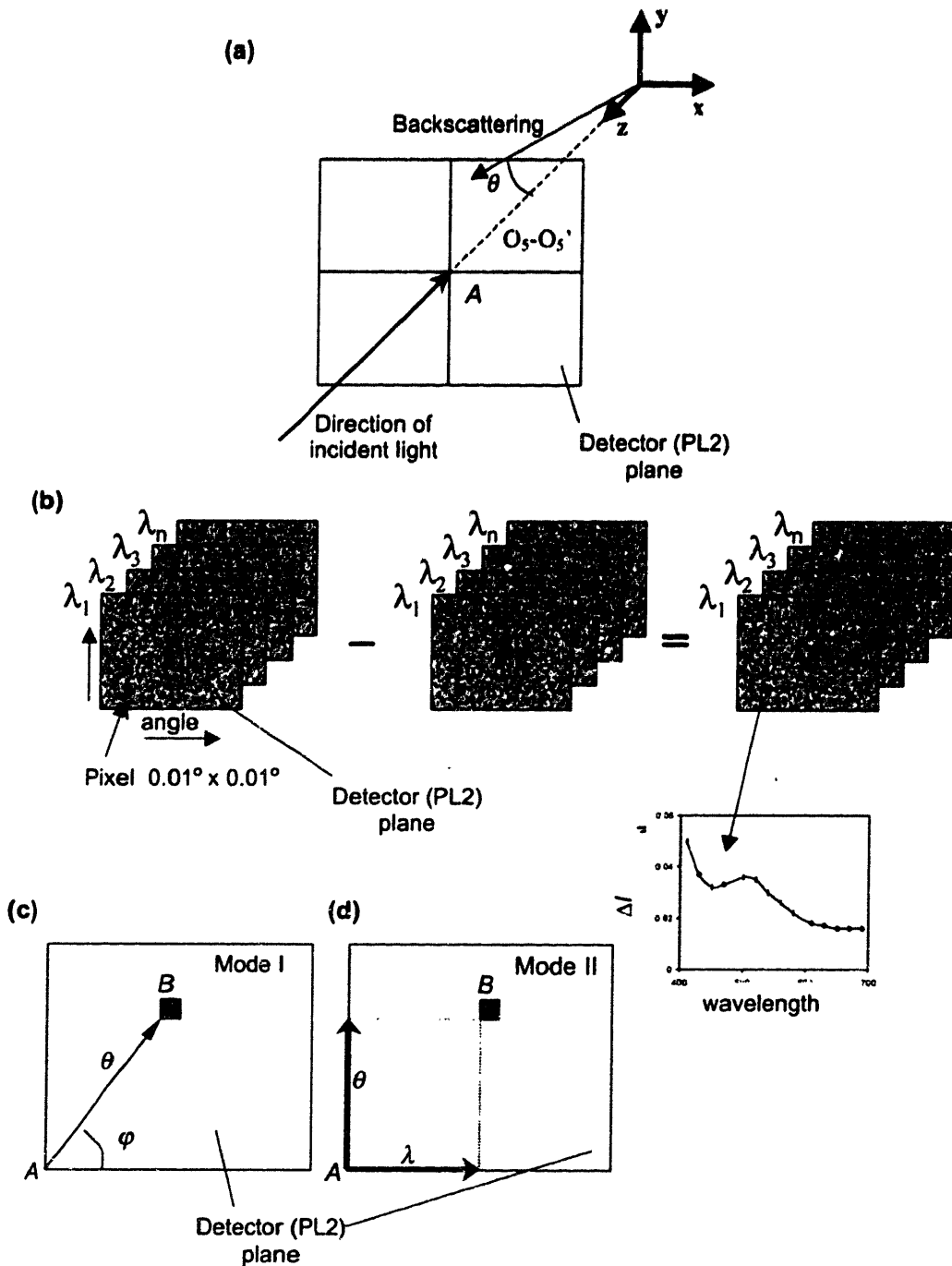
Figure 8.2 Data collection using a/LSS apparatus. (a) Image created by lens L3 on fig. 8.1 in the detector (PL2) plane. (b) Data collection in Mode I. In this mode each pixel B on the CCD collects intensity of light scattered along direction (θ, φ) (c). In mode II, each pixel corresponds to a certain wavelength λ and scattering angle θ (d).

223

avoid specular reflection from the sample surface/air interface. The spurious reflection from the beamsplitter (O_3-O_3' in Fig. 8.1) and the beam transmitted through the sample (O_4-O_4') are eliminated by means of a combination of a polarizer and a beam-stop. The size of the illumination spot can be varied using aperture A2. In most studies it was ~3 mm^2. Light scattered by the sample is reflected by the beamsplitter to the collection arm of the apparatus. This light passes through a rotating analyzer and a 2f-system before reaching the detector.

In section 7.1 we discussed the principles of a 4f-system consisting of two lenses positioned at exactly two focal length distances from each other (Fig. 7.2). The image generated by the first lens in the plane exactly one focal distance away from the lenses (so called Fourier plane, PL2 in Fig. 7.2) is the angular distribution of light passing through a plane located one focal length away from the first lens (PL1 on Fig. 7.2) [Born et al., 1965]. In the 4f-system, this image is transformed into a real image in plane PL3 by the second lens. A 2f-system consists of a single lens positioned one focal distance away from the sample plane. Therefore, a detector located in plane PL2 would collect the angular distribution of light scattered by the sample.

We have developed two modes of data collection. In mode I, the incident light is transmitted through one of the 11 narrow-band (4 nm) filters (Edmund Scientific, Inc.) to select the desired wavelength, λ_i $i=1,\dots,11$, in the range from 450 to 700 nm as in the LSS imaging device. Thus, the sample is illuminated by light at a given wavelength. A CCD is placed in the Fourier plane (PL2 on Fig. 8.1). The CCD detector consists of a 512 x 512 pixel array, with each pixel having dimensions 25 μm x 25 μm. This CCD collects the angular distribution of light

scattered by the sample on a selected wavelength[1]. The data collection is illustrated in Fig. 8.2. First, wavelength λ_1 is selected and the CCD collects the angular distribution of light scattered by the sample, $I_{\parallel}(\theta,\phi;\ \lambda_1)$. In this measurement, the analyzer is oriented to transmit light polarized parallel to the direction of polarization of the incident light. Then the analyzer is rotated 90°, so that the angular distribution of scattered light with orthogonal polarization is collected, $I_{\perp}(\theta,\phi;\ \lambda_1)$. To correct for varying responses of different pixels and non-uniformities in wavelength response, the images are normalized by $I_{\parallel}^{(w)}(\theta,\phi,\lambda_1)$ and $I_{\perp}^{(w)}(\theta,\phi,\lambda_1)$, obtained using a highly diffusive and reflective white standard (Ocean Optics, Inc), which scatters incident light izotropically and uniformly across the visible wavelength range. Moreover, dark background images, $I_{\parallel}^{(b)}(\theta,\phi)$ and $I_{\perp}^{(b)}(\theta,\phi)$, obtained when the illumination is off, are subtracted from the other images. This normalization procedure is similar to one used to normalize polarized LSS signals discussed in Chapter 5. The resulting image

$$\Delta I(\theta,\phi,\lambda_1) = \frac{I_{\parallel}(\theta,\phi,\lambda_1) - I_{\parallel}^{(b)}(\theta,\phi)}{I_{\parallel}^{(w)}(\theta,\phi,\lambda_1) - I_{\parallel}^{(b)}(\theta,\phi)} - \frac{I_{\perp}(\theta,\phi,\lambda_1) - I_{\perp}^{(b)}(\theta,\phi)}{I_{\perp}^{(w)}(\theta,\phi,\lambda_1) - I_{\perp}^{(b)}(\theta,\phi)} \tag{8.1}$$

is the angular distribution of single scattered light. After these measurements are complete, another wavelength is selected and the angular distributions are collected again until the wavelength range of interest is covered.

Each pixel on any of the images corresponds to a unique scattering angle that can be expressed in polar coordinates θ and ϕ (Fig. 8.2(c)). Particularly, light scattered along exact backward direction is projected to point A at the intersection

---

[1] It is important to point out that in the a/LSS studies all the scatterers in the illuminated part of the sample contribute to the measured signal.

225

of the Fourier plane PL2 and axis O_5-O_5'. Light scattered along direction (θ, ϕ) is projected to point B such that $|AB| = f \tan\theta$ and the azimuth φ_B of vector **AB** equals azimuth ϕ. Therefore, spectrum of light scattering can be obtained for each scattering angle.

We notice that the CCD needs not be positioned such that point A is in its center. For example, in some of the applications of the device, CCD was positioned so that it collected light scattered for $0 \le \phi \le \pi/2$. Because the light scattering is the same for ϕ, π-ϕ, π+ϕ, and 2π-ϕ, this scheme ensured that the CCD covers maximal range in θ without sacrificing ϕ-depended information. In our experiments we used lenses with the focal length 12.5 cm and diameter 5 cm. The CCD array was 1.25 cm. Thus, this set-up allowed measurement of light scattered within $\theta \in [0, 5.7°]$ and $\varphi \in [0, 90°]$.

Operating a/LSS device in mode I is convenient for calibration but is laborious and time consuming, because it requires changing several filters. Moreover, the spectral information obtainable in this mode is discrete and measurement of continuous wavelength (cw) spectra is not possible. On the other hand, analysis of cw-spectra is easier and generally does not require signal to noise ratio (S/N) as high as one necessary to analyze discrete spectra. This is due to the fact that white noise as well as $1/f$-noise is mush easier to filter out when more data-points are available. Mode II of operation enables to overcome these limitations.

In mode II, filters are not used and a spectrometer is placed in the Fourier plane instead of a CCD (Fig. 8.1(d)). The CCD is then connected to the spectrometer. The entrance to the spectrometer is a narrow slit whose width may be adjusted. The spectrometer is positioned so that its slit includes the focal point

of the photons scattered along exact the backward direction (A in Fig. 8.1). Let us define axes x and y perpendicular and parallel to the slit respectively. Photons scattered by the sample will reach various points on the slit depending on the scattering angle θ. At the same time, azimuth φ is fixed. The spectrometer diverges these photons depending on the wavelength. Therefore, a coordinate x on the CCD corresponds to a certain wavelength of the scattered light (the exact value of this value depends on the grating of the spectroneter being used) and a coordinate y corresponds to a certain scattering angle θ. Thus, both angular and spectral information can be collected (Fig. 8.2(d)). By a suitable orientation of the polarizer and analyzer the orientation of the backscattering map may be rotated in respect to the slit of the spectrometer. In this mode, one sacrifices a two-dimensional image for ease of operation and increased spectral information.

8.2 Calibration of Scattering Angle Sensitive LSS Device

In Chapters 3 and 4, we have established that the angular distributions of light scattered by large and small particles are quite distinct. Large particles scatter more in the exact and near-backward directions. For many types of epithelial cells, the spectra of light scattered into these angles are dominated by the contribution from the largest intracellular scatterers such as cell nuclei. However, as predicted by the Mie theory (Fig. 4.1), the scattering by large particles vanishes for larger backscattering angles θ and $\phi \approx 45^{\circ}$. In this angular region, the contribution from the intracellular particles with sizes comparable or smaller than the wavelength of

light can dominate, because the small particle scattering is more uniform and has weaker dependence on θ and ϕ.

We performed experiments with polystyrene microspheres in order to establish whether the angular distribution can be used as a means to separate the signals scattered by large and small particles. First we measured the angular distributions $I_\parallel^{(l)}(\theta,\phi;\ \lambda_i)$ of light scattered by 9.8 μm beads (optical thickness $\tau \sim 0.5$) using the a/LSS device in mode I. After the measurements were completed, beads smaller than the wavelength, 0.4 μm in diameter, were added in the amount sufficient to equalize the contribution from large and small particles to the total optical thickness of the sample. The resulting angular distributions $I_\parallel^{(m)}(\theta,\phi;\ \lambda_i)$ were then measured again.

Figure 8.3 shows the ratio of such maps $R = I_\parallel^{(m)}(\theta,\phi;\ \lambda) / I_\parallel^{(l)}(\theta,\phi;\ \lambda)$ collected for $\lambda = 0.532$ μm. It can be seen that this ratio is close to one for angles near the exact backward direction (angular region A on fig. 8.3) and along the axes x and y. Thus, despite the fact that the small beads were added, the backscattering signal did not change. We can conclude therefore, that the scattering in these regions is dominated by the large particles. In contrast, the ratio is higher than one and approaches 7 for angles with azimuths close to 45° and $\theta > 2.5°$ (angular region B in Fig. 8.3). In this region, the contribution from small particles dominates.

This experiment illustrates that by choosing an angular region, one can render LSS to become more sensitive to either large or small scatterers. If region A is used, LSS spectra provide information about larger scatterers in the sample. In contrary, if region B is chosen, LSS signal originates from the scattering by scatterers of smaller sizes.

228
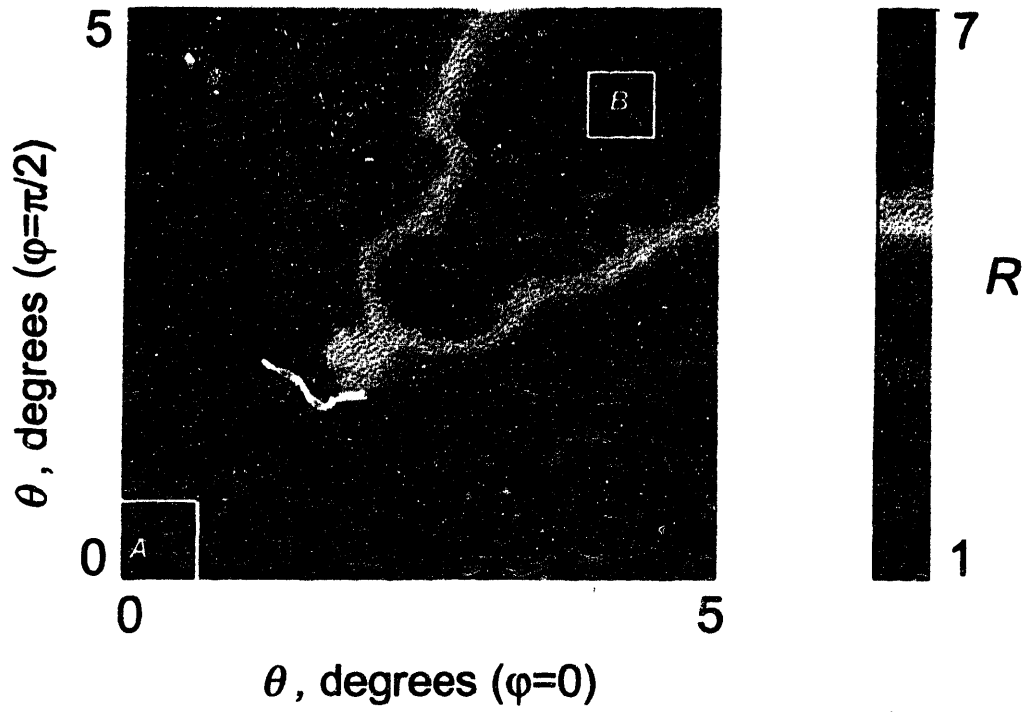
Figure 8.3 Ratio of angular distribution $R=I_\parallel^{(m)}(\theta,\phi;\ \lambda)/\ I_\parallel^{(1)}(\theta,\phi;\ \lambda)$ collected in the experiment with polystyrene microspheres 9.8 μm in diameter for $\lambda=0.532$ μm. See text for details.

8.3 Experiments with Cell Monolayers

To test our approach further, we conducted experiments with monolayers of T84 colon tumor cells and benign mesothelial cells. The cell monolayer experiments employed two-layered tissue models similar to those used in LSS with polarized light (Chapter 5) and LSS imaging (Chapter 6) studies. The upper layer, a monolayer of T84 colon tumor cells or benign mesothelial cells grown on a glass cover slip, simulated epithelium. The lower layer was an optically thick gel containing mixture of powdered Ba_2SO_4 and human blood, simulating tissue scattering and tissue absorption respectively. Confluent T84 cell monolayers were grown on a glass slide and transferred to Hank's balanced salt solution (HBSS). Benign mesothelial cells were planted, transferred to HBSS and settled onto a glass slide. Following the experiments, cells were stained using toluidine blue and imaged using a conventional microscope. By adjusting the concentrations of Ba_2SO_4 and the blood, the absorption and scattering properties of the second layer could be made similar to those of biological tissue, since hemoglobin is known to be the major absorber in most tissues in the visible spectral range (see Chapter 5 as well as [Zonios et al., 1999]). The reduced scattering coefficient of this layer μ'_s was ~ 2.5 mm^{-1} and the concentration of hemoglobin solution was 180mg/dl so that the corresponding absorption coefficient varied from $0.0018mm^{-1}$ to $0.36mm^{-1}$ in the wavelength region 450-780 nm, the parameters close to these of living human tissues such as colon mucosa.

The data were collected as in the experiments with polystyrene beads. A series of polarized images of the angular distributions of light scattered at different wavelengths were taken, and the spectra of the intensity of light scattered into two distinct angular regions, A and B, were constructed. Figure 8.4 shows the angular

230
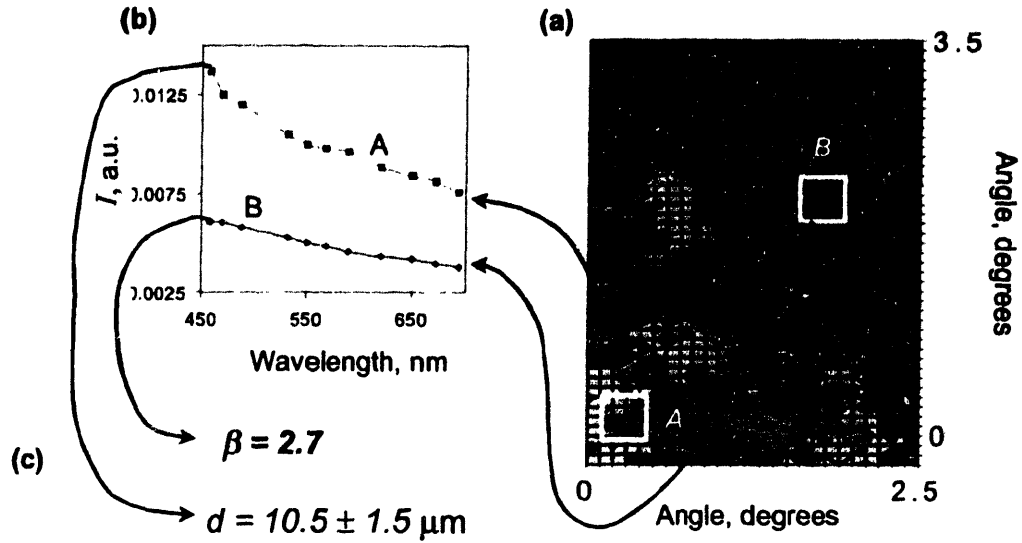
Figure 8.4 Experiments with two-layer tissue models with the upper layer formed by a monolayer of T84 colon tumor cells. (a) A color-coded contour map of the angular distribution collected using a/LSS device operated in mode I. (b) Spectra of light scattered by cells in regions *A* and *B* marked on map (a). The analysis of these spectra enabled to obtained quantitative characteristics of the size distributions of scattering particles responsible for respective scattering spectra (c).

231

distribution of scattering by T84 cells (Fig. 8.4(a)) as well as corresponding spectra from regions A (Fig. 8.4(b)) and B (Fig. 8.4(c)). As in the experiments with polystyrene beads, region A corresponded to small backscattering angles and the directions of scattering close to the exact backward direction (backscattering angle $\theta<0.5°$) while region B corresponded to larger backscattering angles $\theta\sim2.5°$ and directions of scattering with azimuth φ close to $45°$.

We first notice that both spectra shown in Fig. 8.4(b) and (c) lack any features of hemoglobin absorption, i.e. characteristic absorption bands. Since only the second layer contained blood and, thus, hemoglobin, these features would be apparent if light multiply scattered by the particles of the second layer contributed to the resulting LSS signal. On the other hand, the absence of such features indicates that the subtraction of the unpolarized component allows measurement of the single scattering, in agreement with our previous results and [Backman et al., 1999; Gurjar et al., 2001]. Furthermore, we notice that the spectra are distinctly different, illustrating the difference in the origin of scattering into these angular regions. Both spectra were analyzed using the Mie theory-based inversion procedure, which provides the parameters of the size distributions and refractive indexes of the scatterers that best fit the data being evaluated (Chapter 4 and [Backman et al, 1999; Gurjar et al., 2001]). The fits are shown in Fig. 8.4(b) and (c) as well.

Analysis of the spectrum from region A showed that the size distribution of scatterers is similar to the Gaussian distribution with mean diameter 10.5 μm and standard deviation 1.5 μm. As expected, this size distribution matched closely the size distribution of the largest structures inside the cells, the cell nuclei, measured using conventional morphometry after the cells were stained with a nuclear stain. The mean and the standard deviation of the size distribution obtained using

morphometry were 10.4 μm and 1.35 μm respectively. This agrees with the previous studies showing that cell nuclei provide the major contribution to the LSS signal collected in near-backward directions [Perelman et al., 1998; Backman et al., 1999; Gurjar et al., 2001]. In case of normal mesothelial cells, the mean and the standard deviation of the nuclear size distribution measured with LSS were 7.4 μm and 0.8 μm respectively, close to the parameters obtained with morphometry, 7.5 μm and 0.7 μm. A larger mean and standard deviation of nuclear sizes obtained for T84 colon tumor cells agrees with the fact that malignant nuclei are enlarged and exhibit significant degree of pleomorphism (greater size variability) [Cotran et al., 1999; Backman et al., 2000].

For comparison, the spectrum from region *B* showed the presence of smaller structures with sizes in the order of or smaller than the wavelength, which are widely distributed according to a power-law rather than the Gaussian distribution. The number density of particles distributed according to the power-law is $N \propto d^{-\beta}$, where d is a particle diameter and β is the spectral exponent. While such size distribution becomes unphysical for $d \rightarrow 0$, it was modeled as skewed log-normal distribution with a standard deviation approaching infinity [Schmidt et al., 1998]. According to the power-law distribution, the smaller the size of a structural species within a cell, the more numerous this species is. Such distribution is feasible, because the cells tend to build larger structures, i.e. organelles, from smaller sub-units. In turn, these sub-units consist of even smaller building blocks. Spectral analysis enables us to obtain the value of spectral exponent β as a fitting parameter. Spectral exponent, in turn, provides quantitative information about the organization of the cells. In case of T84 tumor cells, β was found to be approximately 2.2, while in case of normal mesothelial cells the best fit

was obtained for $\beta=2.7$, which indicates a higher population of sub-cellular structures of larger sizes in T84 cells.

The experiments with cell monolayers confirmed that

(1)   polarization discrimination results in LSS signals consisting primarily of singly scattered photons;

(2)   light scattered into near-backward directions (region A) and into larger backscattering angles (region B) originates from different subcellular structures;

(3)   light scattered by particles with sizes in the order of or smaller than the wavelength dominates the scattering into region B;

(4)   population density of these small particles in T84 colon tumor cells and normal mesothelial cells can be modeled as a power-law of their size;

(5)   analysis of LSS spectra from region B allows to measure the spectral exponent of the size distribution of subcellular structures;

(6)   the value of spectral exponent for T84 tumor cells is smaller than one for normal mesothelial cells.

The question that remains is whether the value of spectral exponent correlates with the precancerous transformations in living tissues. To address this question we conducted studies with animal models.

8.3 Experiments with Animal Models

The esophagus-specific carcinogen nitrosomethylbenzylamine was administered subcutaneously to male Fisher 344 rats twice a week for five weeks [Wang et al., 1989]. Three different doses were used: 0.125 mg/kg, 0.250 mg/kg, and 0.500 mg/kg. Seven months after the start of the five-week course of carcinogen, the esophagi of the rats was removed and subjected to evaluation by light scattering spectroscopy. Histologically the esophagi showed dysplasia of esophageal epithelium, the severity of which corresponded to the dose of carcinogen.

Because the accuracy of the inversion procedure improves with the number of data points on the LSS spectrum, the measurements were taken with a LSS device in mode II (Fig. 8.1(c)). As mentioned above, this device allows simultaneous measurement of both angular and spectral distribution of light scattered into a range of angles θ for a particular azimuth φ. In our experiments the angular distribution was measured in the range $0 < \theta < 5°$ and any value of φ from 0 to 360° were attainable. In order to change azimuth φ, either the spectrograph along with the CCD or the orientation of polarizer must be changed. In our experiments the polarizer was rotated to change the direction of polarization of the incident light and, thus, the azimuth φ. To measure the size distribution of small structures within the esophageal epithelia, angle φ was fixed at 45° and a spectrum of LSS signal from region B was measured and analyzed. For each sample, a spectral exponent β of the size distribution was obtained.

Figure 8.5 shows the correlation between the values of spectral exponent and the dose of carcinogen. As can be seen, β steadily decreases with the increase

235
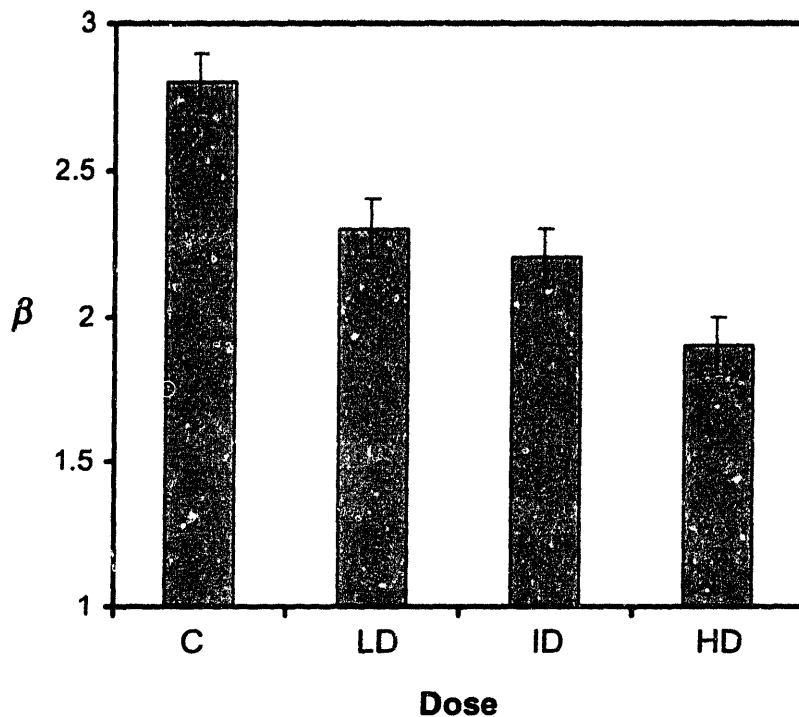
Figure 8.4 Correlation between values of spectral exponent β measured with LSS for living esophageal epithelial cells and dose of carcinogen applied to the esophagi. C – control (no carcinogen applied), LD – low dose, ID – intermediate dose, HD – high dose. In each measurement the value of β is averaged over a population of approximately 10^5 cells.

of the dose (p<0.001), which is consistent with the findings in the experiments with cell monolayers discussed above. The dose of carcinogen applied to rats' esophagi has been shown to correlate with the degree of premalignant transformation, degree of dysplasia, and aggressiveness of the malignancy that originates from the affected epithelium [Wang et al., 1989]. Thus, the value of the spectral exponent may be indicative for the degree of dysplasia as well as the prognosis of the disease.

The smaller values of the spectral exponent for malignant and dysplastic cells can be correlated with certain alterations of normal cell structure associated with precancerous changes. In fact, the list of the parameters characterizing the cell structure that depend on the spectral exponent include the average size of subcellular objects, structural entropy, and the fractal dimension of the cell structure. For example, it can easily be shown that a smaller value of β indicates larger average sizes of the subcellular structures:

$$\langle d \rangle \propto \frac{1}{\beta}.$$ (8.3)

Thus, the studies reported here might indicate that the premalignant cells tend to have the size distributions of their subcellular structures shifted towards larger sizes. In case of a cell nucleus, this shift could be perceived as chromatin clumping.

The density correlation function $\langle \rho(r_1)\rho(r_2) \rangle$, where ρ is the density (concentration) of cell components, is related to β as well:

$$\langle \rho(r_1)\rho(r_2) \rangle \propto \frac{1}{|r_1 - r_2|^{3-\beta}}.$$ (8.4)

This density correlation function shows how well the intracellular structural species located in points r_1 and r_2 are correlated. The faster this function vanishes, the less correlated the structure is. According to (8.4), if $\beta \sim 3$, even the parts of the cell that are far apart are correlated. When β decreases, $\langle \rho(r_1)\rho(r_2) \rangle$ vanishes faster and only the parts of the cell that are close enough are correlated. Therefore, smaller β for precancerous cells might indicate the loss of correlation

among the cell structures and, thus, loss of cooperation between certain parts of the cell.

The entropy of a 3D structure can be defined as

$$S = \sum_j N_j \ln \frac{1}{N_j} \ , \tag{8.5}$$

where N_j is the number (population) density of structural species of type j. This entropy characterizes the degree of internal disorganization of the structure. According to this definition, if there is only one species present, then $N_1=1$ and $S=0$. When the structural species are distributed in size almost continuously according to the power-law with spectral exponent β, the entropy can be approximated as follows

$$S \approx \int N(d') \ln \frac{1}{N(d')} dd' \propto \frac{\beta}{(\beta-1)}. \tag{8.6}$$

Expression (8.4) indicates that the entropy increases monotonously when β decreases and approaches 1. Therefore, smaller values of β for dysplastic and malignant nuclei may indicate higher entropy and, thus, higher disorganization of the cell structure.

Finally, it can be shown that β relates to the fractal dimension $d_f^{(p)}$ of the planar images of the cells and some large subcellular structures such as the nucleus as follows[2]

$$d_f^{(p)} = \frac{3+\beta}{2}. \tag{8.7}$$

Moreover, the fractal dimension $d_f^{(m)}$ of a 3D mass fractal with the power-law distributed internal components is simply $d_f^{(m)} = \beta$. Therefore, the change in β for precancerous and cancerous cells and tissues indicates the change of both $d_f^{(p)}$ and $d_f^{(m)}$, which, in turn, indicates the loss of structural complexity of the cells [Mandelbrod, 1988; Einstein et al., 1998]. Moreover, objects with smaller $d_f^{(p)}$ appear to have coarse, clumped structure and high margination of their structural components. For example, if $d_f^{(p)}$ of a cell nucleus is decreased, such nucleus would be perceived by a pathologist examining a stained histology slide as one exhibiting some of the most important histological markers of precancer and malignancy related to the altered chromatin texture, namely chromatin clumping, coarse texture and prominent margination of chromatin. Further studies are needed to elucidate the histological correlate of this observation as well as its functional implications.

---

[2] A histological image (slide) is an example of such 2D representation of cells and tissues.

References

Backman V, Gurjar R, Badizadegan K, Itzkan I, Dasari R, Perelman LT, Feld MS, "Polarized light scattering spectroscopy for quantitative measurement of epithelial structures in situ", *IEEE J. Sel. Topics Quantum Electron*, **5**, 1019-1027 (1999).

Backman V, Wallace MB, Perelman LT, Arendt JT, Gurjar R, Muller MG, Zhang Q, G. Zonios G, Kline E, McGillican T, Shapshay S, Valdez T, Van Dam J, Badizadegan K, Crawford JM, Fitzmaurice M, Kabani S, Levin HS, Seiler M, Dasari RR, Itzkan I and Feld MS, "Light scattering spectroscopy: a new technique for clinical diagnosis of precancerous and cancerous changes in human epithelia", *Nature*, **406**, 35-36 (2000).

Beauvoit B, T. Kitai, and B. Chance, "Contribution of the mitochondrial compartment to the optical properties of rat liver: a theoretical and practical approach", *Biophys. J.*, **67**, 2501-2510 (1994).

Beuthan J, O. Milner, J. Hefmann, M. Herrig, and G. Muller, *Phys. Med. Biol.*, **41**, 369 (1996).

Boone C.W. *et al.* Quantitative grading of rat esophageal carcinogenesis using computer-assisted image tile analysis. *Cancer Epidemiology, Biomarkers & Prevention*, **9**, 495-500 (2000).

Born M and Wolf E, Principles of Optics (Oxford: Pergamon, 3rd edition, 1965).

Brown, G.L., McEwan, M., Pratt, M. Macromolecular weight and size of deoxypentose nucleic acids. *Nature*, **176**, 161-162 (1955).

Cotran RS, Robbins SL, Kumar V, *Robbins Pathological Basis of Disease* (W.B. Saunders Company, Philadelphia, 1994).

Davies, H.G., Deeley, E. M., Denby, E. F. Attempts at measurement of lipid, nucleic acid and protein content of cell nuclei by microscope-interferometry. *Exp. Cell Res.*, Suppl. 4, 136-149 (1957).

Davies, H.G. *General Cytochemical Methods* (Danielli, J.F., ed.) Vol I. (Academic Press, New York and London, 1958).

Demos SG and Alfano RR, "Temporal gating in highly scattering media by the degree of optical polarization ", *Opt. Lett.*, 21, 161-163 (1996).

Demos SJ and Alfano RR, "Optical polarized imaging", *App. Opt.*, 36, 150-155 (1997).

Einstein AJ, Wu HS and Gil J, "Self-Affinity and Lacunarity of Chromatin Texture in Benign and Malignant Breast Epithelial Cell Nuclei", 80, 397-400 (1998).

Fawcett DW, *A Textbook of Histology*, (Charman & Hall, New York, 1994).

Gurjar R, Backman V, Badizadegan K, Dasari R, Itzkan I, Perelman LT, Feld MS, "Functional Imaging of Human Epithelia with Polarized Light Scattering Spectroscopy", *Nature Medicine*, to be published (2001).

Jackson JD, *Classical Electrodynamics*, (John Wiley & Sons, New York, 1975).

Jacques, S.L., Roman, J.R., Lee, K. Imaging Superficial Tissues with Polarized Light. *Lasers in Surgery and Medicine*, 26, 119-129 (2000).

Hiatt LD, *Color Atlas of Histology*, (Williams & Wilkins, Baltimor, 1994).

Ishimaru A, Wave Propagation and Scattering in Random Media (Academic Press, Orlando, 1978).

Landis SH, Murray T, Bolden S, Wingo PA, "Cancer Statistics 1999", CA – A Cancer Journal for Clinicians, 49, 8-31 (1999).

Lee, L., Pappelis, A. J., Pappelis, G. A., Kaplan, H. M. Cellular and nuclear dry mass and area changes during human oral mucosa cell development. *Acta Cytol.* 17, 214-219 (1973).

Mandelbrot, *Fractal Geometry of Nature* (Freeman & Co, 1988).

Newton RG, *Scattering Theory of Waves and Particles* (McGraw-Hill Book Company, New York, 1969).

Perelman LT, Backman V, Wallace MB, Zonios G, Manoharan R, Nusrat A, Shields S, Seiler M, Lima C, Hamano T, Itzkan I, Van Dam J, Crawford JM and Feld MS, "Observation of periodic fine structure in reflectance from biological tissue: a new technique for measuring nuclear size distribution", *Phys. Rev. Lett.*, **80**, 627-630 (1998).

Sankaran, V., Schonenberger, S., Walsh, Jr., J.T., Maitland, D.J. Polarization discrimination of coherently propagating light in turbid media. *Appl Opt.* **38**, 4252-4261 (1999).

Schmitt JM and G. Kumar, "Optical scattering properties of soft tissue: a discrete particle model", ", *Appl. Opt.* **37**, 2788-2797 (1998).

Van de Hulst HC, *Light Scattering by Small Particles* (Dover Publications, New York, 1957).

Wallace, M. *et al.* Endoscopic Detection of Dysplasia in Patients with Barrett's Esophagus Using Light Scattering Spectroscopy. *Gastroenterology*, **119**, 677-682 (2000).

Wang, Y., You, M., Reynolds, S.H., Stoner, G.D., and Anderson, M.W. "Mutational activation of cellular Harvey ras gene in methylbenzylnitrosamine-induced Fisher 344 rat esophageal papillomas". *Cancer Res.*, **50**:1591-1595 (1989).

Watson JV, *Introduction to Flow Cytometry* (Cambridge U. Press, Cambridge, 1991).

Zonios G, Ph.D. Thesis, Massachusetts Institute of Technology (1998).

Zonios G, Perelman LT, Backman V, Manoharan R, Fitzmaurice M, Feld MS, "Diffuse Reflectance Spectroscopy of Human Adenomatous Colon Polyps *In Vivo*", *Appl. Opt.*, **38**, 6628-6637 (1999).

Chapter 9

Summary and Future Directions

9.1 Summary

Cancer is one of the leading causes of death throughout the world. More than 85% of all cancers arise in the epithelial cells that line the cavities of the body. Most cancers are readily curable if diagnosed at early stages. However, many forms of precancerous and early cancerous lesions such as dysplasia and carcinoma *in situ* (CIS) are difficult to detect and diagnose.

Dysplasia and CIS are characterized by alterations in the epithelial architecture and, particularly, changes in the epithelial cell nuclei, which become enlarged, crowded and hyperchromatic (abnormally darkly stained with a contrast dye), features that can currently be assessed only by histologic examination of biopsy specimens (Chapter 2). In many cases, diseased tissue is flat and

indistinguishable from surrounding healthy tissue. Since it cannot be distinguished, detection is often based on random biopsy. Biopsy is invasive, and the subsequent evaluation is known to be prone to diagnostic error. We have developed a novel optical technology, light scattering spectroscopy (LSS), for diagnostics of the epithelial linings of the body, which has the potential to guide or replace these invasive diagnostic procedures, thus increasing the efficacy of cancer screening and surveillance.

Principles of LSS

Typical non-dysplastic cell nuclei range in size from 5 to 10 microns. Dysplastic nuclei can be as large as 20 micron. Epithelial cell nuclei can be modeled as transparent spheroids, which are large compared to the wavelength of visible light (0.4-0.8 micron), and whose refractive index is higher than that of the surrounding cytoplasm, due to their chromatin content. The spectrum of light backscattered by such large relative to the wavelength of light particles contains a component that varies characteristically with wavelength (Chapter 3) [Newton, 1969]. This variation depends on particle size and refractive index. When nuclei of several sizes are present, the resulting signal is a superposition of these variations. Thus, the nuclear size distribution and refractive index can be determined from the analysis of the spectrum of light backscattered by the nuclei (Chapter 4) [Perelman et al., 1998]. We have developed a novel theoretical approach to describe light scattering by large particles such as cell nuclei and new methods of numerical data analysis, which enable nuclear size distribution to be obtained from the spectrum of the backscattered light (Chapters 3 and 4) [Perelman at al., 1998; Backman, 1998].

Once the nuclear size distribution and refractive index are known, quantitative measures of nuclear enlargement, crowding, and hyperchromasia can be obtained.

However, only a small portion of light incident on the tissue is directly back-scattered by the epithelial cell nuclei. The rest becomes randomized in direction by multiple scattering, producing a large background of diffusely scattered light (diffusive background) that must be subtracted. We have employed two methods to accomplish this (Chapter 5): (1) mathematical modeling of the diffusive background using either diffusion approximation [Zonios et al., 1999] or exponential model [Perelman et al., 1998; Backman, 1998]; and (2) use of polarized incident light, which is depolarized by multiple scattering [Backman et al., 1999]. In method (2), the single backscattering can be observed by subtracting the depolarized component of the backscattered light. The validity of each of these methods was confirmed in the experiments with various models of living tissues as well as ex vivo and in vivo human tissues [Perelman et al., 1998; Backman et al., 1999]. These studies have shown that the populations of normal and cancerous or dysplastic cell nuclei are clearly distinguishable. Cancerous and dysplastic nuclei are noticeably enlarged and have higher refractive index (Chapter 5).

Clinical Diagnosis of Dysplasia using LSS

We have performed in vivo human studies to test the potential of this technique to diagnose dysplasia and CIS in four different organs with three different types of epithelium: columnar epithelia of the colon and Barrett's esophagus, transitional epithelium of the urinary bladder, and stratified squamous epithelium of the oral cavity (Chapter 6) [Backman et al., 2000]. All clinical studies were performed during routine endoscopic screening or surveillance

procedures. In all of the studies an optical fiber probe delivered white light from a xenon arc lamp to the tissue surface and collected the returned light. The probe tip was brought into gentle contact with the tissue to be studied. Immediately after the measurement, a biopsy was taken from the same tissue site. The biopsied tissue was prepared and examined histologically by an experienced pathologist in the conventional manner. The spectrum of the reflected light was analyzed and the nuclear size distribution determined.

This size distribution was then used to obtain the percentage of nuclei larger than 10 micron, and the total number of nuclei per unit area (population density). As noted above, these parameters quantitatively characterize the degree of nuclear enlargement and crowding, respectively. Figure 6.3 displays these LSS parameters in binary plots to show the degree of correlation with histological diagnoses. In all four organs, there is a clear distinction between dysplastic and non-dysplastic epithelium. Both dysplasia and CIS have a higher percentage of enlarged nuclei and, on average, a higher population density, which can be used as the basis for spectroscopic tissue diagnosis.

Recently we have developed a novel optical diagnostic technique, called tri-modal spectroscopy (TMS), that combined the diagnostic capabilities of LSS with those of two other optical techniques: intrinsic fluorescence spectroscopy (IFS) and diffuse reflectance spectroscopy (DRS). Clinical studies in the esophagus and the uterine cervix showed that TMS enables to achieve a higher sensitivity and specificity of dysplasia diagnosis than LSS, IFS, or DRS alone [Georgakoudi et al., 2001].

These results demonstrate that LSS and TMS have the potential to provide a means for detecting epithelial precancerous lesions and pre-invasive cancers

throughout the body. LSS is advantageous compared to conventional diagnostic techniques in that it can provide objective, quantitative results in real time without the need for tissue removal. The first clinical application may be to guide random biopsy of previously undetectable, endoscopically invisible lesions. This could lead to significantly improved efficacy of cancer screening and surveillance procedures.

Imaging with LSS

In the clinical studies reported in Chapter 6, LSS has been restricted to sampling of millimeter-size regions of tissue using a contact probe. We have developed an LSS-based imaging technique, which can map variations in the size of epithelial cell nuclei of living tissues over wide surface areas (Chapter 7) [Gurjar et al., 2001]. The resulting functional images provide direct quantitative measures of nuclear enlargement and chromatin content, which can be translated into clinical diagnoses. The technique can be used for non-invasive or minimally invasive detection of precancerous changes in a variety of organs, such as the colon and oral cavity.

The technique was first tested and the LSS imaging device was calibrated in a series of well-controlled experiments with various tissue models. In order to test the applicability of LSS imaging we performed experiments with *ex vivo* colon tissue samples that were obtained immediately after resection from patients undergoing colectomy for familial adenomatous polyposis.

Colonic adenomas are precancerous dysplastic lesions exhibiting all of the characteristics of dysplastic lesions, including cell nuclear enlargement, pleomorphism and hyperchromasia. The adenomas are surrounded by normal

247

tissue covered by a single layer of epithelial cells. We imaged an adenoma surrounded by nondysplastic colon mucosa using the LSS apparatus. For each pixel (25 μm x 25 μm) of the imaged field (1.3 cm x 1.3 cm) a spectrum of light backscattered by the nuclei was first distinguished from the rest of the reflected light using polarization discrimination and then analyzed using the Mie theory-based computerized algorithm. The parameters obtained were the size and refractive index of the nuclei in each pixel. The imaged field was divided into 125 μm x 125 μm regions and the percentage of nuclei larger than 10 μm was obtained for each of these areas. Our previous studies [Backman et al., 2000] have shown that this statistic, which characterizes the degree of nuclear enlargement, is highly significant for diagnosis of dysplastic lesions in the colon and several other organs.

The resulting color-coded plot is shown in Fig. 7.10(a). As expected, the nuclei are enlarged in the central, adenomatous region, but not in the surrounding non-dysplastic tissue. Figure 7.10(b) is an LSS image of the spatial distribution of the mass of nuclear chromatin displayed in units of picograms per nucleus. These values were derived from the knowledge of the diameter and the refractive index of the nuclei, obtained from our LSS image. It is known that the nuclear solid mass correlates with the chromatin content. One can see that in the region of the polyp, the chromatin content is larger than in the surrounding normal tissue. This condition is an indication of dysplasia.

Measurement of Subcellular Structure on Submicron Scale with Scattering Angle Sensitive LSS

Capabilities of LSS are not limited to measuring cell nuclear size and chromatin content. It can provide quantitative information about internal structure

of the nuclei and other subcellular structures as well (Chapter 8). It has been known that large particles, such as nuclei, scatter predominantly in the near backward directions and, for such angles, cell nuclei are major sources of scattering. On the other hand, light scattered by structures smaller than the wavelength of light dominates the scattering signal at larger angles [Newton, 1969]. Thus, analysis of the spectra of light scattered at larger angles can reveal information about sub-nuclear inclusions and subcellular organization at submicron scale.

We have developed a novel modality of LSS, scattering angle sensitive LSS (a/LSS), which enables to measure both the spectral and angular distributions of the scattered light. The device was calibrated in the experiments with polystyrene beads and cell monolayers. We have found that the cell nuclei scatter predominantly within a narrow cone (1-2°) near the exact backward direction, in agreement with our previous results as well as theoretical calculations. Therefore, the signal measured within such a narrow solid angle provides information about the size and refractive index of the cell nuclei. However, the signal scattered into larger scattering angles (>3°) with 45° azimuth in respect to the polarization of the incident light provides information about subcellular structure at submicron scale. Specifically, it enables to measure the spectral exponent, β, which characterizes the variations of refractive index inside the cells and, thus, the variations of intracellular density.

In the experiments with animal models of carcenogenesis (Fisher 344 rats, which were subcutaneously administered esophagus-specific carcinogen nitrosomethylbenzylamine), we have established that β measured using a/LSS in living epithelia of the rats decreases with the degree of carcinogen administered to the animals and, thus, the degree of dysplasia induced in the rats' esophageal

epithelium. As discussed in Chapter 8, lower values of β for dysplastic cells might indicate 1) increased average size of the structural components within the cell, 2) increased entropy of cell organization, and 3) lower fractal dimension of the intracellular structure as well as that of the relatively large cellular organelles, i.e. the nuclei. Because these characteristics correlate with human visual perception of roughness, clumping, and margination, the parameters characterizing irregularity of subcellular and sub-nuclear structure might be suited to quantify the alterations of nuclear chromatin texture and disorganization of the cell structure in general in an objective manner.

Summary of Summary

1. LSS enables *in vivo* and/or *ex vivo* measurement of (1) nuclear size distribution, (2) nuclear refractive index, (3) amount and concentration of nuclear chromatin, and (4) subcellular structure on submicron scale.

2. LSS enables quantification of (1) nuclear enlargement, (2) pleomorphism, (3) hyperchromasia, (4) cell crowding. LSS has a potential to provide a means to quantify (5) chromatin clumping, (6) abnormal nuclear texture, and (7) disorganized cell and nuclear structure.

3. LSS enables *in vivo* diagnosis of dysplasia in (1) Barrett's esophagus, (2) colon, (3) bladder, (4) oral cavity, (5) cervix.

4. Several modalities of LSS has been developed: (1) LSS with non-polarized light, (2) LSS with polarized light, (3) imaging with LSS, (4) scattering angle sensitive LSS.

5. Accuracy of LSS measurements: nuclear size ~ 0.05-0.1 μm, nuclear refractive index ~ 0.001, concentration of nuclear chromatin ~ 0.02 pg/μm^3 , spatial resolution of LSS imaging – single cell.

9.2 Potential Applications of LSS

LSS is still a young technology that has yet to reach the verge of maturity. We can envision that LSS will evolve in two dimensions: development of new technologies and development of new application (Table 9.1). On the site of technology, four types of instrumentation can be developed in the near future:

1) clinical LSS imaging system (non-endoscopic);

2) endoscope-compatible fiber-optic polarized LSS probe;

3) clinical endoscopic LSS imaging system; and

4) advanced scattering angle sensitive LSS system (a/LSS).

The design of the clinical LSS imaging system can be based on the principles of the existing LSS imaging apparatus used to map quantitative morphologic characteristics of *ex vivo* tissues (Chapter 7). It can be used to obtain LSS images of the surfaces of organs that can be directly accessed with visible light, such as the uterine cervix and the oral cavity.

The endoscope-compatible fiber-optic polarized LSS probe will have an advantage over the existing fiber-optic LSS instrumentation, because it will

provide an experimental means of diffusive background removal and will enable refractive index and nuclear size to be independently extracted from the LSS data.

Clinical endoscopic LSS imaging system can be used to image the surfaces of the endoscopically accessible organs, such as colon, esophagus, lungs, etc.

Applications

	Clinical Diagnosis	Clinical Research	Biological Understanding
Fiber optic probe for polarized LSS	Diagnosis of dysplasia in endoscopically accessible organs (esophagus, colon, lung, etc.)	Natural history of precancer and anticancer therapy in endoscopically accessible organs	*In vivo* study of organization of living tissues at submicron scale and its alterations with disease progression.
Clinical endoscopic LSS imaging system			
Clinical LSS imaging system	Diagnosis of dysplasia in directly accessible organs (cervix, oral cavity, etc.)	Natural history of precancer and anticancer therapy in directly accessible organs	
a/LSS apparatus	Development of novel diagnostic algorithms		Relation between genetics, cell structure, function, and pathogenesis.

Note: "Technologies" labels the rows vertically on the left side.

Table 9.1 Potential applications of LSS technology.

Finally, existing a/LSS system may serve as a prototype for an advanced a/LSS apparatus that will enable to collect information about angular and spectral properties of light scattering in a wider range of angles and will allow easy modification into an LSS imaging device with an adjustable spatial (pixel)

252

resolution. This system can be used to study the origin of light scattering in biological tissues and in some fundamental studies of cell organization and the relation between the structure, genetics, and function of cells.

We can anticipate several potential applications of LSS:

1) Clinical diagnosis: LSS has a potential to become a powerful tool to provide a biopsy-free clinical diagnosis of precancerous and early cancerous transformations in the epithelia of many human organs that can be optically accessed either directly or endoscopically. The relevant instrumentation will include the non-endoscopic and endoscopic LSS imaging systems as well as fiber optic polarized LSS probe. The later will most probably be used to provide TMS[1] diagnosis as well.

2) Clinical research: LSS will enable the first study of natural history of precancerous transformations and efficacy of various cancer therapies *in vivo*. For example, the following question can be answered during these studies, "Does low grade dysplasia in GI tract progress to high grade dysplasia?" The relevant instrumentation can include LSS imaging systems.

3) Fundamental studies / biological understanding of disease: LSS enables to probe the structure of cells and tissues with accuracy unattainable with conventional imaging techniques including optical microscopy. As discussed in the thesis, LSS is sensitive to size differences as small as 5 nm, accuracy comparable to that of electron microscopy. Moreover, LSS works on *living* tissues and cells. These capabilities of LSS will be

253

used to conduct studies that can elucidate the origin of the complexity existing in cells and their organelles, i.e. nuclei, and to reveal the relation between cell structure, genetics, function, and disease pathogenesis. The relevant instrumentation can include the a/LSS device with extended angular diapason and imaging capabilities.

In conclusion, LSS may find applications ranging from clinical diagnosis to fundamental understanding of disease and, thus, become an important technology advancing both the science and the practice of medicine.

---

[1] TMS: tri-modal spectroscopy. TMS combines three spectroscopic diagnostic techniques: LSS, IFS (intrinsic fluorescence spectroscopy), and DRS (diffuse reflectance spectroscopy).

References

Backman V, Gurjar R, Badizadegan K, Zonios G, Itzkan I, Dasari RR, Crawford JM, Van Dam J, Perelman LT and Feld MS, "Light Scattering Spectroscopy for Early Cancer Diagnosis", *Laser Spectroscopy*, World Scientific Publishing Co., Rainer Blatt *et al.* ed., 286-295 (1999).

Backman V, Gurjar R, Badizadegan K, Itzkan I, Dasari R, Perelman LT, Feld MS, "Polarized light scattering spectroscopy for quantitative measurement of epithelial structures in situ", *IEEE J. Sel. Topics Quantum Electron*, 5, 1019-1027 (1999).

Backman V, Wallace MB, Perelman LT, Arendt JT, Gurjar R, Muller MG, Zhang Q, G. Zonios G, Kline E, McGillican T, Shapshay S, Valdez T, Van Dam J, Badizadegan K, Crawford JM, Fitzmaurice M, Kabani S, Levin HS, Seiler M, Dasari RR, Itzkan I and Feld MS, "Light scattering spectroscopy: a new technique for clinical diagnosis of precancerous and cancerous changes in human epithelia", *Nature*, 406, 35-36 (2000).

Backman V, L.T. Perelman, J.T. Arendt, R. Gurjar, M.G. Muller, Q. Zhang, G. Zonios, E. Kline, T. McGillican, T. Valdez, J. Van Dam, M. Wallace, K. Badizadegan. J.M. Crawford, M. Fitzmaurice, S. Kabani, H.S. Levin, M. Seiler, R.R.Dasari, I. Itzkan, and M. S. Feld, "Light Scattering Spectroscopy: A New Technique for Clinical Diagnosis of Precancerous And Cancerous Changes in Human Epithelia", *Lasers in Life Sciences*, in press (2001).

Georgakoudi I, Jacobson BC, Backman V, Wallace M, Muller M, Zhuang Q, Badizadegan K, Sun D, Thomas G, Van Dam V, Feld MS, "The Combination of Fluorescence, Diffuse Reflectance, and Light Scattering Spectroscopy for the Improved Detection of Low- and High-grade Dysplasia in Patients with Barrett's Esophagus ", *Gastrointerology*, in press (2001).

Georgakoudi I, Sheets EE, Müller MG, Backman V, Crum CP, Badizadegan K, Dasari RR, Feld MS, "Tri-Modal Spectroscopy as a Tool for the Detection and Biochemical/Morphological Characterization of Cervical Pre-Cancers *In Vivo*", *Obstet. Gynecol.*, submitted (2001).

Gurjar R, Backman V, Badizadegan K, Dasari R, Itzkan I, Perelman LT, Feld MS, "Functional Imaging of Human Epithelia with Polarized Light Scattering Spectroscopy", *Nature Medicine*, to be published (2001).

Newton RG, *Scattering Theory of Waves and Particles* (McGraw-Hill Book Company, New York, 1969).

Perelman LT, Backman V, Wallace MB, Zonios G, Manoharan R, Nusrat A, Shields S, Seiler M, Lima C, Hamano T, Itzkan I, Van Dam J, Crawford JM and Feld MS, "Observation of periodic fine structure in reflectance from biological tissue: a new technique for measuring nuclear size distribution", *Phys. Rev. Lett.*, **80**, 627-630 (1998).

Zonios G, Perelman LT, Backman V, Manoharan R, Fitzmaurice M, Feld MS, "Diffuse Reflectance Spectroscopy of Human Adenomatous Colon Polyps *In Vivo*", *Appl. Opt.*, **38**, 6628-6637 (1999).

THESIS PROCESSING SLIP

FIXED FIELD: ill. _____ name _____

index _____ biblio _____

► **COPIES:** (Archives) Aero Dewey Barker Hum

Lindgren Music Rotch Science (Sche-Plough)

TITLE VARIES: ► ☐ _____

_____

_____

NAME VARIES: ► ☐ _____

_____

IMPRINT: (COPYRIGHT) _____

_____

► **COLLATION:** _____

_____

► **ADD: DEGREE:** _____ ► **DEPT.:** _____

► **ADD: DEGREE:** _____ ► **DEPT.:** _____

SUPERVISORS: _____

_____

Frhe   yo s +e Fra nce

NOTES:

	cat'r:	date:
		page: ► J104

► **DEPT:** _HST_

► **YEAR:** _2001_ ► **DEGREE:** _Ph. D._

► **NAME:** _BACKMAN, Vadim_